Spectral Finite Element Modelling and Damage Identification of Beam-like Structures Using Linear and Nonlinear Guided Waves

Shuai He

Thesis submitted in fulfilment of the requirements for the degree
of Doctor of Philosophy

The University of Adelaide
Faculty of Engineering, Computer and Mathematical Sciences
School of Civil, Environmental and Mining Engineering

This thesis is dedicated to my beloved parents.

Spectral Finite Element Modelling and Damage Identification of Beam-like Structures Using Linear and Nonlinear Guided Waves

By:

Shuai He

Supervised by:

Senior Lecturer Ching-Tai Ng, *Ph.D.,*
School of Civil, Environmental & Mining Engineering,
The University of Adelaide

Associate Professor Abdul Sheikh, *Ph.D.,*
School of Civil, Environmental & Mining Engineering,
The University of Adelaide

Senior Lecturer Togay Ozbakkaloglu, *Ph.D.,*
School of Civil, Environmental & Mining Engineering,
The University of Adelaide

Thesis submitted in fulfilment of the requirements for the degree of
Doctor of Philosophy
School of Civil, Environmental & Mining Engineering
Faculty of Engineering, Computer and Mathematical Sciences
The University of Adelaide
North Terrace, Adelaide, SA 5005, Australia
Tel: +61(8) 8303 4323
Fax: +61(8) 8303 4359
Email: shuai.he@adelaide.edu.au, zhenghai3336@gmail.com

Abstract

This thesis contains a series of journal papers focused on the development of the model-based approach for damage identification using guided waves. The proposed approach requires no baseline data. It can identify multiple damages such as characterising the number, location and the size of cracks in isotropic beams and delaminations in composite beams efficiently and accurately with quantifying the associated uncertainties using linear guided waves. It also investigate the plausibility of using the nonlinear guided wave for damage identification. Based on the modelling ability, this approach is able to extend to different kinds of structures with various types of damages.

In utilising the linear guided wave for damage detection, the efficient spectral finite element (SFE) method is used to simulate the guided wave propagation in beams for both isotropic and composite materials. An SFE crack element is developed to simulate crack-wave interaction and the guided wave mode-conversion effect resulted from an asymmetric open crack in the isotropic beam. The delamination is simulated by duplicated the nodes of SFE elements in the delaminated regions. The proposed SFE model is verified using three-dimensional (3D) finite element (FE) method and good agreements are found in the results.

Stochastic methods are applied for the proposed model-based approach in the identification of multiple damages. The Bayesian model class selection algorithm is employed to determine the number of damages. The Bayesian model updating method implemented with efficient transitional Markov Chain Monte Carlo (TMCMC) sampler is proposed to identify the location and size of the crack. The Bayesian updating with structural reliability method (BUS) using the efficient and robust algorithm, Subset simulation, is proposed to identify the location, delaminated layer and length of the delaminations. The uncertainties of the identification are provided. For validation, the proposed methods are experimentally executed using Laser vibrometre and good agreements are obtained in the results.

The proposed SFE model is extended to simulate the nonlinear guided waves resulted from both classical and contact nonlinearity. Numerical case studies and parametric study highlight the potential of the SFE model in simulating nonlinear guided waves. This suggests that the model-based approach employed the nonlinear feature of guided waves to identify damages in further research.

Statement of Originality

I, **Shuai He**, hereby declare that this work contains no material which has been accepted for the award of any other degree or diploma in any university or other tertiary institution in my name and, to the best of my knowledge and belief, contains no material previously published or written by another person, except where due reference has been made in the text. In addition, I certify that no part of this work will, in the future, be used in a submission in my name, for any other degree or diploma in any university or other tertiary institution without the prior approval of the University of Adelaide and, where applicable, any partner institution responsible for the joint award of this degree.

I give consent to this copy of my thesis when deposited in the University Library, being made available for loan and photocopying, subject to the provisions of the Copyright Act 1968.

The author acknowledges that copyright of published works contained within this thesis resides with the copyright holder(s) of those works.

I also give permission for the digital version of my thesis being made available on the web, via the University's digital research repository, the Library catalogue, the Australian Digital Thesis Program (ADTP) and also through web search engines, unless permission has been granted by the University to restrict access for a period of time.

Signed: ……………………………………………Date: …………………..

Acknowledgments

I would like to sincerely thank my respectable parents for their financial support to my tuition. Without their unconditional love, I cannot go this far and this work would hardly be completed. I also grateful thank my beloved grandparents for their generous love and understanding. Nothing can I do in return but only keep climbing every mountain in my life.

I gratefully acknowledge my principle supervisor Dr Ching-Tai Ng, Senior Lecturer and my co-supervisors Abdul Hamid Sheikh, Associate Professor and Dr Togay Ozbakkaloglu, Senior Lecturer. Without their supervision and great contributions, this presented thesis would not be possible. I am particularly grateful to Dr Ching-Tai Ng for not only his unreserved guidance but also the encouragement and emotional supports during my candidature.

I would also like to thank those who accompany me sharing their happy life and hardworking time with me in Adelaide. It makes my PhD journey colourful and memorable.

Finally, I would like to thank the University of Adelaide for offering me the precious opportunity to seek the light in the deep ocean of knowledge.

Table of Contents

List of Tables

List of Figures

Chapter 1

Introduction & general overview

Structural health monitoring (SHM) is essential in the monitoring and maintenance of structural serviceability in civil, irrigational and aeronautic engineering industries because of economic and safety reasons. It continuously examines the structural integrity and provides valuable information of early damages and deterioration of the structure. Guided wave-based damage detection techniques play an important role in SHM. It is capable to detect and characterise small and various types of damages for its sensitivity. It is also able to inspect large and inaccessible area of the structures due to its long propagation distance. In recent decades guided wave-based damage detection techniques have been widely applied in SHM to improve the structural safety, durability and reliability, and reduce the maintenance cost.

There are two major approaches using guided wave-based damage detection techniques: the non-model and model-based approaches. Non-model-based approaches detect and identify damages by recognising the subsequent changes in certain features between the damaged and healthy state of structures. However, it is difficult to obtain the baseline data of the intact structures in practice due to some unexpected factors such as environmental noise and natural vibration of the structures. This limits the achievements of the non-model-based approaches. On the other side, the model-based approaches detect and identify damages inversely. They treat the damage parameters e.g. damage location and geometry as input parameters of the model. Though updating the input parameters by minimising the discrepancy between the simulated and measured guided wave signal, the optimal input parameters can be found and used to describe the actual damage situation. The model-based approaches can be performed without any baseline data. Thus, they are able to provide more accurate identification of the structural damages than the non-model-based approach.

The accuracy and efficiency of the model-based approach heavily depend on the modelling method for the structure. Based on the modelling ability, this approach can be potentially applied to various types of structures with different kinds of damage. The identified characteristics of the damage also have the potential to be very detailed such as identifying the location, size and shape of the damage. However, existing modelling methods for guided waves are difficult to achieve both accuracy and efficiency concurrently. Furthermore, the optimisation methods to solve the inverse problem for model-based approach also have the limitation in both accuracy and efficiency. In addition, identifying multiple damages remains challenging for the model-based approach based on guided waves.

With the aim of better identification of damages, this thesis investigates both the modelling and optimisation methods for the model-based approach using guided waves. Two major sections are available in the thesis. The first section, from Chapters 2 to 4, focuses on linear guided waves. A new modelling method i.e. spectral finite element (SFE) method is proposed to simulate the linear guided wave propagation in a beam and its interaction with a crack. Novel model-based approaches are also proposed to identify multiple cracks in an aluminium beam and delaminations in composite. The second section, from Chapters 5 to 6, studies the performance of nonlinear guided waves. The SFE models are extended to simulate the nonlinear guided wave resulted from both contact and classical nonlinearities, respectively. The nonlinear features of guided waves simulated by these models can be further used in the model-based approach for damage identification.

The major research results and contributions in this thesis are presented in five journal papers. The titles of Chapters 2 to 6 are the same as that of the journal papers.

In Chapter 1, the background of the application regarding guided wave damage identification is provided. The research gaps and the research objectives have been clearly defined in this chapter. The general description of each chapter is presented.

In Chapter 2, an efficient time-domain SFE method using one-dimensional (1D) beam element is proposed to simulate the propagation of guided waves in isotropic beams. An SFE crack element is developed to simulate the interaction between the guided wave and an asymmetrical, elliptical shape, open crack. Because of the SFE crack element, the guided wave mode conversion effect is first simulated in the 1D SFE model. Thus, the proposed SFE model is able to provide both efficient and accurate simulation for studying guided waves in beam-like structures.

In Chapter 3, the developed 1D SFE model is employed in the model-based approach for the identification of multiple cracks in beam-like structures using guided waves. The Bayesian methods (i.e. Bayesian model class selection algorithm and Bayesian statistical framework) combined with the Transitional Markov Chain Monte Carlo (TMCMC) sampler are proposed to efficiently determine the number of cracks, the crack sizes and locations, and quantify the associated uncertainties. Numerical and experimental results demonstrate the accuracy and efficiency of the proposed method in multiple crack identification. The proposed method also shows its robustness under measurement noise and different situations of the cracks.

In Chapter 4, a probabilistic approach is proposed to identify multiple delaminations in laminated composite beams using guided waves. The Bayesian model class selection method is proposed to determine the number of delamination. The Bayesian model updating algorithm, which is implemented with Subset simulation, is used to efficiently identify the delamination locations, lengths and through-thickness locations and providing corresponding uncertainties. The proposed probabilistic approach is validated and investigated using data obtained from numerical simulations and experimental data. Results show that the method is accurate in multiple delamination identification considering measurement noise and modelling error.

In Chapter 5, a time-domain SFE model and analysis of the nonlinear guided waves interaction at a breathing crack are proposed. The SFE model is used to predict the nonlinear guided wave generation at breathing cracks. An SFE crack element implemented with a bilinear crack mechanism is proposed to simulate the contact nonlinearity at the crack. Physical insight into the higher harmonics generated due to the contact nonlinearity is presented. Numerical results also show that the mode-converted, nonlinear guided wave provides valuable information for damage identification.

In Chapter 6, the time-domain SFE mothed is extended to simulate the nonlinear guided wave resulted from both the classical and contact nonlinearities. The proposed model allows an efficient and accurate simulation of nonlinear guided waves in beam-like structures. Numerical case studies show that the amplitude of second harmonic increases with the number of cycles and the amplitudes of the excitation guided wave. Results also find that compared with the contact nonlinearity, the contribution due to classical nonlinearity to the second harmonic generation is very small.

In Chapter 7, the conclusions are summarized and recommendations have been provided for further research.

Chapter 2

Analysis of mode conversion and scattering of guided waves at cracks in isotropic beams using a time-domain spectral finite element method

(Paper 1, published)

Shuai He and Ching-Tai Ng

School of Civil, Environmental and Mining Engineering,

The University of Adelaide, Adelaide, South Australia, 5005, Australia

Publication:

HE, S. & NG, C. T 2015. Analysis of mode conversion and scattering of guided waves at cracks in isotropic beams using a time-domain spectral finite element method. *Elec J Struct Eng*, 14, 20-32.

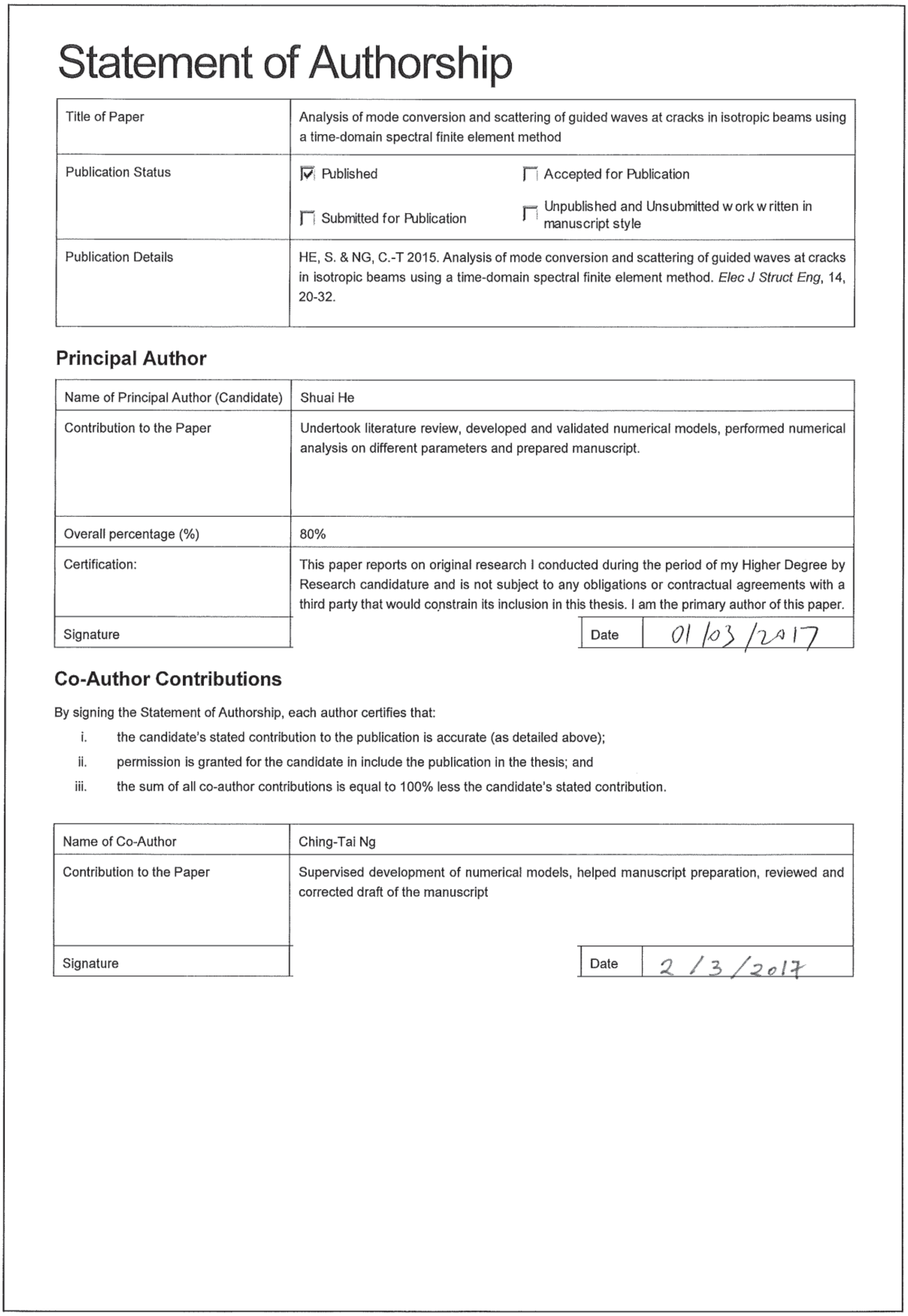

Statement of Authorship

Title of Paper	Analysis of mode conversion and scattering of guided waves at cracks in isotropic beams using a time-domain spectral finite element method
Publication Status	☑ Published ☐ Accepted for Publication ☐ Submitted for Publication ☐ Unpublished and Unsubmitted work written in manuscript style
Publication Details	HE, S. & NG, C.-T 2015. Analysis of mode conversion and scattering of guided waves at cracks in isotropic beams using a time-domain spectral finite element method. *Elec J Struct Eng*, 14, 20-32.

Principal Author

Name of Principal Author (Candidate)	Shuai He
Contribution to the Paper	Undertook literature review, developed and validated numerical models, performed numerical analysis on different parameters and prepared manuscript.
Overall percentage (%)	80%
Certification:	This paper reports on original research I conducted during the period of my Higher Degree by Research candidature and is not subject to any obligations or contractual agreements with a third party that would constrain its inclusion in this thesis. I am the primary author of this paper.
Signature	Date 01/03/2017

Co-Author Contributions

By signing the Statement of Authorship, each author certifies that:

i. the candidate's stated contribution to the publication is accurate (as detailed above);

ii. permission is granted for the candidate in include the publication in the thesis; and

iii. the sum of all co-author contributions is equal to 100% less the candidate's stated contribution.

Name of Co-Author	Ching-Tai Ng
Contribution to the Paper	Supervised development of numerical models, helped manuscript preparation, reviewed and corrected draft of the manuscript
Signature	Date 2/3/2017

Abstract

Detecting damages in its early stage, and hence, to ensure the safety and reliability of structures is of vital important. Guided waves have been recognised as one of the promising damage detection techniques that are sensitive to small and different types of damages. The understanding of guided wave propagation and scattering phenomena at the damages is one of the fundamental elements to facilitate the development of this technique for damage characterisation. This chapter presents a study of scattering characteristics and mode conversion effect of guided waves at cracks in isotropic beams. An efficient time-domain spectral finite element method using one-dimensional (1D) beam element is developed to solve this problem. The developed model is then used to carry out a series of case studies that consider different crack sizes in the beams. These parametric studies provide a fundamental physical insight into the mode conversion phenomena and scattering characteristics of guided wave at the cracks.

***Keywords*:**

Damage Detection, Guided Waves, Spectral Finite Element, Mode Conversion, Scattering

2.1 Introduction

The monitoring and maintenance of structural serviceability have increasingly attracted public attention in civil, mechanical and aeronautic engineering industries due to economic and safety reasons. Structural health monitoring (SHM) is of vital importance as it continuously examines the structural integrity and offers the valuable information of damages and material deterioration. SHM requires damage detection techniques that inspect the performance of individual structural components and detect any damage in its early stage. In recent decades, different methods (Fan and Qiao, 2011, Sohn et al., 2004, Carden and Fanning, 2004, Doebling et al., 1998, Doebling et al., 1996) have been applied to detect and characterise damage for increasing the safety, durability and reliability of structures, and also minimising their maintenance cost.

Among these methods, guided wave based approach has been proven to be one of the promising techniques for damage detection (Ostachowicz and Radzieński, 2012, Raghavan and Cesnik, 2007, Rose, 2002, Rose, 1999). This approach is capable of detecting the location and determining the severity of small damages with high efficiency and outstanding sensitivity. An understanding of guided wave propagation and scattering characteristics plays one of the important roles in the development of damage detection methods.

Accurate prediction of guided wave is difficult due to its complicated propagation characteristics. For example, analytical modelling methods provide exact solutions for guided wave scattering at damages but they are not applicable for three-dimensional (3D) situation and complex structures. Numerical methods, such as finite element (FE) method (Hong et al., 2013, Veidt and Normandin, 2013, Moser et al., 1999), finite difference (FD) method (Xu et al., 2003, Chu and Chaudhuri, 1989) and boundary element (BE) method (Zhao and Rose, 2003) are suitable for solving wave propagation problems in complex structures but they are computationally expensive.

Other numerical methods, such as finite strip element (FSE) method (Bergamini and Biondini, 2004, Liu, 2002), which is developed based on low level of discretisation, has difficulty in obtaining proper strip stiffness and mass matrix. Local interaction simulation approach (LISA) is impractical in constructing the distribution of the mass matrix (Delsanto et al., 1997, Delsanto et al., 1994, Delsanto et al., 1992). The fast Fourier transform (FFT) based spectral finite element (SFE) method (Ajith and Gopalakrishnan, 2013, Deepak et al., 2012, Ng et al., 2009) were reported to be computationally efficient but it is not capable in simulating complex structures. Specifically, this method assumes that one side of the modelled beam must be infinitely long, which is impracticable in real applications for monitoring civil and mechanical engineering structural components.

Among all the numerical methods, the time domain SFE method (Rucka et al., 2012, Li et al., 2012, Kudela et al., 2007, Kudela and Ostachowicz, 2009) is more suitable to simulate the guided wave propagation in geometrically complex structures. It combines the advantages of FE method and spectral method (Boyd, 2001). The SFE method has the same flexibility of discretisation as FE method and the use of high order Gauss-Lobatto-Legendre (GLL) approximation polynomials leads to a diagonal mass matrix, and hence, the guided wave propagation simulation can be solved efficiently using the explicit central difference method.

It is well known that the mode conversion of guided waves occurs when the waves interacting with non-axisymmetric discontinuities. This phenomenon has been investigated by a number of studies (Benmeddour et al., 2008, Shkerdin and Glorieux, 2004, Lowe et al., 2002, Castaings et al., 2002). Understanding this behaviour is of significant importance because it provides more information for damage identification. However, the study of the mode conversion effect usually requires two-dimensional (2D) SFE model with the assumptions based on the through-thickness mechanical displacement-field displacement or 3D SFE models (Xu et al., 2014, Zhou et al., 2013, Zhou and Ichchou, 2011, Benmeddour et al., 2008), which are computational expensive.

In order to solve the problem, a spectral cracked beam element is developed for the 1D SFE model to study the mode conversion effect of guided waves at the cracks in this chapter.

The aims of this chapter are to determine the scattering characteristics of guided waves at the cracks in the isotropic beam with rectangular cross section using 1D SFE method. This method can be easily adapted to 2D and 3D modelling. Also, a 1D spectral crack element is proposed to couple the longitudinal, shear and bending displacements, and hence, enabling the prediction of mode conversion effects. Different locations, depths and widths of the cracks are considered in this study. In addition, this 1D SFE model will be verified by a 3D conventional FE beam model with the response signal measured at the centre of the left end of the beam.

The organisation of this chapter is presented as follow. The simulation of guided wave propagation using the proposed SFE method and the formulation of the SFE crack element are first described in Section 2.2. In Section 2.3, the verification of the SFE model using commercial FE software, ABAQUS, is presented and the mode conversion effect is then discussed in detail. After that, a parametric study is conducted to study the scattering characteristics of guided waves at the cracks in Section 2.4. Finally conclusions are drawn in Section 2.5.

2.2 Time domain spectral finite element method

Guided wave propagation in structures can be expressed using the dynamic equilibrium equation as: (Reddy, 2006)

$$\mathbf{M}\ddot{\mathbf{Q}} + \mathbf{C}\dot{\mathbf{Q}} + \mathbf{K}\mathbf{Q} = \mathbf{F} \tag{2.1}$$

where $\mathbf{M}$, $\mathbf{C}$ and $\mathbf{K}$ are the global mass matrix, damping matrix and stiffness matrix, respectively. $\mathbf{F}$ is the time domain excitation force vector. It is assumed that the global damping matrix $\mathbf{C}$ is proportional to the mass matrix as $\mathbf{C} = \eta\mathbf{M}$, and η is the damping coefficient. $\mathbf{Q}$, $\dot{\mathbf{Q}}$ and $\ddot{\mathbf{Q}}$ are the displacement, velocity and acceleration vectors, respectively.

In Equation (2.1), the global mass matrix $\mathbf{M}$, stiffness matrix $\mathbf{K}$ and force vector $\mathbf{F}$ are determined by assembling the element matrix $\mathbf{M}^e$, $\mathbf{K}^e$ and $\mathbf{F}^e$, which expressions are similar to the conventional FE method (Reddy, 2006) and are defined as

$$\mathbf{M}^e \approx \sum_{i=1}^{n} w_i \mathbf{N}(\xi_i)^T \boldsymbol{\mu} \mathbf{N}(\xi_i) detJ(\xi_i) \tag{2.2}$$

$$\mathbf{K}^e \approx \sum_{i=1}^{n} w_i \mathbf{B}(\xi_i)^T \mathbf{D} \mathbf{B}(\xi_i) detJ(\xi_i) \tag{2.3}$$

$$\mathbf{F}^e \approx \sum_{i=1}^{n} w_i \mathbf{N}(\xi_i)^T \mathbf{p}(\xi_i) detJ(\xi_i) \tag{2.4}$$

where $\boldsymbol{\mu}$, $\mathbf{D}$ and $\mathbf{p}(\xi_i)$ are the mass density matrix, stress-strain matrix and external force vector, respectively. $\mathbf{N}(\xi_i)$ is the spectral shape function, $\mathbf{B}(\xi_i)$ is the strain-displacement operator and J is the Jacobian functions mapping the element nodes from local domain to global domain, which are expressed in a general form

$$\mathbf{N}_i(\xi) = \prod_{m=1, m\neq i}^{n} \frac{\xi - \xi_m}{\xi_i - \xi_m}, \; i(i \in 1, 2, ..., n) \tag{2.5}$$

$$\mathbf{B}(\xi) = \mathbf{L}\mathbf{N}_i(\xi), \quad and \quad J = \frac{\partial x}{\partial \xi} \tag{2.6}$$

where n is the number of total integrated nodes and m is the order of node considered. $\mathbf{L}$ is the differential operator based on wave propagation theories and its formula is given in Section 2.2. The abscissas ξ_i of each integrated

GLL node are shown in Figure 2.1, which can be obtained by calculating the roots of the following equation (Pozrikidis, 2005)

$$\left(1-\xi^2\right)P'_{n-1}\left(\xi\right)=0,\ \xi_i\in[-1,1] \tag{2.7}$$

where P'_{n-1} is the first derivative of the (n-1)th order of Legendre polynomial. The weights w_i corresponding to the abscissa ξ_i can be calculated from the following equation (Pozrikidis, 2005)

$$w_i=\frac{2}{n\left(n-1\right)[P_{n-1}\left(\xi_i\right)]^2} \tag{2.8}$$

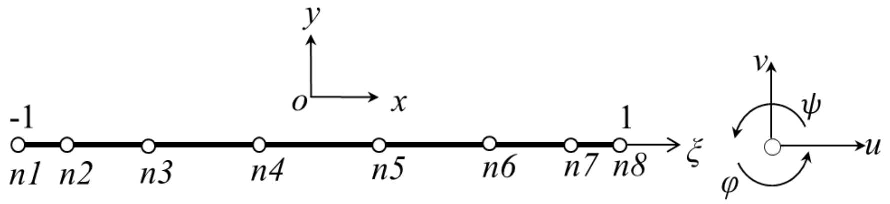

Fig. 2.1 Distribution of GLL nodes and the degrees-of freedom at each node.

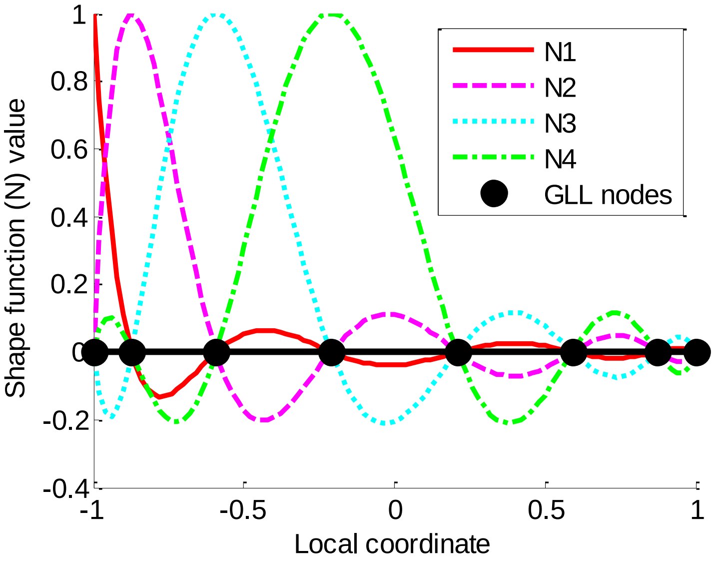

Fig. 2.2 First four 8-node element’s shape functions.

Applying this GLL integration, the spectral shape function has the following properties (Ostachowicz et al., 2012)

$$\mathbf{N}_j\left(\xi_i\right)=\delta_{ji},\ j(j\in 1,2,...,n) \text{ and } \sum_{j=1}^{n}\mathbf{N}_j\left(\xi_i\right)=1 \tag{2.9}$$

where δ_{ji} is the Kroneker delta. As shown in Figure 2.2 (Kudela et al., 2007), the spectral shape function is orthogonal, and hence, a diagonal local mass matrix $\mathbf{M}^e$ can be obtained using this spectral shape function. As a result, the explicit time integration scheme, i.e. central difference method (Ostachowicz et al., 2012) can be used to solve the dynamic Equation (2.1) efficiently. Furthermore, the Runge effect is avoided by the application of this GLL-node element (Pozrikidis, 2005). Based on the aforementioned equations, the SFE model for wave propagation in beams can be developed based on the Mindlin-Herrmann rod and Timoshenko beam theory.

2.2.1 Mindlin-Herrmann rod and Timoshenko beam theory

The Mindlin-Herrmann rod theory is used to simulate the longitudinal wave propagation in the proposed model, while Timoshenko beam theory is employed to simulate the flexural wave propagation. The Mindlin-Herrmann rod theory introduces the independent lateral contraction $\psi(x)$ to approximate the Poisson effect (Mindlin and Herrmann, 1951) due to the longitudinal wave propagation, while the Timoshenko beam theory considers the effect of shear deformation and introduces the independent rotation $\varphi(x)$ as shown in Figure 2.1. The beam element has n nodal points, in which each nodal point has four degree-of-freedoms (DoFs). The displacement field can be expressed as

$$\begin{aligned}\bar{u}\left(x,y\right)&\approx u\left(x\right)-y\varphi\left(\mathrm{x}\right)\\ \bar{v}\left(x,y\right)&\approx\psi\left(x\right)y+v\left(x\right)\end{aligned} \tag{2.10}$$

where $v(x)$ is the independent vertical displacement introduced based on the Timoshenko beam theory, $u(x)$ is the longitudinal displacement by Mindlin-Herrmann rod theory and y is the vertical distance from neutral axis.

The governing equations for Mindlin-Herrmann rod theory are defined as: (Doyle, 1989)

$$\begin{aligned} &\frac{2GA}{1-\upsilon}\left(\frac{\partial^2 u}{\partial x^2}+\upsilon\frac{\partial\psi}{\partial x}\right)=\rho A\ddot{u}-p(x,t) \\ &K_1^M GI\frac{\partial^2\psi}{\partial x^2}-\frac{2GA}{1-\upsilon}\left(\upsilon\frac{\partial\psi}{\partial x}+\psi\right)=K_2^M\rho I\ddot{\psi} \end{aligned} \tag{2.11}$$

where E, G, A, υ, ρ and I denote the Young's modulus, shear modulus, cross-section area, Poisson's ratio, mass density and moment of inertia, respectively. $p(x,t)$ is the longitudinal excitation, and t and x are its temporal and spatial variables, respectively.

The kinetic energy T_M and the strain energy U_M for Mindlin-Herrmann rod theory can be expressed as

$$\begin{aligned} T_M &= \frac{1}{2}\int_L(\rho A\dot{u}^2+K_2^M\rho I\dot{\psi}^2)dx \\ U_M &= \frac{1}{2}\int_L\left\{\frac{EA}{1-\upsilon^2}\left[\left(\frac{\partial u}{\partial \mathrm{x}}\right)^2+\psi^2+2v\frac{\partial u}{\partial \mathrm{x}}\psi\right]+K_1^M GI\left(\frac{\partial\psi}{\partial \mathrm{x}}\right)^2\right\}dx \end{aligned} \tag{2.12}$$

The governing equations for Timoshenko beam theory are defined as: (Doyle, 1989)

$$\begin{aligned} K_1^T GA \frac{\partial}{\partial x}\left(\frac{\partial v}{\partial x} - \varphi\right) &= \rho A \ddot{v} - f\left(x,t\right) \\ I\frac{\partial^2 \varphi}{\partial x^2} - K_1^T GA\left(\frac{\partial v}{\partial \mathrm{x}} - \varphi\right) &= K_2^T \rho I \ddot{\varphi} \end{aligned} \tag{2.13}$$

where $f\left(x,t\right)$ is the transverse excitation.

The kinetic energy T_T and the strain energy U_T for Timoshenko beam theory can be expressed as

$$\begin{aligned} T_T &= \frac{1}{2}\int_L (\rho A \dot{v}^2 + K_2^T \rho I \dot{\varphi}^2) dx \\ U_T &= \frac{1}{2}\int_L \left\{ EI\left(\frac{\partial \varphi}{\partial \mathrm{x}}\right)^2 + K_1^T GA\left(\frac{\partial v}{\partial \mathrm{x}} - \varphi\right)^2 \right\} dx \end{aligned} \tag{2.14}$$

where K_1^M, K_2^M, K_1^T, and K_2^T are adjustable variables that influence the group speed of wave propagation and they can be determined experimentally. (Doyle, 1989)

2.2.2 Spectral element modelling

Considering the Mindlin-Herrmann rod theory and Timoshenko beam theory, the strains can be represented in the following form: (Rucka, 2010)

$$\boldsymbol{\varepsilon} = \begin{Bmatrix} \boldsymbol{\varepsilon}^M \\ \boldsymbol{\varepsilon}^T \end{Bmatrix} = \begin{Bmatrix} \mathbf{L}^M & 0 \\ 0 & \mathbf{L}^T \end{Bmatrix} \begin{Bmatrix} \mathbf{u}^M \\ \mathbf{v}^T \end{Bmatrix} \tag{2.15}$$

where the superscripts *M* and *T* denote the Mindlin-Herrmann rod theory and Timoshenko beam theory, respectively. The total strain consists of $\boldsymbol{\varepsilon}^M$ and $\boldsymbol{\varepsilon}^T$, which have the following forms

$$\boldsymbol{\varepsilon}^M = \begin{bmatrix} \dfrac{\partial u}{\partial x} \\ \psi \\ \dfrac{\partial \psi}{\partial \mathrm{x}} \end{bmatrix} \text{ and } \boldsymbol{\varepsilon}^T = \begin{bmatrix} \dfrac{\partial v}{\partial x} - \varphi \\ \dfrac{\partial \varphi}{\partial x} \end{bmatrix} \tag{2.16}$$

$\mathbf{L}^M$ and $\mathbf{L}^T$ are the differential operators, and $\mathbf{u}^M$ and $\mathbf{u}^T$ are displacements, they are denoted as

$$\mathbf{L}^M = \begin{bmatrix} \dfrac{\partial}{\partial x} & 0 \\ 0 & 1 \\ 0 & \dfrac{\partial}{\partial x} \end{bmatrix} = \begin{bmatrix} \dfrac{1}{J}\dfrac{\partial}{\partial \xi} & 0 \\ 0 & 1 \\ 0 & \dfrac{1}{J}\dfrac{\partial}{\partial \xi} \end{bmatrix}$$

$$\mathbf{L}^T = \begin{bmatrix} \dfrac{\partial}{\partial x} & -1 \\ 0 & \dfrac{\partial}{\partial x} \end{bmatrix} = \begin{bmatrix} \dfrac{1}{J}\dfrac{\partial}{\partial \xi} & -1 \\ 0 & \dfrac{1}{J}\dfrac{\partial}{\partial \xi} \end{bmatrix} \tag{2.17}$$

$$\mathbf{u}^M = \begin{bmatrix} u \\ \psi \end{bmatrix}, \ \mathbf{u}^T = \begin{bmatrix} v \\ \varphi \end{bmatrix} \tag{2.18}$$

The mass density matrix $\boldsymbol{\mu}$ in Equation (2.2) and the stress-strain matrix $\mathbf{D}$ in Equation (2.3) are denoted as below

$$\mathbf{D} = \begin{Bmatrix} \mathbf{D}^M & 0 \\ 0 & \mathbf{D}^T \end{Bmatrix}, \quad \boldsymbol{\mu} = \begin{Bmatrix} \boldsymbol{\mu}^M & 0 \\ 0 & \boldsymbol{\mu}^T \end{Bmatrix} \tag{2.19}$$

where

$$\mathbf{D}^M = \begin{bmatrix} \dfrac{EA}{1-\upsilon^2} & \dfrac{\upsilon EA}{1-\upsilon^2} & 0 \\ \dfrac{\upsilon EA}{1-\upsilon^2} & \dfrac{EA}{1-\upsilon^2} & 0 \\ 0 & 0 & K_1^M GI \end{bmatrix} \tag{2.20}$$

$$\mathbf{D}^T = \begin{bmatrix} K_1^T GA & 0 \\ 0 & EI \end{bmatrix}$$

and

$$\boldsymbol{\mu}^M = \begin{bmatrix} \rho A & 0 \\ 0 & K_2^M \rho I \end{bmatrix}, \ \boldsymbol{\mu}^T = \begin{bmatrix} \rho A & 0 \\ 0 & K_2^T \rho I \end{bmatrix} \tag{2.21}$$

Based on the number of DoFs considered, the spectral shape function has the following expression

$$\mathbf{N}_i(\xi) = \begin{bmatrix} N_i(\xi) & 0 & 0 & 0 \\ 0 & N_i(\xi) & 0 & 0 \\ 0 & 0 & N_i(\xi) & 0 \\ 0 & 0 & 0 & N_i(\xi) \end{bmatrix} \tag{2.22}$$

The element mass matrix $\mathbf{M}^e$, stiffness matrix $\mathbf{K}^e$ and external force matrix $\mathbf{F}^e$ can be obtained by substituting Equations (2.19), (2.20), (2.21) and (2.22) into (2.2), (2.3) and (2.4). The global matrices can be obtained by assembling the element matrices, and hence, the guided wave can be simulated by solving Equation (2.1).

2.2.3 Crack element modelling

The crack element contains a single transverse opened crack, which is modelled using a two-node beam element with three DoFs per node, i.e., $u(x), v(x)$ and $\varphi(x)$. There is no lateral contraction considered in this crack element so when the crack element is connected to the beam elements, the transmitted displacements $\psi\left(x\right)$ are assumed to be zero. This is because the lateral contraction caused by low frequency waveguide (e.g. 100 kHz) in the Mindlin-Herrmann rod theory is inconsequential compared with the rotation $\varphi\left(x\right)$ in the Timoshenko beam theory. Hence, there are totally six DoFs (i.e. $q_1, q_2, ..., q_6$) in this crack element as shown in Figure 2.3(a). In order to account for the presence of the crack, the stiffness matrix has been modified similarly using the approach proposed by Darpe et al. (2004) with considering the coupled effects for three DoFs of each node, i.e., longitudinal, shear and rotation of displacements. It is assumed that the cross-section of the beam is rectangle in this chapter.

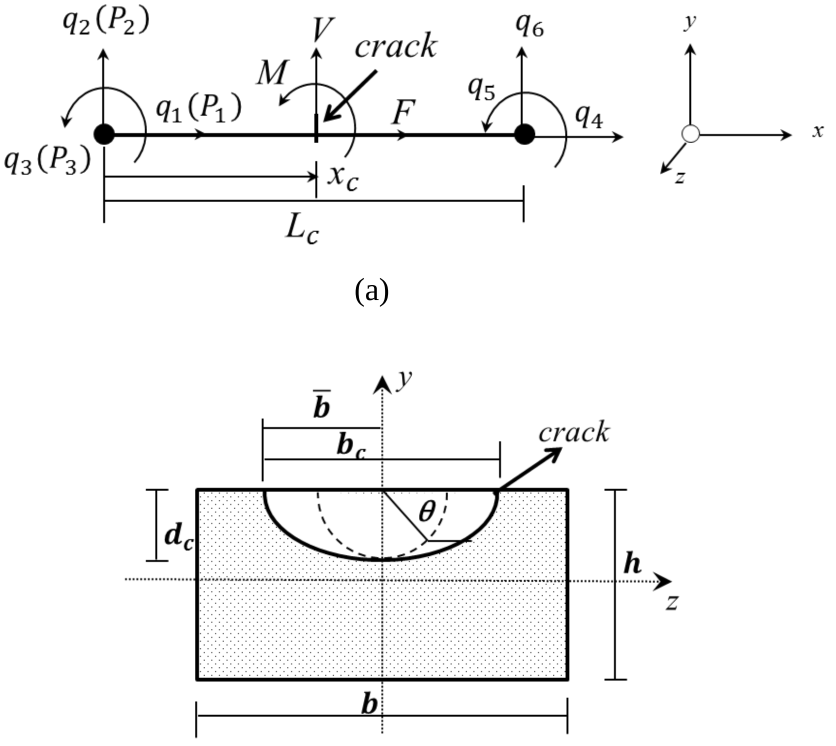

(a)

(b)

Fig. 2.3 (a) Schematic diagram of the crack element; (b) cross-section of the beam at the crack location.

The geometry of the crack element is shown in Figure 2.3(b). It has width (b), depth (h) and length (L_c), with a crack located at a distance x_c from the left end of the element having width b_c and depth d_c. In addition, each DoF at the first node of the crack element is assumed to be loaded with axial force P_1, shear force P_2 and bending moment P_3, correspondingly.

In order to obtain the modified stiffness matrix for the SFE method, the flexibility matrix is first calculated using Castigliano's theorem

$$q_{ii} = \frac{\partial U}{\partial P_{ii}}, \left(ii \in 1, 2, 3\right) \tag{2.23}$$

where q_{ii} is the displacement of the first node corresponded to the *ii*th DoF. U is the total strain energy, which has the following form: (Tada et al., 2000)

$$U = U^u + U^c \tag{2.24}$$

where U^u is the elastic strain energy for uncracked element while U^c is the strain energy caused by the crack. Thus Equation (2.23) becomes

$$q_{ii} = q_{ii}^u + q_{ii}^c = \frac{\partial U^u}{\partial P_{ii}} + \frac{\partial U^c}{\partial P_{ii}} \tag{2.25}$$

where q_{ii}^u and q_{ii}^c are the displacement of uncracked beam and the additional displacement due to crack, respectively.

Considering the action of axial force *F*, shear force *V* and bending moment *M* at x_c (Figure 3a), the uncracked strain energy of the element can be expressed as

$$U^u = \frac{1}{2}\int \left[\frac{\alpha_s V^2}{GA} + \frac{F^2}{EA} + \frac{M^2}{EI} \right] dx \tag{2.26}$$

where $\alpha_s = 10(1+\upsilon)/(12+11\upsilon)$ is the shear coefficient for rectangular cross section (Kawashima, 1996, Cowper, 1966).

In Equation (2.26), F , V and M have the following relationships with external nodal forces

$$F\left(x\right)=p_1,\ V\left(x\right)=p_2 \text{ and } M\left(x\right)=p_2x_c-p_3 \tag{2.27}$$

Thus Equation (2.26) can be rewritten as

$$U^u=\frac{1}{2}\left[\frac{P_1^2L_c}{EA}+\frac{\alpha_s\,P_2{}^2L_c}{GA}+\frac{P_2L_c^3}{3EI}-\frac{P_2\,P_3L_c^2}{EI}+\frac{P_3{}^2L_c}{EA}\right] \tag{2.28}$$

Considering Equation (2.23), the individual displacement of undamaged beam q_{ii}^u can be expressed as

$$\begin{gathered}
q_1^u=\frac{\partial U^u}{\partial P_1}=\frac{P_1L}{EA} \\
q_2^u=\frac{\partial U^u}{\partial P_2}=\left(\frac{\alpha_sL}{GA}+\frac{L^3}{3EI}\right)P_2-\frac{L^2}{2EI}P_3 \\
q_3^u=\frac{\partial U^u}{\partial P_3}=\frac{L}{EA}P_3-\frac{L^2}{2EI}P_2
\end{gathered} \tag{2.29}$$

Similarly, the additional displacement q_{ii}^c due to the crack can be obtained using the cracked strain energy from Equation (2.23)

$$q_{ii}^c=\frac{\partial U^c}{\partial P_{ii}} \tag{2.30}$$

$$U^c=\int_A S\left(A\right)dA \tag{2.31}$$

where $S\left(A\right)$ is the strain energy density function and it is defined as

$$S\left(A\right)=\frac{1}{E'}\left[\left(\sum_{ii=1}^{3}K_{Iii}\right)^2+\left(\sum_{ii=1}^{3}K_{IIii}\right)^2\right] \tag{2.32}$$

where K_{Iii} and K_{IIii} are the stress intensity factors (SIFs) for the first and second mode of the crack displacement corresponding to q_{ii}. $E'=E$ for plane strain, and $E'=E/(1-\upsilon^2)$ for plane stress situation. The derivation of SIFs is written as follows.

SIFs for the first mode I (sliding):

$$K_{I1}=\sigma_1\sqrt{\frac{\pi d_c}{Q}}F_I$$

where $$\sigma_1=\frac{P_1}{bh}$$

Thus $$K_{I1}=\frac{P_1}{bh}\sqrt{\frac{\pi d_c}{Q}}F_I \tag{2.33}$$

$$K_{I3}=\sigma_3 H\sqrt{\frac{\pi d_c}{Q}}F_I$$

where $$\sigma_3=\frac{6M_1}{bh^2}=\frac{6\left(P_2x_c-P_3\right)}{bh^2}$$

Hence $$K_{I3}=\frac{6\left(P_2x_c-P_3\right)}{bh^2}H\sqrt{\frac{\pi d_c}{Q}}F_I \tag{2.34}$$

$$K_{I2}=0$$

SIFs for the second mode II (tearing):

$$K_{II2}=\sigma_2\sqrt{\pi d_c}F_{II}$$

where $$\sigma_2=\frac{\alpha_s P_2}{bh}$$

Hence $$K_{II2} = \frac{\alpha_s P_2}{bh}\sqrt{\pi d_c} F_{II} \tag{2.35}$$

$$Q = 1 + 1.464(coe)^{1.65} \tag{2.36}$$

The function F_I (Newman Jr and Raju, 1981) and F_{II} (He and Hutchinson, 2000) are the boundary-calibration factors corresponding to tension and shear for $0 < d_c/\bar{b} \le 1$, $0 \le d_c/h < 1$, $\bar{b}/b \le 0.5$ and $0 \le \theta \le \pi$, which have the forms

$$F_I = \left[M_1 + M_2\left(\frac{d_c}{h}\right)^2 + M_3\left(\frac{d_c}{h}\right)^4 \right] f_\theta g f_w \tag{2.37}$$

$$F_{II} = \frac{m(d_c/h)\cos\theta}{B\left[\sin^2\theta + (d_c/h)^2\cos^2\theta\right]^{1/4}} \tag{2.38}$$

where

$$M_1 = 1.13 - 0.09(coe)$$
$$M_2 = -0.54 + \frac{0.89}{0.2 + (coe)} \tag{2.39}$$
$$M_3 = -0.5 - \frac{1.0}{0.65 + (coe)} + 14(1.0 - coe)^{24}$$

and

$$g = 1 + \left[0.1 + 0.35\left(\frac{d_c}{h}\right)^2 \right](1 - \sin\theta)^2 \tag{2.40}$$

The angular function f_θ for the half elliptical crack in function F_I is

$$f_\theta = \left[(coe)^2 \cos^2\theta + \sin^2\theta \right]^{1/4} \tag{2.41}$$

The finite width calibrated function f_w is

$$f_w = \left[\sec\left(\frac{\pi b_c}{4b} \sqrt{\frac{d_c}{h}} \right) \right]^{1/2} \tag{2.42}$$

The product of H and F_I is the boundary-calibration factor for bending, where H is expressed as:

$$H = H_1 + \left(H_2 - H_1\right)\left(\sin\theta\right)^{\left(0.2 + coe + 0.6 d_c/h\right)} \tag{2.43}$$

where

$$\begin{gathered} H_1 = 1 - 0.34\frac{d_c}{h} - 0.11\left(coe\right)\left(\frac{d_c}{h}\right) \\ H_2 = 1 - G_1\left(\frac{d_c}{h}\right) + G_2\left(\frac{d_c}{h}\right)^2 \end{gathered} \tag{2.44}$$

where in H_2

$$\begin{gathered} G_1 = \left[1.22 + 0.12\left(coe\right)\right] \\ G_2 = \left[0.55 - 1.05\left(coe\right)^{0.75} + 0.47\left(coe\right)^{1.5}\right] \end{gathered} \tag{2.45}$$

In function F_{II}:

$$m = 1 - (coe)^2 \tag{2.46}$$

$$B = (m - \upsilon)E\left(m\right) + \upsilon(coe)^2 K\left(\mathrm{m}\right) \tag{2.47}$$

where

$$\begin{gathered} E\left(m\right) = \int_0^{\pi/2} \sqrt{1 - m\sin^2\theta}\, d\theta \\ K\left(m\right) = \int_0^{\pi/2} \frac{d\theta}{\sqrt{1 - m\sin^2\theta}} \end{gathered} \tag{2.48}$$

Substituting these SIFs into Equations (2.31) and (2.32), Equation (2.30) becomes:

$$q_1^c = \left[P_1 I_{c1} + \left(xP_2 - P_3\right) I_{c2}\right] \tag{2.49}$$

$$q_2^c = \left[xP_1 I_{c2} + P_2 I_{c3} + \left(xP_2 - P_3 \right) x I_{c4} \right]$$

$$q_3^c = \left[-P_1 I_{c2} - \left(xP_2 - P_3 \right) I_{c4} \right]$$

where

$$\begin{aligned} I_{c1} &= \frac{8\pi \left(coe \right)^2}{Eb^2 h^2 Q} \int_0^{\bar{b}} \int_0^{\pi/2} \bar{b}^2 \sin^2 \theta F_1^2 d\theta d\bar{b} \\ I_{c2} &= \frac{48\pi \left(coe \right)^2}{Eb^2 h^3 Q} \int_0^{\bar{b}} \int_0^{\pi/2} \bar{b}^2 \sin^2 \theta H F_1^2 d\theta d\bar{b} \\ I_{c3} &= \frac{8\alpha_s^2 \pi \left(coe \right)^2}{Eb^2 h^2} \int_0^{\bar{b}} \int_0^{\pi/2} \bar{b}^2 \sin^2 \theta F_{II}{}^2 d\theta d\bar{b} \\ I_{c4} &= \frac{288\pi \left(coe \right)^2}{Eb^2 h^4 Q} \int_0^{\bar{b}} \int_0^{\pi/2} \bar{b}^2 \sin^2 \theta H^2 F_1^2 d\theta d\bar{b} \\ coe &= \frac{d_c}{\bar{b}} \end{aligned} \tag{2.50}$$

Hence, the total displacement q_k of the two-node spectral crack element can be expressed in a matrix form as:

$$\left[q_k \right] = \mathbf{C}_{flex} \left[P_k \right] \quad (k = 1, 2, \ldots, 6) \tag{2.51}$$

where $\mathbf{C}_{flex}$ is the flexibility matrix and it is defined as:

$$\mathbf{C}_{flex} = \begin{pmatrix} c_{11} & c_{12} & c_{13} \\ c_{21} & c_{22} & c_{23} \\ c_{31} & c_{32} & c_{33} \end{pmatrix} \tag{2.52}$$

with

$$\begin{aligned} c_{11} &= \frac{L_c}{EA} + I_{c1}, \\ c_{22} &= \left(\frac{\alpha_s L_c}{GA} + \frac{L_c{}^3}{3EA} \right) + \left(I_{c3} + x_c{}^2 I_{c4} \right), \end{aligned} \tag{2.53}$$

$$c_{33} = \frac{L_c}{EI} + I_{c4}\,,\ c_{12} = c_{21} = x_c I_{c2}\,,$$

$$c_{13} = c_{31} = -I_{c2}\,,\ c_{23} = c_{32} = -\frac{{L_c}^2}{2EA} - x_c I_{c4}$$

The stiffness matrix could be obtained using the transformation matrix $\mathbf{P}$ to consider the static equilibrium of the crack element:

$$\{q_1 \quad q_2 \quad q_3 \quad q_4 \quad q_5 \quad q_6\}^T = \mathbf{P}\{q_1 \quad q_2 \quad q_3\}^T \tag{2.54}$$

where the subscripts of *q* denote the orders of the DoFs of this two-node crack element, and the transformation matrix $\mathbf{P}$ is given by

$$\mathbf{P}^T = \begin{pmatrix} 1 & 0 & 0 & -1 & 0 & 0 \\ 0 & 1 & 0 & 0 & -1 & L_c \\ 0 & 0 & 1 & 0 & 0 & -1 \end{pmatrix} \tag{2.55}$$

The stiffness matrix of the spectral crack element is given as follow

$$\mathbf{K}^c = \mathbf{P}\mathbf{C}_{flex}^{-1}\mathbf{P}^T \tag{2.56}$$

Assembling the spectral crack element stiffness matrix $\mathbf{K}^c$ with other uncrack spectral element stiffness matrices $\mathbf{K}^e$, the global stiffness matrix $\mathbf{K}$ in Equation (2.1) can be obtained, and hence, the axial-flexural coupling effect of the guided wave interaction with cracks is consider in the time domain SFE model.

2.3 Model verification

2.3.1 Comparison of SFE and FE results

The SFE model was verified using a 3D FE model in this section. The goal of this verification is to demonstrate 1) the accuracy of predicting guided wave propagation in the isotropic beam using SFE method and 2) the capability of the developed spectral crack element in simulating the guided wave scattering and mode conversion at cracks.

A beam with length 1 m, width 0.012 m and depth 0.006 m was considered in the verification. The beam having a crack with width $b_c = 0.006$ m and depth $d_c = 0.003$ m located at $x = 0.25$ m of the beam is shown in Figure 2.5. It should be noted that the crack was modelled asymmetrically with regard to x axis. The Young's modulus E, density ρ and Poisson's ratio υ are 200×10^9 GPa, 7556 kg·m^{-3} and 0.3, respectively. The excitation signal was a 100 kHz narrow-band six-cycle sinusoidal tone burst modulated by a Hanning window. It was applied as a nodal displacement in vertical direction at $x = 0$ m to excite the A_0 guided wave. The horizontal and vertical displacement responses were also measured at the same position (i.e. $x = 0$ m).

2.3.1.1 Results calculated by SFE method

The proposed SFE beam model was implemented using MATLAB. The beam was modelled using 40 SFEs, with eight GLL nodes in each element. The crack was modelled using the proposed spectral crack element. Damping was considered and it was assumed that the damping coefficient η is 550 s^{-1}. The central difference method was utilised to solve the dynamic equilibrium Equation (2.1) and the time step Δt was 10^{-7} sec, which ensures the accuracy of the simulations. The simulated displacement response at $x = 0$ m is shown in Figure 2.4.

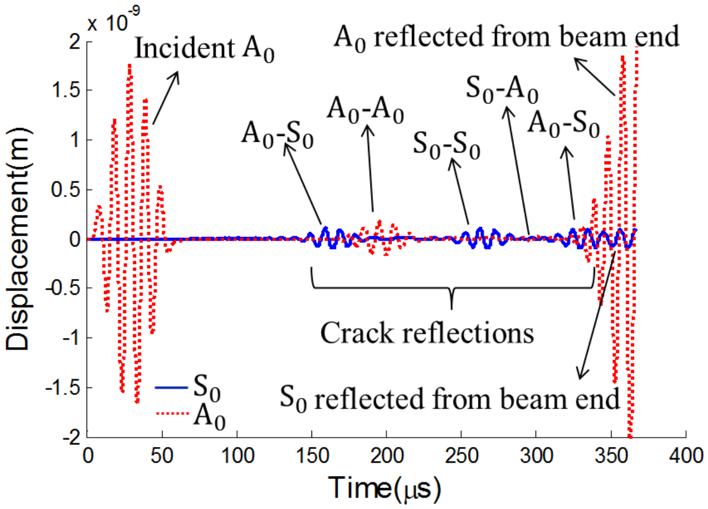

Fig. 2.4 Displacement response measured at *x*=0 m. (S_0: blue solid line; A_0: red dashed line).

The guided wave propagates along the length of the beam. When the incident A_0 pulse first interacted with the crack located at the middle of the beam, the S_0 guided wave was generated due to the mode conversion effect. In Figure 2.4, the solid line shows the mode-converted S_0 guided waves. The first and third wave packs are the mode-converted S_0 guided waves from the crack. The second and fourth wave packs are these mode-converted S_0 guided waves reflected from the crack and the beam end at $x = 0.5$ m, respectively.

The dashed line shows the A_0 guided waves. The first wave pack is the incident wave. The second wave pack is the A_0 guided wave reflected from the crack. The aforementioned mode-converted S_0 guided wave from the crack reflected from the beam end at $x = 0$ m and then propagated toward the crack. When the mode-converted S_0 guided wave interacted with the crack, it produced the mode-converted A_0 guided wave, which is the third wave pack of the dashed line in Figure 2.4. The last wave pack is the A_0 incident wave reflected from the beam end at $x = 0.5$ m. Figure 2.5 shows the details of the guided wave propagations along the beam and the mode conversions between A_0 and S_0 guided waves at the crack.

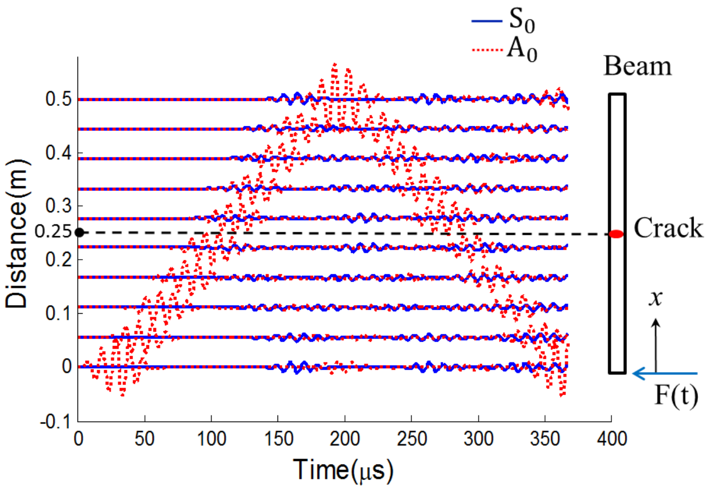

Fig. 2.5 Guided wave propagation in the beam with a crack located at 0.5 m. (S_0: blue solid line; A_0: red dashed line).

2.3.1.2 Results calculated by FE method

A 3D FE model was constructed using the commercial software, ABAQUS, to verify the proposed SFE model. The FE beam geometry and the excitation signal were the same as the SFE model. The 3D explicit linear brick elements with 8 nodes per each element and three DoFs per node were used to model the beam. The 3D stress situation, full integration and the second-order accuracy of integration were considered in the model.

The crack was modelled using seam crack in the ABAQUS and the size of the crack was identical to that in the SFE model. A very small mesh size (i.e. approximately $0.4 \times 0.4\ \text{mm}^2$) was chosen for meshing, and hence, 16 elements along the depth of the beam were generated as shown in Figure 2.6. This ensures the accuracy of simulating the 100 kHz A_0 and S_0 guided waves (Ng et al., 2012, Veidt and Ng, 2011, Ng and Veidt, 2011).

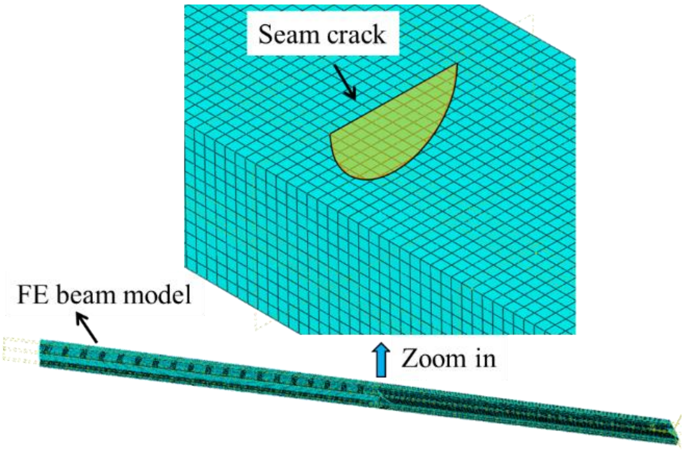

Fig. 2.6 FE mesh of the beam and the seam crack.

A very good agreement was found between the FE and SFE results. A comparison between the A_0 guided waves calculated by the FE and SFE method is shown in Figure 2.7(a), where the solid line represents the displacement response obtained from FE method and the dashed line was from the proposed SFE method. Figure 2.7(a) shows that the arrival time and the amplitudes of A_0 guided waves reflected from the crack and beam end at $x = 0.5$ m have a good agreement between the SFE and FE method. Figure 2.7(b) shows the results of the S_0 guided wave. A good agreement of the results between the FE and SFE method was found from the reflected S_0 guided waves. Figures 7(a) and 7(b) indicate that the proposed SFE model is able to simulate the guided wave propagation, scattering and mode conversion effect at the crack accurately.

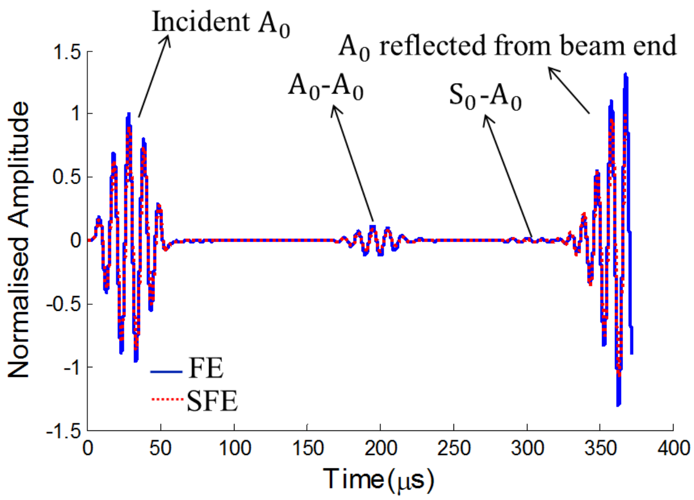

(a) A_0 guided waves

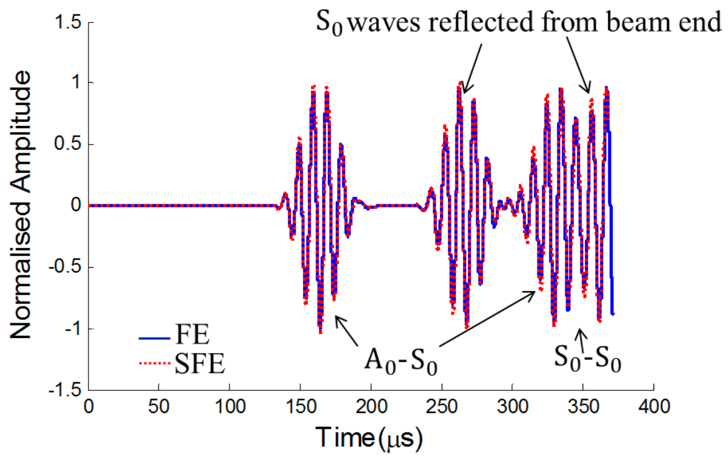

(b) S_0 guided waves

Fig. 2.7 Normalised displacement amplitude of a) A_0 and b) S_0 guided waves. (FE results: blue solid line; SFE results: red dashed line).

2.3.2 Mode conversion effect

In engineering practice, the mode conversion is of great value for damage identification (Ramadas et al., 2010). Because different modes of guided waves have different properties, understanding the fundamental physics of this phenomenon plays an important role in developing damage detection techniques.

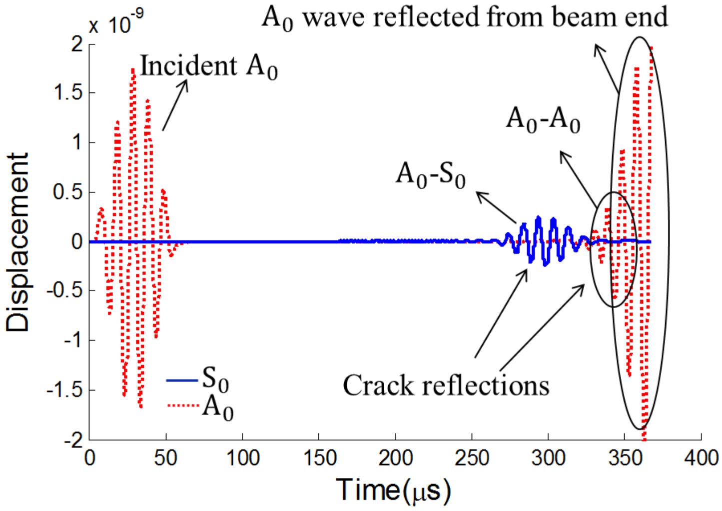

Fig. 2.8 Displacement response measured at the beam end (*x*=0 m) with a crack located at 0.49 m.

For example in a cantilever beam, cracks usually exist closed to the fixed end of the beam. Identification of these cracks using single guided wave mode is difficult as the A_0 guided wave reflection from the crack (e.g. A_0-A_0) is mixed with the A_0 guided wave reflected from the beam end as shown in Figure 2.8. However, the generation of the mode-converted S_0 guided wave signal (i.e. A_0-S_0) clearly reveals the existence of the cracks. As shown in Figure 2.8, the S_0 guided wave pack does not mix with the reflected A_0 guided waves. This is because the group velocity the converted S_0 guided wave travels is much higher than that of A_0 guided wave.

2.4 Parametric study

The proposed SFE model was utilised to investigate the low frequency guided wave scattering characteristics at cracks with different depths and widths in this section. The modelled isotropic beam has length 1 m, depth 0.006 m and width 0.012 m. The crack was located at the middle of the beam. The reflected and transmitted guided wave signals were measured at $x = 0.24$ m and $x = 0.76$ m, and hence, the distances from crack to the both measurement points were 0.26 m.

Two cases were considered to study the mode conversion effect (i.e. A_0 to S_0 and S_0 to A_0, respectively). The excitation signal was a 100 kHz narrow-band six-cycle sinusoidal tone burst modulated by a Hanning window, which was applied through the nodal deformation in the vertical and horizontal direction at the beam end ($x = 0$ m), to excite the A_0 and S_0 guided wave, respectively. The wavelengths of the A_0 and S_0 waveguides at this frequency are 19.72 mm and 51.11 mm, respectively.

When the incident pulse interacts with the crack, the reflected and transmitted waves are generated. The reflected guided wave travels back to the measurement point located at $x = 0.24$ m. For the transmitted wave, it propagates toward the measurement point located at $x = 0.76$ m. It should be noted that no baseline signal was applied to extract the amplitude of the scattered waves from the crack. In this study the measured data was normalised by the maximum absolute amplitude of displacement measured at the middle of the beam, which has the same distance to both measurement points.

One of the aims in this study is to investigate the reflected and transmitted wave amplitudes as a function of the crack size (i.e. asymmetric crack depth d_c and symmetric width b_c). Without loss of generality, the crack depth d_c and width b_c were normalised by the wavelength λ_{in} of the incident wave as:

$$D_d = d_c / \lambda_{in}, \; D_b = b_c / \lambda_{in} \tag{2.57}$$

where D_d and D_b are the crack depth and width to wavelength ratios, respectively.

2.4.1 Mode conversion from A_0 to S_0 guided wave

In this case, the A_0 guided wave was excited. Cracks with different depths were studied but the width of the cracks is a constant at the value of half of the beam width, i.e. 0.006 m. Figure 2.9 shows the normalised amplitude of a crack as a function of D_d while D_b equals to 0.305. It is shown that the normalised amplitude of the reflected A_0 guided wave steadily increases and reaches its local maximum at $D_d = 0.15$ where the amplitude of transmitted A_0 guided wave decreases and reaches the local minimum at around $D_d = 0.2$.

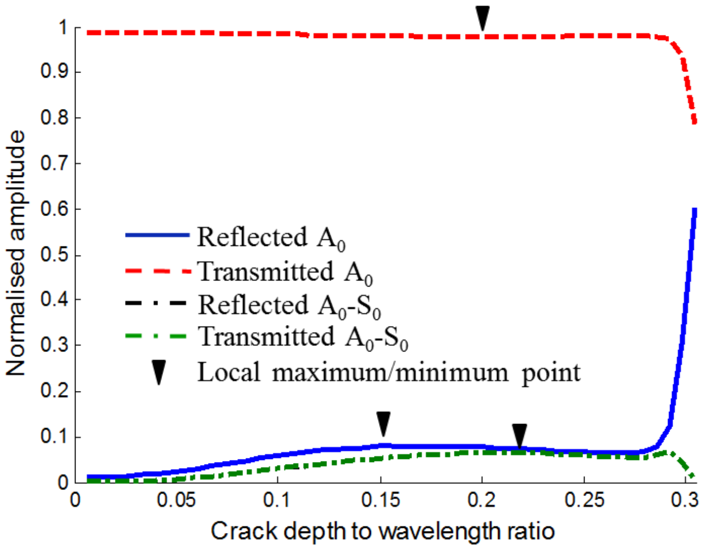

Fig. 2.9 Load-deflection curve of the double cantilever beam with delamination.

The values of D_d that having the local maximum and minimum amplitude of the reflected and transmitted A_0 guided wave are not the same. This is mainly because part of the incident energy was mode-converted from A_0 to S_0 guided waves. As the value of D_d increases, the transmitted A_0 guided wave amplitude increases to reach the local maximum amplitude and then decreases again whereas the reflected wave amplitude behaves the other way around.

Figure 2.9 also shows that the mode-converted transmitted and reflected S_0 guided waves have the same amplitude and the amplitude increase with D_d. The amplitude increases almost linearly and then starts falling when D_d is around 0.22. As D_d approaching its upper considered limit, the transmitted A_0

and the mode-converted S_0 guided wave amplitudes shrank sharply. At the meanwhile, the reflected A_0 guided wave amplitude increases significantly as the depth of the crack almost reaches the depth of the beam.

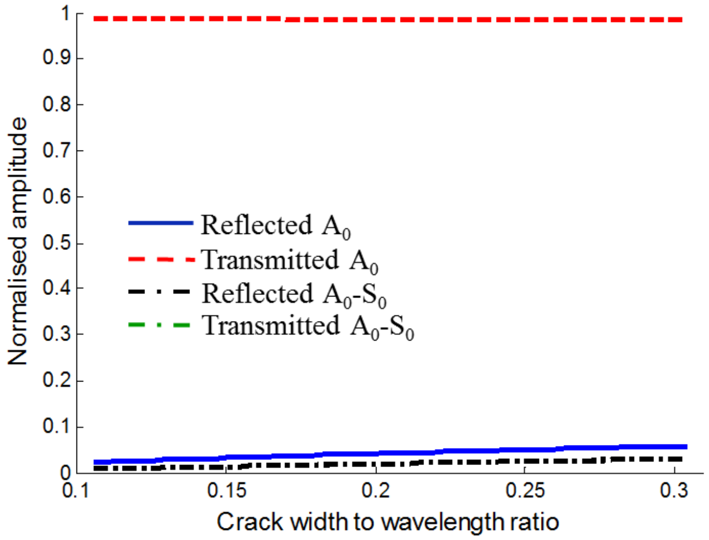

Fig. 2.10 Normalised amplitude as a function of D_b for incident A_0 guided wave.

Figure 2.10 shows the normalised amplitude from a damaged beam with crack width as a variable but the depth remains unchanged at 2 mm. The normalised amplitude is thus a function of D_b and D_d is fixed at 0.101. The transmitted A_0 guided wave amplitude gradually decreases with D_b, while the reflected A_0 guided wave and the mode-converted A_0 guided wave signal gradually increases with different amplitudes. Generally, the amplitude of reflected A_0 guided wave is larger than the mode-converted S_0 guided wave.

2.4.2 Mode conversion from S_0 to A_0 guided wave

Different to Section 2.4.1, the S_0 guided wave was the incident wave in this section. The aim is to investigate the characteristics of the reflected S_0 guided wave and mode-converted A_0 guided wave for different crack sizes. Figure

2.11 shows the normalised reflected and transmitted wave amplitude as a function of D_d with $D_b = 0.12$ (i.e. the crack width is 6 mm). Similarly, as D_d approaching the maximum value, the amplitude of the transmitted S_0 guided wave decreases but the reflected S_0 guided wave increases dramatically. They crosses each other at $D_d = 0.115$.

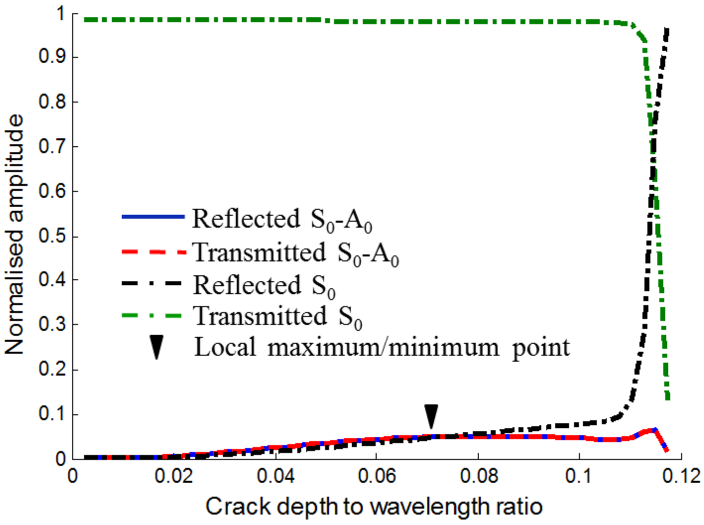

Fig. 2.11 Normalised amplitude as a function of D_d for incident S_0 guided wave.

The amplitude of the mode-converted A_0 guided wave increases significantly with D_d and then decreases after it reaches the maximum value at $D_d = 0.07$. The results show that the amplitudes of reflected and transmitted A_0 guided waves are identical.

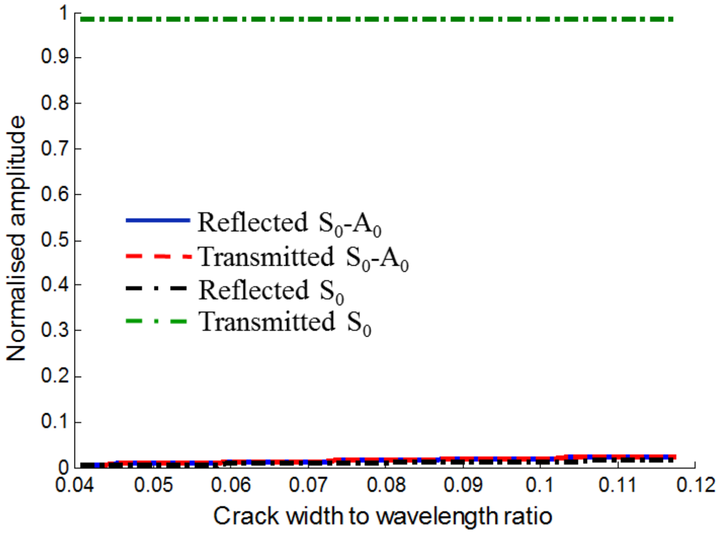

Fig. 2.12 Normalised amplitude as a function of D_b D_b for incident S0 guided wave.

Figure 2.12 shows the normalised amplitude as a function of D_b with $D_d = 0.04$ (i.e. the depth of crack is 2 mm). It shows that the transmitted S_0 wave decreases with D_b. The amplitude of the reflected S_0 guided wave and mode-converted A_0 guided waves increase with D_b. The results show that the amplitudes of mode-converted A_0 guided waves have similar values and they are larger than the reflected S_0 guided waves.

2.5 Conclusions

This chapter studied the fundamental physical insight of guided wave propagation in an isotropic beam using a 4-DoF SFE beam model, which was developed based on the Mindlin-Herrmann rod and Timoshenko beam theory. A spectral two-node crack element with three DoFs per node was developed to model the crack. This proposed beam model was verified using the explicit 3D FE beam model. A good agreement of the wave propagation time history was found between the results of the SFE and FE methods. This study demonstrated that the proposed computational effective crack element could be used to predict the mode conversion effect between A_0 and S_0 guided waves accurately.

Parametric studies of two different cases were conducted to investigate the guided wave reflection and transmission characteristics at the cracks with different depths and widths. The results show that the normalised amplitudes of A_0 and S_0 guided waves were highly dependent on the crack sizes. In general, the amplitudes of reflected and mode-converted guided waves increase for larger crack size except the amplitude of the transmitted guided wave decreases. The results of the parametric studies indicate that the behaviour of the normalised amplitude as a function of D_d was more complicated than that of D_b.

Acknowledgement

This work was supported by the Australian Research Council under Grant Number DE130100261 and partially supported by South Australian Department of State Development under Premier's Research and Industry Fund's Catalyst Research Grant Program. The supports are greatly appreciated.

References for Chapter 2

AJITH, V. & GOPALAKRISHNAN, S. 2013. Wave propagation in stiffened structures using spectrally formulated finite element. *European Journal of Mechanics-A/Solids,* 41**,** 1-15.

BENMEDDOUR, F., GRONDEL, S., ASSAAD, J. & MOULIN, E. 2008. Study of the fundamental Lamb modes interaction with symmetrical notches. *NDT & E International,* 41**,** 1-9.

BERGAMINI, A. & BIONDINI, F. 2004. Finite strip modeling for optimal design of prestressed folded plate structures. *Engineering Structures,* 26**,** 1043-1054.

BOYD, J. P. 2001. *Chebyshev and Fourier spectral methods*, Courier Dover Publications.

CARDEN, E. P. & FANNING, P. 2004. Vibration based condition monitoring: a review. *Structural Health Monitoring,* 3**,** 355-377.

CASTAINGS, M., LE CLEZIO, E. & HOSTEN, B. 2002. Modal decomposition method for modeling the interaction of Lamb waves with cracks. *The Journal of the Acoustical Society of America*, 112**,** 2567-2582.

CHU, S. T. & CHAUDHURI, S. K. 1989. A finite-difference time-domain method for the design and analysis of guided-wave optical structures. *Journal of Lightwave Technology,* 7**,** 2033-2038.

COWPER, G. 1966. The shear coefficient in Timoshenko's beam theory. *Journal of applied mechanics,* 33**,** 335-340.

DARPE, A., GUPTA, K. & CHAWLA, A. 2004. Coupled bending, longitudinal and torsional vibrations of a cracked rotor. *Journal of Sound and Vibration,* 269**,** 33-60.

DEEPAK, B., GANGULI, R. & GOPALAKRISHNAN, S. 2012. Dynamics of rotating composite beams: A comparative study between CNT reinforced polymer composite beams and laminated composite beams using spectral finite elements. *International Journal of Mechanical Sciences,* 64**,** 110-126.

DELSANTO, P. P., R.S., S. & MIGNOGNA, R. B. 1997. Connection machine simulation of ultrasonic wave propagation in materials III: The three-dimensional case. *Wave Motion,* 26**,** 329-339.

DELSANTO, P. P., SCHECHTER, R. S., CHASKELIS, H. H., MIGNOGNA, R. B. & KLINE, R. 1994. Connection Machine Simulation of Ultrasonic Wave Propagation in Materials 2: The Two-dimensional Case. *Wave Motion,* 20**,** 295-314.

DELSANTO, P. P., WHITCOMBE, T., CHASKELIS, H. H. & MIGNOGNA, R. B. 1992. Connection Machine Simulation of Ultrasonic Wave Propagation in Materials I: The One-dimensional Case. *Wave Motion,* 16**,** 65-80.

DOEBLING, S. W., FARRAR, C. R. & PRIME, M. B. 1998. A summary review of vibration-based damage identification methods. *Shock and vibration digest,* 30**,** 91-105.

DOEBLING, S. W., FARRAR, C. R., PRIME, M. B. & SHEVITZ, D. W. 1996. Damage identification and health monitoring of structural and mechanical systems from changes in their vibration characteristics: a literature review. Los Alamos National Lab., NM (United States).

DOYLE, J. F. 1989. *Wave propagation in structures*, Springer.

FAN, W. & QIAO, P. 2011. Vibration-based damage identification methods: a review and comparative study. *Structural Health Monitoring,* 10**,** 83-111.

HE, M. & HUTCHINSON, J. 2000. Surface crack subject to mixed mode loading. *Engineering Fracture Mechanics,* 65**,** 1-14.

HONG, M., ZHOU, C., SU, Z. Q., CHENG, L. & QING, X. L. 2013. Nonlinear Properties of Lamb Waves under Modulation of Fatigue Damage:

Finite Element Simulation with Experimental Validation. *Key Engineering Materials,* 558**,** 195-204.

KAWASHIMA, H. 1996. The shear coefficient for quartz crystal of rectangular cross section in timoshenko's beam theory. *IEEE Transactions on Ultrasonics, Ferroelectrics, and Frequency Control,* 43**,** 434-440.

KUDELA, P., KRAWCZUK, M. & OSTACHOWICZ, W. 2007. Wave propagation modelling in 1D structures using spectral finite elements. *Journal of Sound and Vibration,* 300**,** 88-100.

KUDELA, P. & OSTACHOWICZ, W. 2009. 3D time-domain spectral elments for stress wave modelling. 7th International Conference on Modern Practice in Stress and Vibration Analysis. doi: 10.1088/1742-6596/181/1/012091.

LI, F., PENG, H., SUN, X., WANG, J. & MENG, G. 2012. Wave Propagation Analysis in Composite Laminates Containing a Delamination Using a Three-Dimensional Spectral Element Method. *Mathematical Problems in Engineering.* doi: 10.1155/2012/659849).

LIU, G. 2002. A combined finite element/strip element method for analyzing elastic wave scattering by cracks and inclusions in laminates. *Computational Mechanics,* 28**,** 76-82.

LOWE, M. J., CAWLEY, P., KAO, J. & DILIGENT, O. 2002. The low frequency reflection characteristics of the fundamental antisymmetric Lamb wave a0 from a rectangular notch in a plate. *The Journal of the Acoustical Society of America,* 112**,** 2612-2622.

MINDLIN, R. & HERRMANN, G. 1951. A one-dimensional theory of compressional waves in an elastic rod. Proceedings of the 1st US National Congress of Applied Mechanics, 187-191.

MOSER, F., JACOBS, L. J. & QU, J. 1999. Modeling Elastic Wave Propagation in Waveguides with the Finite Element Method. *NDT & E Ingternational,* 32**,** 225-234.

NEWMAN JR, J. & RAJU, I. 1981. An empirical stress-intensity factor equation for the surface crack. *Engineering Fracture Mechanics,* 15**,** 185-192.

NG, C. T. & VEIDT, M. 2011. Scattering of the fundamental anti-symmetric Lamb wave at delaminations in composite laminates. *The Journal of the Acoustical Society of America,* 129**,** 1288-1296.

NG, C. T., VEIDT, M. & LAM, H. F. 2009. Guided Wave Damage Characterisation in Beams Utilising Probabilistic Optimisation. *Engineering Structures,* 31**,** 2842-2850.

NG, C. T., VEIDT, M., ROSE, L. & WANG, C. H. 2012. Analytical and finite element prediction of Lamb wave scattering at delaminations in quasi-isotropic composite laminates. *Journal of Sound and Vibration,* 331**,** 4870-4883.

OSTACHOWICZ, W., KUDELA, P., KRAWCZUK, M. & ZAK, A. 2012. Spectral Finite Element Method. *Guided Waves in Structures for SHM.* John Wiley & Sons, Ltd.

OSTACHOWICZ, W. & RADZIEŃSKI, M. 2012. Structural health monitoring by means of elastic wave propagation. *Journal of Physics: Conference Series,* (http://iopscience.iop.org/1742-6596/382/1/012003).

POZRIKIDIS, C. 2005. *Introduction to finite and spectral element methods using Matlab,* CRC Press.

RAGHAVAN, A. & CESNIK, C. E. S. 2007. Review of Guided-wave Structural Health Monitoring. *The Shock and Vibration Digest,* 39**,** 91-114.

RAMADAS, C., BALASUBRAMANIAM, K., JOSHI, M. & KRISHNAMURTHY, C. V. 2010. Interaction of guided Lamb waves with an asymmetrically located delamination in a laminated composite plate. *Smart Materials and Structures,* 19**,** 1-11.

REDDY, J. N. 2006. *An introduction to the finite element method,* McGraw-Hill New York.

ROSE, J. L. 1999. *Ultrasonic Waves in Solid Media,* New York, Cambridge University Press.

ROSE, J. L. 2002. A Baseline and Vision of Ultrasonic Guided Wave Inspection Potential. *Journal of Pressure Vessel Technology,* 124**,** 273-282.

RUCKA, M. 2010. Experimental and numerical study on damage detection in an L-joint using guided wave propagation. *Journal of Sound and Vibration,* 329**,** 1760-1779.

RUCKA, M., WITKOWSKI, W., CHRÓŚCIELEWSKI, J. & WILDE, K. 2012. Damage detection of a T-shaped panel by wave propagation analysis in the plane stress. *Archives of Civil Engineering,* 58**,** 3-24.

SHKERDIN, G. & GLORIEUX, C. 2004. Lamb mode conversion in a plate with a delamination. *The Journal of the Acoustical Society of America,* 116**,** 2089-2100.

SOHN, H., FARRAR, C. R., HEMEZ, F. M., SHUNK, D. D., STINEMATES, D. W., NADLER, B. R. & CZARNECKI, J. J. 2004. *A review of structural health monitoring literature: 1996-2001*, Los Alamos National Laboratory Los Alamos,, New Mexico.

TADA, H., PARIS, P. C., IRWIN, G. R. & TADA, H. 2000. *The stress analysis of cracks handbook*, ASME press New York.

VEIDT, M. & NG, C. T. 2011. Influence of stacking sequence on scattering characteristics of the fundamental anti-symmetric Lamb wave at through holes in composite laminates. *The Journal of the Acoustical Society of America,* 129**,** 1280-1287.

VEIDT, M. & NORMANDIN, B. 2013. Single Transducer Pair Lamb Wave Time Reversal for Damage Detection in Composite Laminates. *Key Engineering Materials,* 558**,** 205-217.

XU, F., ZHANG, Y., HONG, W., WU, K. & CUI, T. J. 2003. Finite-difference frequency-domain algorithm for modeling guided-wave properties of substrate integrated waveguide. *Microwave Theory and Techniques, IEEE Transactions on,* 51**,** 2221-2227.

XU, K., TA, D., SU, Z. & WANG, W. 2014. Transmission analysis of ultrasonic Lamb mode conversion in a plate with partial-thickness notch. *Ultrasonics,* 54**,** 395-401.

ZHAO, X. G. & ROSE, J. L. 2003. Boundary element modeling for defect characterization potential in a wave guide. *International Journal of Solids and Structures,* 40**,** 2645-2658.

ZHOU, L., HE, Z. & SUN, H. 2013. Lamb wave mode conversion-based crack detection for plate-like structures without baseline information. *Journal of Vibroengineering,* 15**,** 647-657.

ZHOU, W. J. & ICHCHOU, M. N. 2011. Wave scattering by local defect in structural waveguide through wave finite element method. *Structural Health Monitoring,* 10**,** 335-349.

Chapter 3

Guided wave-based identification of multiple cracks in beams using a Bayesian approach

(Paper 2, published)

Shuai He and Ching-Tai Ng

School of Civil, Environmental & Mining Engineering, The University of Adelaide, Adelaide, SA 5005, Australia

Publication:

HE, S. & NG, C. T. 2017. Guided wave-based identification of multiple cracks in beams using a Bayesian approach. *Mechanical Systems and Signal Processing,* 84, 324-345.

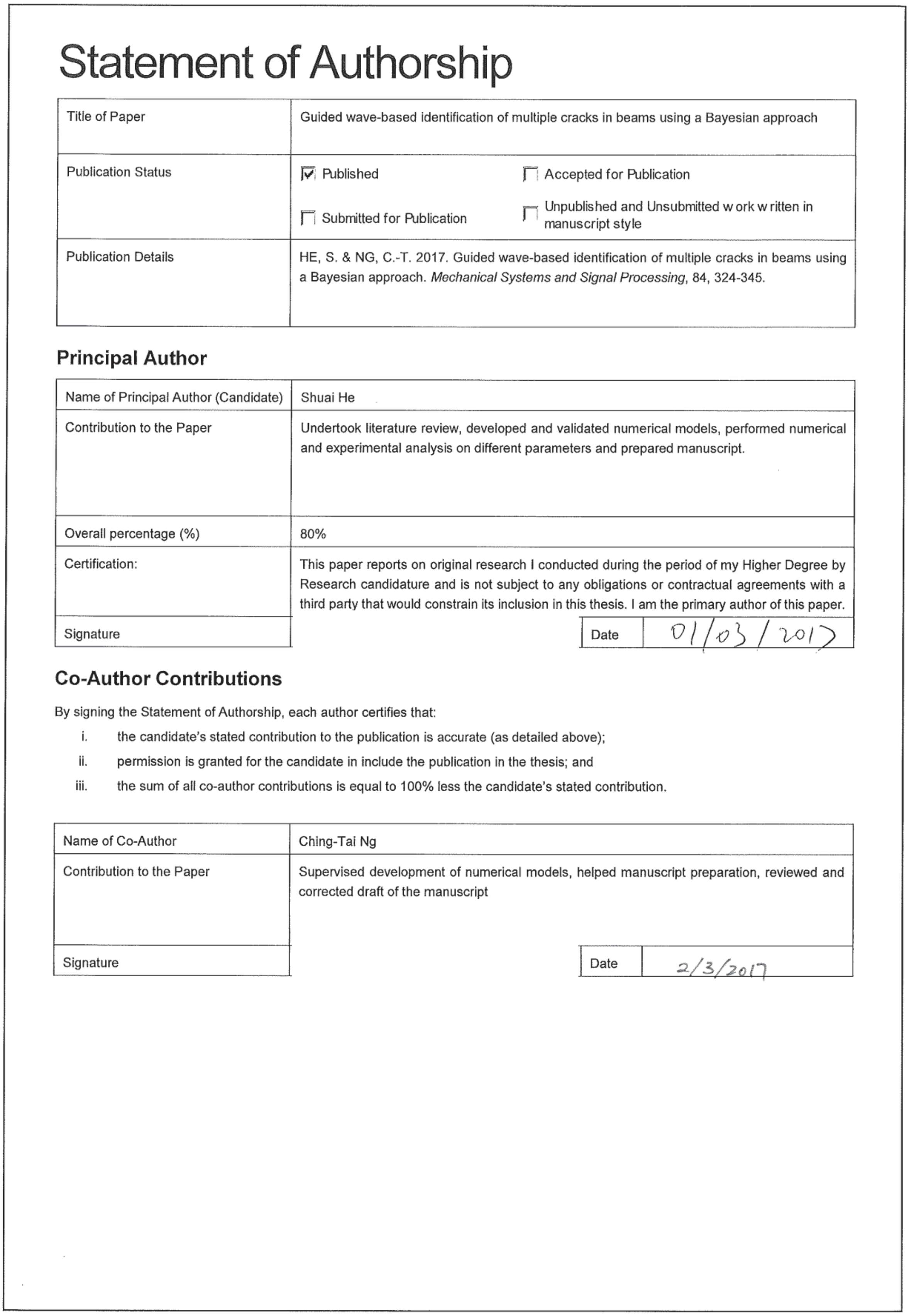

Statement of Authorship

Title of Paper	Guided wave-based identification of multiple cracks in beams using a Bayesian approach
Publication Status	☑ Published ☐ Accepted for Publication ☐ Submitted for Publication ☐ Unpublished and Unsubmitted work written in manuscript style
Publication Details	HE, S. & NG, C.-T. 2017. Guided wave-based identification of multiple cracks in beams using a Bayesian approach. *Mechanical Systems and Signal Processing*, 84, 324-345.

Principal Author

Name of Principal Author (Candidate)	Shuai He
Contribution to the Paper	Undertook literature review, developed and validated numerical models, performed numerical and experimental analysis on different parameters and prepared manuscript.
Overall percentage (%)	80%
Certification:	This paper reports on original research I conducted during the period of my Higher Degree by Research candidature and is not subject to any obligations or contractual agreements with a third party that would constrain its inclusion in this thesis. I am the primary author of this paper.
Signature	Date 01/03/2017

Co-Author Contributions

By signing the Statement of Authorship, each author certifies that:

i. the candidate's stated contribution to the publication is accurate (as detailed above);

ii. permission is granted for the candidate in include the publication in the thesis; and

iii. the sum of all co-author contributions is equal to 100% less the candidate's stated contribution.

Name of Co-Author	Ching-Tai Ng
Contribution to the Paper	Supervised development of numerical models, helped manuscript preparation, reviewed and corrected draft of the manuscript
Signature	Date 2/3/2017

Abstract

A guided wave damage identification method using a model-based approach is proposed to identify multiple cracks in beam-like structures. The guided wave propagation is simulated using spectral finite element method and a crack element is proposed to take into account the mode conversion effect. The Bayesian model class selection algorithm is employed to determine the crack number and then the Bayesian statistical framework is used to identify the crack parameters and the associated uncertainties. In order to improve the efficiency and ensure the reliability of identification, the Transitional Markov Chain Monte Carlo (TMCMC) method is implemented in the Bayesian approach. A series of numerical studies are carried out to assess the performance of the proposed method, in which the sensitivity of different guided wave modes and effect of different levels of measurement noise in identifying different numbers of cracks is studied in detail. The proposed method is also experimentally verified using guided wave data obtained from laser vibrometer. The results show that the proposed method is able to accurately identify the number, locations and sizes of the cracks, and also quantify the associated uncertainties. In addition the proposed method is robust under measurement noise and different situations of the cracks.

***Keywords*:**

Multiple cracks; Damage identification; Bayesian statistical framework; Bayesian model class selection; Guided waves; Spectral finite element; Mode conversion

3.1 Introduction

3.1.1 Structural health monitoring

Structural health monitoring (SHM) has attracted much attention as it plays a vital role in ensuring safety, reliability and serviceability of a range of infrastructures in civil, mechanical and aviation engineering. It provides a tool to continuously examine the integrity of structures and presents essential information of any damage and deterioration at the early stage. Numerous damage detection techniques have been developed to provide safety inspection for structures in the field of SHM. Conventional non-destructive evaluation (NDE) techniques are generally limited in measuring a very small region of the structure and not applicable to inspect inaccessible locations. Efficient damage inspection requires the pre-knowledge of possible damage locations, which is usually not available in practical situation for NDE. Acoustic emission (Aljets et al., 2012) is a passive technique that is able to monitor the generation and growth of defects but it is not applicable to detect existing defects. The vibration-based techniques (Mosavi et al., 2012) have the capability to detect and locate the damage in entire structures. However, they are insensitive to incipient defects as they are based on low vibrational frequency.

3.1.2 Guided wave damage identification

Guided wave (GW) has been proven sensitive to small and various types of damages (Raghavan and Cesnik, 2007, Croxford et al., 2007). GW is a mechanical stress wave, which can be actuated by piezoelectric transducers installed on structures and its propagation is confined to the structures guided by structural boundaries. It can be used to inspect large area of the structures as it is able to propagate a long distance. In recent years, GW has demonstrated significant capabilities in damage detection (Zhou et al., 2014) in a variety of structural components, which are commonly categorised into one- (1D) and two-dimensional (2D) waveguides. The characteristics of GW propagation and its interaction with damage have been studied for 1D waveguides (e.g. pipes) (Lowe et al., 2012) and beams (Ng, 2014a, Ng, 2014b) and 2D waveguides (e.g. plates) (Ng, 2015a).

Based on the identified damage information, the damage detection process has four different levels, i.e. determine i) damage existence, ii) damage location, iii) damage severity and iv) remaining service lifespan of structures prediction (Farrar and Worden, 2007). In the literature different types of damage detection techniques have been developed for 2D waveguide and most of them are able to identify the existence, location and severity of the damages. For example, numerous advance damage detection techniques, such as damage imaging (Veidt et al., 2008, Ng et al., 2009), maximum-likelihood estimation (Flynn et al., 2011b), diffraction tomography (Ng, 2015b, Rose and Wang, 2010), phased-array beamforming (Han and Kim, 2015), model-based approach (Vanli and Jung, 2014, Aryan et al., 2016) and the Bayesian interface (Flynn et al., 2011a, Yang et al., 2015) were developed for plate-like structures. In contrast, most GW based damage detection techniques for 1D waveguides were limited in identifying the existence and location of damage (Rucka, 2010).

3.1.3 Model-based approaches

There are two major approaches in GW damage detection of 1D waveguides: the non-model and model-based approaches. Most research of GW damage identification focuses on non-model-based approaches. Generally, non-model-based approaches apply forward algorithm to detect damage by recognising the subsequent changes in certain features between the damaged and healthy state of structures. However, accurate baseline signal is difficult to obtain because it normally contains numerous unnecessary data, such as noise from environments, natural vibration of the structures and data acquisition systems. Although different signal processing techniques have been recently proposed to extract the damage information in the measured signal, these studies only roughly quantified the severity of the damage. For example, Hossein Abadi et al. (2014) proposed a pattern recognise technique to detect step damage on a thick steel beam based on discrete wavelet transform of GW signal. Experimental results demonstrated that the damage location was appropriately detected and its depth was estimated. Amjad et al. (2015) utilized the changes in time-of-flight and phase to detect circular hole-type damage in 1D waveguide. Different signal processing techniques such as Fast Fourier Transform (FFT), Wigner-Ville Distribution Transform (WVDT), S-Transform (ST) and Hilbert Huang Transform (HHT) were employed to improve the quality of the GW signal in identifying the damage size.

Model-based approach is capable to characterise more complicated damage by updating a damage model. The damage parameters, such as damage location and geometry, are treated as unknown parameters and updated through minimising the discrepancy between the simulated and measured data. This approach is able to provide more quantitative information in the damage identification, and hence, this chapter focuses on using the GW model-based approach for cracks identification of beam-like structures.

3.1.4 Modelling of GW propagation and scattering

Methods of modelling the GW propagation can be found in the literature (Willberg et al., 2015). Generally, GW propagation could be numerically modelled by conventional finite element (FE) method (Zhou and Ichchou, 2011), while this method is impractical for model-based damage identification. The mesh size of the FE element usually needs to be small enough to ensure the accuracy in simulating the GW propagation but it is computational expensive. Other numerical methods, such as finite difference method (Xu et al., 2003), would confront convergence problem when the GW propagates through different materials. Finite strip element method (Bergamini and Biondini, 2004) is difficult to be applied to geometry-complex structures. Boundary element method (Zhao and Rose, 2003) is inefficient for simulating large structures. The frequency-domain spectral finite element (SFE) method has been widely applied in most GW model-based damage detection techniques (Ng, 2014b, Krawczuk, 2002, Nag et al., 2002) because of its computational efficiency. It has been used for damage identification, for example, based on genetic algorithm (GA) in beam-like structure with a symmetric open crack (Krawczuk, 2002) and in composite beams with delamination (Nag et al., 2002), and Bayesian statistical framework combined with simulating annealing (SA) (Ng et al., 2009) and particle swarm optimization (PSO) algorithm (Ng, 2014b) in a beam with a step damage. However, because the frequency-domain SFE method requires one side of the structure to be infinitely long, it is unsuitable for modelling practical and complex structures.

Time-domain SFE method, which is also called the p-version FEM (Patera, 1984), has the same flexibility in model discretisation as conventional FEM. The method uses high-order approximation polynomials to reduce the number of elements. Also, the application of Gauss-Lobatto-Legendre (GLL) nodes, leads to a diagonal mass matrix, and hence, the dynamic equilibrium of the model can be solved efficiently by explicit central difference method. In addition, the Runge effect is avoided by the application of this GLL-node element (Pozrikidis, 2005). The time-domain SFE modelling has been proven to be an effective tool in simulating GW propagation for 1D and 2D waveguides (Kudela et al., 2007). In this chapter, the time-domain SFE method is utilised to simulate both fundamental longitudinal (S_0) and flexural (A_0) GWs propagation based on the Mindlin-Herrmann rod (Mindlin and Herrmann, 1951) and Timoshenko beam theory (Doyle, 1989), respectively. These theories provide more accurate results for the high frequency GW propagation.

GW mode-conversion effect is a general phenomenon occurring at the moment when the GW interacts with asymmetric discontinuity in the waveguide. Additional damage information from the mode-converted GW can be provided to describe the damage features. In the literatures, for example, Xu et al. (2014) determined the depth of a partial-thickness crack in plate by the mode converted energy rate using FE simulation. Li et al. (2015) compared the mode-converted signal with the baseline signal to detect damage in high-speed railway. However, the use of GW mode-conversion effect for model-based damage identification in beam-like structures has not been studied. In this chapter, a time-domain SFE cracked beam element (He and Ng, 2015) was adapted to simulate the mode-conversion effect. The flexibility of the cracked element was formed by applying the Castigliano’s theorem and laws of fracture mechanics to couple the longitudinal and flexural displacement. As a result, the mode converted GW signal was simulated and better performance of damage characterisation in beam-like structure was achieved.

3.1.5 Bayesian approach

Bayesian statistical framework was initially applied in the field of low-frequency vibrational test (Beck and Katafygiotis, 1998). It was then extended to the GW model-based crack identification in beam-like structures (Ng, 2014b, Ng et al., 2009, Krawczuk, 2002, Nag et al., 2002). This method determines the damage parameters using the maximum likelihood method and provides the quantification of the corresponding uncertainties, which is significantly useful for planning the restoration work in engineering practice. However, most of the studies were limited to identify single damage in 1D waveguides. This is because in multiple-damage situation, a numerical model that considers the number of damage more than the actual damage number will always have better fitting between the simulated and measured data in the presence of measurement noise and modelling error. Therefore, the selection of the model with a pre-defined damage number based solely on the fitting between the modelled and measured data can be very misleading. In order to solve this problem, the Bayesian model class selection algorithm (Beck, 2010, Beck and Yuen, 2004) was employed to identify the number of cracks for multiple-damage situation in this chapter, which considers a penalty against the model complexity, i.e. increasing number of cracks.

Crack identification in model-based approach requires determine the optimal crack parameters that minimises the discrepancy between the simulated data of the crack model and measured data. In the case of single crack identification, which is usually treated as an identifiable situation (Beck and Yuen, 2004), there is one or limited number of optimal crack parameter regions in the parameter space. Identification of the crack is equivalent to finding the global optimum by using global optimisation algorithms such as GA, SA and PSO. While in the case of multi-crack identification, the problem is possible to be unidentifiable (Beck and Yuen, 2004) and the aforementioned optimisation tools are inapplicable. In order to solve this difficulty, this chapter utilises Bayesian approach with implementation of the transitional Markov Chain Monte Carlo (TMCMC) sampling method (Ching and Chen, 2007) to identify the number of cracks and the optimal crack parameters

The arrangement of the chapter is listed as follow. The time-domain SFE method and a proposed SFE crack model are presented in Section 3.2. The Bayesian model class selection and Bayesian statistical framework for damage identification are then described in Section 3.3. Section 3.4 describes the TMCMC algorithm. After that a series of numerical case studies for investigating the reliability and computational efficiency of the TMCMC algorithm are presented in Section 3.5. Different GW modes, crack numbers, noise levels and measurement locations are considered in the numerical case studies. In addition, the results of experimental case studies are presented to verify the practicability of this approach in Section 3.6. Finally, conclusions are drawn in Section 3.7.

3.2 Time-domain spectral finite element method

3.2.1 Mindlin-Herrmann rod and Timoshenko beam theory

It has been experimentally proven that the Mindlin-Herrmann rod theory provides better results than the elementary rod theory in simulating the fundamental longitudinal GW propagation (Krawczuk et al., 2006) while the Timoshenko beam theory performs better than the Euler–Bernoulli beam theory in simulating the fundamental flexural GW (Rucka, 2010). Although Love theory provides similar results to the Mindlin-Herrmann rod theory for low frequency (i.e., fundamental mode) GW propagation in thin rods, it changes the diagonal form of the mass matrix by introducing the lateral deformation component (Rucka, 2010). So it is inefficiency in solving the dynamic equilibrium using central difference method. Furthermore, Love theory is not sufficient to simulate the GW propagation in deep rods or at high frequency. Hence, the Mindlin-Herrmann rod theory and Timoshenko beam theory are chosen to model the GW propagation in this study.

In the Mindlin-Herrmann rod theory, the longitudinal displacement $u\left(x\right)$ is coupled with an independent lateral contraction $\psi\left(x\right)$ that used to account for the Poisson effect (Mindlin and Herrmann, 1951). In the Timoshenko beam theory, the effect of shear deformation is considered and the vertical displacement $v\left(x\right)$ is independent from the rotational function $j\left(x\right)$. Thus, as shown in Figure 3.1, four degree-of-freedoms (DoFs) were considered at each node and eight nodes were employed to model a SFE beam element in this chapter.

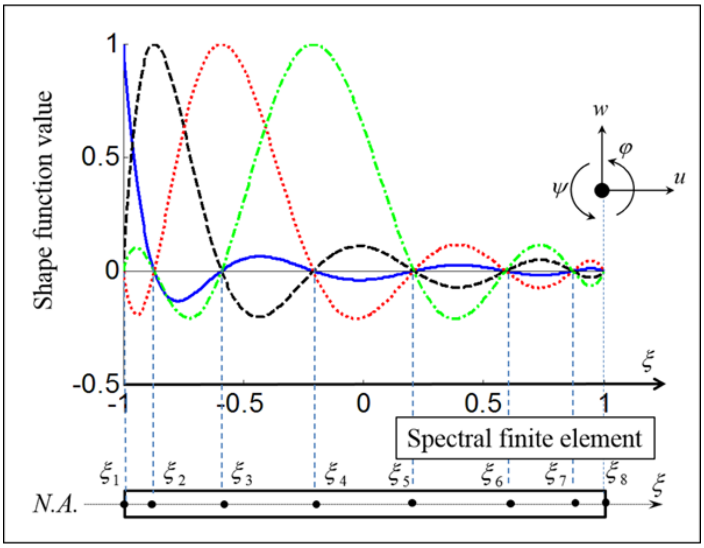

Fig. 3.1 Distribution of GLL nodes and shape function of first four nodes (1st node: solid line; 2nd node: dashed line; 3rd node: dotted line; 4th node: dotted-dashed line).

The displacement fields in the beam have the following forms:

$$\bar{u}(x,y) \approx u(x) - y\varphi(\mathrm{x}) \;\; and \;\; \bar{\upsilon}(x,y) \approx \psi(x)\,y + \upsilon(x) \tag{3.1}$$

where y is the vertical distance from neutral axis. The governing equations of GWs using Mindlin-Herrmann rod theory and Timoshenko beam theory are defined as: (Rucka, 2010, Doyle, 1989)

$$\begin{gathered} \frac{2GA}{1-\nu}\left(\frac{\partial^2 u}{\partial x^2} + \nu\frac{\partial \psi}{\partial x}\right) = \rho A\ddot{u} - F_l(x,t) \\ K_1^M GI\frac{\partial^2 \psi}{\partial x^2} - \frac{2GA}{1-\nu}\left(\nu\frac{\partial u}{\partial x} + \psi\right) = K_2^M \rho I\ddot{\psi} \end{gathered} \tag{3.2}$$

$$\begin{gathered} K_1^T GA\frac{\partial}{\partial x}\left(\frac{\partial \upsilon}{\partial x} - \varphi\right) = \rho A\ddot{\upsilon} - F_v(x,t) \\ EI\frac{\partial^2 \varphi}{\partial x^2} + K_1^T GA\left(\frac{\partial \upsilon}{\partial \mathrm{x}} - \varphi\right) = K_2^T \rho I\ddot{\varphi} \end{gathered} \tag{3.3}$$

where E and G are the Young's and shear modules. A denotes the cross-section area of the beam and I is the moment of inertia. ν and r are Poisson's ratio and mass density of the material, respectively. The external longitudinal and vertical excitation are illustrated by $F_l(x,t)$ and $F_v(x,t)$, which are the function of time t and location variable x, respectively. K_1^M, K_2^M and K_1^T can be adjusted to give the best correspondence with the experimental results in the considered frequency range. In this study $K_1^M = 1.1$, $K_2^M=3.1$ and $K_1^T=0.922$ are obtained from the experimental results reported in this chapter. $K_2^T = 12K_1^T / \pi^2$ to match the cut-off frequency with guided wave modes.

3.2.2 Spectral finite element formulation

The dynamic equilibrium of the model in time-domain can be represented using the following Equation (Kudela et al., 2007)

$$\mathbf{M}\ddot{\mathbf{U}} + \mathbf{C}\dot{\mathbf{U}} + \mathbf{K}\mathbf{U} = \mathbf{F}\left(t\right) \tag{3.4}$$

where the global mass matrix, damping matrix and stiffness matrix are denoted by $\mathbf{M}$, $\mathbf{C}$ and $\mathbf{K}$, respectively. These global matrices can be obtained by assembling the local element matrices. The external excitation force vector $\mathbf{F}\left(t\right)$ is a function of time. $\mathbf{C}$ is the global damping matrix related to the mass matrix, which has the following form $\mathbf{C} = \eta\mathbf{M}$, and h is the damping coefficient. $\mathbf{U}$, $\dot{\mathbf{U}}$ and $\ddot{\mathbf{U}}$ are the vectors of displacement, velocity and acceleration, respectively. For an element of length L_e, the element matrices $\mathbf{M}^e$ and $\mathbf{K}^e$, and the column vector $\mathbf{F}^e$ can be obtained using the following equations:

$$\mathbf{M}^e \approx \sum_{i=1}^{n} w_i \mathbf{S}_e\left(\xi_i\right)^T \mathbf{r}_e \mathbf{S}_e\left(\xi_i\right)\left|J\left(\xi_i\right)\right| \tag{3.5}$$

$$\mathbf{K}^e \approx \sum_{i=1}^{n} w_i \mathbf{B}_e\left(\xi_i\right)^T \mathbf{E}_e \mathbf{B}_e\left(\xi_i\right)\left|J\left(\xi_i\right)\right| \tag{3.6}$$

$$\mathbf{F}^e \approx \sum_{i=1}^{n} w_i \mathbf{S}_e\left(\xi_i\right)^T \mathbf{f}_e\left(\xi_i\right)\left|J\left(\xi_i\right)\right| \tag{3.7}$$

where n is the number of the GLL integration points in the element. $\mathbf{r}_e$ is the mass density matrix. $\mathbf{E}_e$ is the stress-stain matrix indicating the relationship between stress and strain. $\mathbf{f}_e\left(x_i\right)$ is the external excitation. $\mathbf{B}_e$ is the strain-displacement operator and is defined as:

$$\mathbf{B}_e\left(\xi\right) = \mathbf{D}\mathbf{S}_e\left(\xi\right), \quad and \quad J = \frac{\partial x}{\partial \xi} \tag{3.8}$$

where J is the Jacobian functions transferring the local coordinate to the global domain. $\mathbf{D}$ is the differential operator developed on the basis of Mindlin-Herrmann rod and Timoshenko beam theory, which are defined as:

$$\mathbf{D} = \begin{bmatrix} \frac{\partial}{\partial x} & 0 & 0 & 0 \\ 0 & 1 & 0 & 0 \\ 0 & \frac{\partial}{\partial x} & 0 & 0 \\ 0 & 0 & \frac{\partial}{\partial x} & -1 \\ 0 & 0 & 0 & \frac{\partial}{\partial x} \end{bmatrix} = \begin{bmatrix} \frac{1}{J}\frac{\partial}{\partial x} & 0 & 0 & 0 \\ 0 & 1 & 0 & 0 \\ 0 & \frac{1}{J}\frac{\partial}{\partial x} & 0 & 0 \\ 0 & 0 & \frac{1}{J}\frac{\partial}{\partial x} & -1 \\ 0 & 0 & 0 & \frac{1}{J}\frac{\partial}{\partial x} \end{bmatrix} \tag{3.9}$$

$x_i \in [-1,1]$ for $i \in 1,...,n$ is the coordinates of the GLL integration points, which can be obtained as the roots of the equation below:

$$\left(1-\xi^2\right)L'_{n-1}\left(\xi\right)=0 \tag{3.10}$$

where L'_{n-1} is the first derivative of the Legendre polynomial of degree $n-1$. In this study an eight-node element is used, and hence, $n=8$, as shown in Figure 3.1. The weights w_i in Equations (3.5) – (3.7) is accounted for node i and it has the expression: (Pozrikidis, 2005)

$$w_i=\frac{2}{n\left(n-1\right)[L_{n-1}\left(\xi_i\right)]^2} \tag{3.11}$$

As four DoFs (i.e., longitudinal displacement u, lateral contraction ψ, vertical displacement v and rotation φ) are considered at a node, the shape function matrix $\mathbf{S}_e$ has the form:

$$\mathbf{S}_e=\mathbf{S}\otimes\mathbf{I} \tag{3.12}$$

where $\mathbf{S}=[S_1(\xi),...,S_n(\xi)]$ is a row vector. '$\otimes$' denotes the Kronecker product and $\mathbf{I}$ is a 4×4 identity matrix. The shape function $S_i(\xi)$ at node i that is defined as:

$$S_i\left(\xi\right)=\prod_{m=1,m\neq i}^{n}\frac{\xi-\xi_m}{\xi_i-\xi_m}\ \text{for}\ i(i\in 1,2,...,n) \tag{3.13}$$

where n illustrates the number of GLL integration points in each element and m means the sequence of node. The shape function has the orthogonal property as:

$$S_i\left(\xi_j\right)=\begin{cases}1, i=j\\ 0, i\neq j\end{cases}\ \text{for}\ j(j\in 1,2,...,n)\ \text{and}\ \sum_{i=1}^{n}S_i\left(\xi_j\right)=1 \tag{3.14}$$

This property is illustrated in Figure 3.1. With the value of this shape function, the global mass matrix $\mathbf{M}$ in Equation (3.4) can achieve a diagonal form. This contributes to an explicit expression of the integrating equation using central difference scheme, and hence, the dynamic equilibrium of the model can be efficiently calculated.

Based on the Mindlin-Herrmann rod and Timoshenko beam theory, the mass density matrix $\mathbf{r}_e$ in Equation (3.5) and the stress-strain matrix $\mathbf{E}_e$ in Equation (3.6) are denoted as below:

$$\mathbf{r}_e = \begin{bmatrix} rA & 0 & 0 & 0 \\ 0 & K_2^M rI & 0 & 0 \\ 0 & 0 & rA & 0 \\ 0 & 0 & 0 & K_2^T rI \end{bmatrix} \tag{3.15}$$

and

$$\mathbf{E}_e = \begin{bmatrix} \frac{EA}{1-n^2} & \frac{nEA}{1-n^2} & 0 & 0 & 0 \\ \frac{uEA}{1-n^2} & \frac{EA}{1-n^2} & 0 & 0 & 0 \\ 0 & 0 & K_1^M GI & 0 & 0 \\ 0 & 0 & 0 & K_1^T GA & 0 \\ 0 & 0 & 0 & 0 & EI \end{bmatrix} \tag{3.16}$$

Substituting $\mathbf{D}$, $\mathbf{r}_e$, $\mathbf{E}_e$ and $\mathbf{S}_e$ into Equations (3.5) – (3.7), and the element mass matrix $\mathbf{M}^e$, stiffness matrix $\mathbf{K}^e$ and external force matrix $\mathbf{F}^e$ can be obtained to constitute the global matrices $\mathbf{M}$, $\mathbf{C}$ and $\mathbf{K}$ in Equation (3.4).

3.2.3 Crack element modelling

A two-node spectral crack element with length l_c was developed to simulate the scattering of GW and mode-conversion effect when the GW encounters the crack. The crack element can be located continuously at any location L_c along the beam. A transverse surface crack, which has an elliptical shape representing a practical situation of the crack (Irwin, 1962), is modelled in the crack element. The element has a very small length (i.e., 0.1 mm) in the longitudinal direction of the beam, thus, it can be treated as dimensionless in this direction. As a result, the value of the strain in the longitudinal direction is neglected, and hence, the corresponding axis contraction $\psi(x)$ in this crack element is considered zero. The geometric of crack element is shown in Figure 3.2. The elliptical crack has a cross section with width b_c and depth d_c, and it is modelled at the location x_c measured from the left end of the crack element.

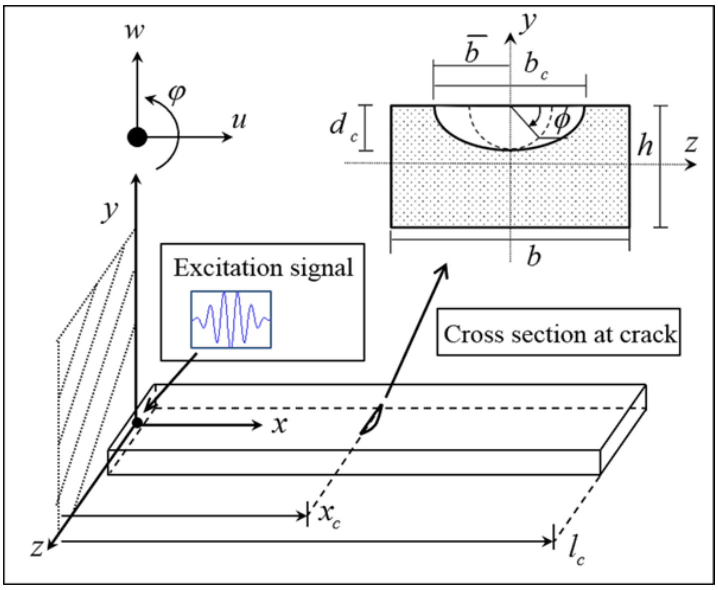

Fig. 3.2 Schematic diagram of the crack element for simulating a part-through surface crack.

The element stiffness matrix $\mathbf{K}_e^c$ for the crack element proposed by Darpe et al. (2004) is modified to account coupling of the longitudinal, transverse and rotational displacement, and hence, it can simulate the mode conversion effect when the incident GW interacts at the crack. The element stiffness matrix $\mathbf{K}_e^c$ is defined as:

$$\mathbf{K}_e^c = \mathbf{Y}\mathbf{Q}_f^{-1}\mathbf{Y}^T \tag{3.17}$$

where the position transformation matrix $\mathbf{Y}$ is a function of crack location and is defined as:

$$\mathbf{Y}^T = \begin{bmatrix} 1 & 0 & 0 & -1 & 0 & 0 \\ 0 & 1 & 0 & 0 & -1 & l_c \\ 0 & 0 & 1 & 0 & 0 & -1 \end{bmatrix} \tag{3.18}$$

$\mathbf{Q}_f$ is the flexibility matrix and is defined as:

$$\mathbf{Q}_f = \begin{pmatrix} q_{11} & q_{12} & q_{13} \\ q_{21} & q_{22} & q_{23} \\ q_{31} & q_{32} & q_{33} \end{pmatrix} \tag{3.19}$$

with

$$\begin{gathered} q_{11} = \frac{l_c}{EA} + I_{c1},\ q_{22} = \left(\frac{\alpha_s l_c}{GA} + \frac{l_c^3}{3EA}\right) + \left(I_{c3} + x_c^2 I_{c4}\right),\ q_{33} = \frac{l_c}{EI} + I_{c4} \\ q_{12} = q_{21} = x_c I_{c2},\ q_{13} = q_{31} = -I_{c2},\ q_{23} = q_{32} = -\frac{l_c^2}{2EI} - x_c I_{c4} \end{gathered} \tag{3.20}$$

where $\alpha_s = 10(1+\nu)/(12+11\nu)$ is the shear coefficient rectangular cross-section of the beam.

$$\begin{gathered} I_{c1} = \frac{8\pi\kappa^2}{Eb^2h^2\left[1+1.464\kappa^{1.65}\right]}\int_0^{\bar{b}}\int_0^{\pi/2}\bar{b}^2\sin^2\phi F_I{}^2 d\phi d\bar{b} \\ I_{c2} = \frac{48\pi\kappa^2}{Eb^2h^3\left[1+1.464\kappa^{1.65}\right]}\int_0^{\bar{b}}\int_0^{\pi/2}\bar{b}^2\sin^2\phi H F_I{}^2 d\phi d\bar{b} \\ I_{c3} = \frac{8\alpha_s^2\pi\kappa^2}{Eb^2h^2}\int_0^{\bar{b}}\int_0^{\pi/2}\bar{b}^2\sin^2\phi F_{II}{}^2 d\phi d\bar{b} \end{gathered} \tag{3.21}$$

$$I_{c4} = \frac{288pk^2}{Eb^2h^4\left[1+1.464k^{1.65}\right]}\int_0^{\bar{b}}\int_0^{p/2}\bar{b}^2\sin^2 f\, H^2 F_I^2\, df\, d\bar{b}$$

where $k = d_c/\bar{b}$ and $\bar{b} = b_c/2$. h is the thickness of the beam. F_I and F_{II} are the empirical boundary calibration factors accounted for tension (Newman Jr and Raju, 1981) and shear (He and Hutchinson, 2000) for the semielliptical surface crack, respectively. They are functions of crack depth d_c and crack width b_c. The details of the F_I, F_{II} and H are summarised in Appendix A.

3.3 Bayesian approach for multiple cracks identification

In order to identify multiple cracks, the proposed Bayesian approach contains two stages. In stage-one the number of cracks (i.e., the most suitable model class) is determined using Bayesian model class selection method. The crack parameters are then identified using Bayesian statistical framework in stage-two.

3.3.1 Stage-one: Bayesian model class selection

In stage-one of the proposed methodology a series of model classes $\mathbf{M} \equiv \{M_j : j = 1, 2, ..., N_M\}$, which represent beams with different number of cracks, are considered. The procedure is shown in Figure 3.3.

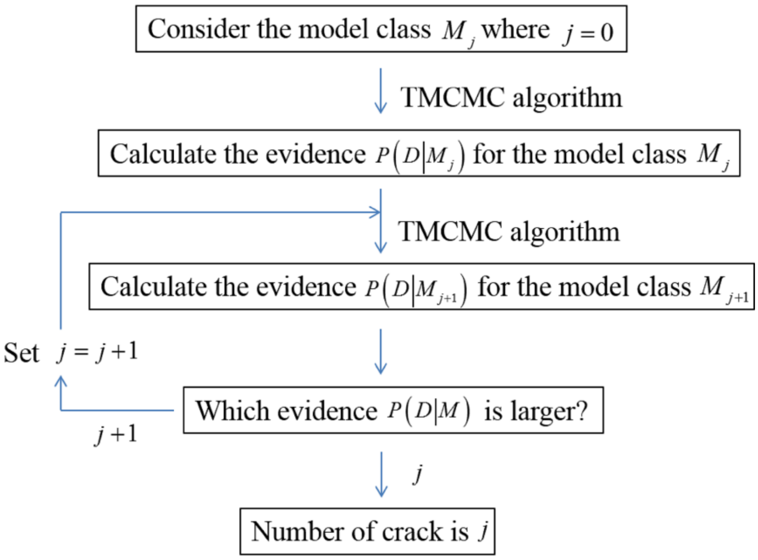

Fig. 3.3 Framework of Bayesian model class selection.

Using the Bayesian model class selection method (Beck, 2010, Beck and Yuen, 2004), the plausibility of the considered model classes can be assessed based on their posterior probability from the Bayes' Theorem, i.e. the probability of the model class conditional on the set of measurements , as, the plausibility of the considered model classes can be assessed based on their posterior probability from the Bayes' Theorem, i.e. the probability of the model class conditional on the set of measurements D, as:

$$P\left(M_j \middle| D,\mathbf{M}\right)=\frac{P\left(D \middle| M_j\right)P\left(M_j \middle| \mathbf{M}\right)}{\sum_{i=1}^{N_M} P\left(D\,|\,M_i\right)P\left(M_i\,|\,\mathbf{M}\right)} \tag{3.22}$$

where M_j denotes a model class with j cracks, $j=1,\ldots,N_M$. N_M is the maximum number of cracks considered. $P\left(M_j \middle| \mathbf{M}\right)$ is the prior probability of the model class M_j and $\sum_{j=1}^{\mathrm{N_M}} P\left(M_j \middle| \mathbf{M}\right)=1$. As there is no available prior information about the number of cracks, the prior probability $P\left(M_j \middle| \mathbf{M}\right)$ is set to be $1/\mathrm{N}_{M_j}$ for each model class in this study. The evaluation of

$P(M_j \mid D, \mathbf{M})$ requires determination of the evidence $P\left(D \middle| M_j\right)$, which can be expressed as:

$$P\left(D \middle| M_j\right) = \int P\left(D \middle| \boldsymbol{\theta}_j, M_j\right) P\left(\boldsymbol{\theta}_j \middle| M_j\right) d\boldsymbol{\theta}_j \tag{3.23}$$

where $\boldsymbol{\theta}_j$ is a vector containing the uncertain crack parameters, such as locations, widths and depths of the cracks, to be identified for the model class M_j (a beam with j cracks). However, Equation (3.23) involves a multi-dimensional integral, it is too complex to analytically integrate this equation. Laplace's method of asymptotic approximation can be used for model class that is globally identifiable. In multiple cracks identification, it involves model classes with different number of cracks from less than to more than the true number of cracks. For a given measured data, the model updating problem becomes unidentifiable when the model class (model class with more number of cracks) is too complex. In this situation, stochastic simulation methods, such as TMCMC (Ching and Chen, 2007) and Subset simulation methods (Vakilzadeh et al., 2017, Au et al., 2015, Straub and Papaioannou, 2014), are practical for calculating the evidence value of these model classes. In this chapter, the TMCMC method will be used to calculate the evidence value in Equation (3.23) and the details will be discussed in Section 3.4.

In the Bayesian model class selection method, the penalty against complexity can be obtained by considering the evidence from an information-theoretic point of view, consider the log of the evidence as: (Muto and Beck, 2008)

$$\begin{aligned} \ln\left[P\left(D \middle| M_j\right)\right] &= \int \ln\left[\frac{P\left(D \middle| \boldsymbol{\theta}_j, M_j\right) P\left(\boldsymbol{\theta}_j \middle| M_j\right)}{P\left(\boldsymbol{\theta}_j \middle| D, M_j\right)}\right] P\left(\boldsymbol{\theta}_j \middle| D, M_j\right) d\boldsymbol{\theta}_j \\ &= \int \ln\left[P\left(D \middle| \boldsymbol{\theta}_j, M_j\right)\right] P\left(\boldsymbol{\theta}_j \middle| D, M_j\right) d\boldsymbol{\theta}_j - \int \ln\left[\frac{P\left(\boldsymbol{\theta}_j \middle| D, M_j\right)}{P\left(\boldsymbol{\theta}_j \middle| M_j\right)}\right] P\left(\boldsymbol{\theta}_j \middle| D, M_j\right) d\boldsymbol{\theta}_j \end{aligned} \tag{3.24}$$

The left side of Equation (3.24) is the log evidence of the model class M_j. It can be decomposed into two different terms on the right hand side of the equation. The first term is the log-likelihood function, which is a data-fit term, indicating the plausibility of the model class M_j. The model class with more number of cracks has larger log-likelihood value. The second term is relative entropy between the prior and posterior distribution, which is a measure of the information gained about $\boldsymbol{\theta}_j$ from the data D. It provides a penalty against more 'complex' model class, i.e. model class with more number of cracks in this study. Thus the log evidence $\ln[p(D \mid M_j)]$ automatically implements a quantitative Ockham's razor in term of a trade-off between a data-fit measure and a complexity measure for each model class. If the selection of the model class is based purely on the log-likelihood function, i.e. the data-fit term in Equation (3.24), then model class with more number of cracks will be preferred over model class with less number of cracks and this is the case for most of the damage detection methods based on the maximum likelihood approach or error minimisation approach. In Bayesian model class selection method, the model class with the maximum value of the log evidence value will be selected and this provides a robust identification of the number of cracks in the beams.

3.3.2 Stage-two: Bayesian approach for identifying crack parameters

The stage-two of the Bayesian approach is to determine the optimal value of the crack parameters $\boldsymbol{\theta}_j$. Given a Bayesian model class M_j, the model response data D defined by the model parameters $\boldsymbol{\theta}_j$ can be used to update the corresponding plausibility of each model. The posterior probability density function (PDF) of uncertain crack parameters conditional on the measurement D and the model class M_j can be estimated as follows:

$$P\left(\boldsymbol{\theta}_j \middle| D, M_j\right) \propto P\left(D \middle| \boldsymbol{\theta}_j, M_j\right) P\left(\boldsymbol{\theta}_j \middle| M_j\right) \tag{3.25}$$

where $P\left(\boldsymbol{\theta}_j \middle| M_j\right)$ is the prior probability of the crack parameters based on the initial engineering judgement about the damage parameters. $P\left(D \middle| \boldsymbol{\theta}_j, M_j\right)$ is the likelihood function indicating the probability of getting the response data D based on the crack parameters $\boldsymbol{\theta}_j$. Based on the Principle of Maximum information Entropy (Gull, 1988), this chapter assumes the likelihood function follows the Gaussian distribution with zero mean and standard deviation of prediction error σ_j as:

$$P\left(D \middle| \boldsymbol{\theta}_j, M_j\right) = \frac{1}{\left(2\pi\sigma_j^2\right)^{\frac{N_t N_o}{2}}} \exp\left(-\frac{1}{2\sigma_j^2} \mathrm{J}\ \left(t;\boldsymbol{\theta}_j\right)\right) \tag{3.26}$$

where J is the goodness-of-fit function and is given as follows:

$$\mathrm{J}\ \left(t;\boldsymbol{\theta}_j\right) = \sum_{o=1}^{N_o} \sum_{t=1}^{N_t} \left[q_m(t) - q\left(t;\boldsymbol{\theta}_j\right)\right]^2 \tag{3.27}$$

where $q_m\left(t\right)$ is the response displacement measured from experiment at t-th time step. $q\left(t;\boldsymbol{\theta}_j\right)$ is the simulated response displacement from the chosen model class M_j defined by the uncertain parameters $\boldsymbol{\theta}_j$. N_t and N_o denote the numbers of measurement time steps and the measured DoF, respectively. The variance of the prediction error σ_j^2 can be treated as an uncertain parameter in the analysis (Ching and Chen, 2007). Since s_j^2 is always positive, its prior distribution can be modelled by an inverse Gamma distribution, and hence, s_j^2 can be sampled from $IG(0.5N_t N_o + 1, 0.5\mathrm{J}\ (t;\boldsymbol{\theta}_j))$ (Nichols et al., 2010) where IG is the inverse Gamma distribution.

For identifiable cases, the posterior PDF in Equation (3.25) can be approximated by a multivariable Gaussian PDF based on the global optimal model parameter $\hat{\boldsymbol{\theta}}_j$ (Beck and Katafygiotis, 1998). However, in multiple cracks identification cases, the problem may become unidentifiable for more complex model, i.e. model with more number of cracks. This make the multivariable Gaussian PDF cannot accurately approximate the posterior PDF. In this regard the Equation (3.25) is estimated alternatively using stochastic sampling method with a set of parameter samples $\boldsymbol{\theta}_j^{(h)}$, $h=1,...,N_s$, drawn from target distribution, where N_m is the number of samples at the m-th stage (final stage). In this chapter the samples are drawn using the TMCMC sampler adapted from Ching and Chen (2007) and the details are described in the Section 3.4. At the final stage of TMCMC, the samples drawn from TMCMC sampler are asymptotically distributed as $P(D|\boldsymbol{\theta}_j,M_j)$, the identified crack parameters can be estimated by the sample means. The marginal posterior PDF of the i-th uncertain parameter can be obtained by adaptive kernel density estimation with Gaussian distribution being the kernel PDF (Lam et al., 2015, Au and Beck, 1999) as:

$$k\left(\boldsymbol{\theta}_j(i)\right)=\frac{1}{N_s}\sum_{h=1}^{N_s}W^{(h)}\mathrm{N}\left(\boldsymbol{\theta}_j^{(h)}(i),\mathbf{C}(i,i)\right) \qquad (3.28)$$

where $\mathrm{N}(\mu,\Sigma)$ is the Gaussian distribution with mean η and covariance matrix S. $W^{(h)}$ is the weighting of the h-th sample. $\mathbf{C}(i,i)$ is the i-th diagonal element of the sample covariance matrix calculated by the samples at the final stage of TMCMC. In details of the adaptive kernel density estimation can be found in the references (Lam et al., 2015, Au and Beck, 1999).

3.4 Transitional Markov Chain Monte Carlo algorithm

Accurate estimation of the posterior PDF $P(D|\boldsymbol{\theta}_j,M_j)$ and evidence $P(D|M_j)$ requires samples drawn from the target distribution. In general samplers generate samples from prior PDF, which is quite different from the posterior PDF in an unidentifiable situation. In this aspect conventional Markov Chain Monte Carlo (MCMC) sampler is inefficient as a large number of samples will be rejected until it converges to the stable distribution of the samples. The TMCMC sampling method is more efficient than conventional MCMC as it generates samples from a series of stages, which gradually approximates the final PDF in Equation (3.24). Other sampling methods, such as Subset Simulation (Vakilzadeh et al., 2017, Au et al., 2015, Straub and Papaioannou, 2014), also have been recently developed to address this problem and they are found to be robust regardless of the dimension of parameters. Since TMCMC has many successful applications, this study employs the TMCMC in the Bayesian approach. The schematic framework for TMCMC algorithm is shown in Figure 3.4.

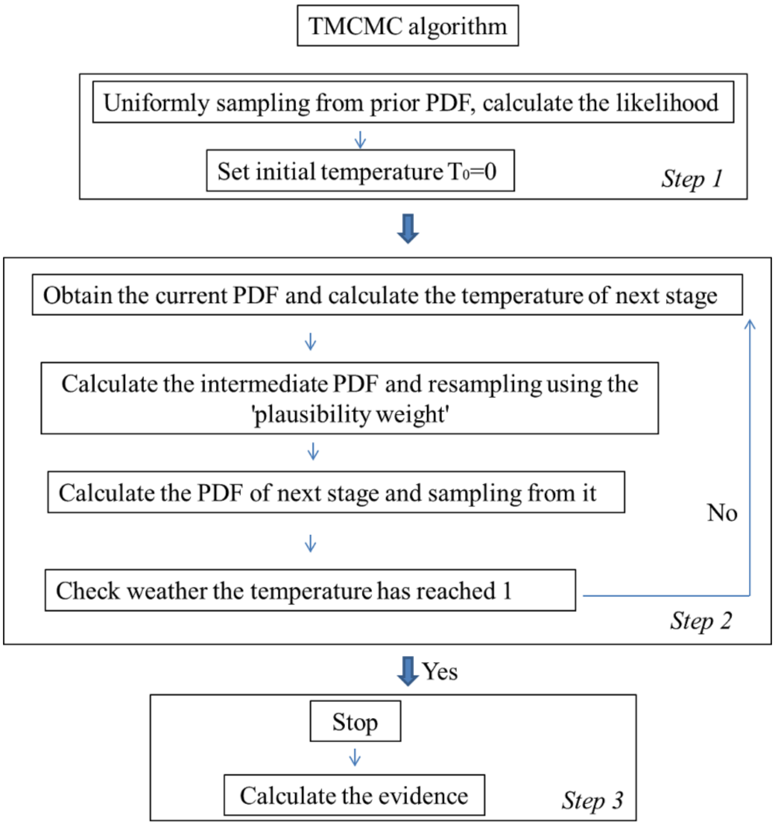

Fig. 3.4 Framework of TMCMC algorithm.

In the beginning stage, the TMCMC sampler generates samples $\{\boldsymbol{\theta}_1^{(h)} : h = 1,...,N_1\}$ for from the prior PDF where N_1 is the number of samples at $s = 1$ stage. The prior PDF is chosen based on engineering experience, and in this study a uniform distribution is employed. In step two the TMCMC sampler uses a series of intermediate stages $s = 2,\ldots,m$ to generate samples gradually converging to the PDF region with high probability. Specifically, the samples are generated twice at each stage. First, it generates samples from the transitional PDFs $P(D \mid M, \boldsymbol{\theta}_s^{(h)})^{T_{s+1}-T_s}$ using a resampling technique. For example, given N_s samples $\{\boldsymbol{\theta}_s^{(h)}, h = 1,\ldots,N_s\}$ generated from the previous stage, redraw N_k^r samples $\{\boldsymbol{\theta}_s^{(h),r}, h = 1,\ldots,N_s\}$ from the N_s samples with the resampling probability $P_{re}(\boldsymbol{\theta}_s^{(h)}) = W(\boldsymbol{\theta}_s^{(h)}) \big/ \sum_{h=1}^{N_s} W(\boldsymbol{\theta}_s^{(h)})$ for each sample. It should be noted that the same sample $\theta_s^{(h),r}$ can be drawn repeatedly and the repeating number of this sample is recorded as $R_s^{(h)}$. $W(\boldsymbol{\theta}_s^{(h)})$ is the 'plausibility weight' of each of the N_s samples and it has the following expression:

$$W(\boldsymbol{\theta}_s^{(h)}) = \frac{P\left(\boldsymbol{\theta}_s^{(h)} | M_j\right) P\left(D | M_j, \boldsymbol{\theta}_s^{(h)}\right)^{T_{s+1}}}{P\left(\boldsymbol{\theta}_s^{(h)} | M_j\right) P\left(D | M_j, \boldsymbol{\theta}_s^{(h)}\right)^{T_s}} = P\left(D | M_j, \boldsymbol{\theta}_s^{(h)}\right)^{T_{s+1}-T_s} \quad \text{and} \quad h = 1,\ldots,N_s \tag{3.29}$$

and the intermediate PDF $P_s(\boldsymbol{\theta})$ in the stage s is expressed as:

$$P_s(\boldsymbol{\theta}) \propto P\left(D | \boldsymbol{\theta}, M_j\right)^{T_s} P\left(\boldsymbol{\theta} | M_j\right),\ s = 1,...,m \quad \text{and} \quad 0 = T_1 < T_2 < \ldots < T_{\mathrm{m}} = 1 \tag{3.30}$$

where T_s is the temperature variable determining the smoothness of transition between two adjacent PDFs. If the T_s value increases slowly, more stages of resampling are applied. However, the convergence of the sampling is slow and more computational resources are required. The value of temperature variable T_s can be determined automatically in the TMCMC algorithm by setting the coefficient of variation (c.o.v.) of the 'plausibility weight' $W(\theta_s^{(h)})$ at each stage s to a prescribed threshold, where the c.o.v. is the standard deviation of the sample vectors over their mean. It is found that 100% is a preferable choice for the prescribed threshold in usual case. As it can be seen from the Equation (3.29), each intermediate PDF is calculated interactively based on the PDF from last stage. This leads to the high performance of TMCMC in the high dimensional situation as the PDF converges gradually.

After the procedure of resampling, N_s^r MCMC chains are generated to draw N_{s+1} ($N_{s+1} = N_s$) new samples $\left\{\theta_{s+1}^{(h)}, h = 1, \ldots, N_s\right\}$ from the next intermediate PDF $P_{s+1}(\boldsymbol{\theta})$. These chains start from each of the N_{s+1} samples $\{\theta_s^{(h),r}, h = 1, \ldots, N_s\}$ and the sample number of each chain is $R_s^{(h)}$. The proposal samples are generated using Gaussian PDF with the covariance matrix $\sum_s$, which has the form:

$$\sum_s = c_s^2 \sum_{h=1}^{N_s} w(\boldsymbol{\theta}_s^{(h)})(\boldsymbol{\theta}_s^{(h)} - \sum_{l=1}^{N_s} P_{re}(\boldsymbol{\theta}_s^{(h)})\boldsymbol{\theta}_s^{(l)})(\boldsymbol{\theta}_s^{(l)} - \sum_{l=1}^{N_s} P_{re}(\boldsymbol{\theta}_s^{(h)})\boldsymbol{\theta}_s^{(l)}) \tag{3.31}$$

where c_s is the step factor that influences the distance between samples in each Markov Chain at stage s. The accepting probability of each proposed sample $\boldsymbol{\theta}_{s+1}^{(h)}$ is $\left[P\left(D|\boldsymbol{\theta}_s^{(h)}, M_j\right) / P\left(D|\boldsymbol{\theta}_s^{(h)}, M_j\right)\right]^{T_{s+1}}$. Step two is repeated until the value of temperature T_{s+1} has reached 1, where concurrently the PDF has converged to the target PDF.

In the final stage (m-th stage), $\{\boldsymbol{\theta}_m^{(h)} : h = 1, \ldots, N_m\}$ samples are asymptotically distributed as $P(D|\boldsymbol{\theta}_j, M_j)$ and evidence $p\left(D|M_j\right)$ of the model class M_j can be estimated using $S = \prod_{s=1}^{m}\left[\sum_{h=1}^{N_s} w(\theta_s^{(h)}) \Big/ N_s\right]$. They are proven an asymptotically unbiased estimation (Ching and Chen, 2007). Therefore, the crack number can be determined by comparing the model evidence of each model class.

3.5 Numerical case studies

The performance of the Bayesian multiple cracks identification method is studied in this section. This section has four subsections that focus on different scenarios, i.e., 1) GW mode selection, 2) different crack numbers, 3) measurement noise levels and 4) cracked locations, as shown in Table 3.1. Aluminium beams with length 500 mm, depth 6 mm and width 12 mm were considered to investigate the capability of the proposed multiple crack identification method. The 3D explicit FE model was built based on the crack parameters described in Table 3.1 and the simulated signals were treated as synthetic experimental data.

Table 3.1 Summary of all numerical and experimental case studies.

Scenario		Numerical case studies												Experimental case studies		
		GW mode selection				Multiple cracks identification			Measurement noise influence			Crack location effect				
Damage case		S1	S2	S3	S4	D1	D2	D3	N1	N2	N3	L1	L2	E1	E2	E3
Incident wave		A_0			S_0	A_0			A_0			A_0		S_0	A_0	
Measurement direction*		*y*-dir.		*x*-dir. & *y*-dir.		*x*-dir. & *y*-dir.			*x*-dir. & *y*-dir.			*x*-dir. & *y*-dir.		*z*-dir.#	*y*-dir.	
Mode conversion effect		N	Y			Y			Y			Y		Y		
Measurement noise (%)		3				3			0	3	6	3		3		
Crack number		2				1	2	3	2			2		1		2
Crack 1 (mm)	L_c	200				250	200		200			200	100	250±1		200±1
	d_c	3				3		2	3			3		3±0.5		
	b_c	6				6			6			6		6±0.5		
Crack 2 (mm)	L_c	350					350	300	350			350				350±1
	d_c	2					2	3	2			2				2±0.5
	b_c	5					5	6	5			5				5±0.5
Crack 3 (mm)	L_c							400								
	d_c							2								
	b_c							4								

* The measurement direction is consistent with the coordinate system in Figure 2

\# The S_0 is measured from *z*-dir. through the Poisson's effect in experiment

L_c = crack location, d_c = crack depth, b_c = crack width

The proposed time-domain SFE model described in Section 3.2 was used to model the GW propagation in the beams with cracks as described in Section 3.3. The uncertain crack parameters are the locations (L_c), depths (d_c) and widths (b_c) of the cracks. In the SFE model, 25 spectral elements with 8 GLL nodes were used for modelling the beam. The Young's module, density and Poisson's ratio of the beam are 70 GPa, 2700 kg/m^3 and 0.3, respectively. Damping was considered to obtain the same ratio between amplitude changes of GW response for simulated and experimental data (Rucka, 2010) and the damping coefficient η was chosen at 550 s^{-1} in this chapter. The interval Δt of each time step was 10^{-7} sec to guarantee a converged solution of the dynamic equilibrium Equation (3.4) solved by central difference method. The excitation signal is a 100 kHz narrow-band six-cycle sinusoidal tone burst pulse modulated by a Hanning window and it was applied to the left beam end to generate GW response. The response signal was calculated at the same location. In the FE model, the commercial software ABAQUS/Explicit v6.12-1 was used to simulate the synthetic experimental GW response. Eight-node 3D reduced integration solid brick elements (C3D8R) were used to model the cracked beam. The enhanced hourglass control was enabled for FE simulation and the mesh size are 0.4×0.4×0.4 mm^3 to ensure the numerical stability of GW simulation. The dynamic explicit solver, which applies the central difference scheme, was employed to solve the FE simulation of GW propagation. The time step used in the SFE is 10^{-7} sec and the time step of the FE is automatically controlled by ABAQUS/Explicit. Measurement error was considered in the study and simulated by applying a percentage of root mean square (RMS) white noise the time-domain response of the GW calculated by the FE model.

The Bayesian statistical framework with TMCMC sampler was used to identify the crack parameters, i.e. locations, widths and depths of the cracks. Since the guided wave based crack identification focuses on early damage detection, it is assumed that the crack widths and depths are not larger than half of the width and depths of the beam cross-section. Thus the assignment of the prior PDF for $\boldsymbol{\theta}_j$ is independently uniformly distributed over [0.02mm

0.48mm], [0mm 3mm] and [0mm 6mm] for crack locations, widths and depths, respectively. 500 samples were drawn at each stage in the TMCMC sampling. The threshold of the c.o.v. of the 'plausibility weight' $W(\boldsymbol{\theta}_s^{(h)})$ was chosen to be 100% and the step factor c_s was set as 0.1.

3.5.1 Selection of GW mode for damage identification

This section is to investigate the performance of S_0 and A_0 GW and the mode conversion effect in identifying the cracks. Two cracks were assumed in the aluminium beam and there are four cases, i.e., Case S1, S2, S3 and S4 as shown in Table 3.1. As the focus of this section is to determine the most suitable wave mode based on the accuracy and uncertainty of the identified crack parameters, we assumed the number of cracks is known, and hence, only the crack parameters are identified in this section.

The mode-conversion effect was studied first by comparing the identified crack parameters using the numerical model without (Case S1) and with (Case S1) considering the GW mode coupling effect. Specifically, two different time-domain SFE models were employed to simulate the response data. In the first model, the normal cracked beam element without coupling the longitudinal and flexural displacement was employed. The second model with the proposed SFE cracked beam element was implemented to simulate the mode-coupled GW signals. In both cases, A_0 GW was excited and only the out-of-plane displacement was measured. The signal was normalised by the maximum absolute amplitude of the indecent wave. Table 3.2 shows the sample means and sample c.o.v.s of the uncertain crack parameters. The sample c.o.v. equals the ratio of the sample standard deviation to the sample mean. The value of the sample means indicate the identified crack parameters. The percentages of error of the identified crack parameters are shown in the brackets in Table 3.2. Compared the results of Cases S1 and S2, it indicates that the signal accounted the mode-conversion effect provides additional crack information, and hence, it enables more accurate crack identification.

Table 3.2 : Sample means and c.o.v.s of crack parameters calculated using TMCMC samples for Cases S1-S3 (errors of the identified crack parameters are shown in the bracket).

Case		Crack1 (mm)			Crack 2 (mm)		
		L_c	d_c	b_c	L_c	d_c	b_c
	Actual	200	3	6	350	2	5
S1	Sample mean	200.21 (0.11%)	2.73 (8.97%)	5.91 (1.53%)	350.51 (0.15%)	1.62 (19.15%)	5.40 (7.96%)
	Sample c.o.v (%)	0.0446	0.3749	0.3193	0.0352	6.7854	4.1015
S2	Sample mean	200.12 (0.06%)	2.84 (5.33%)	5.98 (0.33%)	350.31 (0.09%)	1.80 (9.85%)	5.19 (3.79%)
	Sample c.o.v (%)	0.0175	0.2142	0.1299	0.0258	4.5132	3.0037
S3	Sample mean	200.03 (0.02%)	2.99 (0.08%)	5.99 (0.07%)	350.02 (0.01%)	2.01 (0.05%)	4.79 (4.17%)
	Sample c.o.v (%)	0.0016	0.2196	0.1153	0.0157	0.3367	0.1534
S4	Sample mean	200.09 (0.05%)	2.99 (0.21%)	5.99 (0.17%)	350.49 (0.14%)	1.90 (4.88%)	5.09 (1.82%)
	Sample c.o.v (%)	0.0331	0.6404	0.3498	0.1550	5.0371	4.4294

The accuracy of the crack identification utilising A_0 GW (Case S3) and S_0 GW (Case S4) as excitation signal was investigated. Figure 3.5 shows the SFE simulated GW signals used in Case S3, in which the incident wave is A_0 GW. Figures 3.5a and 3.5b show the out-of-plane and in-plane measurement, respectively. Similarly Figure 3.6 shows the simulated GW signal of Case S4. The indicate wave is S_0 in Case S4. Figures 3.6a and 6b show the in-plane and out-of-plane measurement, respectively. Both Cases S3 and S4 consider the mode conversion effect. Figures 3.5 and 3.6 show that the mode converted signals provide additional information of the cracks. The results in Table 3.2 show that the crack parameters are identified accurately in both Cases S3 and S4. In generally, the case using the incident A_0 GW (Case S3) has better performance than the case using incident S_0 GW (Case S4). Comparing the results of the Cracks 1 and 2, the error and c.o.v. of the identified location, width and depth of Crack 2 are small than that of Crack 1. This is because the width and depth of Crack 2 are smaller than Crack 1, and hence, the amplitude of the scattered waves from Crack 2 is smaller than that from Crack 1. Based on the aforementioned findings, the use of incident A_0 GW with both in-plane and out-of-plane measurements could provide better accuracy in identifying the crack parameters. Hence, the rest of the numerical case studies use the A_0 GW as the incident wave signal and both in-plane and out-of-plane data as the measurements.

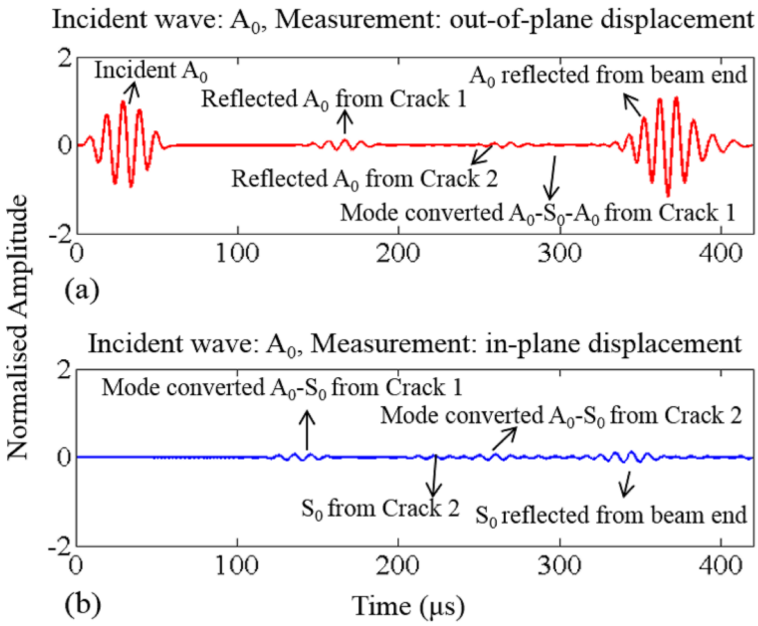

Fig. 3.5 Signal measured at excitation location for Case S3, incident wave: A_0 GW, (a) out-of-plane, and (b) in-plane displacement measurement.

The accuracy of the crack identification utilising A_0 GW (Case S3) and S_0 GW (Case S4) as excitation signal was investigated. Figure 3.5 shows the SFE simulated GW signals used in Case S3, in which the incident wave is A_0 GW. Figures 3.5a and 3.5b show the out-of-plane and in-plane measurement, respectively. Similarly Figure 3.6 shows the simulated GW signal of Case S4. The indicate wave is S_0 in Case S4. Figures 3.6a and 6b show the in-plane and out-of-plane measurement, respectively. Both Cases S3 and S4 consider the mode conversion effect. Figures 3.5 and 3.6 show that the mode converted signals provide additional information of the cracks. The results in Table 3.2 show that the crack parameters are identified accurately in both Cases S3 and

S4. In generally, the case using the incident A_0 GW (Case S3) has better performance than the case using incident S_0 GW (Case S4). Comparing the results of the Cracks 1 and 2, the error and c.o.v. of the identified location, width and depth of Crack 2 are small than that of Crack 1. This is because the width and depth of Crack 2 are smaller than Crack 1, and hence, the amplitude of the scattered waves from Crack 2 is smaller than that from Crack 1. Based on the aforementioned findings, the use of incident A_0 GW with both in-plane and out-of-plane measurements could provide better accuracy in identifying the crack parameters. Hence, the rest of the numerical case studies use the A_0 GW as the incident wave signal and both in-plane and out-of-plane data as the measurements.

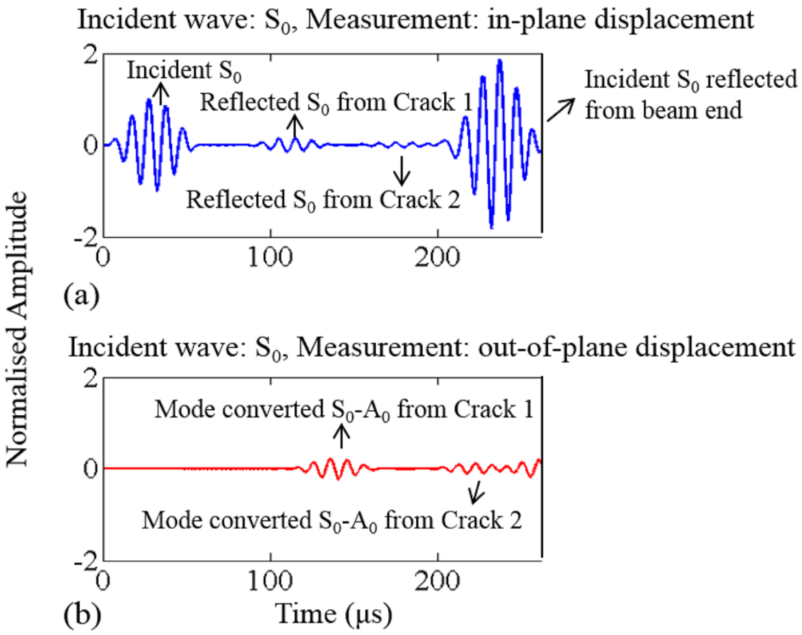

Fig. 3.6 Signal measured at excitation location for Case S4, incident wave: S_0 GW, (a) in-plane, and (b) out-of-plane displacement measurement.

3.5.2 Multiple cracks identification

In this section the capability of the proposed multiple crack identification method in determining the number, locations, widths and depths of the cracks is investigated. Three cases (Cases D1, D2 and D3 as shown in Table 3.1) with different number of cracks and crack parameters for multiple damage identification are considered in this section. Four SFE model classes $M_j, j = 1,...,4$ were considered in each case, where the subscript j denotes the number of cracks in the model class.

The identified number of cracks is presented in Table 3.3. The table shows the log-likelihood, information gain, log-evidence factor and probability of model classes. The log-likelihood factor shows the ability of the model class in fitting the measurement. It increase when the complexity of the model class increase (beam with more cracks). The results in Table 3.3 shows that the log-likelihood factor increases with the model complexity, and hence, it is not possible to determine the crack number based on the log-likelihood factor only. However, the information gain factor also increases with the model complexity, which penalises the complexity of the model class in the log-evidence factor. Hence, the log-evidence factor can be used to determine the optimal modal class, i.e. the number of cracks in the beam. As shown in Table 3.3, the probability of the model classes is also calculated from the log-evidence and it is closed to 1 for the correct model class (i.e. correct number of cracks) in each case.

Table 3.3 Bayesian model class selection results of Cases D1-D3.

Case	Model class	Log-likelihood	Information gain	Log-evidence	Probability
D1	**M_1**	**3447.43**	**17.08**	**3430.35**	**0.9289**
	M_2	3448.42	20.62	3427.80	0.0711
D2	M_1	3458.31	11.52	3446.79	0
	M_2	**3815.65**	**12.37**	**3803.28**	**0.9998**
	M_3	3816.28	21.28	3795.00	0.0002
D3	M_1	3345.90	11.52	3334.38	0
	M_2	3940.62	29.80	3910.82	0

	M_3	**4160.19**	**65.69**	**4094.50**	**1**
	M_4	4202.60	125.63	4076.97	$2.43e^{-8}$

The identified crack parameters for each case are summarised in Table 3.4. It is found that the performance of the TMCMC sampler is reliable in each case as the errors and the c.o.v.s of the identified results are reasonably small. It is also found that TMCMC algorithm is robust in term of the dimension of crack parameters as the c.o.v. of the identified results increases slightly from Cases D1 to D3. Table 3.4 also shows that Crack 3 in Case D3 has the smallest crack depth and width, and hence, the corresponding identified crack parameters have largest value c.o.v. This indicates that the accuracy of identifying the crack size will decrease when the crack becomes smaller. One possible solution to further improve the crack identification results is to use A_0 GW with shorter wavelength as it is more sensitive to smaller cracks. This can be achieved by increasing the frequency of the excitation signal in practice.

Table 3.4 Sample means and c.o.v.s of crack parameters calculated using TMCMC samples for Cases D1-D3 (errors of the identified crack parameters are shown in the bracket).

Case		Crack 1 (mm)			Crack 2 (mm)			Crack 3 (mm)		
		L_c	d_c	b_c	L_c	d_c	b_c	L_c	d_c	b_c
D1	Actual	250	3	6	-	-	-	-	-	-
	Sample mean	250.09 (0.04%)	2.71 (9.67%)	5.99 (0.17%)	-	-	-	-	-	-
	Sample c.o.v (%)	0.0125	0.6450	0.2990	-	-	-	-	-	-
D2	Actual	200	3	6	350	2	5	-	-	-
	Sample mean	200.20 (0.10%)	2.99 (0.07%)	5.71 (4.83%)	350.50 (0.23%)	2.09 (4.50%)	4.99 (0.19%)	-	-	-
	Sample c.o.v (%)	0.0784	0.3251	0.3982	0.0515	1.1788	0.9194	-	-	-
D3	Actual	200	2	6	300	3	6	400	2	4
	Sample mean	200.20 (0.10%)	1.99 (0.49%)	5.90 (1.67%)	300.50 (0.16%)	2.99 (0.07%)	5.99 (0.18%)	401.01 (0.25%)	1.12 (43.51%)	3.13 (21.75%)
	Sample c.o.v (%)	0.0071	0.0330	0.0480	0.0079	0.0250	0.0059	0.0288	1.5149	3.9409

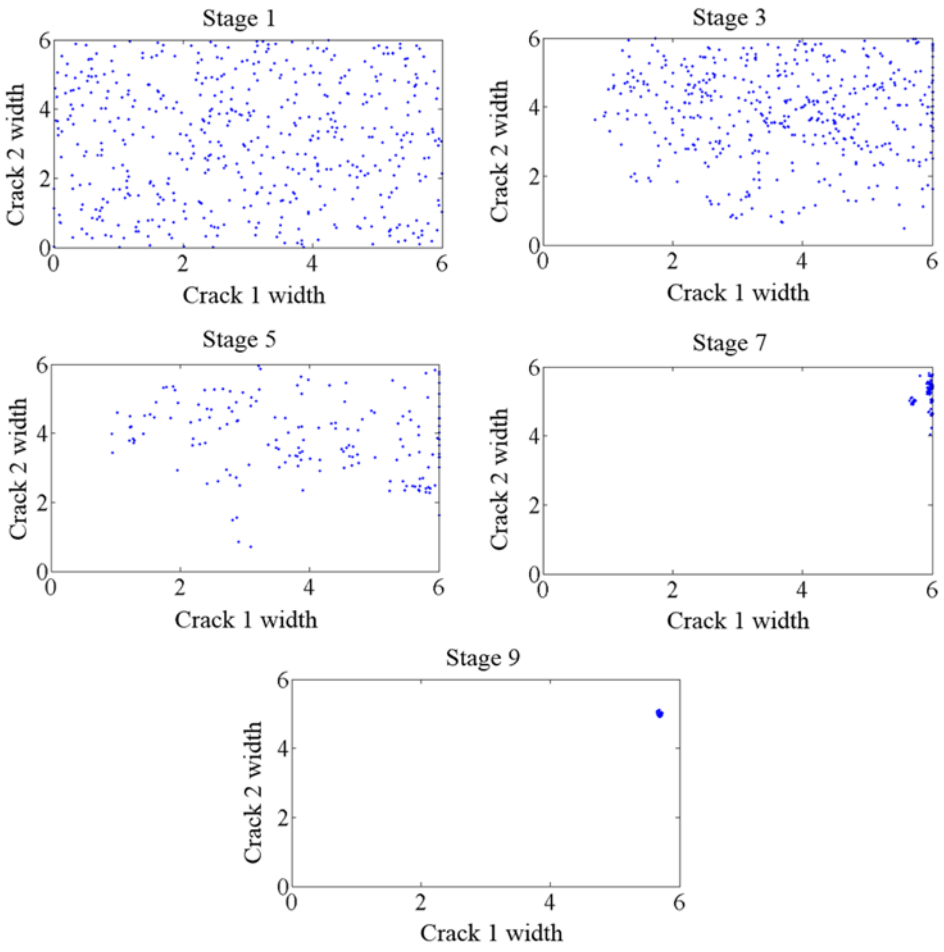

Fig. 3.7 Evolution of the TMCMC samples for the width of Crack 1 and Crack 2 in Case D2.

The evolution of the TMCMC samples of the width of Cracks 1 and 2 at different stages in Case D2 is shown in Figure 3.7. When the stage number increases, the TMCMC samples converge to the target PDF quickly and finally concentrate in the global optimal region. This shows that the proposed Bayesian approach with TMCMC sampler is efficient in crack identification. Figure 3.8 shows the posterior marginal PDFs calculated by kernel density estimation (Equation (3.28)) based on the set of samples in the final stage of the TMCMC sampling as shown in Figure 3.7. Comparing the posterior marginal PDFs shown in Figure 3.8, the drop in PDF value away from the peak for the width in Crack 1 is much faster than that for Crack 2. This implies that the uncertainty of the identified width of Crack 2 is higher than that of Crack 1 and this is consistent with the c.o.v.s in Table 3.4.

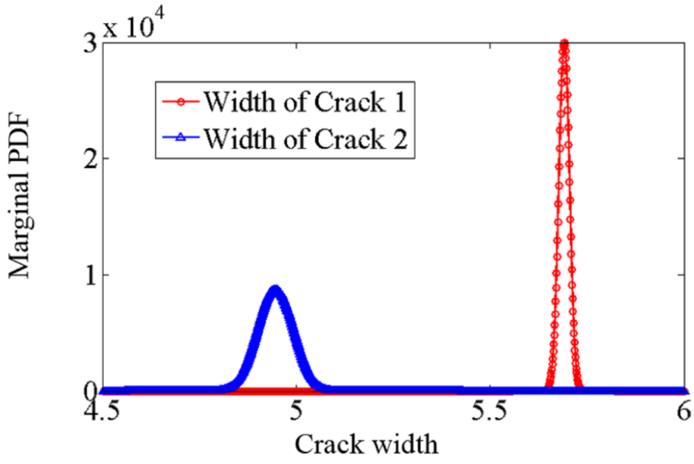

Fig. 3.8 Posterior marginal PDFs for the width of Crack 1 and Crack 2 in Case D2.

3.5.3 Influence of noise level

This section investigates the robustness of the proposed Bayesian approach under different measurement noise levels. Three cases (i.e. Cases N1, N2 and N3) with increasing level of measurement noise (0%, 3% to 6% of the RMS of the measured signal) are considered. The results in Table 3.5 shows that the numbers of cracks in all cases are correct identified under different measurement noise levels. The probability of model class with the correct number of cracks is prominent (i.e., almost equals to 1) for the Cases N1 and N2, in which measurement noise level 0% and 3% are considered. However, the probability of the optimal model class drops to 0.832 for the measurement noise level 6%. The sample means and sample c.o.v.s of the crack parameters are shown in Table 3.6. The results show that errors and c.o.v.s increase with the measurement noise level. Specifically, the c.o.v. of the smaller crack (Crack 2) increases notably in the case of the 6% measurement noise level. This indicates that measurement noise increases the uncertainties in the crack identification.

Table 3.5 Bayesian model class selection results for Cases N1-N3.

Case	Model class	Log-likelihood	Information gain	Log-evidence	Probability
N1	M_1	3605.23	10.71	3594.52	0
	M_2	**4156.31**	**21.07**	**4135.24**	**0.9589**
	M_3	4156.75	24.66	4132.09	0.0411
N2	M_1	3458.28	10.52	3447.76	0
	M_2	**3815.82**	**12.37**	**3803.45**	**0.9999**
	M_3	3816.17	22.08	3794.09	0.0001
N3	M_1	3126.59	10.50	3116.09	0
	M_2	**3307.80**	**18.87**	**3288.93**	**0.8468**
	M_3	3309.17	21.95	3287.22	0.1532

Table 3.6 Sample means and c.o.v.s of crack parameters calculated using TMCMC samples for Cases N1-N3 (errors of the identified crack parameters are shown in the bracket).

Case		Crack 1 (mm)			Crack 2 (mm)		
		L_c	d_c	b_c	L_c	d_c	b_c
	Actual	200	3	6	350	2	5
N1	Sample mean	200.01 (0.01%)	2.99 (0.07%)	5.99 (0.09%)	350.09 (0.03%)	1.97 (1.49%)	4.98 (0.41%)
	Sample c.o.v (%)	0.0015	0.0542	0.0292	0.0126	0.172	0.132
N2	Sample mean	200.5 (0.25%)	2.99 (0.13%)	5.90 (1.67%)	350.81 (0.23%)	1.91 (4.52%)	4.98 (0.40%)
	Sample c.o.v (%)	0.0016	0.2196	0.1153	0.0157	0.3367	0.1534
N3	Sample mean	200.9 (0.45%)	2.99 (0.32%)	5.80 (3.33%)	350.1 (0.03%)	1.89 (5.47%)	5.49 (9.79%)
	Sample c.o.v (%)	0.0106	0.2431	0.1612	0.0234	2.7934	2.4198

3.5.4 Influence of crack location

This section investigates the influence of the location of the crack in the proposed Bayesian crack identification method. Two damage cases (Cases L1 and L2) considering two cracks are studied in this section. The details of the cracks are summarised in Table 3.1. The location of Crack 2 is the same in both cases while the location of Crack 1 in Case L2 is closer to the measurement position (left beam end) than that in Case L1.

Table 3.7 Bayesian model class selection results for Cases L1 and L2.

Case	Model class	Log-likelihood	Information gain	Log-evidence	Probability
L1	M_1	3458.33	10.52	3447.81	0
	$\mathbf{M_2}$	**3815.79**	**12.37**	**3803.42**	**0.9999**
	M_3	3816.21	22.08	3794.13	0.0001
L2	M_1	3602.14	13.30	3588.84	0
	$\mathbf{M_2}$	**4432.05**	**15.14**	**4416.91**	**0.8375**
	M_3	4432.13	16.86	4415.27	0.1625

Table 3.8 Sample means and c.o.v.s of crack parameters calculated using TMCMC sample for Cases L1 and L2 (errors of the identified crack parameters are shown in the bracket).

Case	Model class	Log-likelihood	Information gain	Log-evidence	Probability
L1	M_1	3458.33	10.52	3447.81	0
	$\mathbf{M_2}$	**3815.79**	**12.37**	**3803.42**	**0.9999**
	M_3	3816.21	22.08	3794.13	0.0001
L2	M_1	3602.14	13.30	3588.84	0
	$\mathbf{M_2}$	**4432.05**	**15.14**	**4416.91**	**0.8375**
	M_3	4432.13	16.86	4415.27	0.1625

The identified crack number is shown in Table 3.7 and the proposed method correctly identifies the number of cracks based on the probability of the model class. The sample means and sample c.o.v.s of the crack parameters are summarised in Table 3.9. The results show that the identified crack parameters for Crack 1 has smaller errors and sample c.o.v.s in Case L2 than in Case L1. This is because Crack 1 is closer to the measurement point in Case L2, and hence, there are more reflected wave pulses from the Crack 1 than that in Case L1 as shown in Figure 3.9. Figures 3.9a and 3.9b show the GW data in out-of-plane and in-plane direction for Cases L1 and L2, respectively, in which Figure 3.9a is zoomed-in to focus on the reflected wave pulses only for the out-of-plane GW data.

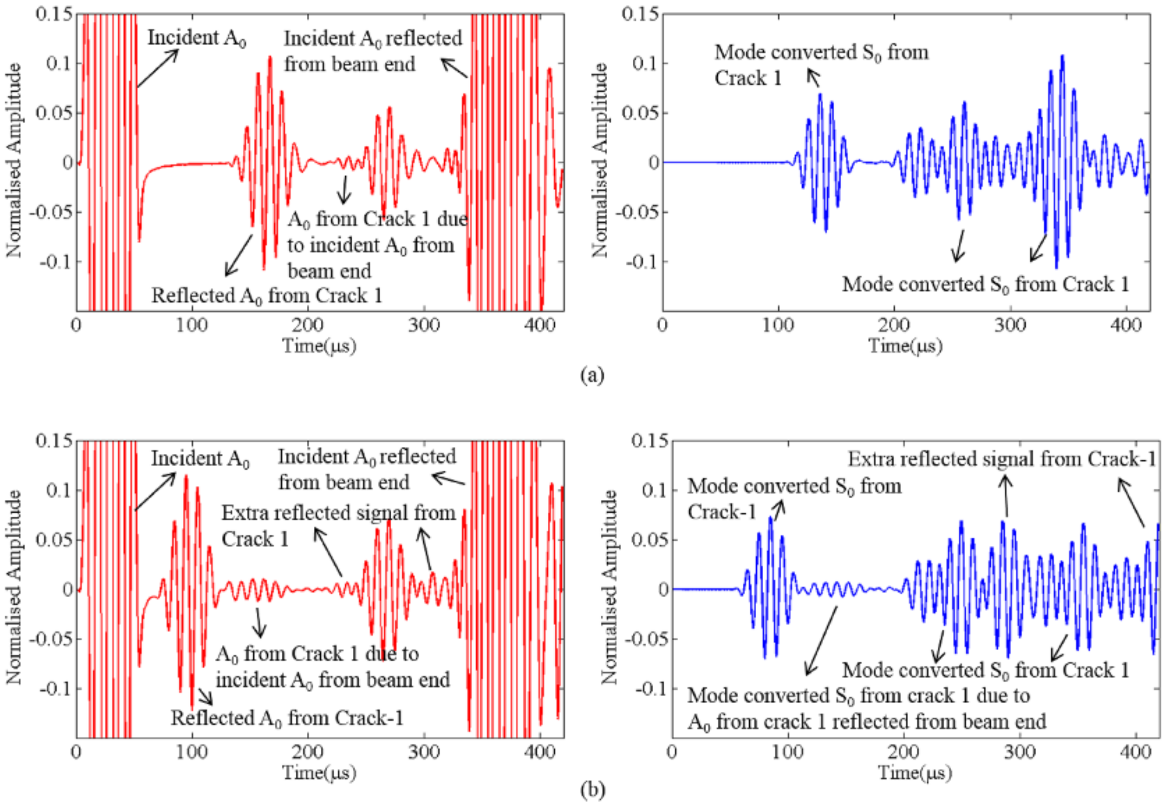

(a)

(b)

Fig. 3.9 Signal measured at excitation location for Cases (a) L1 and (b) L2.

3.6 Experimental case studies

3.6.1 Experimental setup

Two aluminium beams (Grade 6060-T5) with length 500 mm, width 12 mm and depth 6 mm were utilised to experimentally demonstrate the effectiveness of the proposed Bayesian multiple cracks identification method. The experimental setup is shown in Figure 3.10. As shown in Figure 3.11, a 12×6×2 mm^3 rectangular PZT was bonded to the surface at the left end of each beam using the silver loaded epoxy adhesive. A 12×6×4 mm^3 brass mass was attached on the top of the PZT to increase the excitability of the GW. The excitation signal is a narrow-band 7.5-cycle sinusoidal tone burst modulated by a Hanning window. The excitation signal was synthetised by a central computer and generated by a junction box with maximal 10V output voltage. It was then amplified to the voltage ranged from 10-50V using a signal amplifier (SERVO AMP). Afterward, this amplified signal was applied to the piezoceramic transducer installed on the beam to excite the GW at the left end of the beam.

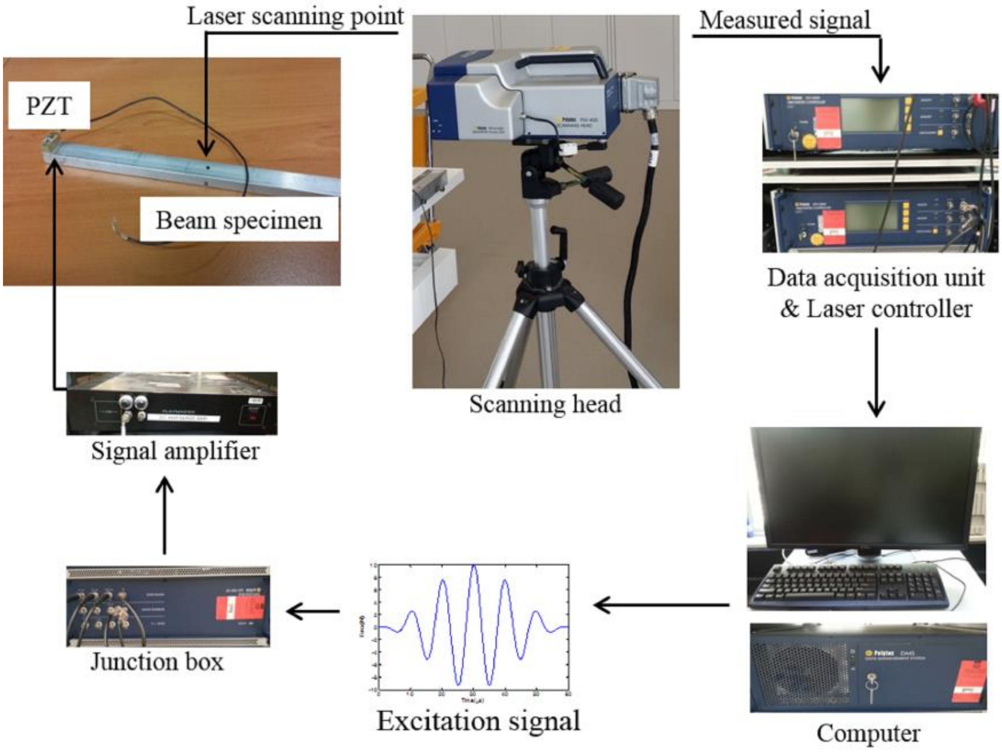

Fig. 3.10 Schematic diagram of the experimental setup.

The response displacement was recorded using a 1D laser Doppler vibrometer (PSV-400) head with Laser controller (OFV5000), and hence, only the out-of-plane displacement can be measured in the experiment. Signal averaging and band-pass filter were used to reduce the noise from environmental influence. The measured GW signal data was finally transferred back to the central computer through the data acquisition unit. The measurement location was chosen at 50 mm from the left beam end as shown in Figure 3.11. For measuring the A_0 GW, the laser measurement position was located at the centre of the longer side of the beam cross-section as shown in Figure 3.11a. For the S_0 GW the laser measurement position was located at the shorter side of the beam cross-section, and hence, the S_0 GW can be measured through the out-of-plane motion due to the Poisson effect (Ng, 2014b). The cracks were manufactured in the aluminium beams using electric drill, which produced a tolerance of ±1 mm for the crack location and ±0.5 mm for the crack depth and width. The locations and cracks manufactured in the beams are shown in Figure 3.12.

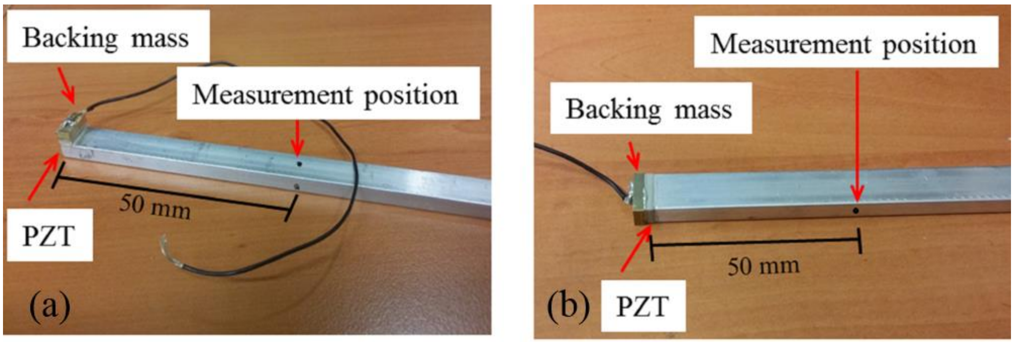

Fig. 3.11 Installed piezoceramic transducers and measurement locations in Cases E1-E3 for measuring (a) A_0 and (b) S_0 incident wave.

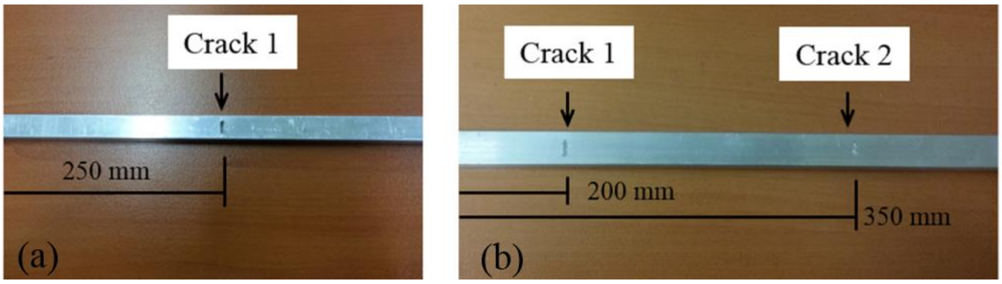

Fig. 3.12 (a) The crack in Cases E1 and E2 and (b) the Cracks 1 and 2 in Case E3.

3.6.2 Experimental results and discussions

The proposed SFE model with GW mode conversion effect was used to simulate the numerical data for identifying the cracks in the beams. Cases E1, E2 and E3 were conducted to experimentally verify the proposed multiple cracks identification method. Case E1 used S_0 mode GW as the excitation signal while Case E2 employed A_0 GW. The excitation frequency was 80 kHz and a single crack was considered in both cases. Case E3 considered two cracks in the beam and the excited signal was a 110 kHz A_0 GW.

Table 3.9 Bayesian model class selection for the experimental results.

Case	Model class	Log-likelihood	Information gain	Log-evidence	Probability
E1	**M_1**	**485.69**	**7.75**	**477.95**	**0.9989**
	M_2	483.80	24.63	471.17	0.0011
E2	**M_1**	**1099.90**	**-6.89**	**1093.01**	**1**
	M_2	1106.21	-24.88	1081.33	8.46e-06
E3	M_1	1050.02	-10.37	1039.65	1.07e-57
	M_2	**1193.21**	**-22.47**	**1170.74**	**0.9183**
	M_3	1203.59	-35.27	1168.32	0.0817

Table 3.10 Sample means and c.o.v.s of crack parameters calculated using TMCMC sample for Cases E1-E3 (errors of the identified crack parameters are shown in the bracket).

Case		Crack 1 (mm)			Crack 2 (mm)		
		L_c	d_c	b_c	L_c	d_c	b_c
E1	Actual	250	3	6	-	-	-
	Sample mean	260.10 (4.04%)	2.80 (6.67%)	5.71 (4.83%)	-	-	-
	Sample c.o.v (%)	0.0148	0.9735	3.3643	-	-	-
E2	Actual	250	3	6	-	-	-
	Sample mean	250.31 (-0.12%)	2.81 (6.33%)	5.80 (3.33%)	-	-	-
	Sample c.o.v (%)	0.0094	0.2051	1.5048	-	-	-
E3	Actual	200	3	6	350	2	6
	Sample mean	200.53 (0.27%)	2.42 (19.33%)	5.03 (16.17%)	349.92 (0.02%)	1.33 (33.5%)	5.89 (1.83%)
	Sample c.o.v (%)	0.0169	0.3504	0.3389	0.0278	0.6413	0.4152

The identified numbers of cracks are summarised in Table 3.9. It is shown that the crack number is correctly identified and the probability of the correct crack number is closed to 1 in all cases. This proves that the proposed Bayesian approach is able to identify the correct number of cracks in practice situation. The sample means and sample c.o.v.s of the identified crack parameters are shown in Table 3.10. For Cases E1 and E2, the identified crack parameters and corresponding sample c.o.v.s are compared to determine a suitable excitation GW signal. Specifically, it is found that the Case E2 using A_0 GW as the incident wave has smaller errors and sample c.o.v.s than Case E1, in which S_0 GW is used as the incident wave. This experimentally confirms that using A_0 GW as the incident wave is superior to using S_0 GW as the incident wave in identifying small cracks, i.e. Crack 2. The sample c.o.v. of the identified crack parameters increases as the smaller amplitude of the GW reflected from the crack with smaller size, and hence, less information is available for the crack identification. To illustrate how well the simulated signals, which is calculated by the SFT beam model with the identified crack parameters, matches the experimental results, a comparison between the simulated and measured time-domain response for Cases E1, E2 and E3 are shown in Figure 3.13.

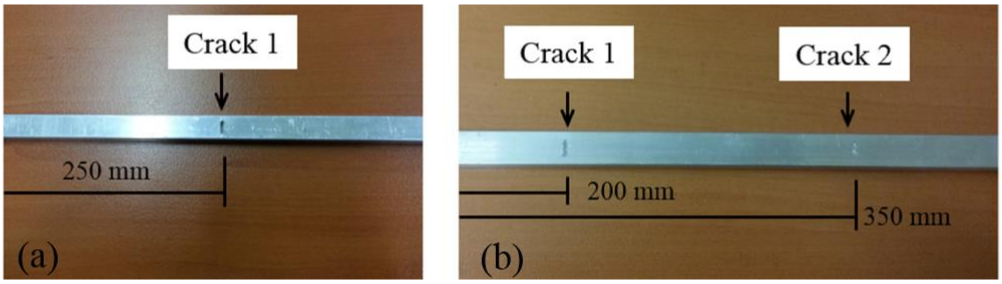

Fig. 3.13 Comparison of the simulated and measured time-domain GW signals for Cases a) E1, b) E2 and c) E3.

3.7 Conclusions

In this chapter the GW Bayesian identification of multiple cracks using TMCMC algorithm in beams has been presented. This study has extended the crack identification using GW model-based approach to identify the number of cracks and the crack parameters (i.e., crack location, depth and width). The time-domain SFE method based on Mindlin-Herrmann rod and Timoshenko beam theory has been presented and a spectral cracked beam element simulating the mode conversion effect when the GW interacting with the cracks has been proposed for crack identification.

Numerical case studies have been conducted to study the performance of different GW modes in identifying the crack parameters. Also, the influences of mode conversion effect, measurement noise level and distance between the cracks and the excitation location on the accuracy of the crack identification results have been investigated in detail. The uncertainties associated with the identified crack parameters have been indicated by the sample c.o.v.s of the identified crack parameters. It is found that the A_0 GW performs better than S_0 GW as the sample c.o.v.s of the identified crack parameters is smaller, which shows that the A_0 GW is more sensitive for identifying the cracks with smaller sizes. Furthermore, it has demonstrated that the proposed Bayesian approach is robust to the different measurement noise and location. The findings have indicated that the use of the mode conversion effect could effectively improve the accuracy of the crack identification.

Different crack scenarios have been studied numerically to investigate the performance of the proposed Bayesian multiple cracks identification method. The Bayesian model class selection method has been used to determine the number of the cracks and the uncertainties of identified crack parameters have been indicated by the sample c.o.v.s of the crack parameters. The results are encouraging as the number of crack and the crack parameters in each scenario have been accurately identified. Finally, this Bayesian damage identification algorithm has been experimentally verified to demonstrate the practicability of the proposed method.

Acknowledgement

The work was supported by the Australian Research Council under grant number DE130100261. The support is greatly appreciated.

Appendix A

This appendix presents the details of the F_I, F_{II} and H required for calculating the I_{c1}, I_{c2}, I_{c3} and I_{c4} in Equation (3.21). The details of derivations can be found in Irwin (1962) and Newman Jr and Raju (1981). The F_I and F_{II} shown in Equation (3.21) are defined as

$$F_I = \left[\gamma_1 + \gamma_2 \left(\frac{d_c}{h} \right)^2 + \gamma_3 \left(\frac{d_c}{h} \right)^4 \right] f_\phi g f_w \tag{3.32}$$

$$F_{II} = \frac{\beta (d_c/h) \cos\phi}{B_1 \left[\sin^2\phi + (d_c/h)^2 \cos^2\phi \right]^{1/4}} \tag{3.33}$$

where $b = 1 - k^2$,

$$B_1 = (\beta - \nu) \int_0^{\pi/2} \sqrt{1 - \beta \sin^2\phi}\, d\phi + \nu\kappa \int_0^{\pi/2} \frac{1}{\sqrt{1 - \beta \sin^2\phi}} d\phi \tag{3.34}$$

$$g_1 = 1.13 - 0.09k \tag{3.35}$$

$$g_2 = -0.54 + \frac{0.89}{0.2 + k} \tag{3.36}$$

$$g_3 = -0.5 - \frac{1.0}{0.65 + k} + 14\left(1.0 - k\right)^{24} \tag{3.37}$$

$$g = 1 + \left[0.1 + 0.35 \left(\frac{d_c}{h} \right)^2 \right] \left(1 - \sin\phi\right)^2 \tag{3.38}$$

The angular function f_f for the half elliptical crack in F_I is

$$f_f = \left[k^2 \cos^2 f + \sin^2 f \right]^{1/4} \tag{3.39}$$

The finite width calibrated function f_w is

$$f_w = \left[\sec\left(\frac{\pi b_c}{4b} \sqrt{\frac{d_c}{h}} \right) \right]^{1/2} \tag{3.40}$$

The function F_I is the boundary-correction factor for tension. The product of H and F_I shown in Equation (3.21) is the boundary-calibration factor for bending, where H is expressed:

$$H = H_1 + \left(H_2 - H_1\right)\left(\sin\phi\right)^{\left(0.2+\kappa+\frac{0.6d_c}{h}\right)} \tag{3.41}$$

where

$$H_1 = 1 - 0.34\frac{d_c}{h} - 0.11\kappa\left(\frac{d_c}{h}\right) \text{ and } H_2 = 1 - G_1\left(\frac{d_c}{h}\right) + G_2\left(\frac{d_c}{h}\right)^2 \tag{3.42}$$

$$G_1 = 1.22 + 0.12k \text{ and } G_2 = 0.55 - 1.05k^{0.75} + 0.47k^{1.5} \tag{3.43}$$

References for Chapter 3

ALJETS, D., CHONG, A., WILCOX, S. & HOLFORD, K. 2012. Acoustic emission source location on large plate-like structures using a local triangular sensor array. *Mechanical Systems and Signal Processing,* 30**,** 91-102.

AMJAD, U., YADAV, S. K. & KUNDU, T. 2015. Detection and quantification of pipe damage from change in time of flight and phase. *Ultrasonics,* 62**,** 223-236.

ARYAN, P., KOTOUSOV, A., NG, C. T. & CAZZOLATO, B. 2016. A model-based method for damage detection with guided waves. *Structural Control and Health Monitoring,* doi: 10.1002/stc.1884.

AU, S. K., DIAZDELAO, F. A. & YOSHIDA, I. 2015. Bayesian updating and model class selection with Subset Simulation, 317**,** 1102-1121.

AU, S. K. & BECK, J. L. 1999. A new adaptive importance sampling scheme for reliability calculations. *Structural Safety,* 21**,** 135-158.

BECK, J. L. 2010. Bayesian system identification based on probability logic. *Structural Control and Health Monitoring,* 17**,** 825-847.

BECK, J. L. & KATAFYGIOTIS, L. S. 1998. Updating Models and Their Uncertainties I: Bayesian Statistical Framework. *Journal of Engineering Mechanics, ASCE,* 124**,** 455-461.

BECK, J. L. & YUEN, K.-V. 2004. Model selection using response measurements: Bayesian probabilistic approach. *Journal of Engineering Mechanics,* 130**,** 192-203.

BERGAMINI, A. & BIONDINI, F. 2004. Finite strip modeling for optimal design of prestressed folded plate structures. *Engineering Structures,* 26**,** 1043-1054.

CHING, J. & CHEN, Y. C. 2007. Transitional Markov chain Monte Carlo method for Bayesian model updating, model class selection, and model averaging. *Journal of engineering mechanics,* 133**,** 816-832.

CROXFORD, A. J., WILCOX, P. D., DRINKWATER, B. W. & KONSTANTINIDIS, G. Strategies for Guided-wave Strucdtural Health Monitoring. Proceedings of the Royal Society, 2007. 2961-2981.

DARPE, A., GUPTA, K. & CHAWLA, A. 2004. Coupled bending, longitudinal and torsional vibrations of a cracked rotor. *Journal of Sound and Vibration,* 269**,** 33-60.

DOYLE, J. F. 1989. *Wave propagation in structures*, Springer.

FARRAR, C. R. & WORDEN, K. 2007. An introduction to structural health monitoring. *Philosophical Transactions of the Royal Society A: Mathematical, Physical and Engineering Sciences,* 365**,** 303-315.

FLYNN, E. B., TODD, M. D., CROXFORD, A. J., DRINKWATER, B. W. & WILCOX, P. D. 2011a. Enhanced detection through low-order stochastic modeling for guided-wave structural health monitoring. *Structural Health Monitoring,* 11**,** 149-160, doi: 10.1177/1475921711414232.

FLYNN, E. B., TODD, M. D., WILCOX, P. D., DRINKWATER, B. W. & CROXFORD, A. J. Maximum-likelihood estimation of damage location in guided-wave structural health monitoring. Proceedings of the Royal Society of London A: Mathematical, Physical and Engineering Sciences, 2011b. The Royal Society, doi: 10.1098/rspa.2011.0095.

GULL, S. F. 1988. Bayesian inductive inference and maximum entropy. *Maximum-entropy and Bayesian methods in science and engineering.* Springer.

HAN, J.-H. & KIM, Y. J. 2015. Time–frequency beamforming for nondestructive evaluations of plate using ultrasonic Lamb wave. *Mechanical Systems and Signal Processing,* 54**,** 336-356.

HE, M. & HUTCHINSON, J. 2000. Surface crack subject to mixed mode loading. *Engineering Fracture Mechanics,* 65**,** 1-14.

HE, S. & NG, C. T. 2015. Analysis of mode conversion and scattering of guided waves at cracks in isotropic beams using a time-domain spectral finite element method. *Elec J Struct Eng,* 14**,** 20-32.

HOSSEIN ABADI, H. Z., AMIRFATTAHI, R., NAZARI, B., MIRDAMADI, H. R. & ATASHIPOUR, S. A. 2014. GUW-based structural damage detection using WPT statistical features and multiclass SVM. *Applied Acoustics,* 86**,** 59-70.

IRWIN, G. R. 1962. Crack-extension force for a part-through crack in a plate. *Journal of Applied Mechanics,* 29**,** 651-654.

KRAWCZUK, M. 2002. Application of spectral beam finite element with a crack and iterative search technique for damage detection. *Finite Elements in Analysis and Design,* 38**,** 537-548.

KRAWCZUK, M., GRABOWSKA, J. & PALACZ, M. 2006. Longitudinal wave propagation Part I - Comparison of rod theories. *Journal of Sound and Vibration,* 295**,** 461-478.

KUDELA, P., KRAWCZUK, M. & OSTACHOWICZ, W. 2007. Wave propagation modelling in 1D structures using spectral finite elements. *Journal of Sound and Vibration,* 300**,** 88-100.

LAM, H. F., YANG, J. & AU, S.-K. 2015. Bayesian model updating of a coupled-slab system using field test data utilizing an enhanced Markov chain Monte Carlo simulation algorithm. *Engineering Structures,* 102**,** 144-155.

LI, F., SUN, X., QIU, J., ZHOU, L., LI, H. & MENG, G. 2015. Guided wave propagation in high-speed train axle and damage detection based on wave mode conversion. *Structural Control and Health Monitoring,* 22**,** 1133-1147.

LOWE, M. J., CAWLEY, P. & GALVAGNI, A. 2012. Monitoring of corrosion in pipelines using guided waves and permanently installed transducers. *The Journal of the Acoustical Society of America,* 132**,** 1932-1932.

MINDLIN, R. & HERRMANN, G. A one-dimensional theory of compressional waves in an elastic rod. Proceedings of the 1st US National Congress of Applied Mechanics, 1951. 187-191.

MOSAVI, A. A., DICKEY, D., SERACINO, R. & RIZKALLA, S. 2012. Identifying damage locations under ambient vibrations utilizing vector autoregressive models and Mahalanobis distances. *Mechanical systems and signal processing,* 26**,** 254-267.

MUTO, M. & BECK, J. L. 2008. Bayesian updating and model class selection for hysteretic structural models using stochastic simulation. *Journal of Vibration and Control,* 14**,** 7-34.

NAG, A., MAHAPATRA, D. & GOPALAKRISHNAN, S. 2002. Identification of Delamination in a Composite Beam Using a Damaged Spectral Element. *Structural Health Monitoring,* 1**,** 105-126.

NEWMAN JR, J. & RAJU, I. 1981. An empirical stress-intensity factor equation for the surface crack. *Engineering Fracture Mechanics,* 15**,** 185-192.

NG, C. T. 2014a. On the selection of advanced signal processing techniques for guided wave damage identification using a statistical approach. *Engineering Structures,* 67**,** 50-60.

NG, C. T., VEIDT, M. & LAM, H. 2009. Guided wave damage characterisation in beams utilising probabilistic optimisation. *Engineering Structures,* 31**,** 2842-2850.

NG, C. T. 2015a. On accuracy of analytical modeling of Lamb wave scattering at delaminations in multilayered isotropic plates. *International Journal of Structural Stability and Dynamics,* 15**,** doi:10.1142/S021945 5415400106.

NG, C. T. 2014b. Bayesian model updating approach for experimental identification of damage in beams using guided waves. *Structural Health Monitoring,* 13**,** 359-373.

NG, C. T. 2015b. A two-stage approach for quantitative damage imaging in metallic plates using Lamb waves. *Earthquake and Structures,* 8**,** 821-841.

NG, C. T., VEIDT, M. & RAJIC, N. Integrated piezoceramic transducers for imaging damage in composite laminates. Proceedings of SPIE - The International Society for Optical Engineering, 2009, doi: 10.1117/12.840150.

NICHOLS, J. M., LINK, W. A., MURPHY, K. D. & OLSON, C. C. 2010. A Bayesian approach to identifying structural nonlinearity using free-decay response: Application to damage detection in composites. *Journal of Sound and Vibration,* 329**,** 2995-3007.

PATERA, A. T. 1984. A spectral element method for fluid dynamics: laminar flow in a channel expansion. *Journal of Computational Physics,* 54**,** 468-488.

POZRIKIDIS, C. 2005. *Introduction to finite and spectral element methods using Matlab,* CRC Press.

RAGHAVAN, A. & CESNIK, C. E. S. 2007. Review of Guided-wave Structural Health Monitoring. *The Shock and Vibration Digest,* 39**,** 91-114.

ROSE, L. R. F. & WANG, C. H. 2010. Mindlin plate theory for damage detection: Imaging of flexural inhomogeneities. *Journal of Acoustical Society of America,* 127**,** 754-763.

RUCKA, M. 2010. Experimental and numerical studies of guided wave damage detection in bars with structural discontinuities. *Archive of Applied Mechanics,* 80**,** 1371-1390.

STRAUB, D. & PAPAIOANNOU, I. 2014. Bayesian updating with structural reliability methods. *Journal of Engineering Mechanics,* 141**,** 04014134.

VAKILZADEH, M. K., HUANG, Y., BECK, J. L. & ABRAHAMSSON, T. 2017. Approximate Bayesian Computation by Subset Simulation using hierarchical state-space models. *Mechanical Systems and Signal Processing,* 84**,** 2-20.

VANLI, O. A. & JUNG, S. 2014. Statistical updating of finite element model with Lamb wave sensing data for damage detection problems. *Mechanical Systems and Signal Processing,* 42**,** 137-151.

VEIDT, M., NG, C. T., HAMES, S. & WATTINGER, T. Imaging laminar damage in plates using Lamb wave beamforming. Advanced Materials Research, 2008. Trans Tech Publ, 666-669.

WILLBERG, C., DUCZEK, S., VIVAR-PEREZ, J. & AHMAD, Z. 2015. Simulation Methods for Guided Wave-Based Structural Health Monitoring: A Review. *Applied Mechanics Reviews,* 67**,** doi: 10.1115/1.4029 539.

XU, F., ZHANG, Y., HONG, W., WU, K. & CUI, T. J. 2003. Finite-difference frequency-domain algorithm for modeling guided-wave properties of substrate integrated waveguide. *Microwave Theory and Techniques, IEEE Transactions on,* 51**,** 2221-2227.

XU, K., TA, D., SU, Z. & WANG, W. 2014. Transmission analysis of ultrasonic Lamb mode conversion in a plate with partial-thickness notch. *Ultrasonics,* 54**,** 395-401.

YANG, J., HE, J., GUAN, X., WANG, D., CHEN, H., ZHANG, W. & LIU, Y. 2015. A probabilistic crack size quantification method using in-situ Lamb wave test and Bayesian updating. *Mechanical Systems and Signal Processing,* 78**,** 118-133.

ZHAO, X. G. & ROSE, J. L. 2003. Boundary element modeling for defect characterization potential in a wave guide. *International Journal of Solids and Structures,* 40**,** 2645-2658.

ZHOU, W., LI, H. & YUAN, F. G. 2014. Guided wave generation, sensing and damage detection using in-plane shear piezoelectric wafers. *Smart Materials and Structures,* 23**,** doi: 10.1088/09641726/23/1/015 014.

ZHOU, W. J. & ICHCHOU, M. N. 2011. Wave scattering by local defect in structural waveguide through wave finite element method. *Structural Health Monitoring,* 10**,** 335-349.

Chapter 4

A Probabilistic Approach for Quantitative Identification of Multiple Delaminations in Laminated Composite Beams Using Guided Waves

(Paper 3, published)

Shuai He and Ching-Tai Ng

School of Civil, Environmental & Mining Engineering, The University of Adelaide, Adelaide, SA 5005, Australia

Publication:

HE, S. & NG, C. T. 2016. A probabilistic approach for quantitative identification of multiple delaminations in laminated composite beams using guided waves. *Engineering Structures,* 127, 602-614.

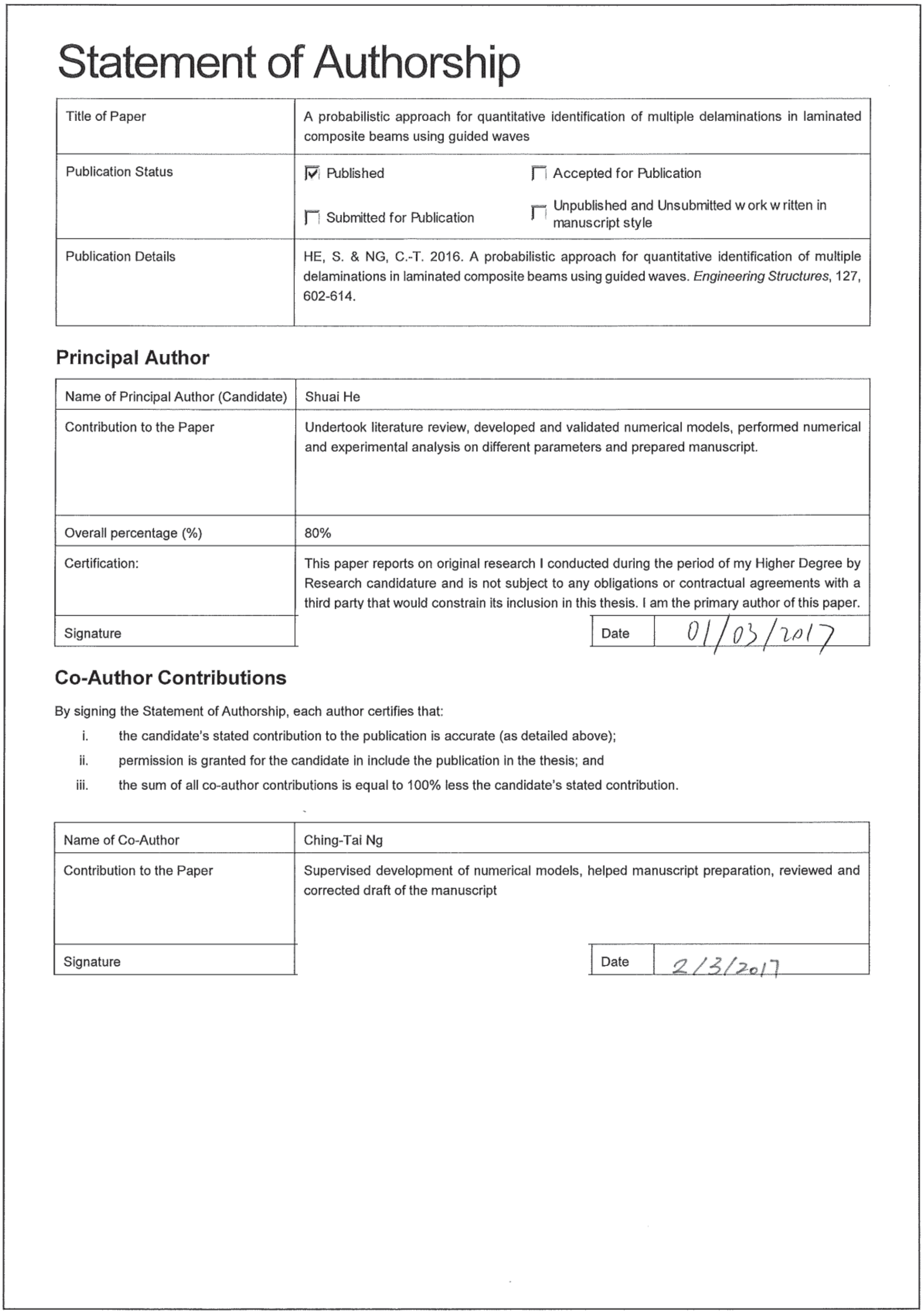

Statement of Authorship

Title of Paper	A probabilistic approach for quantitative identification of multiple delaminations in laminated composite beams using guided waves
Publication Status	☑ Published ☐ Accepted for Publication ☐ Submitted for Publication ☐ Unpublished and Unsubmitted w ork w ritten in manuscript style
Publication Details	HE, S. & NG, C.-T. 2016. A probabilistic approach for quantitative identification of multiple delaminations in laminated composite beams using guided waves. *Engineering Structures*, 127, 602-614.

Principal Author

Name of Principal Author (Candidate)	Shuai He		
Contribution to the Paper	Undertook literature review, developed and validated numerical models, performed numerical and experimental analysis on different parameters and prepared manuscript.		
Overall percentage (%)	80%		
Certification:	This paper reports on original research I conducted during the period of my Higher Degree by Research candidature and is not subject to any obligations or contractual agreements with a third party that would constrain its inclusion in this thesis. I am the primary author of this paper.		
Signature		Date	01/03/2017

Co-Author Contributions

By signing the Statement of Authorship, each author certifies that:

i. the candidate's stated contribution to the publication is accurate (as detailed above);

ii. permission is granted for the candidate in include the publication in the thesis; and

iii. the sum of all co-author contributions is equal to 100% less the candidate's stated contribution.

Name of Co-Author	Ching-Tai Ng		
Contribution to the Paper	Supervised development of numerical models, helped manuscript preparation, reviewed and corrected draft of the manuscript		
Signature		Date	2/3/2017

Abstract

In this study a probabilistic approach is proposed to identify multiple delaminations in laminated composite beams using guided waves. The proposed method is a model-based approach, which provides a quantitative identification of the delaminations. This study puts forward a practical damage identification method, and hence, it can identify multiple delaminations using guided wave signal measured at a single measurement point on the laminated composite beams. The proposed method first determines the number of delaminations using Bayesian model class selection method. The Bayesian statistical framework is then employed to not only identify the delamination locations, lengths and through-thickness locations, but also quantify the associated uncertainties, which provides valuable information for engineers in making decision on necessary remedial work. In addition the proposed method employs the time-domain spectral finite element method and Bayesian updating with Subset simulation to further improve the computational efficiency. The proposed probabilistic approach is verified and demonstrated using data obtained from numerical simulations, which consider both measurement noise and modelling error, and experimental data. The results show that the proposed method can accurately determine the number of delaminations, and the identified delamination locations, lengths and through-thickness locations are closed to the true values.

***Keywords*:**

Multiple delaminations; Damage identification; Bayesian statistical framework; Bayesian model class selection; Guided waves; Spectral finite element; Subset simulation; Experiment

4.1 Introduction

4.1.1 Composite and non-destructive evaluation techniques

Laminated composite materials have been extensively used in many engineering applications, such as aerospace, mechanical and automotive engineering, due to their high strength, anti-corrosion and lightweight characteristics. Common defects occur in the laminated composite materials are fibre breaking, matrix cracking and delamination (Toft et al., 2011). In particular the delamination could cause significant reduction in the stiffness and strength of structures and leads to structural failure. Detecting and identifying the delamination before structural failure are essential in improving the safety, durability and serviceability of the structures made by laminated composite materials.

Delamination is a separation of adjacent sub-surface laminae without any obvious visual evidence on the surface, and hence, non-destructive evaluation (NDE) techniques are required for detecting the delamination. Conventional NDE techniques, such as ultrasonic C-scan and A-scan, are point-to-point inspecting methods. They are time consuming and not able to inspect inaccessible locations of the structures. Low frequency vibration techniques (Mosavi et al., 2012) are efficient in inspecting large area of structures, however, they are insensitive to local defects, such as delamination.

4.1.2 Damage detection using guided waves

Guided wave has been widely recognized as one of the promising techniques for detecting the local defects (Raghavan and Cesnik, 2007, Croxford et al., 2007). It is elastic stress wave, whose propagation characteristics depend on structural boundaries. Guided wave can be used to inspect large area of structural components due to its long propagation distances. Because guided waves are excited at high frequency, i.e. in the order of kilohertz, their wavelengths are small, and hence, they are sensitive to the local and incipient defects, e.g. delamination.

Recently, guided wave based damage detection techniques have been widely employed in identifying the defects in one-dimensional (1D), e.g. beams (Sun et al., 2012) and rods (Raisutis et al., 2010), and two-dimensional (2D) waveguides, e.g. plates (Aryan et al., 2016, Ng, 2015a, Ng, 2015b, Yan, 2013) and shells (Schulte et al., 2010). For 2D waveguides, a number of damage detection techniques have been developed in the literature. With the use of a transducer network, guided wave and scattered waves could be actuated and measured at different directions from the defect, respectively. This provides sufficient information for characterising the defects in 2D waveguides, e.g. defect location, size and shape. In the literature a number of damage characterisation techniques have been developed, such as pre-stack reverse-time migration technique (Lin and Yuan, 2001), tomography (Malyarenko and Hinders, 2000) and diffraction tomography (Rose and Wang, 2010, Ng et al., 2009). For 1D waveguides, most of the methods focused on determining the defect location based on the time-of-flight information of the reflected wave from the defect (Grabowska et al., 2008, Quek et al., 2003). There was relatively less work focused on the defect characterization, especially for delamination in the laminated composite beams.

Model-based approach has been employed to characterise the defects based on the measured guided wave signals in 1D waveguides. This approach treats defect parameters, such as defect location and size, as variables, by which the damage identification is achieved by minimising the discrepancy between the modelled and the measured guided wave signals. A number of model-based approaches have been developed for characterising different types of defects, such as step damages (Ng, 2014b, Pau and Vestroni, 2011, Ng et al., 2009) and cracks (He and Ng, 2017, Noureini and Khaji, 2012, Krawczuk, 2002) in aluminium rods and beams. However, there were limited studies focused on delamination in laminated composite beams (Nag et al., 2002).

Recently the Bayesian statistical framework (Beck, 2010) has been applied to provide a quantitative identification of the defect in 1D waveguides (Ng et al., 2009) and this method was verified using experimentally measured guided wave signals (Ng, 2014b). It incooperated a spectral finite element (SFE) model in the Bayesian statitiscal framework to provide a computational efficient and quantatitive identification of the defect. One of the advantages of the Bayesian statistical framework is that it not only provides a characterization of the defect, i.e. identifying the defect location and size, but also quantifies the uncertainties associated with the defect identification results. This provides valuable information on making decision about the remedial work necessary to repair the strucutral damage.

4.1.3 Challenges in multiple delamination identification

In practical situation, the number of defects is unknown before the damage detection, and hence, the identification of multiple defects is a challenging issue for 1D waveguides, especially for a situation that the number of transducers is limited. For non-model-based approach, it is difficult to determine the number of defects based on the information of the scattered waves as a number of scattered waves can be induced by multiple wave reflections between the defects. For multiple delaminations, the problem is more complicated. At each delamination region, the waveguide is divided into two individual sub-waveguides, and hence, reflection happens when the wave entering and leaving each of the delamination.

Although the model-based approach is able to provide quantitative identification of one defect, it has a difficulty in identifying multiple defects. In the situation that the number of defects is unknown, the model considered more number of defects always has better fitting between the modelled and measured guided wave signals. Therefore, damage detection method based solely on the fitting between the modelled and the measured guided wave signals can be very misleading given the existence of modelling error and measurement noise in the measured data.

The aim of this study is to address the challenges in quantitative identification of multiple delaminations in laminated composite beams. The proposed method is developed based on the Bayesian statistical framework. The quantitative identification of the delaminations is achieved by solving a Bayesian updating problem, and hence, it could provide quantitative information of the delaminations, such as number of delaminations, delamination locations, lengths and through-thickness locations, and also the uncertainties associated with the damage identification results. To overcome the aforementioned challenge in identifying the multiple delaminations in laminated composite beams, the proposed method employs the Bayesian model class selection (Mthembu et al., 2011, Beck and Yuen, 2004) to provide a robust determination of the number of delaminations. In addition the proposed method employs the formulation of Bayesian updating with structural reliability method (BUS) (Straub and Papaioannou, 2014), and hence, the Bayesian updating problem can be solved by a computational efficient and robust algorithm, Subset simulation (Au et al., 2015, Papaioannou et al., 2015, Chiachio et al., 2014). In this study both numerical calculated and experimentally measured guided wave signals are used to verify and demonstrate the capability of the proposed method.

The chapter is organised as follows. In Section 4.2 the details of the Bayesian approach for multiple delaminations identification are presented first. This section describes the Bayesian model class selection, Bayesian model updating, BUS formulation and Subset simulation for improving the computational efficiency and robustness of the proposed multiple delaminations identification method. Section 4.3 describes the SFE method and modelling of the delaminations. Section 4.4 presents the results of the numerical case studies to verify the proposed multiple delaminations identification method. The numerical case studies consider different situations, such as different number of delaminations, delamination locations, lengths and through-thickness locations, to assess the performance of proposed method. Experimental verification is provided in Section 4.5 to demonstrate the practicability of the proposed method. Finally conclusions are drawn in Section 4.6.

4.2 Bayesian approach for multiple delaminations identification

The proposed Bayesian approach is developed based on the Bayesian model class selection and Bayesian model updating, which are used to determine the number of delaminations and provide quantitative identification of the delaminations. In the Bayesian approach, a laminated composite beam with length *L* and different number of delaminations are considered. A schematic diagram of the laminated composite beam with multiple delamination is shown in Figure 4.1. In this study we assume there are N_M delaminations existed in the laminated composite beam and they are represented by different model classes $\mathbf{M} = \{M_j : j = 1,2,...,N_M\}$. M_j is the model class representing the laminated composite beam with j delaminations. The delamination parameters l_j and d_j are used to describe the location and length of *j*-th delamination. For the through-thickness location, k_j is used to describe the delamination located between the *k*-th and (*k*+1)-th layers of the laminated composite beam.

The selection of the ‘optimal’ model class solely based on the fitting between measured and simulated data is impractical. In order to address this problem, this study used the Bayesian model class selection method in selecting the “optimal” model class to identify the number of delaminations. In addition the delamination parameters and their associated uncertainties are identified by the Bayesian statistical framework. The following sub-sections describe the Bayesian model class selection, Bayesian model updating, and BUS formulation with Subset simulation for identifying multiple delaminations in the laminated composite beam.

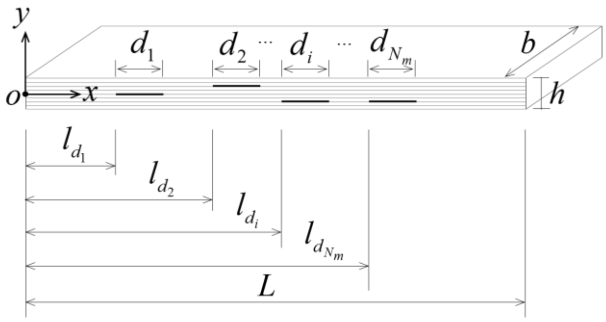

Fig. 4.1 Schematic diagram of the laminated composite beam with multiple delaminations

4.2.1 Bayesian mode class selection for determining the number of delaminations

Consider a set of possible model classes $\mathbf{M} = \{M_j : j = 1, 2, ..., N_M\}$, which represent laminated composite beams with j delaminations. Bayesian model class selection can be used to determine the probability of each model class conditional on a set of measured guided wave data D as: (Beck, 2010, Muto and Beck, 2008, Beck and Yuen, 2004)

$$P\left(M_j \middle| D, \mathbf{M}\right) = \frac{P\left(D \middle| M_j\right) P\left(M_j \middle| \mathbf{M}\right)}{P\left(D \middle| \mathbf{M}\right)} \tag{4.1}$$

where $P\left(M_j \middle| \mathbf{M}\right) = 1/\mathrm{N}_M$ is the prior probability of each model class M_j. $P\left(D \middle| \mathbf{M}\right)$ is a normalising constant and $P\left(D \middle| M_j\right)$ is the evidence of the model class M_j that has the following expression:

$$P\left(D \middle| M_j\right) = \int P\left(D \middle| \boldsymbol{\theta}_j, M_j\right) P\left(\boldsymbol{\theta}_j \middle| M_j\right) d\boldsymbol{\theta}_j \tag{4.2}$$

where $\boldsymbol{\theta}_j$ is a vector that consists of the uncertain delamination parameters, such as delamination locations l_j , lengths d_j and through-thickness locations k_j. $P\left(D \mid \boldsymbol{\theta}_j, M_j\right)$ is the likelihood function, a larger value of which means there is a better fitting between the simulated and experimentally measured guided wave signals. However, direct numerical integration of Equation (4.2) is impractical because it involves a multi-dimensional integral (Beck and Au, 2002). Asymptotic approach can be used for calculating Equation (4.2) but they are only applicable to globally identifiable situation (Beck and Yuen, 2004). In order to evaluate the model evidence, this study employs an improved BUS formulation (Au et al., 2015), and hence, the Bayesian updating with Subset Simulation can be used to efficiently calculate the evidence of the model class. The details of the BUS formulation and Subset simulation will be described in the sub-section 4.2.3.

A challenging issue in the identifying multiple delaminations is that the model class with more delamination parameters can have better fitting between the simulated and the experimentally measured data as the extra delamination parameters tend to fit the measurement noise and modelling error. However, the Bayesian model class selection algorithm addresses this issue by automatically penalising more ‘complex’ model class, i.e. the model classes with more delaminations. This can be illustrated by considering the evidence from an information-theoretic point of view. Consider the logarithmic form of Equation (4.2) (Beck, 2010, Muto and Beck, 2008, Ching and Chen, 2007) as:

$$\begin{aligned}
\ln P\left(D \middle| M_j\right) &= \int \ln\left[\frac{P\left(D \middle| \boldsymbol{\theta}_j, M_j\right) P\left(\boldsymbol{\theta}_j \middle| M_j\right)}{P\left(\boldsymbol{\theta}_j \middle| D, M_j\right)}\right] P\left(\boldsymbol{\theta}_j \middle| D, M_j\right) d\boldsymbol{\theta}_j \\
&= \int \ln\left[P\left(D \middle| \boldsymbol{\theta}_j, M_j\right)\right] P\left(\boldsymbol{\theta}_j \middle| D, M_j\right) d\boldsymbol{\theta}_j \\
&\quad - \int \ln\left[\frac{P\left(\boldsymbol{\theta}_j \middle| D, M_j\right)}{P\left(\boldsymbol{\theta}_j \middle| M_j\right)}\right] P\left(\boldsymbol{\theta}_j \middle| D, M_j\right) d\boldsymbol{\theta}_j
\end{aligned} \tag{4.3}$$

where $\ln P\left(D\middle|M_j\right)$ is the log-evidence for the model class M_j. The log-evidence consists of the log-likelihood function and relative entropy between the prior and posterior distribution, which are the first and second term at the right side of Equation (4.3), respectively. The log-likelihood function is a data-fit term that indicates the plausibility of the model class M_j. The relative entropy between the prior and posterior distribution is a measure of the information gained about the complexity of the model class, and hence, it provides a penalty against more 'complex' model class. Therefore, the log-evidence value is able to provide a robust determination of the number of delaminations in the laminated composite beams.

4.2.2 Bayesian model updating for identifying the delamination parameters

For identifying the delamination parameters of a given model class M_j, i.e. the delamination locations, lengths and through-thickness locations, the measured guided wave data D can be used to update the corresponding plausibility of the uncertain delamination parameters. The posterior probability density function (PDF) of the delamination parameters $\boldsymbol{\theta}_j$ is obtained as: (Beck and Au, 2002, Yuen and Katafygiotis, 2002)

$$P\left(\boldsymbol{\theta}_j\middle|D,M_j\right)\propto P\left(D\middle|\boldsymbol{\theta}_j,M_j\right)P\left(\boldsymbol{\theta}_j\middle|M_j\right) \tag{4.4}$$

where $P\left(\boldsymbol{\theta}_j\middle|M_j\right)$ is the prior probability that reflects the initial engineering judgement of the delamination parameters. $P\left(D\,|\,\boldsymbol{\theta}_j,M_j\right)$ is the likelihood function and is assumed following the Gaussian distribution with zero mean and standard deviation of the prediction error σ_j based on the Principle of Maximum information Entropy: (Beck, 2010)

$$P\left(D\middle|\boldsymbol{\theta}_j,M_j\right)=\frac{1}{\left(2\pi\sigma^2\right)^{N_oN_t/2}}\exp\left(-\frac{1}{2\sigma_j^2}\mathrm{J}\;\left(t;\boldsymbol{\theta}_j\right)\right) \tag{4.5}$$

where N_o is the number of measurement points and $N_t=T/\Delta t$ is the number of time steps. T is the duration of measurement and Δt is the time steps. $\mathrm{J}\;\left(t;\boldsymbol{\theta}_j\right)$ is the goodness-of-fit function and is defined as:

$$\mathrm{J}\;\left(t;\boldsymbol{\theta}_j\right)=\sum_{o=1}^{N_o}\sum_{t=1}^{N_t}\left[q_m\left(t\right)-q_s\left(t;\boldsymbol{\theta}_j\right)\right]^2 \tag{4.6}$$

where q_s is the simulation data and q_m is the experimentally measured data. In this study the simulation data is obtained from the SFE model described in Section 4.3. The variance σ^2 in the likelihood function is normally a positive real number and it is sampled randomly from the inverse of Gamma distribution $IG(0.5N_tN_o+1,0.5\mathrm{J}\;\;(t;\boldsymbol{\theta}_j))$.

The BUS formulation with Subset simulation, which will be described in Section 4.2.3, is used in this study to draw samples from the target distribution, and hence, approximating the posterior PDF in Equation (4.4). Once the samples are asymptotically distributed as $P\left(\boldsymbol{\theta}_j\,|\,D,M_j\right)$, the delamination parameters can be estimated by the sample means, where the sample c.o.v.s of the delamination parameters can be obtained by calculating the ratio of the sample standard deviation to the sample means. For determining the marginal posterior PDF of the each of the uncertain delamination parameters, the adaptive kernel density estimation with Gaussian distribution being the kernel PDF (Lam et al., 2015, Au and Beck, 1999) can be used and it is defined as:

$$k\left(\boldsymbol{\theta}_j(i)\right)=\frac{1}{N_s}\sum_{h=1}^{N_s}W^{(h)}\mathrm{N}\left(\boldsymbol{\theta}_j^{(h)}(i),\mathbf{C}(i,i)\right) \tag{4.7}$$

where $\mathrm{N}(\mu,\Sigma)$ is the multivariate Gaussian PDF with mean μ and covariance matrix Σ. $W^{(h)}$ is the weighting of the h^{th} sample and i is an index for choosing the uncertain delamination parameter in the marginal posterior PDF calculation. $\mathbf{C}(i,i)$ is the i^{th} diagonal element of the sample covariance matrix calculated by the samples when they are asymptotically distributed as $P\left(\boldsymbol{\theta}_j \mid D, M_j\right)$.

4.2.3 BUS formulation

This section describes the BUS formulation that allows the Bayesian updating problem to be solved by a computational efficient algorithm, Subset simulation. The BUS formulation converts the Bayesian problem to a reliability problem (Straub and Papaioannou, 2014) with the purpose of determining the failure probability $P(F)$ of the failure event F. In the context of BUS, F can be defined as:

$$F=\left\{cP\left(D\middle|\boldsymbol{\theta}_j, M_j\right)-U>0\right\} \tag{4.8}$$

where U is a random value between 0 and 1. c is a constant denoted the 'likelihood multiplier' satisfied the following inequality:

$$cP\left(D\middle|\boldsymbol{\theta}_j, M_j\right)\leq 1 \tag{4.9}$$

For any $c<c_{\max}$, the posterior samples $\boldsymbol{\theta}_j$ follows the posterior PDF $P\left(\boldsymbol{\theta}_j\middle|D, M_j\right)$ (Au et al., 2015). While the selected $c_{\max}$ for the multiplier significantly influences the efficiency and correctness of the sampling, its value is not available before the determination of the maximum likelihood value $P\left(\hat{\boldsymbol{\theta}}_j\middle|D, M_j\right)$ with the optimal parameter $\hat{\boldsymbol{\theta}}_j$. This is contradictory since $c_{\max}$ is required for seeking the correct optimal parameter $\hat{\boldsymbol{\theta}}_j$. In order

to overcome this problem, the BUS formulation has recently been improved by Au et al. (2015), by which the failure event is transformed into the followed inequality:

$$F = \left\{ \ln \left[\frac{P\left(D \middle| \boldsymbol{\theta}_j, M_j\right)}{U} \right] > -\ln c \right\} \tag{4.10}$$

It can be rewritten as:

$$F = \{Y > O\} \tag{4.11}$$

where $O = -\ln c$ and Y denotes the driving variable, which has the form:

$$Y = \ln \left[\frac{P\left(D \middle| \boldsymbol{\theta}_j, M_j\right)}{U} \right] \tag{4.12}$$

Let O be an admissible threshold level, when O is larger than $O_{\min} = -\ln c_{\max}$ the posterior samples $\boldsymbol{\theta}_j$ will follow the posterior PDF $P\left(\boldsymbol{\theta}_j \middle| D, M_j\right)$. Consider the failure probability $P(F)$ can be estimated using the posterior samples from Subset simulation, $P(F)$ can be expressed as the evidence of the model class $P(D \mid M_j)$: (Au et al., 2015)

$$P(F) = e^{-O} P\left(D \middle| M_j\right) \text{ for } O > O_{\min} \tag{4.13}$$

For sufficiently large O, Equation (4.13) shows that $P(F)$ will decay exponentially with O as $P(D \mid M_j)$ is constant for a given problem. $P(F)$ can be interpreted as the complementary cumulative distribution function (CCDF) of Y, where the exponential decay is similar to a typical CCDF in reliability analysis.

As shown in Equation (4.13), when $O > O_{\min}$ the failure probability $P(F)$ is theoretically related to the evidence $P(D \mid M_j)$. However, $O_{\min}$ is not known in the actual implementation, therefore, it is essential to determine whether $O > O_{\min}$, and hence, the samples conditional on $\{Y > O\}$ are confidently collected as the correct posterior samples in the Subset simulation. In order to determine when the value of O has become larger than the unknown $O_{\min}$, the characteristic trends of the logarithmic failure probability in Equation (4.13) are investigated. Consider $\ln P(F) = -O + V(O)$, hence,

$$V(O) = \ln P(F) + O \tag{4.14}$$

At the beginning, $V(O)$ increases linearly with O as $\ln P(F) \approx 0$. This means $V(O)$ first increase linearly and then go through a transition until it settles at $V(O) = \ln P(D \mid M_j)$ when $O > O_{\min}$. Therefore, the log-evidence $\ln P(D \mid M_j)$ can be obtained as:

$$\ln P(D \mid M_j) = O + \ln P(F) \text{ for } O > O_{\min} \tag{4.15}$$

4.2.4 Subset simulation for generating posterior samples

Based on the BUS formulation, the failure probability $P(F)$ can be evaluated using the posterior samples obtained from the conditional samples in the efficient Subset simulation (Au et al., 2015). Essentially, Subset simulation progressively generates conditional samples towards the target failure events through a series of intermediate failure events, which converts a rare reliability problem into a series of more frequent one. It is efficient and sustainable to the high dimension problem as the Markov Chain Monte Carlo (MCMC) sampling technique (Beck and Au, 2002) is implemented in each intermediate step. As shown in Equation (4.15) once the failure probability $P(F)$ is evaluated and $O > O_{\min}$, the evidence $P(D|M_j)$ of the model class can be determined.

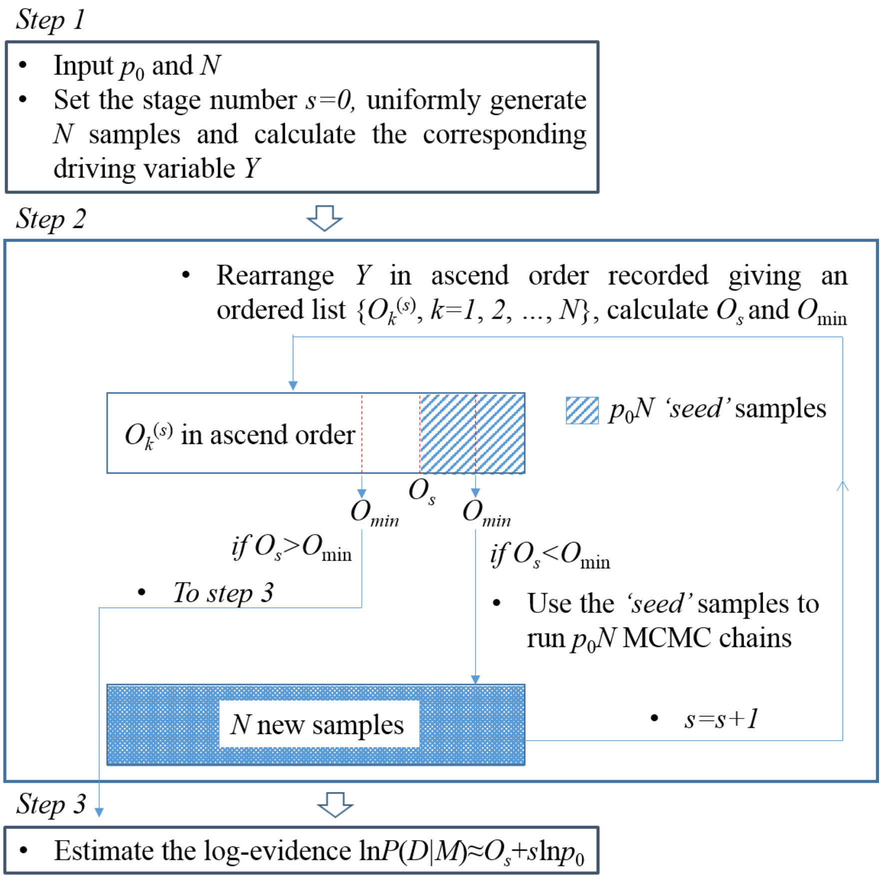

Fig. 4.2 Schematic framework of Subset simulation.

The schematic framework of Subset simulation is shown in Figure 4.2. In the Step 1 of the Subset simulation, the number of samples N for each stage and the probability level of the intermediate simulation p_0 need to be defined. It should be noted that Np_0 and $1/p_0$ are positive integrates. N i.i.d. (independent and identically distributed) samples are uniformly generated from the prior distribution using the standard Monte Carlo method and the corresponding driving variable Y is calculated using Equation (4.12).

In Step 2, Y is firstly rearranged in ascending order, giving an ordered list denoted by $\{O_r^{(s)} : r = 1, ..., N\}$ for stage s. For $O_s < O_{\min}$, at which $O_s = O_{N(1-p_0)}^{(s)}$ is the $N(1-p_0)$-th sample in the ordered list, the last $p_0 N$ samples in the ordered list are used as 'seed' samples to simulate $p_0 N$ MCMC chains. These chains have equal sampling length as $1/p_0$, and hence, producing N new samples for the next Subset simulation level $s = s+1$. The failure probability at each stage s is obtained conditionally on the failure events from the previous stages as:

$$P(F_r^{(s)}) = \prod_{f=0}^{s} P(F_r^{(s)} \mid F_r^{(s-1)}) = p_0^s \frac{N-r}{N} \quad \text{for} \quad r = 1, ..., N \tag{4.16}$$

where $F_r^{(s)}$ is the failure event of stage s. From Equation (4.16) it is shown that the probability of the rare failure event can be gradually approximated in the Subset simulation. The failure probability $P(F_r^{(s)})$ is then used to evaluate the $O_{\min}$ as stated in the Section 4.2.3. Step 2 is repeated until $O_s > O_{\min}$.

Finally, in Step 3, the log-evidence of model class M_j is evaluated using Equations (4.15) and (4.16), and hence

$$\ln P(D \mid M_j) = O + \ln P(F) \approx O_s + s \ln p_0 \tag{4.17}$$

In the Bayesian approach the number of delamination and the delamination parameters are assumed unknown initially. The approach first considers a model class with a delamination and identifies the delamination parameters by solving the Bayesian updating problem using the BUS formulation with Subset simulation. Once the delamination parameters are identified, the evidence of this model class is then evaluated. After that the Bayesian approach considers a more "complex" model class, e.g. two delaminations and repeated the aforementioned calculations. The procedure stops when the value of the evidence of the currently considered model class is smaller than the less "complex" model class. Therefore, the number of delaminations and the delamination parameters can be determined by the model class with the largest evidence value.

4.3 Time-domain spectral finite element method for modelling laminated composite beams with multiple delaminations

The modelling of guided wave propagation in laminated composite laminated using the SFE method is similar to the conventional FE method, in which the problem can be represented by the time-domain ordinary differential equation: (He and Ng, 2015, Rucka, 2010, Kudela et al., 2007)

$$\mathbf{M}\ddot{\mathbf{U}}+\mathbf{C}\dot{\mathbf{U}}+\mathbf{K}\mathbf{U}=\mathbf{F}(t) \tag{4.18}$$

where $\mathbf{U}$, $\dot{\mathbf{U}}$ and $\ddot{\mathbf{U}}$ are the displacement, velocity and acceleration vector in time domain, respectively. $\mathbf{M}$ is the global mass matrix, $\mathbf{C}$ is the global damping matrix, $\mathbf{K}$ is the global stiffness matrix and $\mathbf{F}(t)$ is the global force vector at time *t*. The global mass matrix **M** and the stiffness matrix **K** are assembled using their element matrices (Rucka, 2010, Kudela et al., 2007). In this study the guided wave propagation in the laminated composite beam is simulated using the higher order theory along with the Poisson's contraction effect (Kudela and Ostachowicz, 2009). The displacement field in the composite beam can be written as:

$$\bar{u}(x,y)\approx u(x)-\varphi(x)y \tag{4.19}$$

$$\bar{v}(x,y)\approx v(x)+\psi(x)y \tag{4.20}$$

where u and v are the axial and transverse displacements in the neutral axis of the beam as shown in Figure 4.3. φ is the rotation of the cross section and

ψ is the contraction due to Poisson's effect. y is the vector of distance measured from the neutral axis. The strain field can be expressed as: (Kudela and Ostachowicz, 2009)

$$\varepsilon = \begin{bmatrix} \dfrac{\partial u}{\partial x} - y\dfrac{\partial \varphi}{\partial x} \\ \psi \\ \dfrac{\partial v}{\partial x} + y\dfrac{\partial \psi}{\partial x} - \varphi \end{bmatrix} \tag{4.21}$$

Based on the higher order theory along with the Poisson's contraction effect, the element mass matrix $\mathbf{M}^e$, element stiffness matrix $\mathbf{K}^e$ and the element force vector $\mathbf{F}^e(t)$ at time t used to formulated the corresponding global matrices in Equation (4.18) are:

$$\mathbf{M}^e \approx \sum_{i=1}^{n} w_i \mathbf{N}_e(\xi_i)^T \mathbf{r} \mathbf{N}_e(\xi_i) \det\left(J(\xi_i)\right) \tag{4.22}$$

$$\mathbf{K}^e \approx b \sum_{i=1}^{n} w_i \sum_{k=1}^{N_k} \int_{h_{k-1}}^{h_k} \mathbf{B}_e(\xi_i)^T \bar{\mathbf{Q}}_k \mathbf{B}_e(\xi_i) \det\left(J(\xi_i)\right) dy \tag{4.23}$$

$$\mathbf{F}^e(t) \approx \sum_{i=1}^{n} w_i \mathbf{N}_e(\xi_i)^T \mathbf{f}_e(t) \mathbf{N}_e(\xi_i) \det\left(J(\xi_i)\right) \tag{4.24}$$

where b and N_k are the width and the total number of layer of the laminated composite beam. $J = \partial x / \partial \xi$ is the Jacobian function transferring the local coordinate to the global coordinate. h_k and h_{k-1} denote the height of upper and lower surface of the k-th layer, respectively. $\mathbf{f}_e$ is the external excitation. Different to the conventional FE method, the SFE method employs the Gauss-Lobatto-Legendre (GLL) nodes ξ_i in each element. This leads to the diagonal form of the mass matrix that can be solved efficiently by the central difference scheme, and hence, reducing the mesh density. The local coordinate of the ξ_i can be determined by:

$$\left(1-\xi_i^{2}\right)L'_{n-1}\left(\xi_i\right)=0 \text{ for } \xi_i\in[-1,1] \text{ and } i\in 1,\dots,n \tag{4.25}$$

where L'_{n-1} is the first derivative of the (n-1)th order Legendre polynomial. In this study n = 6. The distribution of the GLL nodes and their corresponding shape function value are shown in Figure 4.3. w_i is the weight of the corresponding GLL node ξ_i and is defined as:

$$w_i=\frac{2}{n\left(n-1\right)[L_{n-1}\left(\xi_i\right)]^2} \tag{4.26}$$

where L_{n-1} is the (n-1)th order Legendre polynomial.

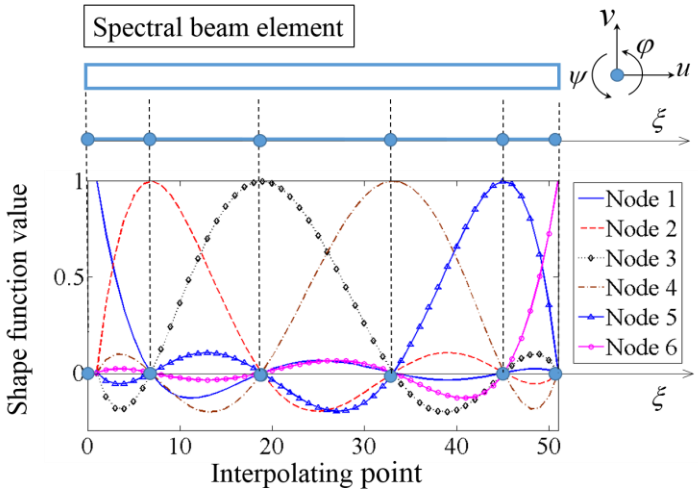

Fig. 4.3 Distribution of the 5th order GLL nodes and the corresponding shape function value of a spectral beam element.

$\mathbf{B}_e$ is the strain-displacement operator and is defined as:

$$\mathbf{B}^e=\begin{bmatrix}\dfrac{\partial}{\partial x} & -y\dfrac{\partial}{\partial x} & 0 & 0\\ 0 & 0 & 0 & 1\\ 0 & -1 & \dfrac{\partial}{\partial x} & y\dfrac{\partial}{\partial x}\end{bmatrix}\mathbf{N}^e \tag{4.27}$$

where $\partial/\partial x = J^{-1}\partial/\partial\xi$. $\mathbf{N}_e$ is the shape function matrix of the SFE element, which has the form:

$$\mathbf{N}_e = \mathbf{N}\otimes\mathbf{I} \tag{4.28}$$

where $\mathbf{N} = [N_1(\xi),...,N_n(\xi)]$ is a row vector. $\mathbf{I}$ is a 4×4 identity matrix. '$\otimes$' is the Kronecker product. The shape function $N_i(\xi)$ at node i has the orthogonal property and can be calculated by

$$N_i(\xi) = \prod_{m=1,m\neq i}^{n}\frac{\xi-\xi_m}{\xi_i-\xi_m} \text{ for } i(i\in 1,2,...,n) \tag{4.29}$$

where n is the number of GLL integration points in each element and m is the sequence of node. Using the shape function, the displacement fields are approximated as follow:

$$\begin{bmatrix} u^e(\xi) \\ \varphi^e(\xi) \\ v^e(\xi) \\ \psi^e(\xi) \end{bmatrix} = \mathbf{N}^e\mathbf{q}^e = \sum_{i=1}^{n}\begin{bmatrix} N_i(\xi) & & & \\ & N_i(\xi) & & \\ & & N_i(\xi) & \\ & & & N_i(\xi) \end{bmatrix}\begin{bmatrix} q_u^e(\xi_i) \\ q_\varphi^e(\xi_i) \\ q_v^e(\xi_i) \\ q_\psi^e(\xi_i) \end{bmatrix} \tag{4.30}$$

where $\mathbf{q}^e$ is the vector of nodal displacement in the corresponding degrees-of-freedom. The matrix $\mathbf{r}$ from Equation (4.22) has the form:

$$\mathbf{r} = \begin{bmatrix} I_0 & 0 & 0 & 0 \\ 0 & I_2 & 0 & 0 \\ 0 & 0 & I_0 & 0 \\ 0 & 0 & 0 & I_2 \end{bmatrix} \tag{4.31}$$

where

$$I_0 = b\sum_{k=1}^{N_k}\rho_k\left(h_k - h_{k-1}\right) \tag{4.32}$$

$$I_2 = b\sum_{k=1}^{N_k} \rho_k \left(h_k^3 - h_{k-1}^3\right) / 3$$

where ρ_k is the density of the k-th layer. In Equation (4.23), $\overline{\mathbf{Q}}_k$ is the material property matrix of the k^{th} layer of the laminated composite beam in the defined orientation and is defined as:

$$\overline{\mathbf{Q}}_k = \begin{bmatrix} \overline{Q}_{11} & \overline{Q}_{13} & 0 \\ \overline{Q}_{13} & \overline{Q}_{33} & 0 \\ 0 & 0 & \overline{Q}_{55} \end{bmatrix} \tag{4.33}$$

where $\overline{Q}_{11}$, $\overline{Q}_{13}$, $\overline{Q}_{33}$ and $\overline{Q}_{55}$ can be found in (Vinson and Sierakowski, 2012). In order to model the delamination, the intact beam elements e_1 and e_2, as shown in Figure 4.4, are separated into $e_{1\text{-up}}$, $e_{2\text{-up}}$ and $e_{1\text{-low}}$, $e_{2\text{-low}}$ elements to form a delamination element. Specifically, the nodes in the intact beam elements are duplicated at the delaminated region and only the nodes at the delamination tips are connected. In this study the aforementioned SFE is used to model the laminated composite beam and the delamination element is used to model each of the delmainations. In addition the Hilbert transform (Ng, 2014a) is first used to obtain the signal envelopes for the modeled and experimentally measured data guided wave signals. The signal envelopes are then used in the proposed Bayesian approach in Section 4.2 for identifying the number of delaminations, delamination locations, lengths and through-thickness locations.

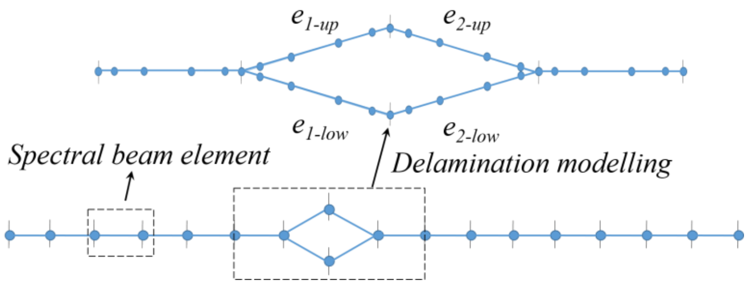

Fig. 4.4 Modelling of the laminated composite beam with a delamination and zoom-in at the delamination.

4.4 Numerical case studies

A series of numerical case studies were used to systematically assess the performance of the proposed Bayesian multiple delaminations identification method with the consideration of different delamination scenarios. The numerical case studies considered a 500 mm long and 6 mm wide cross-ply laminated composite beam with stacking sequence of $[0/90/0/90]_s$. The total thickness of the beam is 2 mm, which consists of eight 0.25 mm thick unidirectional carbon/epoxy prepreg plies. The elastic properties of the each ply are shown in Table 4.1. In this study the fundamental anti-symmetric mode (A_0) guided wave was used as the incident wave as it has been demonstrated that it is sensitive to the delamination (Ng et al., 2012). The excitation signal was an 80 kHz narrow-band five-cycle sinusoidal tone burst modulated by a Hanning window. The excitation was applied to the left end of the laminated composite beam and the guided wave signal was calculated at the same location. The duration of the calculated guided wave data in the numerical case studies allows the incident A_0 guided wave propagates from the excitation location to the beam end, and then reflects and propagates back to the excitation location but the beam end reflected wave pulse was not included in the data.

The time-domain SFE method described in Section 4.3 was used to model the laminated composite beams with different numbers of delaminations and the models were treated as the identification model for simulating guided wave data q_s in Equation (4.6) of the proposed Bayesian approach. For each model class, the uncertainty delamination parameters are the locations l_j, lengths d_j and through-thickness locations k_j of the delaminations. In the time-domain

SFE model, 12 mm long spectral elements with 8 GLL nodes were used to model the laminated composite beam. The time step Δt used in the simulation was 0.75e^{-7} sec to ensure the solution of the time-domain ordinary differential Equation (4.18) to be converged.

Table 4.1 Elastic properties of the the prepreg ply of the laminated composite beam in the numerical case studies.

Properties	E_1 (GPa)	E_2 (GPa)	E_3 (GPa)	G_{12} (GPa)	G_{13} (GPa)	G_{23} (GPa)	υ_{12}	υ_{13}	υ_{23}	ρ (kg/m^3)
Value	128.75	8.35	8.35	4.47	4.47	2.9	0.33	0.33	0.44	1517

The laminated composite beams with delaminations were also modeled using the three-dimensional (3D) finite element method and the calculated data was treated as synthetic experimental data as q_m in Equation (4.6). Therefore the modeling error was considered in the numerical case studies as the synthetic experimental data was generated by 3D FE method. Commercial software ABAQUS v6.12-1 (Hibbett et al., 1998) was used to simulate the guided wave in this study. Eight-node 3D reduced integration solid brick element (C3D8R) was used and the mesh size was 0.3 mm. The A_0 guided wave was generated by applying shear traction at the edge of the left beam end. Enhanced hourglass control was enabled and the dynamic explicit solver was employed to solve the guided wave propagation. The time step in the simulation was automatically decided by ABAQUS. In this study the signal envelope calculated by the Hilbert transform (Ng, 2014a) was used as the simulated data by SFE and synthetic experimental data by 3D FE to reduce the complexity of the signals. Measurement noise was considered in synthetic experimental data. It is assumed to be white noise and was taken to be 3% of the RMS of the noise-free signals.

Five cases, i.e. Cases N1, N2, N3, N4 and N5, shown in Table 4.2 were used to study the performance of the proposed multiple delaminations identification method. For Cases N1, N2 and N3, one delamination was considered in the laminated composite beam and the length of delaminations (d_1) were 6 mm, 10 mm and 20 mm, respectively. They are all located at l_1 = 200 mm from the left beam end of the laminated composite beam. Case N4 considers two delaminations while Case N5 considers three delaminations. The Subset simulation was employed to generate the posterior samples, and hence, approximating the posterior PDF of the delamination parameters and probability of the model classes for each case. The assignment of the prior PDF for the location and length of the delamination are uniformly distributed over [10mm 490mm] and [1.3mm 18mm], respectively. The through-thickness location of the delamination is an integer and it has equal probability from $k_j = 1$ to 7. It should be noted that the delamination located at $k_j = 1$, 2 and 3 has the same effect for $k_j = 7$, 6 and 5, respectively, on the guided wave. The number of samples N at each stage of Subset simulation was set as 500 and the probability level of the intermediate simulation p_0 was chosen as 0.1.

Table 4.2 Summary of all cases in the numerical case studies.

Case	Number of delaminations	Delamination location (mm)	Delamination length (mm)	Delamination through-thickness location*
N1	1	$l_1 = 200$	$d_1 = 6$	$k_1 = 3$ or 5
N2	1	$l_1 = 200$	$d_1 = 10$	$k_1 = 3$ or 5
N3	1	$l_1 = 200$	$d_1 = 20$	$k_1 = 3$ or 5
N4	2	$l_1 = 200$	$d_1 = 10$	$k_1 = 4$
		$l_2 = 300$	$d_2 = 6$	$k_2 = 3$ or 5
N5	3	$l_1 = 150$	$d_1 = 4$	$k_1 = 2$ or 6
		$l_2 = 250$	$d_2 = 6$	$k_2 = 3$ or 5
		$l_3 = 350$	$d_3 = 10$	$k_3 = 4$

* Due to the symmetric stacking sequence of the laminated composite beam, the delamination at $k_j = 1, 2, 3$ has the same effect for $k_j = 7, 6, 5$, respectively, on the guided wave reflection and transmission

4.4.1 Identifying the number of delaminations

The numbers of delaminations were identified using the proposed Bayesian approach described in Section 4.2. From Equation (4.1), it shows that the probability of a model class M_j is proportional to the evidence value, which can be evaluated using Equation (4.17) when $O > O_{\min}$.

In order to determine the $O_{\min}$, the value of $V(O)$ is investigated. Figure 4.5 is used as an example to illustrate the determination of $O_{\min,M_3}$ and the log-evidence for model class M_3 in Case N5. In the figure, $O_{\min,M_3}$ is the value that needs to be determined for model class M_3. Firstly, after the rearrangement of *Y*, the value of $V(O)$ is calculated at each stage. If $V(O)$ reaches its maximal value at this stage, the ranking of the sample corresponding to this maximal $V(O)$ in the ordered list is taken. If this ranking is higher than the ranking $(1-p_0)N$-th (i.e., 450-th for N = 500 and p_0 = 0.1), the Subset simulation proceeds to the next stage. As shown in Figure 4.5, at stage s =13 the recorded ranking corresponding to the maximal value of $V(O)$ is 77-th, which is indicated by the vertical dotted line. As this recorded ranking (i.e. 77-th) is higher than 450-th, the Subset simulation stops at this stage, and the value of *O* corresponding to the 77-th sample is chosen as the $O_{\min,M_3}$, i.e. $O_s > O_{\min,M_3}$ where O_s is the value corresponding to the 450-th sample. Finally, the log-evidence can be obtained using Equation (4.17). Using the similar approach the estimation of the model log-evidence for all the model classes in Case N5 is shown in Figure 4.6. The values needs to determined for model class M_1, M_2 and M_3 are $O_{\min,M_1}$, $O_{\min,M_2}$ and $O_{\min,M_3}$, respectively. It is clear from the figure that the model class M_3 has the largest log-evidence value, indicating the most plausible number of delaminations is three for Case N5.

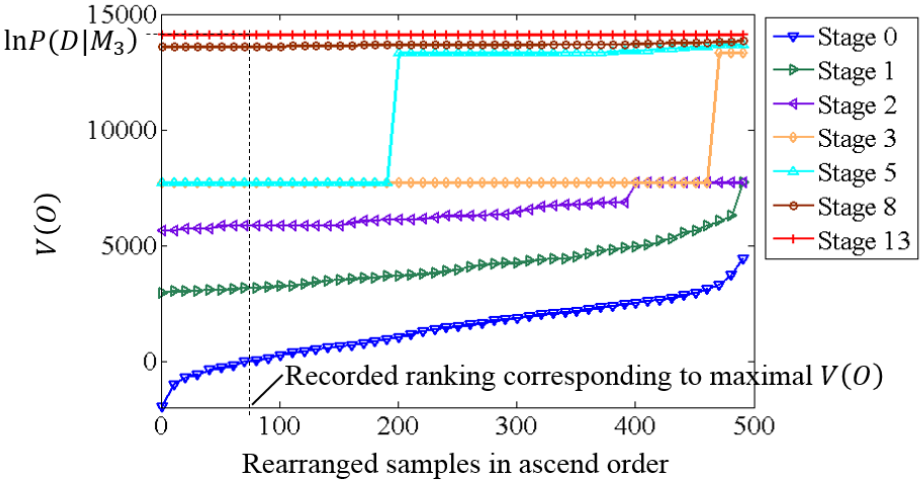

Fig. 4.5 Estimated log-evidence at each stage for model class M$_3$ in Case N5.

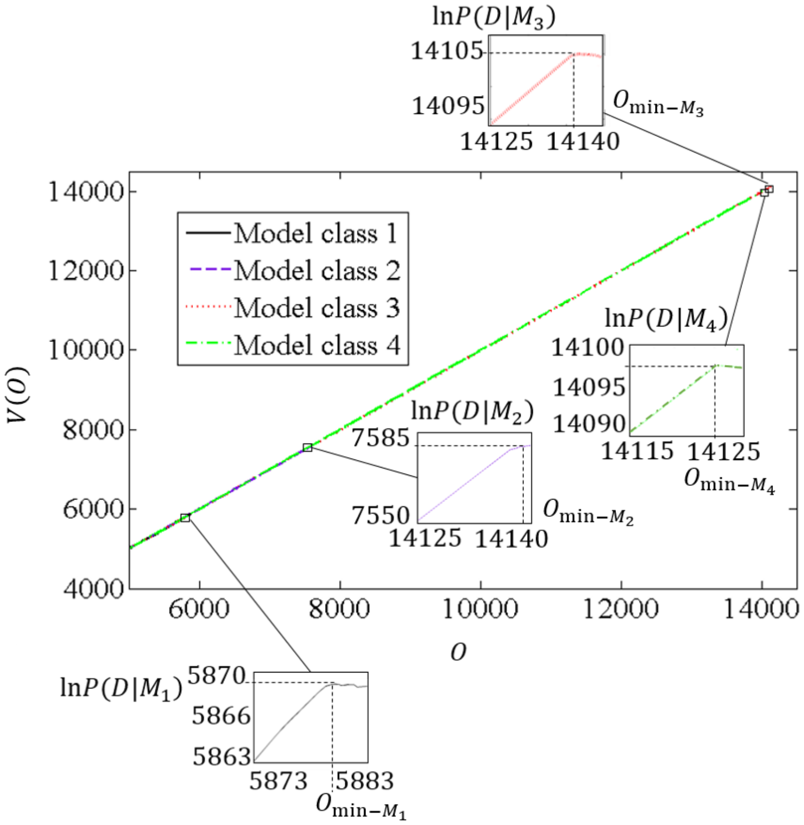

Fig. 4.6 Estimate of the log-evidence of each model class for Case N5.

The identification result of the delamination number for Cases N1 to N5 are summarised in Table 4.3. In the third column, the log-likelihood is taken as the average of the log-likelihood value of the posterior samples for each model class. In the fourth column, the information gain is calculated as the difference between the model log-likelihood and the log-evidence value illustrating the penalty against the model class with more delaminations. The fifth column is the determined log-evidence of the model class from Equation (4.15) and the last column is the probability of the model class calculated based on the value of the log-evidence. From Table 4.3 it is shown that the numbers of delaminations are correctly identified for all cases as the probability of the correct model class is the largest for each case. Specifically, the probability of the model class M_1 with one delamination in Cases N1 to N3 is distinct (e.g., over 98%) from other the model class. While the uncertainty slightly increases in Case N4 as the probability of the model class M_2 with the correct number of delamination is 95.69%. In Case N5, where the actual number of delamination is 3, the probability of the correct identification increases to 99.59%. This is due to the increase of the information gain for the more complex model class, i.e. more delaminations.

Table 4.3 Identificatied results of the number of delaminations in the numerical case studies.

Case	Number of delaminations	Log-likelihood	Information gain	Log-evidence	Probability (%)
N1	**1**	**15853.63**	**4.24**	**15849.39**	99.51
	2	15865.10	21.03	15844.07	0.49
N2	**1**	**15892.59**	**6.72**	**15885.87**	**99.67**
	2	15903.37	23.22	15880.15	0.33
N3	**1**	**14962.32**	**3.83**	**14958.49**	**98.22**
	2	14977.15	22.87	14954.48	1.78
N4	1	6516.87	0.33	6516.54	0
	2	**13787.37**	**18.62**	**13768.75**	**95.69**
	3	13799.22	33.57	13765.65	4.35
N5	1	5877.96	13.63	5864.33	0
	2	7587.29	18.65	7568.63	**0**
	3	**14135.66**	**32.28**	**14103.38**	99.59
	4	14153.14	55.27	14097.87	0.41

In general, as the number of delamination increases, the log-likelihood indicating the goodness of fitting between the simulation and the measurement also increases. The information gain penalising the complexity of the model class. This provides the log-evidence value for the Bayesian model class selection. Specifically, when the number of delaminations of the corresponding model class is less than the actual situation (e.g., M_1 in Case N4 and M_1 and M_2 in Case N5), the log-likelihood is significantly less than that of other model classes indicating the simulation data is not very well fitted with the measurement data in this situation. On the other hand, when the number of delaminations (e.g., M_2 in Case N1, M_3 in Case N4 and M_4 in Case N5) is larger than the correct number of delaminations, the log-likelihood increases slightly as the reflected wave from the additional delamination in the SFE model is used to fit the measurement noise and modelling error.

4.4.2 Identifying the delamination parameters and quantifying the associated uncertainties

In this section the parameters for the delamination are identified for all cases. The influence of the length of delamination on the damage identification is studied in Cases N1 to N3. Cases N1, N2 and N3 considers a delamination with length of 6 mm, 10 mm and 20 mm, respectively, and they are all located at 200 mm from the left beam end. Cases N4 and N5 increase the identification difficulty by considering two and three delaminations with different delamination lengths and though-thickness locations.

The identified results are shown in Table 4.4. The results of Cases N1 to N5 show that all the delamination parameters are accurately identified. The percentage of error and percentage of sample c.o.v. are also shown in the brackets and squared brackets, respectively. The maximum percentage of error for the identification delamination location and length are 2.34% and 10.09%, respectively. The identified delamination lengths in Cases N1 to N3 show that the error increases with the delamination length. This is because the wave reflection occurs when the incident guided wave entering and leaving the delamination region, and hence, the reflected wave pulse used in the damage identification process is a combination of the two reflected waves. For longer delamination, the reflected wave is usually more complicated. For the identified through-thickness location, although the results of the Delamination 1 in Case N3, and the Delaminations 2 and 3 in Case N5 are one layer different to the true through-thickness location, the delamination location and length are still very close to the true value. The results show that for cases considered more than one delamination, there is an error in the identified through-thickness location but the delamiatnion location and length can still be accurately identified. In general the sample c.o.v. of the identified delamination length is larger than the delamination location. It should be noted that the amplitude of the reflected wave from the delamination is not a linearly proportional to the delamination size due to the multiple wave reflection when the incident wave entering and leaving the delaminations.

Table 4.4 Identified results for the delamination parameters for numerical case studies.

Case	Location (mm)	Length (mm)	Through-thickness location
	l_j (c.o.v. %) [error %]	d_j (c.o.v. %) [error %]	k_i
N1	l_1 = 200.65 (0.019) [0.33]	d_1 = 5.89 (0.298) [1.83]	$k_1 = 3$
N2	l_1 = 199.85 (0.040) [0.08]	d_1 = 10.73 (0.010) [7.28]	$k_1 = 3$
N3	l_1 = 197.15 (0.101) [1.43]	d_1 = 22.02 (0.221) [10.09]	$k_1 = 3$
N4	l_1 = 197.06 (0.001) [2.34] l_2 = 299.31 (0.009) [0.96]	d_1 = 9.45 (0.006) [5.56] d_2 = 5.82 (0.112) [3.33]	$k_1 = 3$ $k_2 = 3$
N5	l_1 = 149.35 (0.065) [0.43] l_2 = 249.86 (0.048) [0.06] l_3 = 350.15 (0.029) [0.04]	d_1 = 3.81 (1.596) [4.77] d_2 = 10.57 (0.232) [5.70] d_3 = 5.68 (0.853) [5.33]	$k_1 = 2$ $k_2 = 4$ $k_3 = 3$

The evolution of the generated samples at each stage in Case N5 using the Subset simulation is shown in Figure 4.7. The samples converged efficiently to their target distribution from the initial prior distribution, which shows the high efficiency of Subset simulation in generating posterior samples. At Stage 4, the figure show that there are two local optimums and it reduced to a global optimum at Stage 7 and it converged to the final solution at Stage 13.

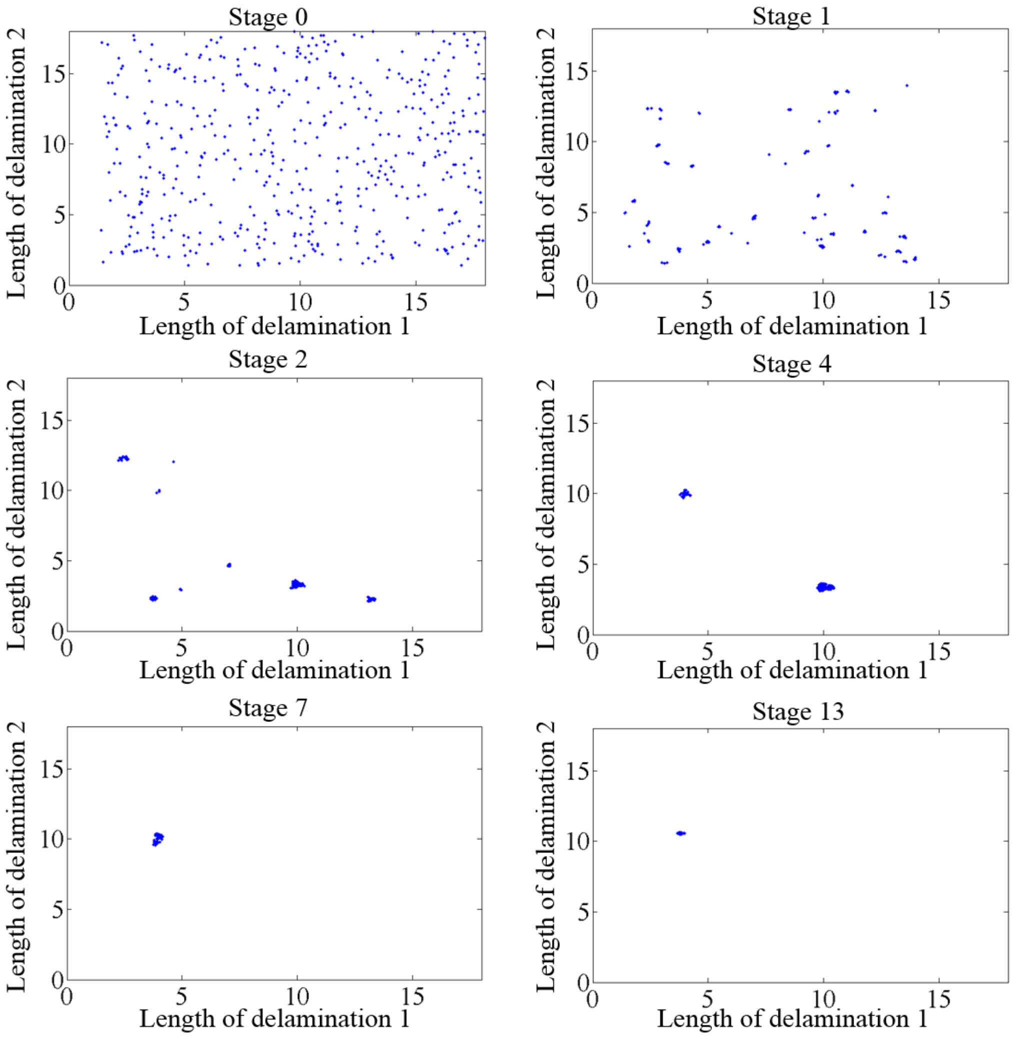
Stage 0

Stage 1

Stage 2

Stage 4

Stage 7

Stage 13

Fig. 4.7 Evolution of the Subset samples for the length of delamination 1 and 2 in Case N5.

In Figure 4.8 the marginal PDFs of the delamination length of the Delaminations 1, 2 and 3 in Case N5 were calculated using the adaptive kernel density estimation (Equation (4.7)) based on the posterior samples generated from Subset simulation. A comparison of the posterior marginal PDFs is shown in Figure 4.8, the drop in PDF value away from the peak for the Delamination 3 is faster than the Delamination 1 but slower than the Delamination 2. This is consistent to the corresponding sample c.o.v. as shown in Table 4.4.

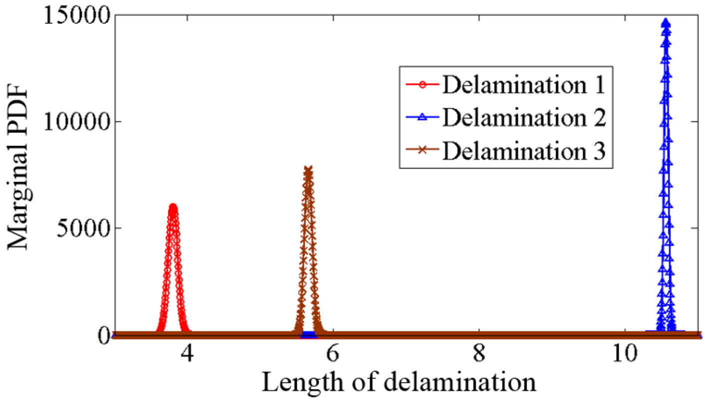

Fig. 4.8 Posterior marginal PDFs for the length of delamination 1, 2 and 3 in Case N5.

4.5 Experimental case studies

4.5.1 Experimental setup

Two laminated composite beams with width 6 mm were manufactured from eight HexPly®M21/IM7 unidirectional carbon/epoxy pre-preg with a stacking sequence of $[0/90/0/90]_S$. The pre-preg lamina has a fibre volume fraction of 0.592 and the density is 1.58 g/cm^3. The thickness of each lamina is 0.184 mm. The initial values of the elastic properties were obtained from the material data sheet and calculated using micro-mechanics theory with the consideration of the constituents. The elastic properties were then adjusted such that the discrepancy between the simulated and experimentally measured incident guided wave pulse in the laminated composite beams is minimised. The elastic properties of the lamina are given in Table 4.5. One of the laminated composite beams has a delamination and the other has two delaminations, and they are named as Cases E1 and E2, respectively. Table 4.6 summarises the numbers, locations, lengths and through-thickness locations of the delaminations in Cases E1 and E2. The delaminations were generated by inserting thin release films between two laminae at the appropriate though-thickness locations.

Table 4.5 Material properties of the M21/IM7 pre-preg laminate.

Properties	E_1 (GPa)	E_2 (GPa)	E_3 (GPa)	G_{12} (GPa)	G_{13} (GPa)	G_{23} (GPa)	υ_{12}	υ_{13}	υ_{23}	ρ (kg/m^3)
Value	160	8.50	8.50	4.20	4.20	2.70	0.35	0.35	0.53	1580

Table 4.6 Summary of experimental case studies.

Case	Number of delamination	Delamination location (mm)	Delamination length (mm)	Delamination through-thickness location *
E1	1	$l_1 = 100 \pm 1$	$d_1 = 6 \pm 0.5$	$k_1 = 3$ or 5
E2	2	$l_1 = 100 \pm 1$	$d_1 = 10 \pm 0.5$	$k_1 = 4$
		$l_2 = 200 \pm 1$	$d_2 = 6 \pm 0.5$	$k_2 = 3$ or 5

* Due to the symmetric stacking sequence of the laminated composite beam, the delamination at k_j = 1, 2, 3 has the same effect for k_j = 7, 6, 5, respectively, on the guided wave reflection and transmission

A schematic diagram of the experimental setup is shown in Figure 4.9. Both sides of the laminated composite beams were fixed at two rigid clamping systems. The length of the laminated composite beams between the fixed supports is 300 mm. A 6×6×2 mm^3 piezoceramic transducer was bonded to the left end of each of the laminated composite beam. A 6×6×4 mm^3 brass mass was used as the backing mass to enhance the excitability of the A_0 guided wave. The excitation signal was a 50 kHz narrow-band five-cycle sinusoidal tone burst pulse modulated by a Hanning window. The signal was synthetised by a computer and generated by a junction box with the output voltage of 10V. It was then amplified by SERVO-AMP signal amplifier to 50V and applied to the piezoceramic transducer. The out-of-plane displacement of the guided wave signal was recorded using a 1D laser scanning Doppler vibrometer (Polytec PSV-400) with laser controller

(OFV5000). The measurement position was located at 60 mm from the left beam end. Signal averaging and band-pass filter were used to further reduce the noise in the measured data. The measured data was then processed by a data acquisition unit and then transmitted back to the computer.

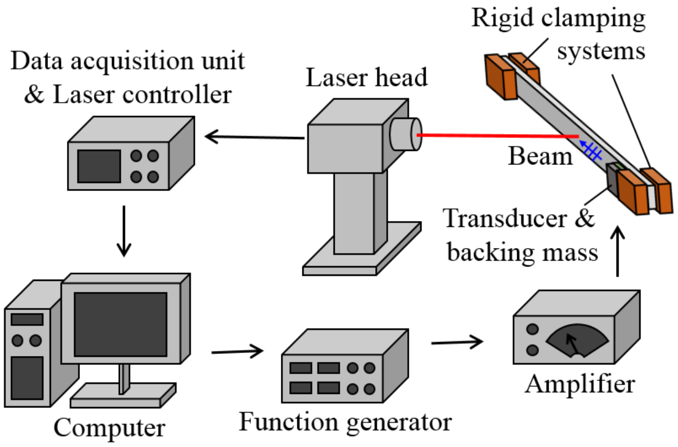

Fig. 4.9 Schematic diagram of the experimental setup.

4.5.2 Results and discussions

The identified numbers of delaminations for the experimental case studies are summarised in Table 4.7. The model class M_1 (single delamination) is selected for Case E1 while the M_2 (two delaminations) is selected for Case E2 based on the calculated probability of the model classes. The results show that the proposed Bayesian approach is able to accurately determine the number of delaminations experimentally.

Table 4.7 Identificatied results of the number of delaminations in the experimental case studies.

Case	Number of delaminations	Log-likelihood	Information gain	Log-evidence	Probability (%)
E1	**1**	**9387.94**	**29.84**	**9358.10**	**99.99**
	2	9408.82	60.15	9348.67	0.01
E2	1	6707.91	15.63	6692.28	0
	2	**7342.14**	**24.15**	**7317.99**	**98.39**
	3	7346.68	32.80	7313.88	1.61

Figure 4.10 plots the estimate of the log-evidence, i.e., $V(O)$ versus O for Case E2, in which the log-evidence was computed using Equation (4.17).

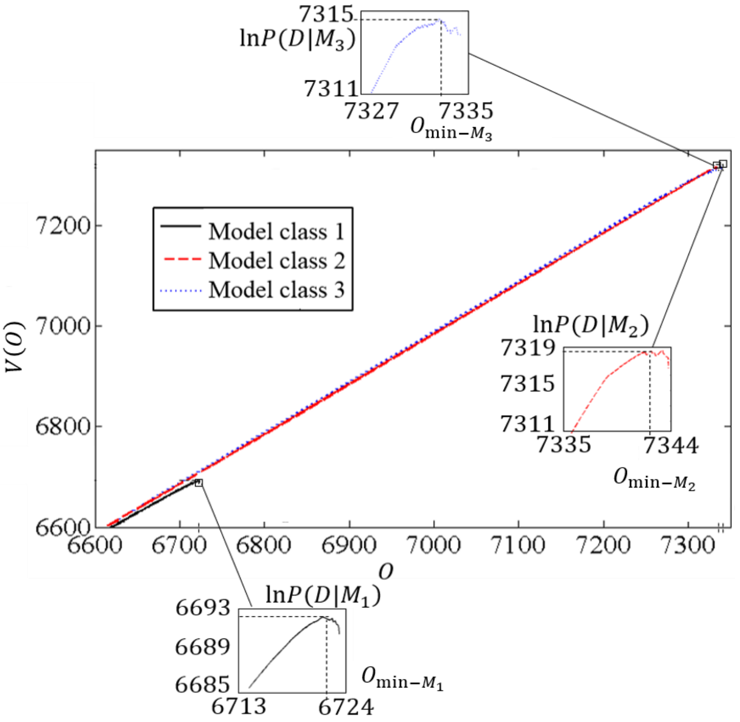

Fig. 4.10 Estimate of the log-evidence of each model class for Case E2.

The identified delamination parameters and the corresponding sample c.o.v.s are shown in Table 4.8. It is shown that for Case E1 the delamination location and length are accurately identified and the corresponding percentages of error are 0.10% and 1.57%, respectively. In addition the through-thickness location of the delamination is also correctly determined. Table 8 also show that sample c.o.v.s of the delamination location and length, which are 0.018% and 0.361%, respectively.

Figure 4.11 shows the evaluation of the samples generated by Subset simulation for the length of the delaminations 1 and 2. It is shown that the samples of delamination lengths efficiently converges to two local optimal regions at Stage 4, and finally converges to the global optimum at Stage 10. The marginal PDF in Figure 12 shows the uncertainties of the identified delamination length for Delaminations 1 and 2 in Case E2. The uncertainties of both delamination lengths indicated by the marginal PDF are consistent with sample c.o.v.s in Table 4.8. Figure 4.12 shows that the drop in PDF value away from the peak for the length of Delamination 1 is much faster than that for Delamination 2, which indicates the uncertainty of the identified delamination length of Delamination 1 is smaller than the Delamination 2.

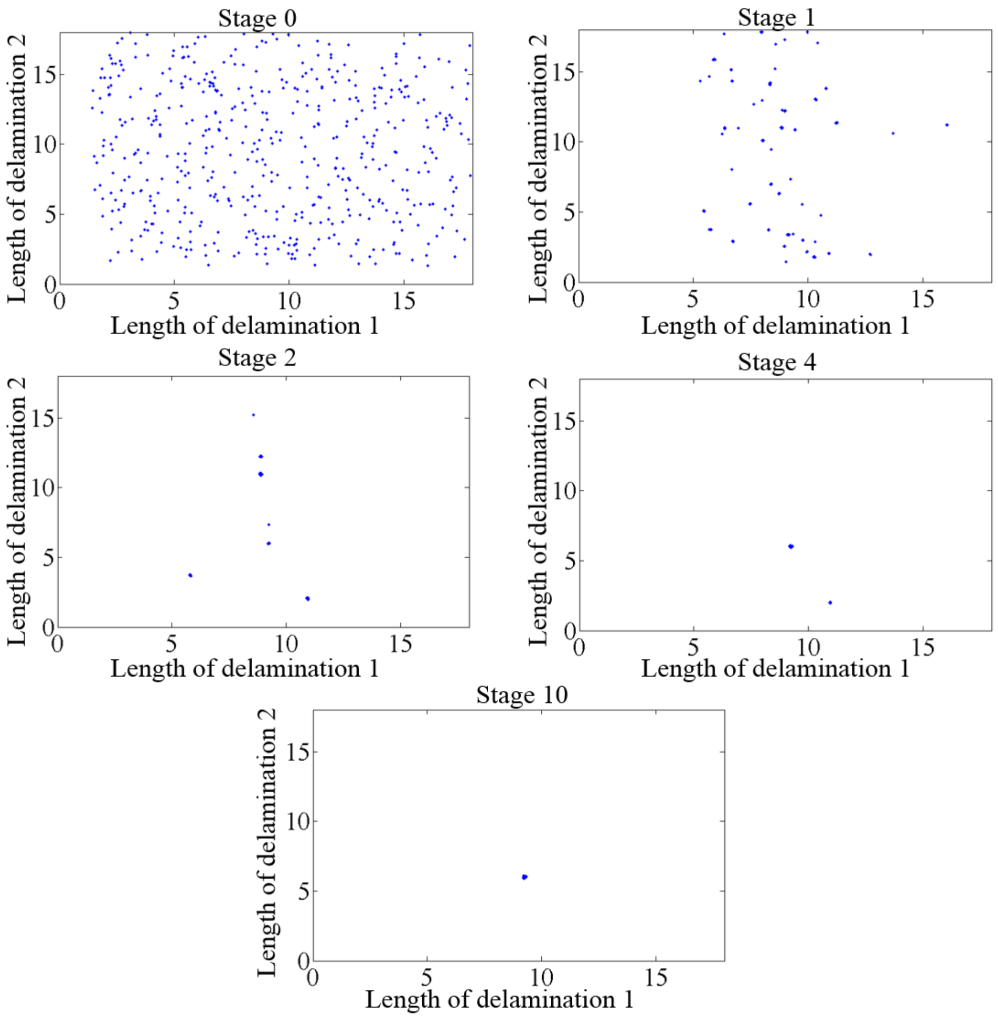

Fig. 4.11 Evolution of the Subset samples for the length of delamination 1 and 2 in Case E2.

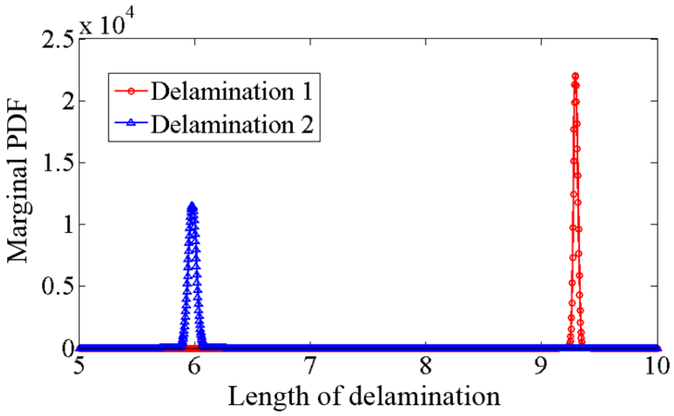

Fig. 4.12 Posterior marginal PDFs for the length of delamination 1 and 2 in Case E2.

Table 4.8 Identified results for the delamination parameters for experimental case studies.

Case	Location (mm)	Length (mm)	Through-thickness location
	l_j (c.o.v. %) [error %]	d_j (c.o.v. %) [error %]	k_i
E1	l_1 = 99.90 (0.018) [0.10]	d_1 = 6.09 (0.361) [1.57]	k_1 = 3
E2	l_1 = 100.10 (0.013) [0.10] l_2 = 195.95 (0.011) [2.03]	d_1 = 9.29 (0.147) [7.06] d_2 = 5.98 (0.472) [0.28]	k_1 = 5 k_2 = 3

4.6 Conclusions

A probabilistic approach has been presented for quantitative identification of multiple delaminations in laminated composite beams using guided waves. The proposed method has addressed a practical situation in the damage detection using model-based approaches, i.e. the number of delaminations is not known in advance for guided wave based damage identification. The proposed method employs the Bayesian model class selection method to select the optimal model class, and hence, the number of delaminations can be accurately identified. In addition to the quantitative identification of the delaminations, i.e. identifying the number of delaminations, delamination locations, lengths and through-thickness locations, the proposed probabilistic approach also quantifies the associated uncertainties. This provides valuable information for engineers in making decision on the remedial work. In this study the time-domain SFE developed based on the higher-order theory and Bayesian updating with Subset simulation have been proposed to further improve the computational efficiency of the multiple delaminations identification. A series of numerical and experimental case studies have been carried out to verify and demonstrate the capability of the proposed probabilistic approach. The number of delaminations has been determined based on the probability of the modal class calculated using Bayesian model class selection method. The delamination parameters and their associated uncertainties have been identified by calculating their sample means and sample c.o.v.s based on the posterior samples obtained in Bayesian updating with Subset simulation. The results have shown that the probabilistic approach is able to identify multiple delaminations using guided wave signal measured at a single measurement point in the laminated composite beam. All the identified delamination parameters were very close to the true values.

Acknowledgement

The work was supported by the Australian Research Council under grant number DE130100261. The support is greatly appreciated.

References for Chapter 4

ARYAN, P., KOTOUSOV, A., NG, C. T. & CAZZOLATO, B. 2016. A baseline-free and non-contact method for detection and imaging of structural damage using 3D laser vibrometry. *Structural Control and Health Monitoring***,** doi: 10.1002/stc.1894.

AU, S. K., DIAZDELAO, F. A. & YOSHIDA, I. 2015. Bayesian updating and model class selection with Subset Simulation. *arXiv preprint arXiv:1510.06989*.

AU, S. K. & BECK, J. L. 1999. A new adaptive importance sampling scheme for reliability calculations. *Structural Safety,* 21**,** 135-158.

BECK, J. L. 2010. Bayesian system identification based on probability logic. *Structural Control and Health Monitoring,* 17**,** 825-847.

BECK, J. L. & AU, S. K. 2002. Bayesian updating of structural models and reliability using Markov chain Monte Carlo simulation. *Journal of Engineering Mechanics,* 128**,** 380-391.

BECK, J. L. & YUEN, K. V. 2004. Model selection using response measurements: Bayesian probabilistic approach. *Journal of Engineering Mechanics,* 130**,** 192-203.

CHIACHIO, M., BECK, J. L., CHIACHIO, J. & RUS, G. 2014. Approximate Bayesian computation by subset simulation. *SIAM Journal on Scientific Computing,* 36**,** A1339-A1358.

CHING, J. & CHEN, Y. C. 2007. Transitional Markov chain Monte Carlo method for Bayesian model updating, model class selection, and model averaging. *Journal of engineering mechanics,* 133**,** 816-832.

CROXFORD, A. J., WILCOX, P. D., DRINKWATER, B. W. & KONSTANTINIDIS, G. 2007. Strategies for guided-wave structural health monitoring. *Proceedings of the Royal Society,* 463**,** 2961-2981.

GRABOWSKA, J., PALACZ, M. & KRAWCZUK, M. 2008. Damage identification by wavelet analysis. *Mechanical systems and signal processing,* 22**,** 1623-1635.

HE, S. & NG, C. T. 2017. Guided wave-based identification of multiple cracks in beams using a Bayesian approach. *Mechanical Systems and Signal Processing,* 84**,** 324-345.

HE, S. & NG, C. T. 2015. Analysis of mode conversion and scattering of guided waves at cracks in isotropic beams using a time-domain spectral finite element method. *Electronic Journal of Structural Engineering,* 14**,** 20-32.

HIBBETT, KARLSSON & SORENSEN 1998. *ABAQUS/standard: User's Manual,* Hibbitt, Karlsson & Sorensen.

KRAWCZUK, M. 2002. Application of spectral beam finite element with a crack and iterative search technique for damage detection. *Finite Elements in Analysis and Design,* 38**,** 537-548.

KUDELA, P., KRAWCZUK, M. & OSTACHOWICZ, W. 2007. Wave propagation modelling in 1D structures using spectral finite elements. *Journal of Sound and Vibration,* 300**,** 88-100.

KUDELA, P. & OSTACHOWICZ, W. 2009. A multilayer delaminated composite beam and plate elements: reflections of Lamb waves at delamination. *Mechanics of Advanced Materials and Structures,* 16**,** 174-187.

LAM, H. F., YANG, J. & AU, S.-K. 2015. Bayesian model updating of a coupled-slab system using field test data utilizing an enhanced Markov chain Monte Carlo simulation algorithm. *Engineering Structures,* 102**,** 144-155.

LIN, X. & YUAN, F. G. 2001. Damage Detection of a Plate Using Migration Technique. *Journal of Intelligent Material Systems and Structures,* 12**,** 469-482.

MALYARENKO, E. V. & HINDERS, M. K. 2000. Fan beam and double crosshole Lamb wave tomography for mapping flaws in aging aircraft structures. *The Journal of the Acoustical Society of America,* 108**,** 1631-1639.

MOSAVI, A. A., DICKEY, D., SERACINO, R. & RIZKALLA, S. 2012. Identifying damage locations under ambient vibrations utilizing vector autoregressive models and Mahalanobis distances. *Mechanical systems and signal processing,* 26**,** 254-267.

MTHEMBU, L., MARWALA, T., FRISWELL, M. I. & ADHIKARI, S. 2011. Model selection in finite element model updating using the Bayesian evidence statistic. *Mechanical Systems and Signal Processing,* 25**,** 2399-2412.

MUTO, M. & BECK, J. L. 2008. Bayesian updating and model class selection for hysteretic structural models using stochastic simulation. *Journal of Vibration and Control,* 14**,** 7-34.

NAG, A., MAHAPATRA, D. R. & GOPALAKRISHNAN, S. 2002. Identification of delamination in composite beams using spectral estimation and a genetic algorithm. *Smart Materials and Structures,* 11**,** 899-908.

NG, C. T. 2014a. On the selection of advanced signal processing techniques for guided wave damage identification using a statistical approach. *Engineering Structures,* 67**,** 50-60.

NG, C. T. 2015a. On accuracy of analytical modeling of Lamb wave scattering at delaminations in multilayered isotropic plates. *International Journal of Structural Stability and Dynamics,* 15**,** doi: 10.1142/S0219455415400106.

NG, C. T. 2014b. Bayesian model updating approach for experimental identification of damage in beams using guided waves. *Structural Health Monitoring,* 13**,** 359-373.

NG, C. T. 2015b. A two-stage approach for quantitative damage imaging in metallic plates using Lamb waves. *Earthquake and Structures,* 8**,** 821-841.

NG, C. T., VEIDT, M. & LAM, H. F. 2009. Guided Wave Damage Characterisation in Beams Utilising Probabilistic Optimisation. *Engineering Structures,* 31**,** 2842-2850.

NG, C. T., VEIDT, M. & RAJIC, N. Integrated piezoceramic transducers for imaging damage in composite laminates. Proceedings of SPIE - The International Society for Optical Engineering, 2009, doi: 10.1117/12.840150.

NG, C. T., VEIDT, M., ROSE, L. & WANG, C. H. 2012. Analytical and finite element prediction of Lamb wave scattering at delaminations in quasi-isotropic composite laminates. *Journal of Sound and Vibrations,* 331**,** 4870-4883.

NOUREINI, H. K. & KHAJI, N. 2012. Detection of a through-thickness crack based on elastic wave scattering in plates part II: Inverse solution. *Asian Journal of Civil Engineering,* 13**,** 431-454.

PAPAIOANNOU, I., BETZ, W., ZWIRGLMAIER, K. & STRAUB, D. 2015. MCMC algorithms for subset simulation. *Probabilistic Engineering Mechanics,* 41**,** 89-103.

PAU, A. & VESTRONI, F. 2011. Wave propagation in one-dimensional waveguides for damage characterization. *Journal of Intelligent Material Systems and Structures,* 22**,** 1869–1877.

QUEK, S. T., TUA, P. & WANG, Q. 2003. Detecting anomalies in beams and plate based on the Hilbert–Huang transform of real signals. *Smart materials and structures,* 12**,** 447-460.

RAGHAVAN, A. & CESNIK, C. E. S. 2007. Review of Guided-wave Structural Health Monitoring. *The Shock and Vibration Digest,* 39**,** 91-114.

RAISUTIS, R., KAZYS, R., ZUKAUSKAS, E., MAZEIKA, L. & VLADISAUSKAS, A. 2010. Application of ultrasonic guided waves for non-destructive testing of defective CFRP rods with multiple delaminations. *NDT & E International,* 43**,** 416-424.

ROSE, L. F. & WANG, C. H. 2010. Mindlin plate theory for damage detection: imaging of flexural inhomogeneities. *The Journal of the Acoustical Society of America,* 127**,** 754-763.

RUCKA, M. 2010. Experimental and numerical studies of guided wave damage detection in bars with structural discontinuities. *Archive of Applied Mechanics,* 80**,** 1371-1390.

SCHULTE, R., FRITZEN, C. & MOLL, J. Spectral element modelling of wave propagation in isotropic and anisotropic shell-structures including different types of damage. IOP Conference Series: Materials Science and Engineering, 2010. IOP Publishing, doi:10.1088/1757-899X/10/1/012065.

STRAUB, D. & PAPAIOANNOU, I. 2014. Bayesian updating with structural reliability methods. *Journal of Engineering Mechanics,* 141**,** doi: 10.1061/(ASCE)EM.1943-7889.0000839.

SUN, X., LI, F., MIAO, X., MENG, G. & ZHOU, L. 2012. Research on propagation of guided waves in thick beam and crack damage identification. *Jixie Gongcheng Xuebao/Journal of Mechanical Engineering,* 48**,** 1-10.

TOFT, H. S., BRANNER, K., BERRING, P. & SØRENSEN, J. D. 2011. Defect distribution and reliability assessment of wind turbine blades. *Engineering Structures,* 33**,** 171-180.

VINSON, J. R. & SIERAKOWSKI, R. L. 2012. *The behavior of structures composed of composite materials*, Springer Science & Business Media.

YAN, G. 2013. A Bayesian approach for damage localization in plate-like structures using Lamb waves. *Smart Materials and Structures,* 22**,** doi:10.1088/0964-1726/22/3/035012.

YUEN, K. V. & KATAFYGIOTIS, L. S. 2002. Bayesian Modal Updating Using Complete Input and Incomplete Response Noisy Measurement. *Journal of Engineering Mechanics, ASCE,* 128**,** 340-350.

Chapter 5

Modelling and analysis of nonlinear guided waves interaction at a breathing crack using time-domain spectral finite element method

(Paper 4, submitted)

Shuai He and Ching-Tai Ng

School of Civil, Environmental & Mining Engineering, The University of Adelaide, Adelaide, SA 5005, Australia

Publication:

HE, S. & NG, C. T. 2017. Modelling and analysis of nonlinear guided waves interaction at a breathing crack using time-domain spectral finite element method. *Smart Materials and Structures,* Submitted for review: March 2017.

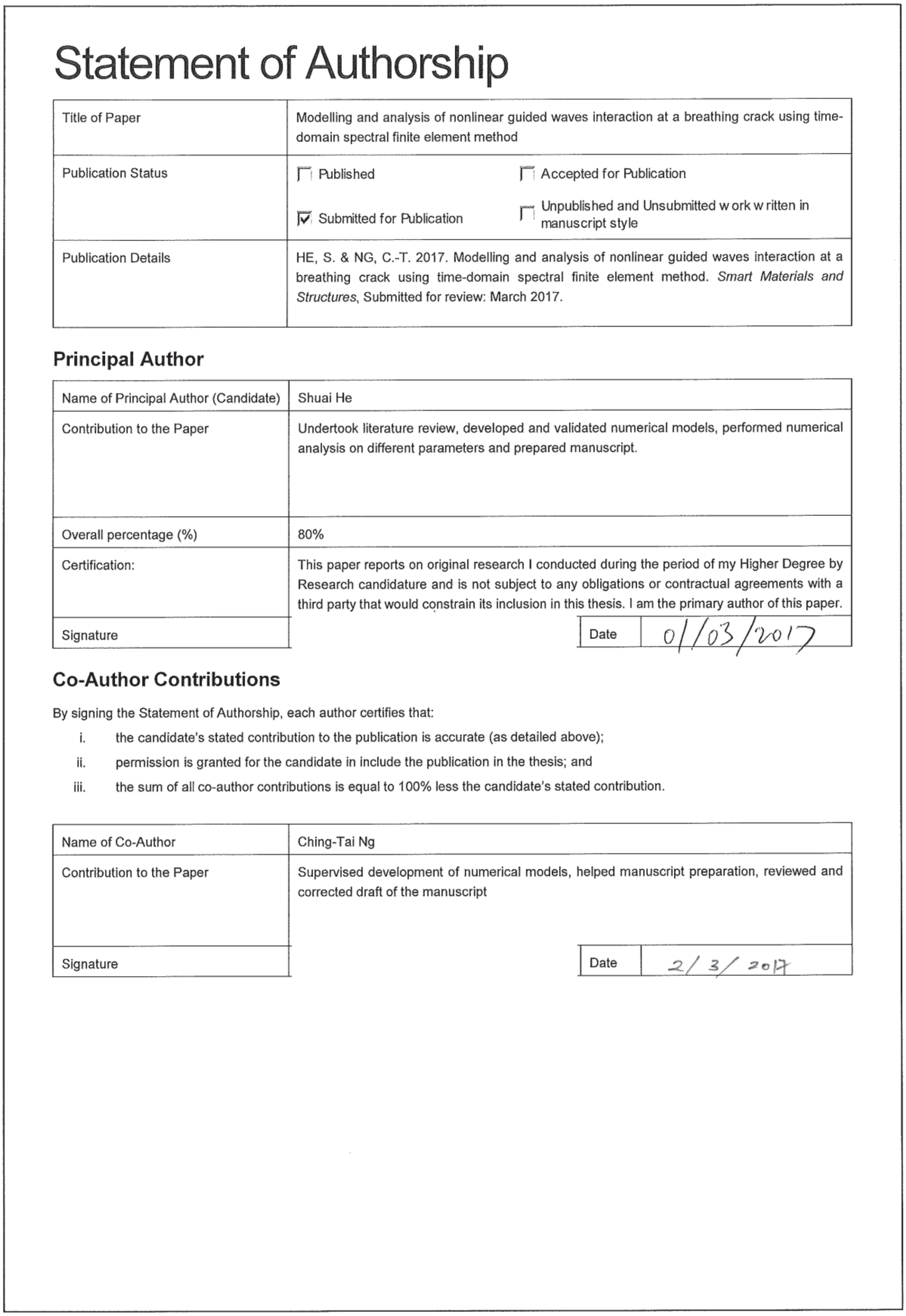

Statement of Authorship

Title of Paper	Modelling and analysis of nonlinear guided waves interaction at a breathing crack using time-domain spectral finite element method
Publication Status	☐ Published ☐ Accepted for Publication ☑ Submitted for Publication ☐ Unpublished and Unsubmitted work written in manuscript style
Publication Details	HE, S. & NG, C.-T. 2017. Modelling and analysis of nonlinear guided waves interaction at a breathing crack using time-domain spectral finite element method. *Smart Materials and Structures*, Submitted for review: March 2017.

Principal Author

Name of Principal Author (Candidate)	Shuai He		
Contribution to the Paper	Undertook literature review, developed and validated numerical models, performed numerical analysis on different parameters and prepared manuscript.		
Overall percentage (%)	80%		
Certification:	This paper reports on original research I conducted during the period of my Higher Degree by Research candidature and is not subject to any obligations or contractual agreements with a third party that would constrain its inclusion in this thesis. I am the primary author of this paper.		
Signature		Date	01/03/2017

Co-Author Contributions

By signing the Statement of Authorship, each author certifies that:

i. the candidate's stated contribution to the publication is accurate (as detailed above);

ii. permission is granted for the candidate in include the publication in the thesis; and

iii. the sum of all co-author contributions is equal to 100% less the candidate's stated contribution.

Name of Co-Author	Ching-Tai Ng		
Contribution to the Paper	Supervised development of numerical models, helped manuscript preparation, reviewed and corrected draft of the manuscript		
Signature		Date	2/3/2017

Abstract

This study proposes a time-domain spectral finite element (SFE) model and investigates nonlinear guided wave interaction at a breathing crack. An extended time-domain SFE method based on the Mindlin-Hermann rod and Timoshenko beam theory is proposed to predict the nonlinear guided wave generation at the breathing crack. An SFE crack element is proposed to simulate the mode-conversion effect, in which a bilinear crack mechanism is implemented to take into account the contact nonlinearity at the breathing crack. There is good agreement between the results calculated using the proposed time-domain SFE method and three-dimensional (3D) finite element (FE) simulation. This demonstrates the accuracy of the proposed SFE method in simulating contact nonlinearity at the breathing crack. Parametric studies using the fundamental symmetric (S_0) and anti-symmetric (A_0) modes of guided waves are also carried out to provide physical insights into the higher harmonics generated due to the contact nonlinearity at the breathing crack. The magnitude of the higher harmonics generated as a function of the crack depth is investigated in detail. The results show that the mode-converted higher harmonic guided waves provide valuable information for damage detection.

***Keywords*:**

Nonlinear guided wave; higher harmonic; spectral finite element; breathing crack; contact nonlinearity

5.1 Introduction

Detecting and identifying damage at its early stages is essential for maintaining the safety and serviceability of structures in a wide range of engineering fields, including aerospace, civil and mechanical engineering. Different non-destructive damage detection techniques have been developed for safety inspection. For example, low frequency vibration (Magalhães et al., 2012, Lam and Yin, 2010, Yin et al., 2009), acoustic emission (Nair and Cai, 2010) and conventional ultrasonic techniques (Achenbach, 2000). Recently, guided waves have been shown to provide a potential cost-effective and reliable safety inspection of structures (Mitra and Gopalakrishnan, 2016). Guided waves have been sucessfully applied in plates (He and Yuan, 2016, Ng, 2015a, Ng, 2015b, Gangadharan et al., 2010, Kim and Sohn, 2007), beams (Ng, 2014b), and rods (Kažys et al., 2010, Pau and Vestroni, 2011) for damage detection. Numerous guided wave-based damage detection techniques have been developed, such as time-of-flight approach (Quek et al., 2003), maximum-likelihood estimation (Flynn et al., 2011), damage imaging (Aryan et al., 2016a, Tian et al., 2015, Sohn et al., 2011, Ng et al., 2009, Zhao et al., 2007), phase array beamforming (Han and Kim, 2015), model based approach (He and Ng, 2016, Ng, 2014b) and time-reversal techniques (Sohn et al., 2007).

5.1.1 Nonlinear guided wave

Most of the aforementioned guided wave-based damage detection techniques assume that the geometry of the damage (e.g. open crack) remains unchanged during the inspection process. The damage detection relies on the linear signal from the damage-wave interaction, i.e. signals at the same frequency as the incident wave. Contact nonlinearity induced by the contact behaviour between crack interfaces was experimentally observed in the literature (Kawashima et al., 2002, Solodov et al., 2002). Early developments in contact nonlinearity focused on bulk waves; later, nonlinear guided waves attracted significant research attention because of their ability to inspect larger areas compared to bulk waves. When guided wave interacts with a contact-type damage, the compressive pressure of the wave closes the crack, and the tensile pressure opens the crack (Mitra and Gopalakrishnan, 2016, Pieczonka et al., 2016). This phenomenon alters the stiffness of the structure, and produces nonlinear guided wave in the measured signal. In order to improve the accuracy of identification, implementation of the nonlinear guided waves for different types of damages, such as fatigue crack (Dziedziech et al., 2016), kissing bond (Najib and Nobari, 2015, Yan et al., 2012), delamination (Soleimanpour et al., 2016, Soleimanpour and Ng, 2016) and breathing crack (Broda et al., 2014) have been investigated.

5.1.2 Numerical methods for predicting nonlinear guided waves

Different methods have been developed to simulate the guided wave propagation in structures (Willberg et al., 2015). Numerical methods, such as the conventional finite element (FE) method (Aryan et al., 2016b, Zhou and Ichchou, 2011), have been used for simulating guided wave propagation in complex structures. However, the FE method is computationally inefficient because the size of the FE elements should be sufficiently smaller than the wavelength of the guided wave to ensure the simulation accuracy. The fast Fourier transform (FFT) based spectral finite element (SFE) method (Nag et al., 2002, Park et al., 2013, Mahapatra et al., 2006) is computationally efficient in simulating the guided wave propagation, but it is limited in simulating the cases of finite-length waveguides due to the wrap-around effect (Joglekar and Mitra, 2016). The wavelet spectral finite element (WSFE) overcomes this problem by using the Daubechies scaling functions to approximate the time-dependant variable (Samaratunga et al., 2014, Gopalakrishnan and Mitra, 2010), while it is a semi-analytical method that is impractical for simulating geometrically complicated structures. Other numerical methods also have their limitations in simulating guided wave propagation. For example, the boundary element method (Zhao and Rose,

2003) would also be significantly inefficient in simulating guided wave propagation when the structure is large. The finite difference (FD) method is unable to simulate guided wave propagation in the waveguide that material property changes with geometry (Xu et al., 2003). The finite strip element method (Hayashi and Kawashima, 2002) is also unsuitable for simulating the geometrically complicated structures.

Recently, the time-domain SFE method has been used to study the guided wave propagation (Wang et al., 2012), and damage detection (Rucka et al., 2012, Li et al., 2012, Żak et al., 2012, Ostachowicz, 2008). The time-domain SFE method (Kudela and Ostachowicz, 2009, Kudela et al., 2007) has the same flexibility as the FE method in structural discretisation, but it requires fewer elements because it uses high-order shape function to achieve the same level of accuracy as the FE method. The time-domain SFE method applies the Gauss-Lobatto-Legendre (GLL) nodes in the formulation; as a result, a diagonal form of the mass matrix can be obtained. By using the explicit central difference method, therefore, the wave propagation problem can be solved efficiently.

In the literature modelling nonlinear guided waves caused by contact nonlinearity, has been investigated using different methods. These include the FE method (Giannini et al., 2013), FD method (Xu et al., 2007), local interaction simulation approach (LISA) (Shen and Cesnik, 2016), and the FFT-based SFE method (Joglekar and Mitra, 2016, Joglekar and Mitra, 2015). However, an efficient time-domain SFE method has not yet been developed for this purpose. In this study, the time-domain SFE method is extended to simulate the nonlinear guided wave generated at cracks, where the nonlinear crack-wave interaction is simulated by contact mechanism. This study also provides physical insights into the generation of nonlinear guided waves (e.g. higher harmonics) resulting from the contact nonlinearity. This helps to further advance the use of the nonlinear guided waves in damage detection.

In practical situations, the mode-conversion phenomenon occurs when guided waves interact with an asymmetric discontinuity. Specifically, the mode-conversion effect of guided waves is a phenomenon by which a purely axial input gives rise to flexural response and vice versa. The fundamental anti-symmetric mode (A_0) guided wave can be generated when the fundamental symmetric mode (S_0) guided wave interacts with an asymmetric discontinuity and vice versa. In the literature, the study of the mode-conversion effect has been limited to linear guided waves. For example, the mode-converted linear guided wave signal has been employed to detect delaminations in composite laminates (He and Ng, 2016), and cracks in aluminium beams (He and Ng, 2017). In contrast, there are a very limited number of studies focused on the mode conversion of nonlinear guided waves. In this study the mode-conversion effect of the nonlinear guided waves is investigated using the proposed time-domain SFE method and the SFE crack element. The mode-conversion effect of A_0 guided waves converted to S_0 nonlinear guided waves, and vice versa, is studied in detail.

This chapter is organised as follows. The time-domain SFE method is first presented in Section 5.2, where a bilinear crack model is embedded in the SFE crack element to simulate contact nonlinearity at the breathing crack. In Section 5.3, the proposed time-domain SFE method is validated using the conventional 3D FE method. This section compares SFE and 3D FE simulated signals with generated higher harmonics that result from the contact nonlinearity at the breathing crack. The detailed comparison examines both time and frequency of the signals. Section 5.4 provides an observation of the generated nonlinear guided waves and investigates the mode-conversion effect of the nonlinear guided waves at the crack. Section 5.5 presents a series of parametric studies that investigate the characteristics of the generated, higher harmonic guided waves, in which the magnitude of the generated higher harmonics as a function of the crack depth is studied. Finally, the conclusions are drawn in Section 5.6.

5.2 Time-domain spectral finite element method

5.2.1 Spectral finite element (SFE) formulation

The SFE method employs a similar time-domain dynamic equilibrium as the conventional FE method, which has the following form: (He and Ng, 2015, Rucka, 2010, Kudela and Ostachowicz, 2009)

$$\mathbf{M}\ddot{\mathbf{U}}+\mathbf{C}\dot{\mathbf{U}}+\mathbf{K}\mathbf{U}=\mathbf{F}(t) \tag{5.1}$$

where $\mathbf{U}$, $\dot{\mathbf{U}}$ and $\ddot{\mathbf{U}}$ are the global vectors corresponding to nodal displacement, velocity and acceleration, respectively. $\mathbf{M}$, $\mathbf{C}$, $\mathbf{K}$ and $\mathbf{F}(t)$ denote the global mass matrix, global damping matrix, global stiffness matrix and global force vector at time t, respectively. Specifically, the damping matrix $\mathbf{C}$ is proportional to the global mass matrix as $\mathbf{C}=\eta\mathbf{M}$, where η is the damping coefficient. In addition, the global matrixes, $\mathbf{M}$ and $\mathbf{K}$ and the global force vector $\mathbf{F}(t)$, are assembled from their corresponding elemental terms $\mathbf{M}^e$, $\mathbf{K}^e$ and $\mathbf{F}^e$, which can be expressed as:

$$\mathbf{M}^e \approx \sum_{i=1}^{n} w_i \mathbf{S}_e(\xi_i)^T \rho_e \mathbf{S}_e(\xi_i) \left| J(\xi_i) \right| \tag{5.2}$$

$$\mathbf{K}^e \approx \sum_{i=1}^{n} w_i \mathbf{B}_e(\xi_i)^T \mathbf{E}_e \mathbf{B}_e(\xi_i) \left| J(\xi_i) \right| \tag{5.3}$$

$$\mathbf{F}^e \approx \sum_{i=1}^{n} w_i \mathbf{S}_e(\xi_i)^T \mathbf{f}_e(\xi_i) \left| J(\xi_i) \right| \tag{5.4}$$

where n is the node number in the element, $\mathbf{f}_e(\xi_i)$ is the external force and ξ_i is the local coordinate of the node i in the element, respectively. $J=\partial x/\partial\xi$ is the Jacobian function mapping the local coordinate ξ to the global coordinate x. Distinct from the conventional FE method, the nodes in the SFE are called GLL nodes (He and Ng, 2017). The local coordinate ξ of each node in the SFE can be obtained as the roots of the following equation:

$$\left(1-\xi_i^2\right)L'_{n-1}\left(\xi_i\right)=0,\ i\in 1,\ldots,n \tag{5.5}$$

where L_{n-1} is the Legendre polynomial in (n-1)-th order and the symbol “$'$” denotes the differential operation. w_i is the weighting function of node i and it can be calculated as:

$$w_i=\frac{2}{n\left(n-1\right)[L_{n-1}\left(\xi_i\right)]^2} \tag{5.6}$$

$\mathbf{S}_e$ is the shape function matrix defined as:

$$\mathbf{S}_e=\mathbf{S}\otimes\mathbf{I} \tag{5.7}$$

where $\mathbf{S}=\left[S_1(\xi)\quad\ldots\quad S_n(\xi)\right]^T$, ‘$\otimes$’ is the Kronecker product and **I** is a square identity matrix having the same size as the number of nodal degree-of-freedoms (DoFs), respectively. $S_i(\xi)$ is the spectral shape function value for node i defined as:

$$S_i\left(\xi\right)=\prod_{m=1,m\neq i}^{n}\frac{\xi-\xi_m}{\xi_i-\xi_m} \tag{5.8}$$

Due to the Kronecker property of the shape function value, the mass matrix achieves a diagonal form. It can be solved efficiently by the explicit central difference method. The number of elements needed to capture guided wave propagation accurately can be significantly reduced by using the GLL nodes, thus improving the computational efficiency of the SFE method.

In this study, Equation (5.1) is governed by the Mindlin-Herrmann rod theory and Timoshenko beam theory. The independent lateral contraction $\psi(x)$ is introduced to account for the Poisson effect. The first order shear deformation is considered by employing an independent rotation $\varphi(x)$. Based on the Mindlin-Herrmann rod theory and Timoshenko beam theory, the displacement field of the beam is

$$\begin{aligned} \bar{u}(x,y) &\approx u(x) - \varphi(x)y \\ \bar{v}(x,y) &\approx v(x) + \psi(x)y \end{aligned} \tag{5.9}$$

where $u(x)$ and $v(x)$ are the longitudinal and transverse displacements at x axis, respectively. The strain field $\boldsymbol{\varepsilon}$ at the x axis of the beam can be obtained in a matrix form as:

$$\boldsymbol{\varepsilon} = \mathbf{B}_e \mathbf{q} \tag{5.10}$$

where $\mathbf{q} = \begin{bmatrix} u & \psi & v & \varphi \end{bmatrix}^T$ is the displacement field vector and $\mathbf{B}_e$ is the constitutive relation between strain and displacement. It is defined as:

$$\mathbf{B}_e = \begin{bmatrix} \frac{\partial}{\partial x} & 0 & 0 & 0 \\ 0 & 1 & 0 & 0 \\ 0 & \frac{\partial}{\partial x} & 0 & 0 \\ 0 & 0 & \frac{\partial}{\partial x} & -1 \\ 0 & 0 & 0 & \frac{\partial}{\partial x} \end{bmatrix} \mathbf{S}_e \tag{5.11}$$

According to the Mindlin-Herrmann rod and Timoshenko beam theories the mass density matrix $\boldsymbol{\rho}_e$ and the stress-strain matrix $\mathbf{E}_e$ in Equations (5.2) and (5.3) have the following form:

$$\boldsymbol{\rho}_e = \begin{bmatrix} \rho A & 0 & 0 & 0 \\ 0 & K_2^M \rho I & 0 & 0 \\ 0 & 0 & \rho A & 0 \\ 0 & 0 & 0 & K_2^T \rho I \end{bmatrix} \tag{5.12}$$

and

$$\mathbf{E}_e = \begin{bmatrix} \frac{EA}{1-\nu^2} & \frac{\nu EA}{1-\nu^2} & 0 & 0 & 0 \\ \frac{\nu EA}{1-\nu^2} & \frac{EA}{1-\nu^2} & 0 & 0 & 0 \\ 0 & 0 & K_1^M GI & 0 & 0 \\ 0 & 0 & 0 & K_1^T GA & 0 \\ 0 & 0 & 0 & 0 & EI \end{bmatrix} \tag{5.13}$$

where ρ, A and I denotes the density of the material, the cross-section area of the beam, and the moment of inertia, respectively. E, G and ν are the Young's modules, shear modules and Poisson's ratio, respectively. K_1^M, K_2^M, K_1^T and K_2^T are adjustable parameters that calibrate the accuracy guided wave propagation simulation. In this chapter, the value K_1^M = 1.1, K_2^M = 3.1 and K_1^T = 0.922 are determined from the experimental data in our previous study (He and Ng, 2017), by which the SFE simulation has the best fitting to the experimental data. K_2^T is set as $12K_1^T/\pi^2$ to match the cut-off frequency of guided wave modes.

5.2.2 Open crack model

An SFE crack element was developed to model an open crack. The mode-conversion effect is simulated by coupling the longitudinal, transverse and rotational DoFs in the crack element. The crack element has two nodes and has a very small length, i.e. $l = 0.1$ mm. As shown in Figure 5.1, in the aluminium beam with thickness *b* and height *h*, the crack is located at l_c in the SFE crack element. The cross-section of the crack is rectangular, where the width and depth are b and d_c, respectively. In the crack element, lateral contraction due to the longitudinal guided wave propagation is not considered because the length of the element is very small. Hence, the nodes in the crack element consider only the longitudinal, transverse and rotational DoFs. The stiffness matrix $\mathbf{K}_e^c$ is developed for the crack element using a similar approach (Darpe et al., 2004), but it has been modified because of the rectangular cross-section of the beam in this chapter.

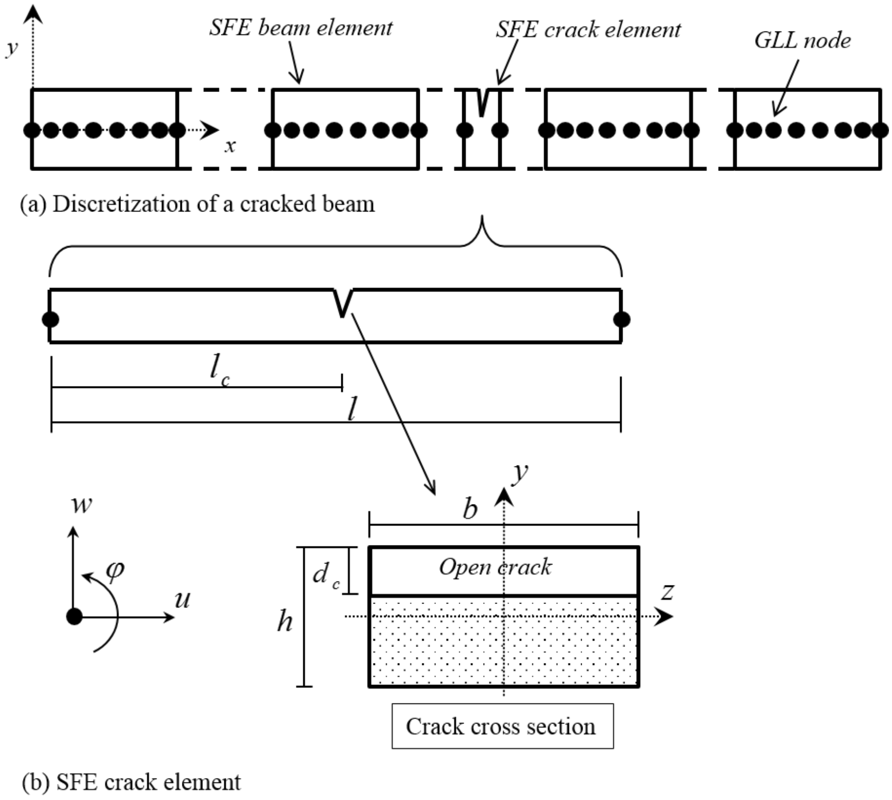

Fig. 5.1 Schematic diagram of the two-node crack element for simulating an opened crack. (a) Discretization of a cracked beam; (b) SFE crack element.

In this chapter, the crack element stiffness matrix $\mathbf{K}_e^c$ has the form:

$$\mathbf{K}_e^c = \mathbf{P}\mathbf{G}_c^{-1}\mathbf{P}^T \tag{5.14}$$

where **P** is the spatial transformation matrix as a function of the crack element length l:

$$\mathbf{P}^T = \begin{bmatrix} 1 & 0 & 0 & -1 & 0 & 0 \\ 0 & 1 & 0 & 0 & -1 & l \\ 0 & 0 & 1 & 0 & 0 & -1 \end{bmatrix} \tag{5.15}$$

$\mathbf{G}$ is the flexibility matrix given as follows:

$$\mathbf{G}_c = \begin{pmatrix} g_{11}^c & g_{12}^c & g_{13}^c \\ g_{21}^c & g_{22}^c & g_{23}^c \\ g_{31}^c & g_{32}^c & g_{33}^c \end{pmatrix} \tag{5.16}$$

with

$$\begin{gathered} g_{11} = \frac{l}{EA} + I_{g1},\ g_{22} = \left(\frac{\kappa l}{GA} + \frac{l^3}{3EA}\right) + \left(I_{g3} + l_c^2 I_{g4}\right),\ g_{33} = \frac{l}{EI} + I_{g4} \\ g_{12} = g_{21} = l_c I_{g2},\ q_{13} = q_{31} = -I_{g2},\ q_{23} = q_{32} = -\frac{l^2}{2EI} - l_c I_{g4} \end{gathered} \tag{5.17}$$

where $\kappa = 10(1+\nu)/(12+11\nu)$ is the shear coefficient for the rectangular beam cross section. I_{g1}, I_{g2}, I_{g3} and I_{g4} are functions of the crack depth, defined as:

$$\begin{aligned} I_{g1} &= \frac{2\pi}{Eb}\int_0^\alpha \alpha F_1^2 d\alpha \\ I_{g2} &= \frac{12\pi}{Ebh}\int_0^\alpha \alpha F_1 F_2 d\alpha \\ I_{g3} &= \frac{2\kappa\pi}{Eb}\int_0^\alpha \alpha F_{II}{}^2 d\alpha \\ I_{g4} &= \frac{72\pi}{Ebh^2}\int_0^\alpha \alpha F_2{}^2 d\alpha \end{aligned} \tag{5.18}$$

where $\alpha = d_c / h$. F_1 , F_2 and F_{II} are the empirical boundary calibration factors accounted for tension, bending and shear for the surface crack, for which formulations are given by Tada et al. (2000) as:

$$F_1(\alpha) = \sqrt{\frac{2}{\pi\alpha}\tan\left(\frac{\pi\alpha}{2}\right)}\,\frac{0.752 + 2.02\alpha + 0.37\left[1 - \sin\left(\frac{\pi\alpha}{2}\right)\right]^3}{\cos\left(\frac{\pi\alpha}{2}\right)} \tag{5.19}$$

$$F_2(\alpha) = \sqrt{\frac{2}{\pi\alpha}\tan\left(\frac{\pi\alpha}{2}\right)}\,\frac{0.923 + 0.199\left[1 - \sin\left(\frac{\pi\alpha}{2}\right)\right]^4}{\cos\left(\frac{\pi\alpha}{2}\right)} \tag{5.20}$$

$$F_{II}(\alpha) = \frac{1.122 - 0.561\alpha + 0.085\alpha^2 + 0.18\alpha^3}{\sqrt{1-\alpha}} \tag{5.21}$$

According to Tada et al. (2000), the factors F_1, F_2 and F_{II} produce less than 0.5% errors for a crack with any depth d_c. It should be noted that if the crack is closed, the crack element is treated as an intact SFE beam element, and its stiffness matrix $\mathbf{K}_e^c$ in Equation (5.14) becomes:

$$\mathbf{K}_e^c = \mathbf{P}\mathbf{G}_e^{-1}\mathbf{P}^T \tag{5.22}$$

where $\mathbf{G}_e$ is the flexibility matrix for the closed crack element as follows:

$$\mathbf{G}_e = \begin{pmatrix} g_{11}^e & g_{12}^e & g_{13}^e \\ g_{21}^e & g_{22}^e & g_{23}^e \\ g_{31}^e & g_{32}^e & g_{33}^e \end{pmatrix} \tag{5.23}$$

with

$$\begin{gathered} g_{11}^e = \frac{l}{EA}\,,\ g_{22}^e = \left(\frac{\kappa l}{GA} + \frac{l^3}{3EA}\right),\ g_{33}^e = \frac{l}{EI} \\ g_{12}^e = g_{21}^e = g_{13}^e = g_{31}^e = 0\,,\ g_{23}^e = g_{32}^e = -\frac{l^2}{2EI} \end{gathered} \tag{5.24}$$

5.2.3 Crack-breathing mechanism

When the incident guided wave interacts with the crack, the contact nonlinearity occurs due to the crack-breathing phenomenon. There are numerous methods for simulating the contact nonlinearity of guided waves, but the bilinear crack model is one of the most commonly used (Bovsunovsky and Surace, 2015, Broda et al., 2014). In this chapter, a bilinear crack mechanism is proposed for taking into account the contact nonlinearity effect, and it is incorporated in the SFE crack model. Specifically, when the out-of-plane excitation is applied, the nodal rotations φ_1 and φ_2 of the two-node crack element are examined at each step. On the other hand, when the in-plane excitation is applied, the nodal longitudinal displacements u_1 and u_2 are examined. These are shown in the following equations:

Out-of-plane excitation:

Crack open:

$$\varphi_1 - \varphi_2 > 0 \tag{5.25}$$

Crack closed:

$$\varphi_1 - \varphi_2 <= 0 \tag{5.26}$$

In-plane excitation:

Crack open:

$$u_1 - u_2 < 0 \tag{5.27}$$

Crack closed:

$$u_1 - u_2 >= 0 \tag{5.28}$$

These mechanisms are indicated in Figure 5.2. If the crack is open, the proposed SFE crack element is used. When the crack is closed, the SFE crack element is treated as an intact SFE beam element. By replacing the stiffness matrix of the crack element, the contact nonlinearity effect can be simulated.

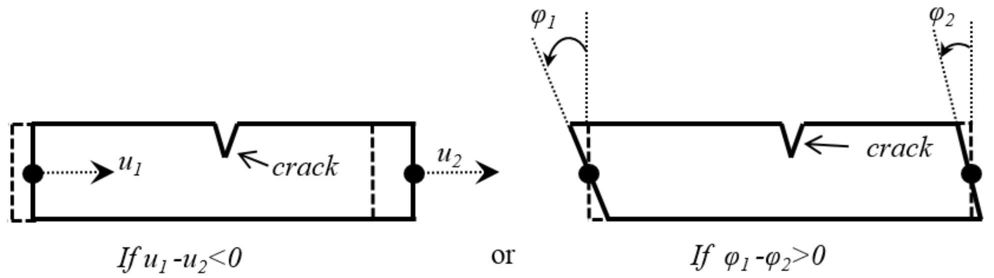

(a) Crack is opened, $\mathbf{K}_e^c = \mathbf{P}\mathbf{G}_c^{-1}\mathbf{P}^T$

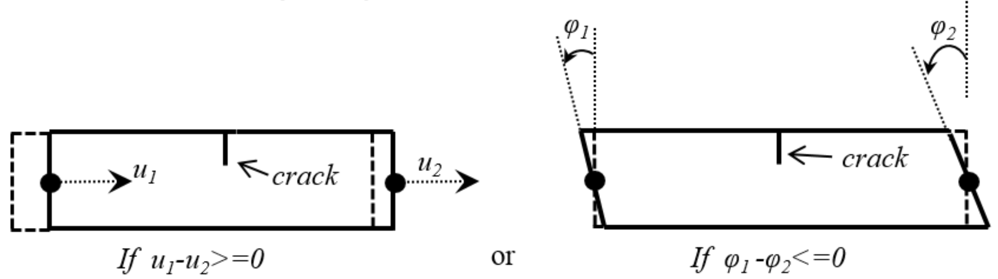

(b) Crack is closed, $\mathbf{K}_e^c = \mathbf{P}\mathbf{G}_e^{-1}\mathbf{P}^T$

Fig. 5.2 Degrees-of-freedom at the crack element when the crack is (a) opened and (b) closed.

5.3 Validation using three-dimensional finite element simulation

In order to verify the accuracy of the proposed SFE method, the results of a beam modelled using the time-domain SFE method are compared with the results calculated using the conventional explicit three-dimensional (3D) FE method. The verification was conducted in two different situations: 1) exciting S_0 and 2) A_0 incident guided waves. It is assumed that the beam is made of aluminium and the material properties are shown in Table 5.1. The width and height of the beam are b = 12 mm and h = 6 mm, respectively. A schematic diagram of the beam is shown in Figure 5.3. The beam length, crack location and number of SFE elements used for these two different situations are shown in Table 5.1.

Table 5.1 Summary of the time-domain SFE models used in the validation.

Incident guided wave	S_0	A_0
Beam length L (m)	1	
Crack location L_c (m)	0.5	
Crack depth d_c (m)	0.003	
Young's modulus (GPa)	70	
Density (kg/m^3)	2700	
Poisson's ratio	0.3	

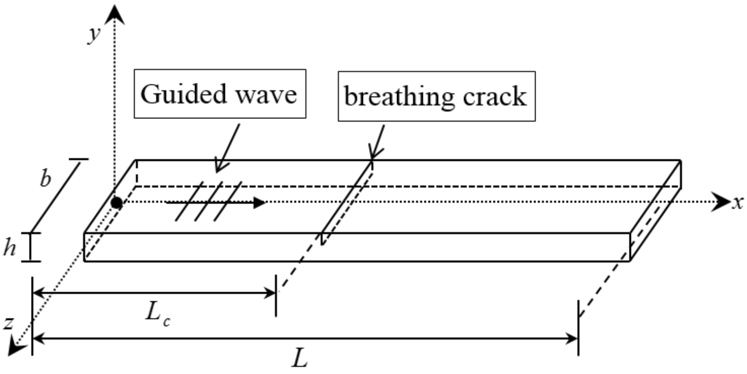

Fig. 5.3 Schematic diagram of a beam with a surface breathing crack.

The excitation signal is a f_0 = 25 kHz, narrow-band, 5-cycle sinusoidal tone burst modulated by a Hanning window (Aryan et al., 2016c). Using this frequency is to ensure that only the fundamental guided wave modes (e.g. A_0 and S_0) are generated in both the fundamental and higher harmonic frequencies. The excitation signal was induced by applying a boundary displacement in the in-plane and out-of-plane directions of the SFE node at the beam's left end (x = 0 m) to generate the S_0 and A_0 incident guided waves, respectively. According to the dispersion relation predicted by the SFE model in Figure 5.4, only the S_0 and A_0 incident guided waves are generated. The nodal velocity is calculated at x = 0 m, which is the same location as the excitation. The calculated velocity is normalised by the maximum amplitude of incident wave velocity. The calculated duration is long enough to cover the incident guided wave propagates from the excitation to the right beam end, and back to the measurement location. The damping coefficient η is chosen to be 550 s^{-1} (He and Ng, 2017). Eight GLL nodes in each SFE beam element are used in the model. The time step for solving the dynamic Equation (5.1) is 0.25×10^{-7} s.

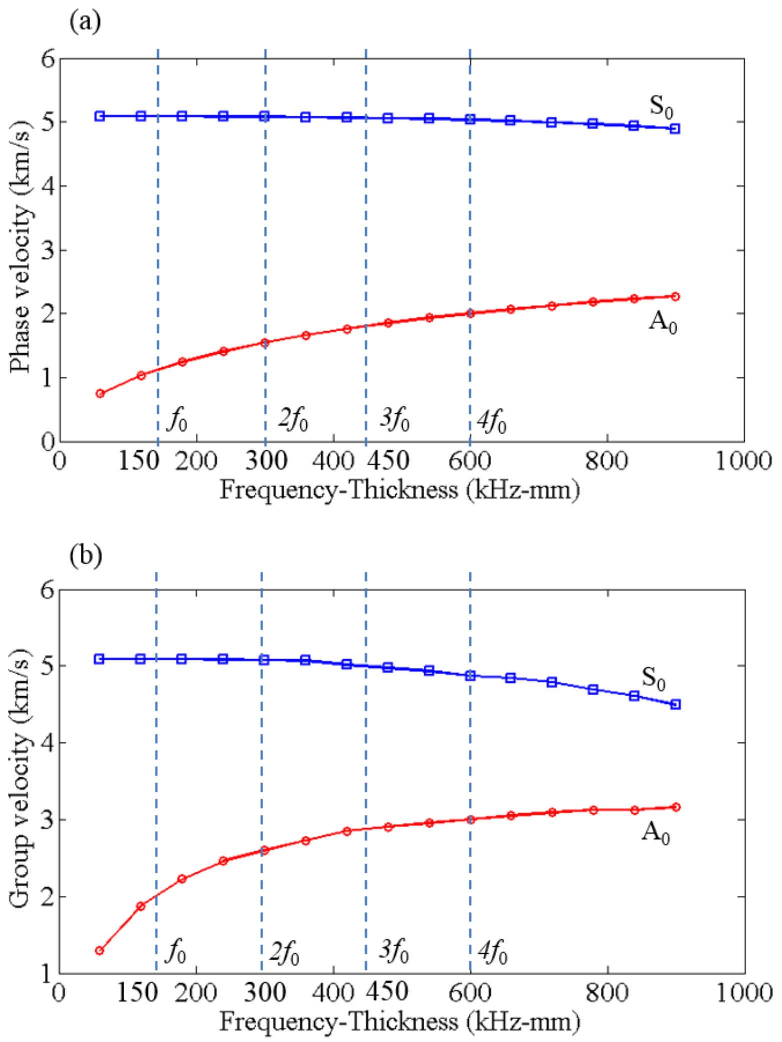

Fig. 5.4 Dispersion relations for an aluminium beam predicted by the SFE model (a) Phase velocity; (b) Group velocity.

For the 3D FE model, commercial FE software, ABAQUS v6.12-1, is used to simulate the guided waves in the beam. Eight-node 3D incompatible modes solid brick elements (C3D8I) are employed to model the cracked beam and the second-order accuracy is enabled in the modelling. The S_0 and A_0 incident guided wave are generated by applying the excitation signal as a surface traction in in-plane and out-of-plane direction, respectively, at the vertical surface of the beam's left end. The mesh size of the FE element is 0.4mm×0.4mm×0.4mm to ensure the stability of the simulations. The dynamic problem is solved by explicit solver, ABAQUS/Explicit. The time step in the FE simulation is automatically controlled by ABAQUS/Explicit. The breathing crack is modelled by duplicating the nodes at the crack surfaces and the ‘frictionless hard contact’ property is assigned to the crack surfaces, which allows the simulation of the contact nonlinearity when guided waves interact with the crack.

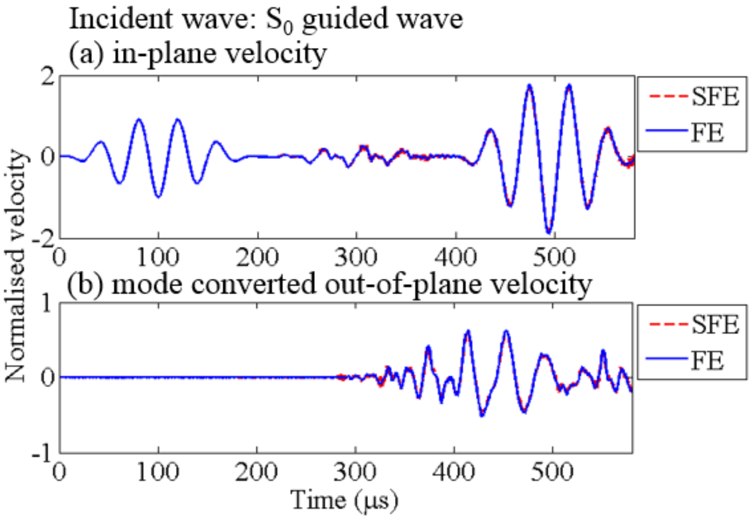

Fig. 5.5 Time-domain (a) in-plane and (b) mode-converted out-of-plane velocity at $x = 0$ m for incident S_0 guided wave.

The comparison of the SFE and explicit 3D FE simulated results are shown in Figures 5.5 to 5.6, where S_0 guided wave is used as the incident wave first. Figures 5.5a and 5.5b show the in-plane and out-of-plane velocity in time-domain. The signals are normalized such that the maximum amplitude of S_0 incident wave package is unity. For the incident S_0 guided wave, there is good agreement between signals calculated by the time-domain SFE method and the explicit 3D FE method in the arrival time, amplitude of in-plane velocity (S_0 guided wave), the mode-converted out-of-plane velocity (mode-converted A_0 guided wave) and the signal distortion due to the contact nonlinearity at the crack. The corresponding normalized spectral amplitudes of the Fourier-transformed time-domain velocity are shown in Figures 5.6a and 5.6b, respectively. There is good agreement between the results of the Fourier-transformed velocity responses calculated using SFE and explicit 3D FE methods at the excitation frequency and higher harmonic frequencies. Comparing Figures 5.6a and 5.6b, it indicates that the energy of higher harmonics generated due to the interaction of the S_0 incident guided wave with the crack is mainly concentrated in the mode-converted A_0 nonlinear guided waves.

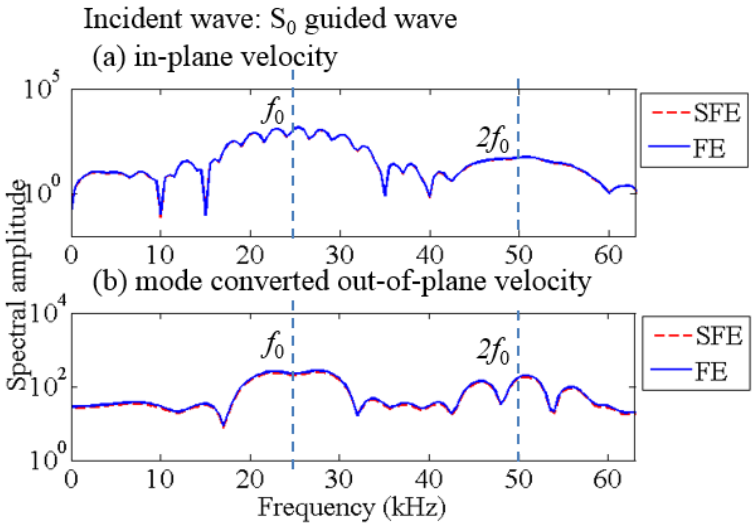

Fig. 5.6 Fourier-transformed (a) in-plane and (b) mode-converted out-of-plane velocity at $x = 0$ m for incident S_0 guided wave.

Figures 5.7 and 5.8 show the time domain velocity response and the corresponding spectral amplitude when the incident wave is the A_0 guided wave. Similar to the incident S_0 guided wave, there is good agreement between the time-domain SFE and explicit 3D FE simulations. However, there is a slight difference in the out-of-plane velocity responses as shown in Figure 5.8a. The very small discrepancy shown in Figure 5.8a is mainly due to the one-dimensional (1D) assumption in the time-domain SFE but the FE simulations are in 3D, and the limitation of the first order beam theory used in the SFE beam formulation. Comparing Figure 5.8 with Figure 5.6, it shows that the energy of the higher harmonics in the mode-converted S_0 guided wave, which is induced by the crack-wave interaction using the A_0 incident guided wave, is much less than that in the mode-converted A_0 guided wave when the incident wave is the S_0 guided wave.

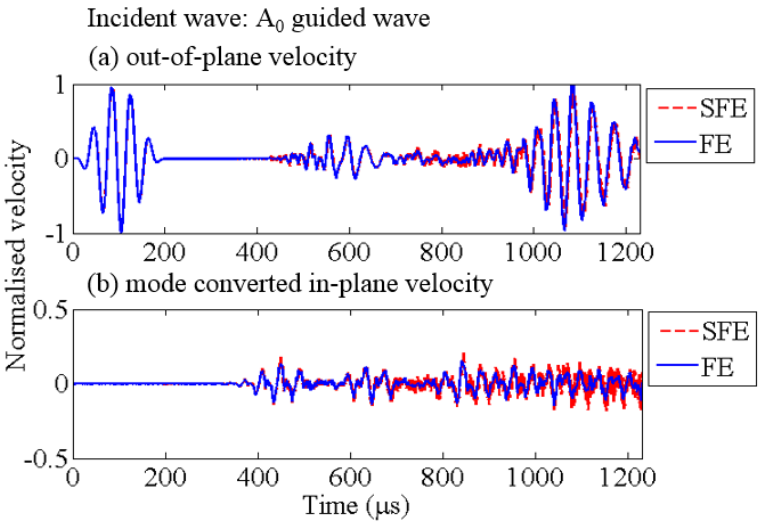

Fig. 5.7 Time-domain (a) out-of-plane and (b) mode-converted in-plane velocity at x = 0 m for incident A_0 guided wave.

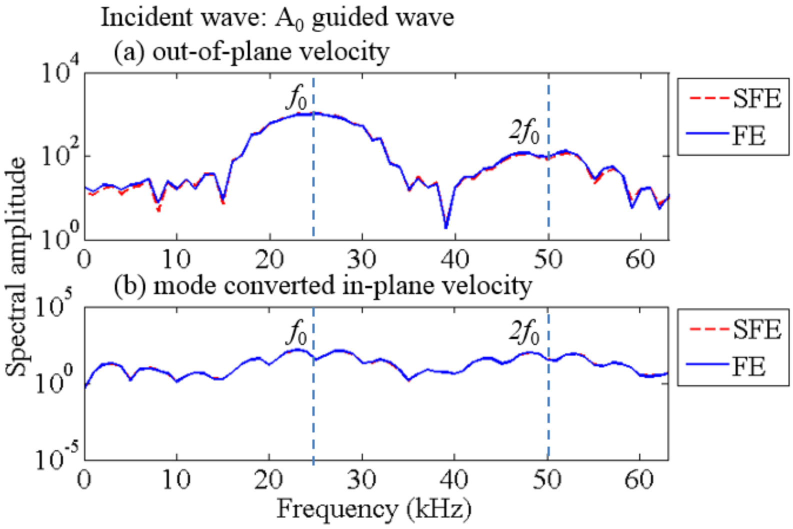

Fig. 5.8 Fourier-transformed (a) out-of-plane and (b) mode-converted in-plane velocity at x = 0 m for incident A_0 guided wave.

The results in Figures 5.5 – 5.8 show reasonably good agreement, including the generated higher harmonics due to contact nonlinearity at the breathing crack. Therefore, the proposed time-domain SFE model is able to simulate the nonlinear guided wave induced due to contact nonlinearity and the mode-conversion effect accurately.

5.4 Higher harmonics generation due to contact nonlinearity at breathing crack

The generation of higher harmonics is studied in this section using the time-domain SFE method. An aluminium beam is modelled, which has the same cross-section and material properties as the aluminium beam used in Section 5.3. Two scenarios, S_0 and A_0 incident guided waves, are considered separately. The length L of the beam, the crack locations L_c and the measured locations are different in these two scenarios, and they are summarised in Table 5.2. For each scenario, we investigate three different cases considering different effects of the contact nonlinearity and mode-conversion. The excitation signal is an f_0 = 25 kHz, narrow-band, 5-cycle sinusoidal tone burst modulated by a Hanning window, and it is applied as a force at the left end of the beam.

Table 5.2 Summary of case studies for higher harmonic generation due to contact nonlinearity at crack.

Incident guided wave	S_0				A_0			
Damage cases	S1	S2	S3	S4	A1	A2	A3	A4
Beam length L (m)	6				3			
Crack location L_c (m)	1.9				0.95			
Crack depth d_c (m)	0.003							
Measured location (m)	$x = 5$				$x = 1.65$			
Contact nonlinearity effect	No	Yes	Yes	No	No	Yes	Yes	No
Mode conversion effect	No	No	Yes	Yes	No	No	Yes	Yes

5.4.1 Incident S_0 guided wave

The incident S_0 guided wave is excited by applying the in-plane external force to the left end of the beam. The in-plane response is investigated in subsection 5.4.1.1 and the mode-converted out-of-plane response is studied in subsection 5.4.1.2.

5.4.1.1 In-plane response

In this subsection the excitation is applied in the in-plane direction to generate the incident S_0 guided wave. Four different cases, S1, S2, S3 and S4, as shown in Table 2, are considered in studying the generation of higher harmonics due to the S_0 guided wave's interaction with the breathing crack. Case S1 does not simulate the contact nonlinearity and mode-conversion effect at the breathing crack. The mode conversion effect is not considered by removing the coupling terms e.g., g_{12} and g_{13} in Equation (5.17) in the SFE crack element. Case S2 only simulates the contact nonlinearity effect by utilising the bilinear crack model. Case S3 simulates both contact nonlinearity and the mode-conversion effect. Case S4 considers only the mode conversion effect without the contact nonlinearity.

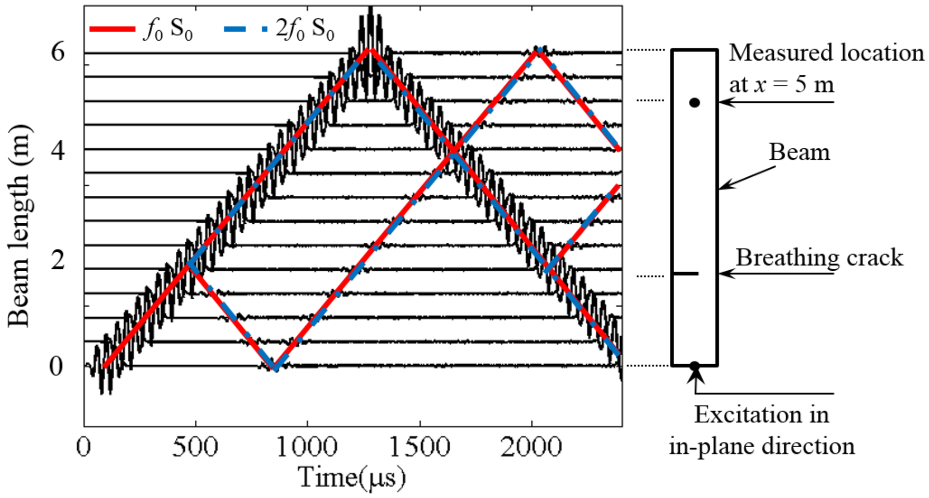

Fig. 5.9 In-plane velocity of S_0 guided wave time histories at different locations along the beam for Case S3.

The S_0 guided wave propagation is studied first. Figure 5.9 shows the in-plane velocity time histories at different locations along the beam for Case S3, in which both contact nonlinearity and the mode-conversion effect are considered. It should be noted that Figure 5.9 only shows the in-plane velocity, where only the linear and second harmonic S_0 guided waves are visualized in the time histories. Figure 5.9 shows that when the incident S_0 guided wave (indicated by the solid red lines) encounters the breathing crack, it separates into two wave packages: transmitted waves and reflected waves. The second harmonic guided wave, indicated by the blue dashed line at the frequency $2f_0$, which occurred induced due to the contact nonlinearity effect, is not observed from the in-plane velocity in the time-domain. This is because the linear (f_0) and the second harmonic ($2f_0$) S_0 guided waves have very similar group velocities as shown in Figure 5.4. As a result, they mix together during the wave propagation.

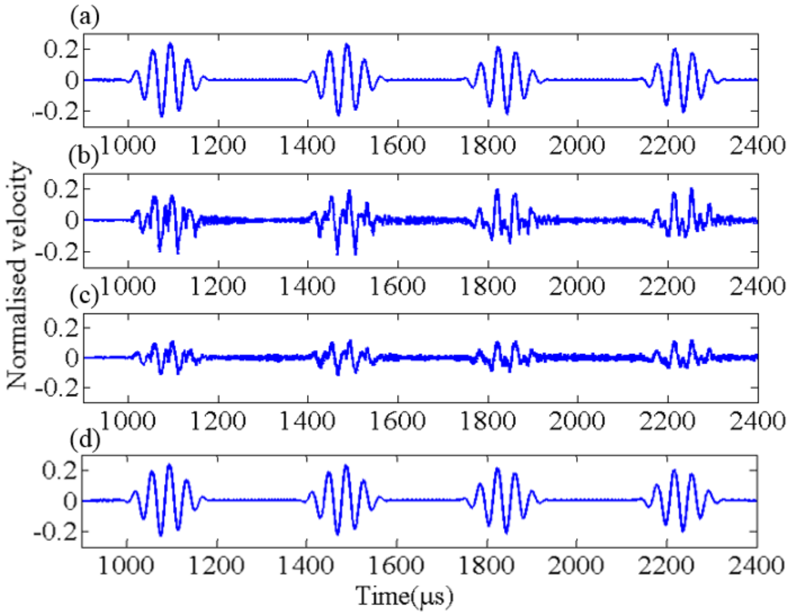

Fig. 5.10 Extracted time-domain in-plane velocity signal from 900 - 2400 μs at x = 5 m for (a) Cases S1, (b) S2, (c) S3 and (d) S4.

In order to investigate the higher harmonics induced by the contact nonlinearity at the breathing crack, the energy density spectrum for each damage case is calculated using the Gabor wavelet transform (Ng, 2014a, Ng et al., 2009). The baseline subtraction technique (Ng et al., 2009) is used to extract the scattered wave signals from the breathing crack, i.e. the linear scattered S_0 guided waves and the nonlinear S_0 guided waves. The S_0 guided wave signal is measured at x = 5 m and the baseline data is obtained from an intact SFE beam. The extracted wave signals for Cases S1-S4 are shown in Figure 5.10. Figure 5.10 shows that the time-domain response is plotted from

900 to 2400 μs because there is no extracted guided wave signal before 900 μs, where each of the wave packages can be identified using Figure 5.9. Note that resulting from the similar group velocity of S_0 guided wave for each harmonic shown Figure 5.4, each guided wave package contains both the fundamental and second harmonics if considering the contact nonlinearity effect.

Figures 5.10a considers no contact nonlinearity and mode-conversion effect. Each guided wave package has the largest amplitude compared with other cases. Comparing Figures 5.10b and 5.10d, it is shown that when the mode conversion effect is considered alone, the amplitude of each guided wave package decreases less than that only considering the contact nonlinearity. While in Figure 5.10(c), where both the contact nonlinearity and mode conversion effect are considered, the amplitude of each guided wave package becomes the smallest compared with other cases.

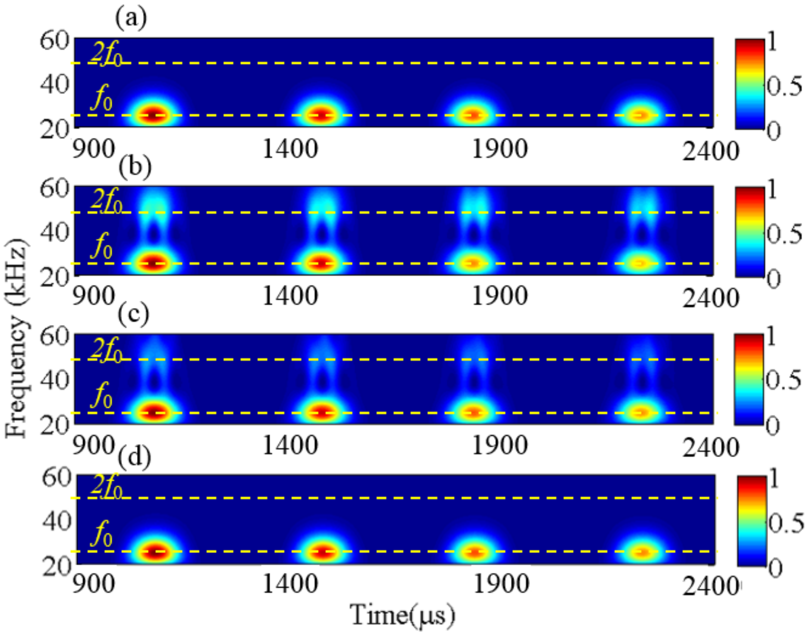

Fig. 5.11 Energy density spectrum of the in-plane velocity signal from 900 - 2400 μs at measurement location x = 5 m for (a) Cases S1, (b) S2, (c) S3 and (d) S4.

The corresponding energy density spectra are shown in Figure 5.11. It should be noted that the magnitude of the energy density spectrum is normalized to 1 for the first wave package of the extracted signal of the transmitted guided wave. Figure 5.11a shows the energy density spectrum of Case S1, in which the contact nonlinearity and mode-conversion effect are not considered. Hence, the energy of the extracted wave signals concentrates at the excitation frequency (f_0 = 25 kHz) and no higher harmonics are generated.

Case S2 considered the contact nonlinearity effect. As shown in Figure 5.11b, the second harmonic at the frequency $2f_0$ = 50 kHz is observed in the energy density spectrum. This shows that the nonlinear S_0 guided wave is generated due to the contact nonlinearity effect.

Case S3 in Figure 5.11c considers both the contact nonlinearity and mode-conversion effect. The energy at the second harmonic frequency ($2f_0$ = 50 kHz) is weaker compared to that in Case S2. This indicates that part of the energy of the S_0 nonlinear guided wave is converted to the A_0 nonlinear guided wave due to the mode-conversion effect. However, the linear components of the energy spectrum are similar to Figure 5.11b. This is because the spectral amplitude of the higher harmonic is very small compared to the linear component, and the energy spectrum has linear relation to the square of the spectral amplitude, this results a small change to the linear component than the higher harmonic in the energy spectrum in Figure 5.11c.

Case S4, as shown in Figure 5.11d, considers only the mode conversion effect without the contact nonlinearity. It is shown that the energy spectrum at the frequency f_0 of each guided wave package is slightly less than that in Figure 5.11a. Also, no higher harmonics are generated. The results of the out-of-plane velocity, i.e. the A_0 linear and nonlinear guided waves are presented in the next sub-section.

5.4.1.2 Mode-converted out-of-plane response

The mode-converted out-of-plane velocity at different locations along the SFE beam for Case S3 is shown in Figure 5.12, in which both the contact nonlinearity and the mode-conversion effect are considered in the simulation. As shown in Figure 5.12, the mode-converted S_0-A_0 guided waves (i.e., A_0 guided waves converted from S_0 incident-guided waves) are generated when the S_0 incident-guided wave interacts with the crack. Due to the contact nonlinearity effect, higher harmonics with frequencies at f_0, $2f_0$, $3f_0$ and $4f_0$, are generated in the out-of-plane velocity. These mode-converted A_0 higher harmonic guided waves propagate at different velocities, in which the first harmonic has the lowest group velocity, while the fourth harmonic has the highest group velocity. As shown in Figure 5.12, the S_0-A_0 guided waves at frequency f_0, $2f_0$, $3f_0$ and $4f_0$ are denoted by a solid red line, a dash-dot blue line, a dashed blue line and a dotted red line, respectively. This shows that the mode-conversion effect induces not only the linear mode-converted waves but also the nonlinear mode-converted guided waves due to the contact nonlinearity at the asymmetrical breathing crack.

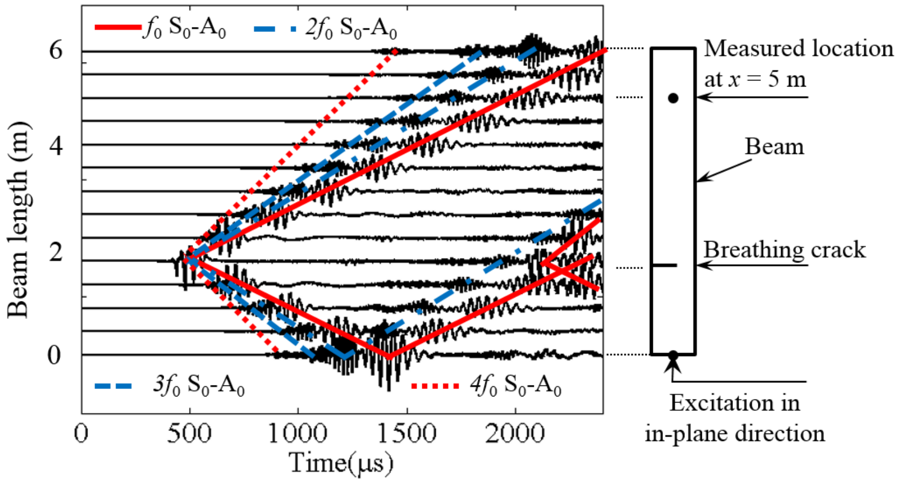

Fig. 5.12 Out-of-plane velocity of mode-converted S_0-A_0 guided wave time histories at different locations along the beam for Case S3 (the normalised amplitude is amplified by a factor of 3.

The energy density spectrum of the mode-converted A_0 guided wave measured at $x = 5$ m is shown in Figure 5.13. There are four wave packages as shown in Figure 5.13a, and the corresponding energy density spectrum of the first (f_0) and the second ($2f_0$) harmonics are shown in Figure 5.13b. The energy of the third ($3f_0$) and the fourth ($4f_0$) harmonics are too small to be shown after the normalisation. Hence, the energy density spectrum only shows the first and the second harmonics. The results in Figure 5.13 successfully demonstrate mode-converted A_0 higher harmonic guided waves generated as a result of the contact nonlinearity effect.

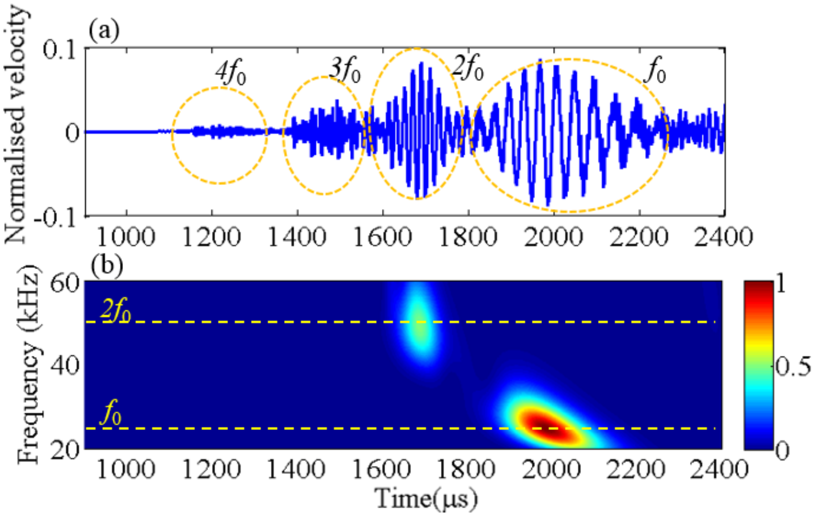

Fig. 5.13 Time history and energy density spectrum of the out-of-plane velocity signal from 900 - 2400 μs at measurement location $x = 5$ m for Cases S3.

5.4.2 Incident A_0 guided wave

The incident A_0 guided wave is excited by applying the out-of-plane external force to the left end of the beam. The out-of-plane response is investigated in subsection 5.4.2.1 and the mode-converted in-plane response is studied in subsection 5.4.2.2.

5.4.2.1 Out-of-plane response

This subsection investigates the nonlinear guided wave generated due to the interaction of the A_0 guided wave with the breathing crack. The calculated time histories at different locations along the beam for Case A3, in which both contact nonlinearity and mode-conversion effect are considered, are shown in Figure 5.14. When an $f_0 = 25$ kHz incident A_0 guided wave encounters the crack, a linear reflected wave and a linear transmitted wave ($f_0 = 25$ kHz) occur, which are indicated by solid red lines in Figure 5.14. Due to the contact nonlinearity, the higher harmonic A_0 guided waves ($2f_0 = 50$ kHz) are also generated. They propagate in forward and backward directions from the crack, and they are indicated by dashed blue lines. Because of the dispersive nature of the low frequency A_0 guided waves, the A_0 guided waves at f_0 and $2f_0$ frequency propagate at different group velocities. Since the crack is asymmetric, the S_0 guided wave is also converted from the incident A_0 guided wave. It is not shown in the Figure 5.14, however, because only the out-of-plane velocity is shown. When the mode-converted S_0 guided wave interacts with the asymmetrical crack, it induces the mode-converted A_0 guided wave, i.e. A_0-S_0-A_0 guided waves. The A_0-S_0-A_0 guided waves at f_0 and $2f_0$ frequency are indicated by the dotted red line and dashed-dotted blue line, respectively.

Figures 5.15a, 5.15b, 5.15c and 5.15d show the out-of-plane velocity time history at measurement location $x = 1.65$ m for Cases A1, A2, A3 and A4, respectively. The scattered wave is extracted using a baseline subtraction technique (Ng et al., 2009). Figure 5.16 shows the corresponding energy density spectrum of the time histories depicted in Figure 5.15. The energy density spectrum is used to investigate the influence of the contact nonlinearity and mode-conversion effect. The magnitude of the energy density spectrum is normalised to 1 for the extracted, transmitted guided wave package, i.e., GW-1 shown in Figure 5.15a. Figure 5.16 only shows the magnitude in the range from 0 to 0.2 for the normalised energy density spectrum.

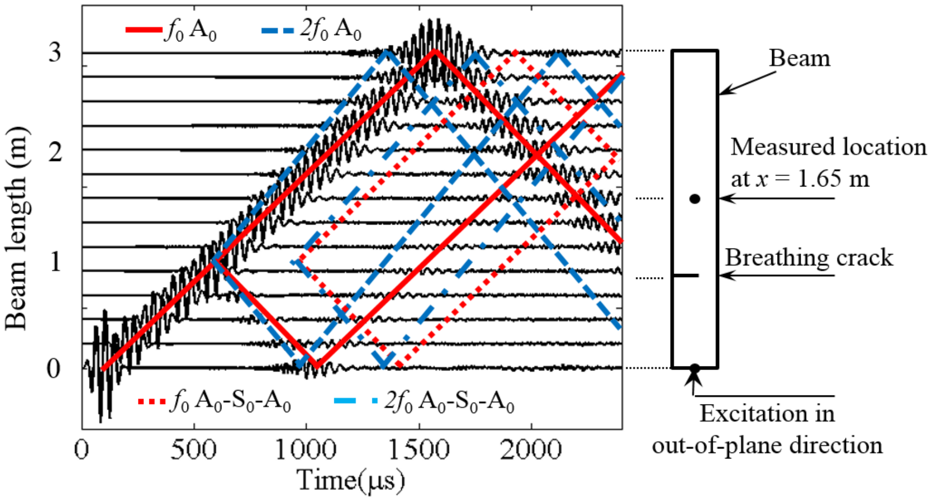

Fig. 5.14 Out-of-plane velocity of A_0 guided wave and mode-converted A_0-S_0-A_0 guided wave time histories at different locations along the beam for Case A3.

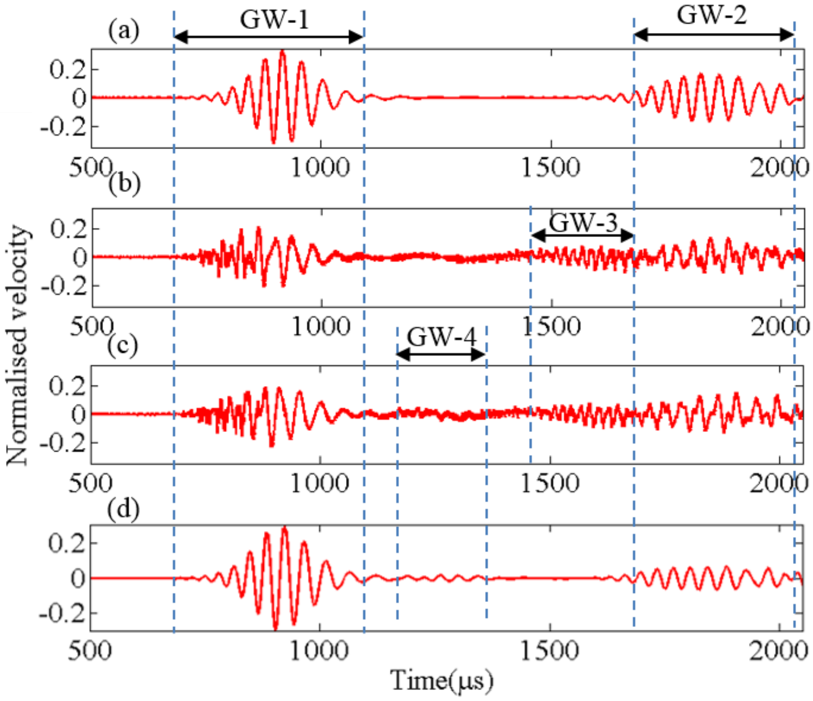

Fig. 5.15 Extracted time-domain out-of-plane velocity signal from 500 - 2100 μs at x = 1.65 m for (a) Cases A1, (b) A2, (c) A3 and (d) A4.

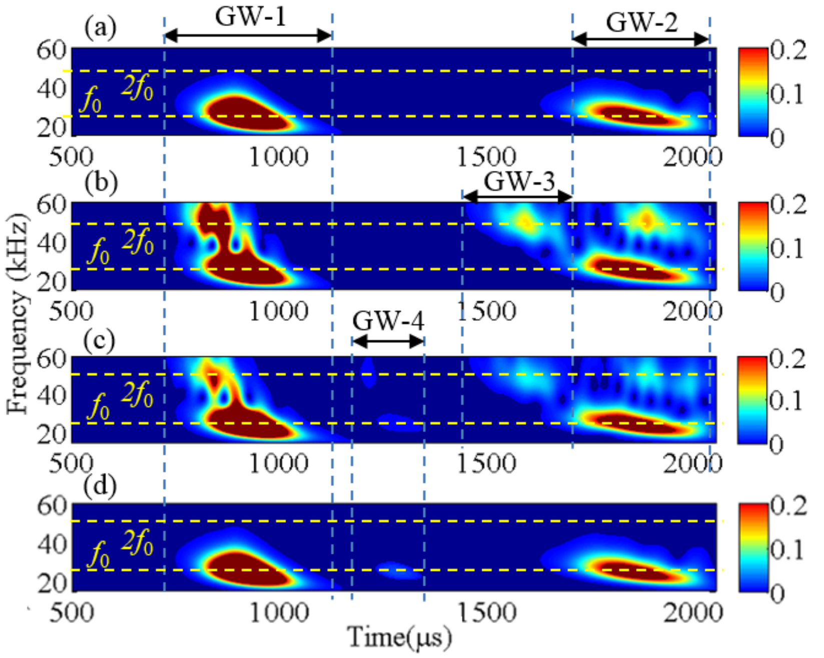

Fig. 5.16 Energy density spectrum of the out-of-plane velocity signal from 500 - 2100 μs at measurement location x = 1.65 m for (a) Cases A1, (b) A2, (c) A3 and (d) A4.

For Case A1 no contact nonlinearity or mode-conversion effects are considered. There are only two guided wave packages: the forward scattered wave passing through the crack, and its reflection from the right beam end, which are labelled as GW-1 and GW-2 in Figure 5.15a, respectively. The corresponding energy density spectrum shown in Figure 5.16a indicates that there is no higher harmonic. In contrast, the results from Case A2, in which the contact nonlinearity effect is considered, indicate the existence of higher harmonic guided waves in Figure 5.16b. In that figure, guided wave packages, GW-1 and GW-2, contain signals at two different frequencies: the excitation frequency f_0 and the second harmonic frequency $2f_0$, respectively. For GW-3, it only has signal at the second harmonic $2f_0$. Case A3 considers both contact nonlinearity and the mode-conversion effect. In addition to GW-1, GW-2 and GW-3, a guided wave package GW-4 is observed in Figure 5.16c. GW-4 contains the mode-converted A_0-S_0-A_0 guided waves at the excitation frequency f_0 and at the second harmonic frequency $2f_0$. They are induced by the contact nonlinearity and mode-conversion effect at the asymmetric crack.

In Case A4, the contact nonlinearity is removed and only the mode-conversion effect is considered in the simulation. The guided wave package GW-3 caused by contact nonlinearity is disappeared in Figure 5.15d. The guided wave packages GW-1 and GW-2 and GW-4 only contain the linear component as shown in the energy spectrum in Figure 5.16d.

5.4.2.2 Mode-converted in-plane response

Figure 5.17 shows the propagation of the mode-converted A_0-S_0 guided waves. The amplitude is increased by a coefficient of 5. The mode-converted A_0-S_0 guided wave is generated at the moment when the incident A_0 guided wave encountered the asymmetrical crack. Due to the contact nonlinearity effect, both mode-converted A_0-S_0 guided waves at f_0 and $2f_0$ are generated. The solid red line and dash-dot blue line indicate the f_0 and $2f_0$ mode-converted A_0-S_0 guided waves, respectively. As they have similar group velocities, they are mixed together in the time-domain. The reflected, mode-converted A_0-S_0 guided waves are then reflected from the beam’s left end. These waves propagate forwards and encounter the breathing crack. They then generate the mode-converted A_0-S_0-A_0 guided waves observed in Figure 5.14 (dotted red line for the linear A_0-S_0-A_0 guided waves and dashed-dotted blue line for the second harmonic A_0-S_0-A_0 guided waves).

The velocity time history and the corresponding energy density spectrum of the mode-converted A_0-S_0 guided waves at the measurement location $x = 1.65$ m for Case A3 are shown in Figures 5.18a and 5.18b, respectively. The mode-converted A_0-S_0 guided waves at frequencies f_0 and $2f_0$ are mixed together in the time-domain as they have similar group velocities. This is consistent with the energy density spectrum as the energy for each guided wave package in Figure 5.18b is centred at both the f_0 and $2f_0$ frequencies. In addition, by comparing the energy density spectrum in Figure 18b with that in Figure 16c, we can see that the mode-converted A_0-S_0 higher harmonic guided waves are easier to observe as they have larger magnitudes.

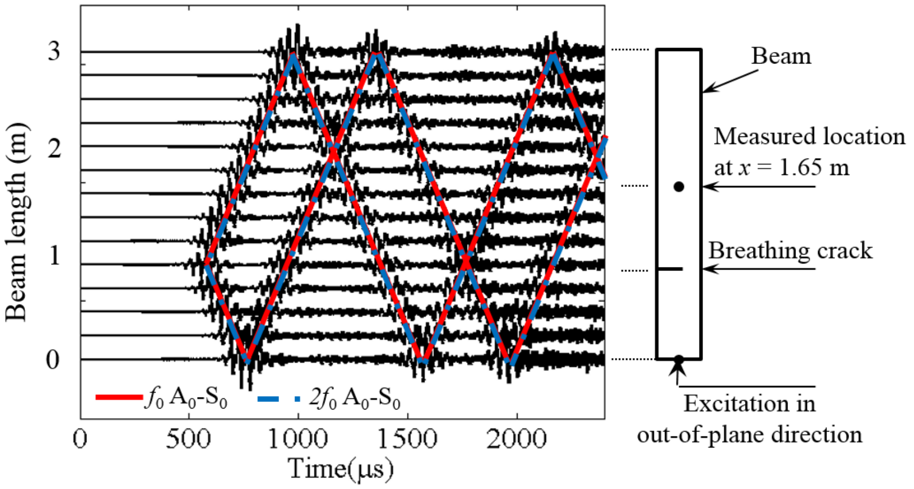

Fig. 5.17 In-plane velocity of mode-converted A$_0$-S$_0$ guided wave time histories at different locations along the beam for Case A3 (the normalised amplitude is amplified by a factor of 5).

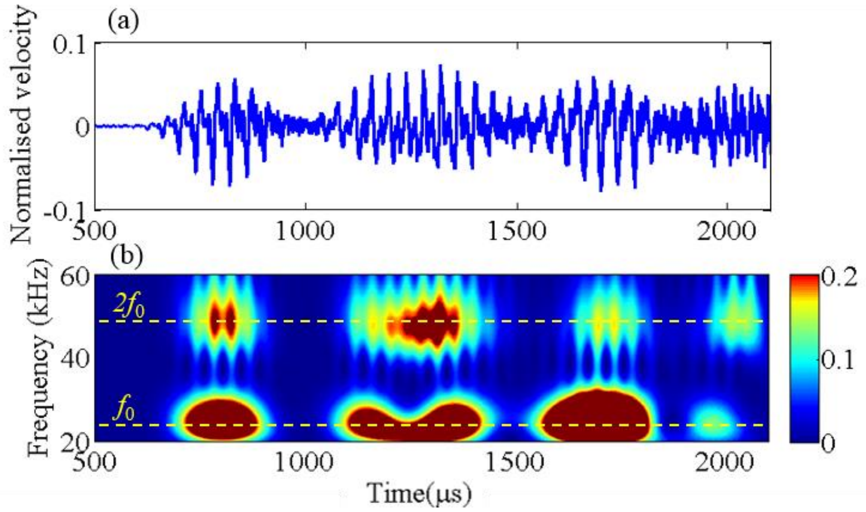

Fig. 5.18 Energy density spectrum of the in-plane velocity signal from 500 - 2100 μs at measurement location x = 1.65 m for Cases A3.

5.5 Parametric studies

This section investigates the characteristics of incident guided waves and mode-converted higher harmonic guided waves for different crack depths. In each study, the excitation force was an f_0 = 25 kHz, narrow-band, 5-cycle sinusoidal tone burst modulated by a Hanning window. The excitation is applied in both in-plane and out-of-plane directions to generate the S_0 and A_0 guided waves, respectively. The length of the aluminium beam is 1 m and the crack location is x = 0.5 m. The baseline subtraction technique (Ng et al., 2009) is used in the study to extract the scattered wave signals from the breathing crack. The signal is calculated at both ends of the beam to capture both the forward and backward scattered guided wave signals. The measurement duration covers the incident guided wave propagating to the beam end and reflecting back to the measurement location.

5.5.1 Incident S_0 guided wave

The first parametric study investigates the spectral amplitudes at the excitation frequency and each higher harmonic frequency as a function of crack depth when the incident wave is S_0 guided wave. Without loss of generality, the crack depth to beam height ratio (d_c/h) is used to present the results. A comparison of the Fourier-transformed in-plane velocity (S_0 guided wave) and mode-converted out-of-plane velocity (A_0 guided wave) is shown in Figure 5.19 for the backward crack-scattered guided wave and Figure 5.20 for the forward crack-scattered guided wave. It should be noted that the spectral amplitudes of the S_0 and mode-converted A_0 guided waves are normalised to the incident S_0 guided wave magnitude at f_0 =25 kHz.

Comparing Figure 5.19 with Figure 5.20, we can see that the FFTs of the backward and forward scattered guided wave signals from the crack are almost identical when using S_0 incident guided waves. Specifically, the spectral amplitudes at f_0 and $2f_0$ of the in-plane velocity, as shown in Figures 5.19(a) and 5.20(a), increase with the crack depth to beam height ratio d_c/h. We found that the spectral amplitude at f_0 increases sharply with d_c/h while that at $2f_0$ increases slowly and stably. We can see that the normalised spectral amplitude of the in-plane velocity at $2f_0$ is comparable to that at f_0 when d_c/h is less than 0.3. This indicates that the nonlinear in-plane response is very sensitive to small cracks when using S_0 incident guided waves.

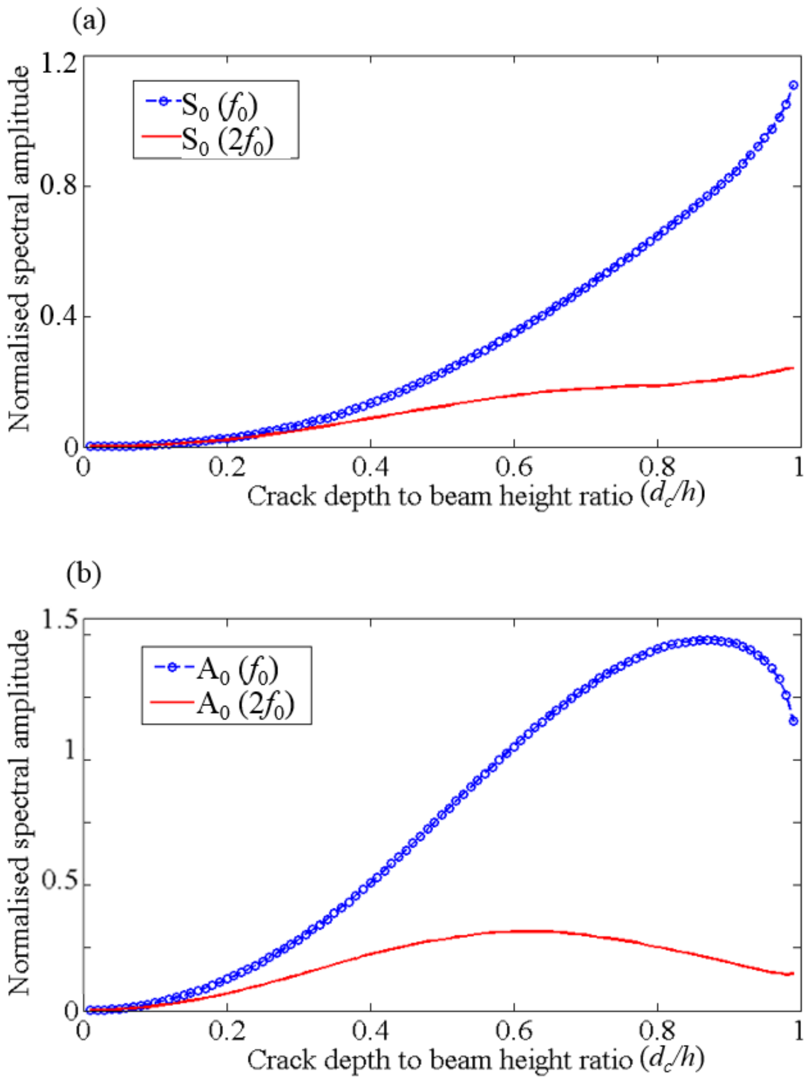

Fig. 5.19 Fourier transformed (a) in-plane and (b) mode-converted out-of-plane velocity as a function of crack depth to beam height ratio (d_c/h) at measurement location $x = 0$ m when the incident wave is S_0 guided wave.

The spectral amplitudes of the mode-converted out-of-plane A_0 guided waves are shown in Figures 5.19(b) and 5.20(b). We can see that the normalised spectral amplitude of the fundamental harmonic (f_0) increases significantly with d_c/h and reaches its maximum at around 1.2 at $d_c/h = 0.87$. Then it decreases to 0.9 at $d_c/h = 0.99$. The normalised spectral amplitude of the second harmonic (at $2f_0$) begins to increase slowly with d_c/h. It reaches the maximal value just below 0.3 when $d_c/h = 0.65$. Later, it starts to decrease stably with d_c/h and finally reaches 0.13. Overall, the amplitude of the second harmonic is small when compared with the linear signal in the mode-converted out-of-plane velocity.

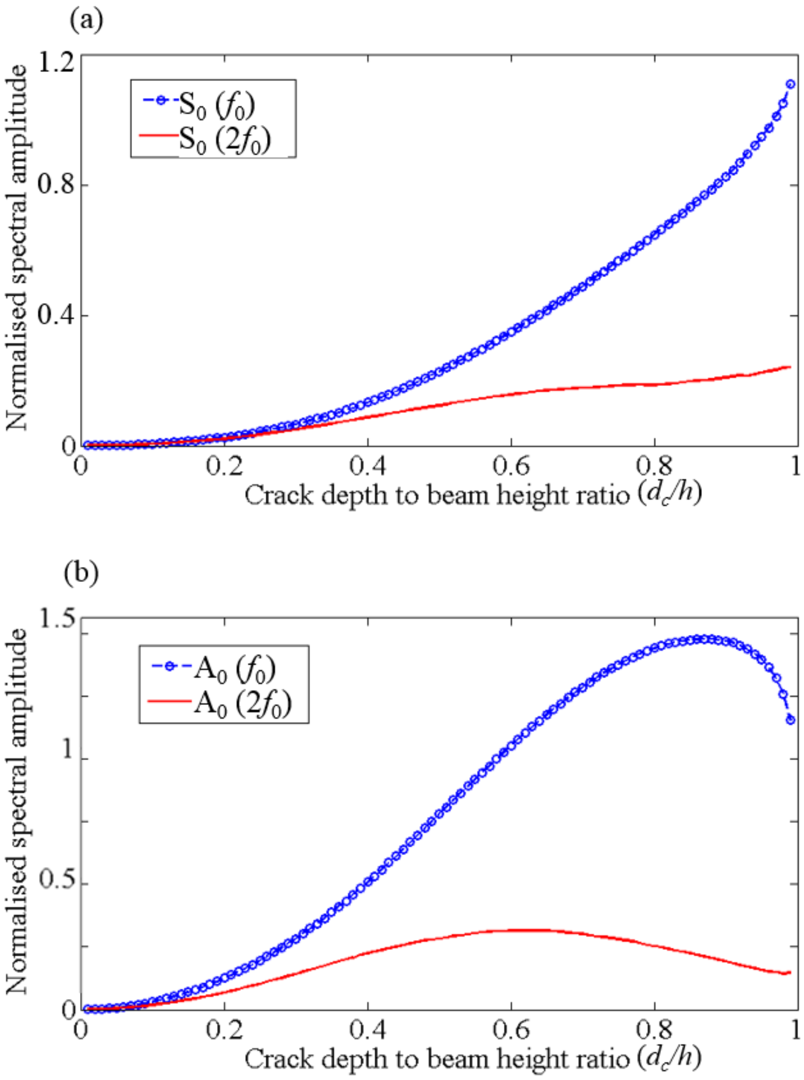

Fig. 5.20 Fourier transformed (a) in-plane and (b) mode-converted out-of-plane velocity as a function of crack depth to beam height ratio (d_c/h) at measurement location x = 1 m when the incident wave is S_0 guided wave.

Comparing Figures 5.19(a) and 5.20(a) with Figures 5.19(b) and 5.20(b), the results show that the normalised spectral amplitude of the second harmonic (at $2f_0$) of the mode-converted A_0 guided waves are generally larger than the S_0 guided waves when the crack is small (i.e., d_c/h < 0.65). As the crack continues to grow (i.e., d_c/h > 0.75), the normalised spectral amplitude of the second harmonic ($2f_0$) of the mode-converted A_0 becomes smaller than that of the S_0 guided wave signal. This indicates that the second harmonic of the mode-converted out-of-plane A_0 guided wave is more sensitive than the in-plane S_0 guided wave in detecting smaller cracks when the incident wave is the S_0 guided wave.

5.5.2 Incident A_0 guided wave

The second parametric study examines the A_0 guided wave excited in the aluminium beam. The Fourier-transformed out-of-plane (A_0 guided wave) and in-plane (S_0 guided wave) velocities are shown in Figures 5.21 and 5.22. The spectral amplitudes are normalised to the maximal spectral amplitude of the A_0 incident wave at f_0 =25 kHz. Figure 5.21(a) shows the FFT out-of-plane velocity of the backward scattered guided wave induced by the crack. The normalised spectral amplitude of the fundamental harmonic (f_0) increases significantly from 0 to just below 0.4 at d_c/h = 0.65. Then it decreases sharply with the crack growth, to around 0.05 when $d_c/h = 0.99$. This pattern is different to that using the S_0 incident guided wave in Figure 5.19(a) due to the difference of the mode-shape between S_0 and A_0 guided waves (Lowe et al., 2002). In contrast, the normalised spectral amplitude of the second harmonic ($2f_0$) increases slowly from 0 to 0.11 at $d_c/h = 0.55$, while it decreases to 0.8 when $d_c/h = 0.85$. After that, it increases suddenly to 0.35 at $d_c/h = 0.99$.

On the other hand, Figure 5.22(a) illustrates the FFT out-of-plane velocity of the forward scattered A_0 guided wave induced by the crack. The normalised spectral amplitude of the fundamental harmonic (f_0) increases with d_c/h. When d_c/h < 0.65, it increases significantly from 0 to around 0.5. When 0.65 < d_c/h < 0.9, it slowly increases from 0.5 to 0.6. After d_c/h > 0.9, the amplitude increases dramatically to just below 1. In comparison, the spectral amplitude of the second harmonic of the forward scattered guided wave has a similar trend to the backward scattered guided wave as shown in Figure 5.21. The amplitude of the second harmonic forward scattered guided wave is larger than the backward scattered guided wave. As shown in Figure 5.22(a), the second harmonic has the first peak at d_c/h = 0.55 with a normalised amplitude around 0.18, then it reduces to 0.15 at d_c/h = 0.85. Finally, it increases to around 0.6 when d_c/h = 0.99.

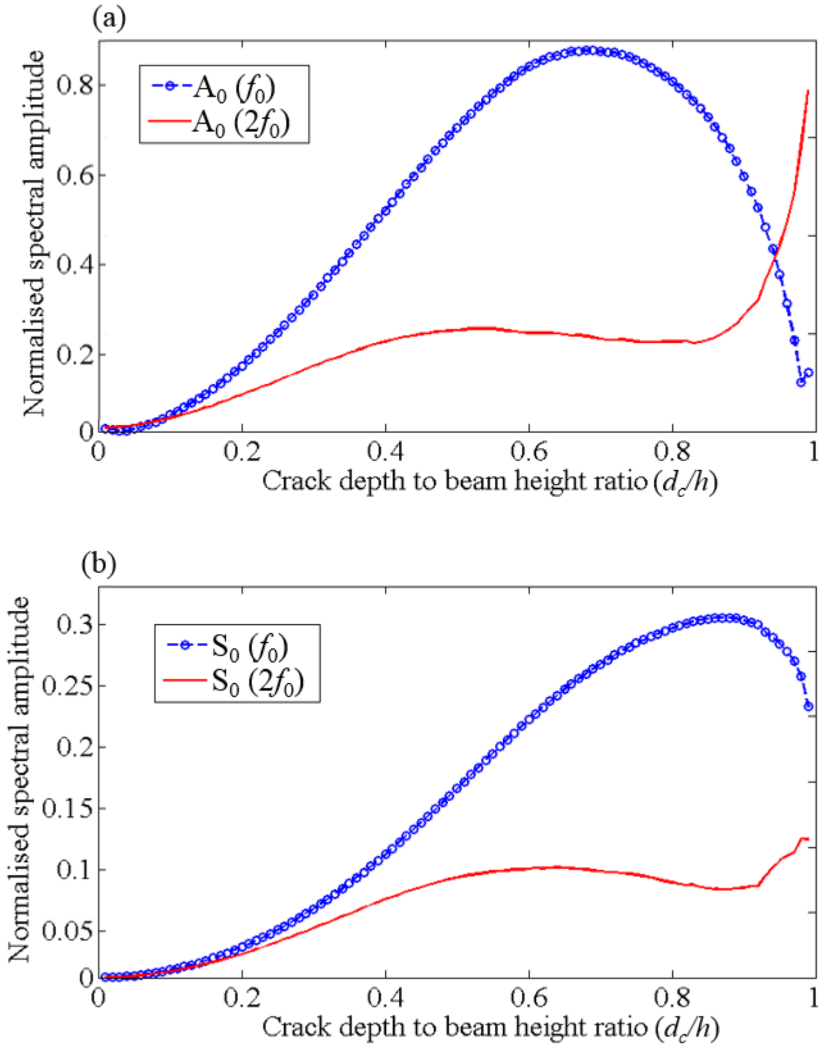

Fig. 5.21 Fourier transformed (a) out-of-plane and (b) mode-converted in-plane velocity as a function of crack depth to beam height ratio (d_c/h) at measurement location x = 0 m when the incident wave is A_0 guided wave.

Figures 5.21(b) and 5.22(b) show the normalised spectral amplitude of the mode-converted S_0 guided wave (in-plane velocity), which are almost identical. We can see that the normalised spectral amplitude of the mode-converted fundamental harmonic increases with the crack growth, and peaks at d_c/h = 0.9 with the value 0.28. After that, it decreases to just above 0.2 at

$d_c/h = 0.99$. The amplitude of the second harmonic increases slowly to around 0.08 at $d_c/h = 0.65$, then it decreases slightly to 0.07 at $d_c/h = 0.9$. After that, it increases again to 0.11 at $d_c/h = 0.99$.

Comparing Figure 5.21 with Figure 5.22, it is shown that the energy of the reflected out-of-plane linear guided wave decreases from $d_c/h = 0.65$, while that of the transmitted out-of-plane guided wave increases. This indicates that the energy of the reflected out-of-plane linear guided wave converts to that of the transmitted out-of-plane guided wave from $d_c/h = 0.65$. After $d_c/h = 0.85$, the energy of the reflected out-of-plane linear guided wave decreases dramatically. Also, the energy of both the mode-converted reflected and transmitted in-plane linear guided waves decrease from $d_c/h = 0.85$. However, the energy of the transmitted out-of-plane linear guided wave and the energy of all the in-plane and out-of-plane nonlinear guided waves increase significantly from $d_c/h = 0.85$. This demonstrates the energy conversion from the reflected out-of-plane linear guided wave and the mode-converted in-plane guided waves to transmitted out-of-plane linear guided wave and other nonlinear guided waves.

Comparing Figures 5.19 and 5.20 with Figures 5.21 and 5.22, we can see that when the incident wave is an S_0 guided wave, the spectral amplitudes of the second harmonics due to contact nonlinearity are larger than that of using the A_0 guided wave as the incident wave for small crack (e.g. $d_c/h < 0.3$). When the crack becomes large (e.g. $d_c/h > 0.8$), the second harmonics induced by contact nonlinearity when using an S_0 incident wave becomes smaller than when an A_0 incident wave is used. This indicates that the S_0 guided wave is more suitable as the incident wave for detecting small cracks when we consider contact nonlinearity and the mode-conversion effect. In contrast, A_0 guided waves are more suitable for larger cracks.

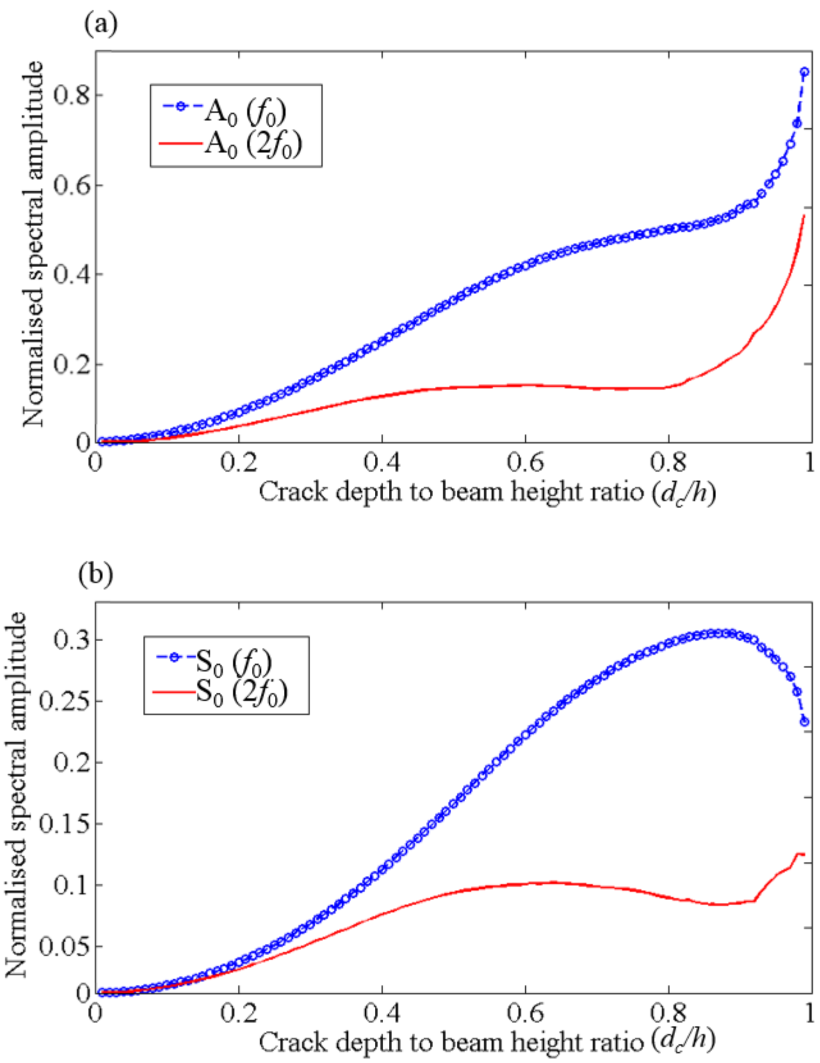

Fig. 5.22 Fourier transformed (a) out-of-plane and (b) mode-converted in-plane velocity as a function of crack depth to beam height ratio (d_c/h) at measurement location $x = 1$ m when the incident wave is A_0 guided wave.

5.6 Conclusions

This study has proposed the modelling and investigated of the interaction of nonlinear guided waves at breathing cracks. An extended time-domain SFE method has been proposed to improve the efficiency of simulation. The method considers the coupling of longitudinal, transverse and rotation DoFs based on the Mindlin-Hermann rod and Timoshenko beam theories. An SFE crack element has been developed to simulate the mode-conversion effect of guided waves when they interact with an asymmetric crack. A bilinear crack mechanism has been proposed to simulate the crack opening and closing. This has been embedded in the SFE crack element to simulate contact nonlinearity.

This chapter has presented numerical verification to demonstrate the accuracy of the proposed SFE model in simulating the contact nonlinearity. Very good agreement has been found between the time-domain SFE and explicit 3D FE results, which shows the accuracy of the proposed SFE model. The characteristics of the higher harmonics generated by the contact nonlinearity and mode-conversion effect at the asymmetric crack have been studied in detail using the extended SFE model. This chapter has also presented parametric studies to investigate the magnitude of the higher harmonics generation by S_0 and A_0 guided waves. The normalised spectral amplitude as a function of the crack depth to beam height ratio has been investigated. The chapter has shown that with the consideration of the mode-conversion effect, the higher harmonic generation by the S_0 incident guided wave has a larger magnitude than that by the A_0 incident guided wave.

Overall the study has provided physical insights into the higher harmonic generation at the breathing crack by S_0 and A_0 guided waves. The simulation has been conducted using the proposed computationally efficient SFE model. This SFE model can be further applied in the fields of damage identification.

Acknowledgement

This work was supported by the Australian Research Council (ARC) under Grant Numbers DP160102233 and DE130100261. The support is greatly appreciated.

References for Chapter 5

ACHENBACH, J. 2000. Quantitative nondestructive evaluation. *International Journal of Solids and Structures,* 37**,** 13-27.

ARYAN, P., KOTOUSOV, A., NG, C. & CAZZOLATO, B. 2016a. A baseline-free and non-contact method for detection and imaging of structural damage using 3D laser vibrometry. *Structural Control and Health Monitoring*.

ARYAN, P., KOTOUSOV, A., NG, C. & WILDY, S. 2016b. Reconstruction of baseline time-trace under changing environmental and operational conditions. *Smart Materials and Structures,* 25**,** 035018.

ARYAN, P., KOTOUSOV, A., NG, C. T. & CAZZOLATO, B. 2016c. A model-based method for damage detection with guided waves. *Structural Control and Health Monitoring*.

BOVSUNOVSKY, A. & SURACE, C. 2015. Non-linearities in the vibrations of elastic structures with a closing crack: A state of the art review. *Mechanical Systems and Signal Processing,* 62**,** 129-148.

BRODA, D., STASZEWSKI, W. J., MARTOWICZ, A., UHL, T. & SILBERSCHMIDT, V. V. 2014. Modelling of nonlinear crack–wave interactions for damage detection based on ultrasound—A review. *Journal of Sound and Vibration,* 333**,** 1097-1118.

DARPE, A., GUPTA, K. & CHAWLA, A. 2004. Coupled bending, longitudinal and torsional vibrations of a cracked rotor. *Journal of Sound and Vibration,* 269**,** 33-60.

DZIEDZIECH, K., PIECZONKA, L., KIJANKA, P. & STASZEWSKI, W. J. 2016. Enhanced nonlinear crack-wave interactions for structural damage detection based on guided ultrasonic waves. *Structural Control and Health Monitoring*.

FLYNN, E. B., TODD, M. D., WILCOX, P. D., DRINKWATER, B. W. & CROXFORD, A. J. Maximum-likelihood estimation of damage location in guided-wave structural health monitoring. Proceedings of the Royal Society of London A: Mathematical, Physical and Engineering Sciences, 2011. The Royal Society, rspa20110095.

GANGADHARAN, R., BHAT, M., MURTHY, C. & GOPALAKRISHNAN, S. 2010. A geodesic-based triangulation technique for damage location in metallic and composite plates. *Smart Materials and Structures,* 19**,** 115010.

GIANNINI, O., CASINI, P. & VESTRONI, F. 2013. Nonlinear harmonic identification of breathing cracks in beams. *Computers & Structures*.

GOPALAKRISHNAN, S. & MITRA, M. 2010. *Wavelet methods for dynamical problems: with application to metallic, composite, and nano-composite structures*, CRC Press.

HAN, J. H. & KIM, Y. J. 2015. Time–frequency beamforming for nondestructive evaluations of plate using ultrasonic Lamb wave. *Mechanical Systems and Signal Processing,* 54**,** 336-356.

HAYASHI, T. & KAWASHIMA, K. 2002. Multiple reflections of Lamb waves at a delamination. *Ultrasonics,* 40**,** 193-197.

HE, J. & YUAN, F. G. 2016. A quantitative damage imaging technique based on enhanced CCRTM for composite plates using 2D scan. *Smart Materials and Structures,* 25**,** 105022.

HE, S. & NG, C. T. 2016. A probabilistic approach for quantitative identification of multiple delaminations in laminated composite beams using guided waves. *Engineering Structures,* 127**,** 602-614.

HE, S. & NG, C. T. 2017. Guided wave-based identification of multiple cracks in beams using a Bayesian approach. *Mechanical Systems and Signal Processing,* 84**,** 324-345.

HE, S. & NG, C. 2015. Analysis of mode conversion and scattering of guided waves at cracks in isotropic beams using a time-domain spectral finite element method. *Elec J Struct Eng,* 14**,** 20-32.

JOGLEKAR, D. & MITRA, M. 2015. Analysis of nonlinear frequency mixing in 1D waveguides with a breathing crack using the spectral finite element method. *Smart Materials and Structures,* 24**,** 115004.

JOGLEKAR, D. & MITRA, M. 2016. Analysis of flexural wave propagation through beams with a breathing crack using wavelet spectral finite element method. *Mechanical Systems and Signal Processing,* 76**,** 576-591.

KAWASHIMA, K., OMOTE, R., ITO, T., FUJITA, H. & SHIMA, T. 2002. Nonlinear acoustic response through minute surface cracks: FEM simulation and experimentation. *Ultrasonics,* 40**,** 611-615.

KAŽYS, R., RAIŠUTIS, R., ŽUKAUSKAS, E., MAŽEIKA, L. & VLADIŠAUSKAS, A. 2010. Air- coupled ultrasonic testing of CFRP rods by means of guided waves. *Physics Procedia,* 3**,** 185-192.

KIM, S. B. & SOHN, H. 2007. Instantaneous reference-free crack detection based on polarization characteristics of piezoelectric materials. *Smart Materials and Structures,* 16**,** 2375.

KUDELA, P., KRAWCZUK, M. & OSTACHOWICZ, W. 2007. Wave propagation modelling in 1D structures using spectral finite elements. *Journal of sound and vibration,* 300**,** 88-100.

KUDELA, P. & OSTACHOWICZ, W. 2009. A multilayer delaminated composite beam and plate elements: reflections of Lamb waves at delamination. *Mechanics of Advanced Materials and Structures,* 16**,** 174-187.

LAM, H. F. & YIN, T. 2010. Statistical detection of multiple cracks on thin plates utilizing dynamic response. *Engineering structures,* 32**,** 3145-3152.

LI, F., PENG, H., SUN, X., WANG, J. & MENG, G. 2012. Wave Propagation Analysis in Composite Laminates Containing a Delamination Using a Three-Dimensional Spectral Element Method. *Mathematical Problems in Engineering,* 2012.

LOWE, M. J., CAWLEY, P., KAO, J. & DILIGENT, O. 2002. The low frequency reflection characteristics of the fundamental antisymmetric Lamb wave a 0 from a rectangular notch in a plate. *The Journal of the Acoustical Society of America,* 112**,** 2612-2622.

MAGALHÃES, F., CUNHA, A. & CAETANO, E. 2012. Vibration based structural health monitoring of an arch bridge: from automated OMA to damage detection. *Mechanical Systems and Signal Processing,* 28**,** 212-228.

MAHAPATRA, D. R., SINGHAL, A. & GOPALAKRISHNAN, S. 2006. A higher-order finite waveguide model for spectral analysis of composite structures. *Computer methods in applied mechanics and engineering,* 195**,** 1116-1135.

MITRA, M. & GOPALAKRISHNAN, S. 2016. Guided wave based structural health monitoring: A review. *Smart Materials and Structures,* 25**,** 053001.

NAG, A., MAHAPATRA, D. R. & GOPALAKRISHNAN, S. 2002. Identification of delamination in composite beams using spectral estimation and a genetic algorithm. *Smart Materials and Structures,* 11**,** 899.

NAIR, A. & CAI, C. S. 2010. Acoustic emission monitoring of bridges: Review and case studies. *Engineering Structures,* 32**,** 1704-1714.

NAJIB, M. F. & NOBARI, A. S. 2015. Kissing bond detection in structural adhesive joints using nonlinear dynamic characteristics. *International Journal of Adhesion and Adhesives,* 63**,** 46-56.

NG, C. T. 2014a. On the selection of advanced signal processing techniques for guided wave damage identification using a statistical approach. *Engineering Structures,* 67**,** 50-60.

NG, C. T. 2015a. A two-stage approach for quantitative damage imaging in metallic plates using Lamb waves.

NG, C. T. 2015b. On accuracy of analytical modeling of Lamb wave scattering at delaminations in multilayered isotropic plates. *International Journal of Structural Stability and Dynamics,* 15**,** 1540010.

NG, C. T., VEIDT, M. & RAJIC, N. Integrated piezoceramic transducers for imaging damage in composite laminates. Second International Conference on Smart Materials and Nanotechnology in Engineering, 2009. International Society for Optics and Photonics, 74932M-74932M-8.

NG, C. T. 2014b. Bayesian model updating approach for experimental identification of damage in beams using guided waves. *Structural Health Monitoring,* 13**,** 359-373.

OSTACHOWICZ, W. M. 2008. Damage detection of structures using spectral finite element method. *Computers & structures,* 86**,** 454-462.

PARK, I., KIM, S. & LEE, U. 2013. Dynamics and guided waves in a smart Timoshenko beam with lateral contraction. *Smart Materials and Structures,* 22**,** 075034.

PAU, A. & VESTRONI, F. 2011. Wave propagation in one-dimensional waveguides for damage characterization. *Journal of Intelligent Material Systems and Structures,* 22**,** 1869-1877.

PIECZONKA, L., KLEPKA, A., MARTOWICZ, A. & STASZEWSKI, W. J. 2016. Nonlinear vibroacoustic wave modulations for structural damage detection: an overview. *Optical Engineering,* 55**,** 011005-011005.

QUEK, S. T., TUA, P. & WANG, Q. 2003. Detecting anomalies in beams and plate based on the Hilbert–Huang transform of real signals. *Smart materials and structures,* 12**,** 447.

RUCKA, M. 2010. Experimental and numerical studies of guided wave damage detection in bars with structural discontinuities. *Archive of Applied Mechanics,* 80**,** 1371-1390.

RUCKA, M., WITKOWSKI, W., CHRÓŚCIELEWSKI, J. & WILDE, K. 2012. Damage detection of a T-shaped panel by wave propagation analysis in the plane stress. *Archives of Civil Engineering,* 58**,** 3-24.

SAMARATUNGA, D., JHA, R. & GOPALAKRISHNAN, S. 2014. Wavelet spectral finite element for wave propagation in shear deformable laminated composite plates. *Composite Structures,* 108**,** 341-353.

SHEN, Y. & CESNIK, C. E. 2016. Modeling of Nonlinear Interactions between Guided Waves and Fatigue Cracks Using Local Interaction Simulation Approach. *Ultrasonics*.

SOHN, H., DUTTA, D., YANG, J., DESIMIO, M., OLSON, S. & SWENSON, E. 2011. Automated detection of delamination and disbond from wavefield images obtained using a scanning laser vibrometer. *Smart Materials and Structures,* 20**,** 045017.

SOHN, H., PARK, H. W., LAW, K. H. & FARRAR, C. R. 2007. Damage detection in composite plates by using an enhanced time reversal method. *Journal of Aerospace Engineering,* 20**,** 141-151.

SOLEIMANPOUR, R. & NG, C. T. 2016. Locating delaminations in laminated composite beams using nonlinear guided waves. *Engineering Structures*.

SOLEIMANPOUR, R., NG, C. T. & WANG, C. H. 2016. Higher harmonic generation of guided waves at delaminations in laminated composite beams. *Structural Health Monitoring***,** 1475921716673021.

SOLODOV, I. Y., KROHN, N. & BUSSE, G. 2002. CAN: an example of nonclassical acoustic nonlinearity in solids. *Ultrasonics,* 40**,** 621-625.

TADA, H., PARIS, P. C., IRWIN, G. R. & TADA, H. 2000. *The stress analysis of cracks handbook,* ASME press New York.

TIAN, Z., YU, L., LECKEY, C. & SEEBO, J. 2015. Guided wave imaging for detection and evaluation of impact-induced delamination in composites. *Smart Materials and Structures,* 24**,** 105019.

WANG, X., WANG, F., XU, C. & GE, L. 2012. New spectral plate element for simulating lamb wave propagations in plate structures. *Nanjing Hangkong Hangtian Daxue Xuebao/Journal of Nanjing University of Aeronautics and Astronautics,* 44**,** 645-651.

WILLBERG, C., DUCZEK, S., VIVAR-PEREZ, J. & AHMAD, Z. 2015. Simulation Methods for Guided Wave-Based Structural Health Monitoring: A Review. *Applied Mechanics Reviews,* 67**,** 010803.

XU, F., WU, K. & HONG, W. 2007. Equivalent resonant cavity model of arbitrary periodic guided-wave structures and its application to finite-difference frequency-domain algorithm. *IEEE Transactions on Microwave Theory and Techniques,* 55**,** 697-702.

XU, F., ZHANG, Y., HONG, W., WU, K. & CUI, T. J. 2003. Finite-difference frequency-domain algorithm for modeling guided-wave properties of substrate integrated waveguide. *Microwave Theory and Techniques, IEEE Transactions on,* 51**,** 2221-2227.

YAN, D., NEILD, S. A. & DRINKWATER, B. W. 2012. Modelling and measurement of the nonlinear behaviour of kissing bonds in adhesive joints. *NDT & E International,* 47**,** 18-25.

YIN, T., LAM, H. F., CHOW, H. M. & ZHU, H. 2009. Dynamic reduction-based structural damage detection of transmission tower utilizing ambient vibration data. *Engineering Structures,* 31.

ŻAK, A., RADZIEŃSKI, M., KRAWCZUK, M. & OSTACHOWICZ, W. 2012. Damage detection strategies based on propagation of guided elastic waves. *Smart Materials and Structures,* 21**,** 035024.

ZHAO, X., GAO, H., ZHANG, G., AYHAN, B., YAN, F., KWAN, C. & ROSE, J. L. 2007. Active Health Monitoring of an Aircraft Wing with

Embedded Piezoelectric Sensor/actuator Network: I Defect Detection, Localization and Growth Monitoring. *Smart Materials and Structures,* 16**,** 1208-1217.

ZHAO, X. G. & ROSE, J. L. 2003. Boundary element modeling for defect characterization potential in a wave guide. *International Journal of Solids and Structures,* 40**,** 2645-2658.

ZHOU, W. J. & ICHCHOU, M. N. 2011. Wave scattering by local defect in structural waveguide through wave finite element method. *Structural Health Monitoring,* 10**,** 335-349.

Chapter 6

Time-domain spectral finite element method for modelling material, geometric and contact nonlinearities of guided waves in beams

(Paper 5, submitted)

Shuai He and Ching-Tai Ng

School of Civil, Environmental & Mining Engineering, The University of Adelaide, Adelaide, SA 5005, Australia

Publication:

HE, S. & NG, C. T. 2017. Simulation of classical and non-classical nonlinear guided waves in beam using spectral finite element method. *Structural Control and Health Monitoring,* Submitted for review: May 2017.

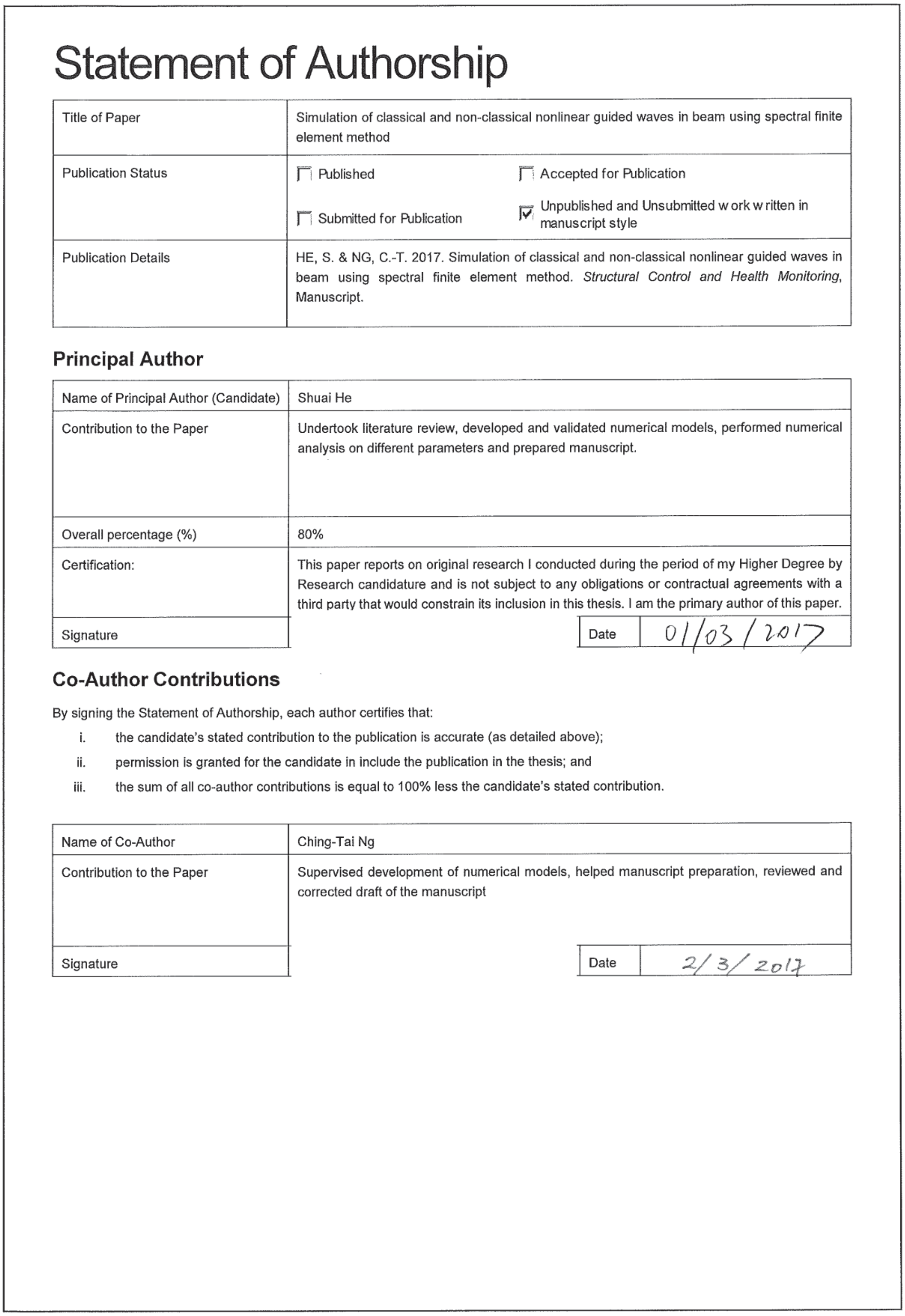

Statement of Authorship

Title of Paper	Simulation of classical and non-classical nonlinear guided waves in beam using spectral finite element method
Publication Status	☐ Published ☐ Accepted for Publication ☐ Submitted for Publication ☑ Unpublished and Unsubmitted work written in manuscript style
Publication Details	HE, S. & NG, C.-T. 2017. Simulation of classical and non-classical nonlinear guided waves in beam using spectral finite element method. *Structural Control and Health Monitoring*, Manuscript.

Principal Author

Name of Principal Author (Candidate)	Shuai He
Contribution to the Paper	Undertook literature review, developed and validated numerical models, performed numerical analysis on different parameters and prepared manuscript.
Overall percentage (%)	80%
Certification:	This paper reports on original research I conducted during the period of my Higher Degree by Research candidature and is not subject to any obligations or contractual agreements with a third party that would constrain its inclusion in this thesis. I am the primary author of this paper.

Signature		Date	01/03/2017

Co-Author Contributions

By signing the Statement of Authorship, each author certifies that:

i. the candidate's stated contribution to the publication is accurate (as detailed above);

ii. permission is granted for the candidate in include the publication in the thesis; and

iii. the sum of all co-author contributions is equal to 100% less the candidate's stated contribution.

Name of Co-Author	Ching-Tai Ng
Contribution to the Paper	Supervised development of numerical models, helped manuscript preparation, reviewed and corrected draft of the manuscript

Signature		Date	2/3/2017

Abstract

This study proposes a time-domain spectral finite element (SFE) method for simulating the second harmonic generation of nonlinear guided wave due to material, geometric and contact nonlinearities in beams. The time-domain SFE method is developed based on the Mindlin-Hermann rod and Timoshenko beam theory. The material and geometric nonlinearities is modelled by adapting the constitutive relation between strain and stress using a second order approximation. The contact nonlinearity induced by a breathing crack is simulated by implementing a bilinear crack mechanism. The material and geometric nonlinearities of the SFE model are validated analytically and the contact nonlinearity is verified numerically using three-dimensional (3D) finite element (FE) simulation. There is good agreement between the analytical, numerical and SFE results, demonstrating the accuracy of the proposed method in the second harmonic generation.

A series of numerical case studies are conducted to investigate the influence of number of cycles and amplitude of the excitation on the second harmonic generation. The results show that the amplitude of the second harmonic increases with the numbers of cycles and amplitude of the excitation signal. The amplitudes of the second harmonics due to material and geometric nonlinearities are also compared with the contact nonlinearity when a breathing crack exists in the beam. The results show that the material and geometric nonlinearities has much less contribution to the generation of second harmonic than the contact nonlinearity. The results and findings of this study help to further advance the use of second harmonic for damage detection.

***Keywords*:**

Nonlinear guided waves; second harmonic; spectral finite element; material nonlinearity; geometric nonlinearity; contact nonlinearity; breathing crack

6.1 Introduction

Structural health monitoring (SHM) has attracted increasing attention in last two decades as it has played a vital role in maintaining the structural safety and serviceability in civil, aerospace and mechanical engineering. Different techniques were developed to provide early detection of damages in structures. For example, conventional non-destructive evaluation (NDE) techniques, such as visual inspection, eddy current, ultrasonic technique and thermographic inspection, were developed to provide offline inspection of the structural integrity. However, the majority of the NDE techniques are not suitable for online and in-situ monitoring of the structures due to transducer sustainability, integration and/or cost issues. Most NDE techniques are not applicable to inspect inaccessible location of the structures, costly, time consuming, and are still carried out manually according to schedule maintenance cycles. Vibration based approach is the other commonly used damage detection technique (Lam and Yin, 2010, Yin et al., 2009, Qian and Mita, 2007). It mainly relies on changes of modal parameters of the structural vibration. However, there are two reasons that limit the application of this technique to detect damage in practice, 1) significant damage usually causes very small changes in the modal parameters, and 2) changes of modal parameters due to damage may be undetected due to varying environmental and operational condition.

6.1.1 Guided wave

The other approach that has attracted significant attention is based on guided waves to evaluate the integrity of structures. Guided waves are mechanical stress waves that propagate along the structure and are guided by the boundaries of the structures. They propagate at high speeds, up to thousand m/s. Guided waves could be used for in-situ monitoring of relatively large area of the structure. Different techniques were developed to employ the guided waves for damage detection of different types of structures, such as rod (Rucka et al., 2012, Ostachowicz, 2008), beam (He and Ng, 2017, Aryan et al., 2016a, Ng, 2014, Rucka, 2010) and plate (Ng, 2015a, Ng, 2015b, Huang et al., 2012, An and Sohn, 2010) made by metallic and composite materials (He and Ng, 2016, Mahapatra et al., 2006). The damage detection is achieved based on the change of the characteristics of the guided wave responses at the same frequency of the input signal. But this technique is only effective when the damage size is similar or larger to the wavelength of the guided waves. The majority of the techniques based on the linear guided waves require reference (baseline) data obtained when the structure is intact to extract the information of the damage from the measured signals. However, the stability of the baseline data is significantly affected by the varying temperature (Aryan et al., 2016b) and operational condition (Putkis and Croxford, 2013, Zhu and Rizzo, 2013), which can make the extraction of the damage information from baseline data fail.

To achieve early detection of damage, nonlinear features of guided waves, such as higher harmonics (Rauter et al., 2016, Hong et al., 2014, Matlack et al., 2011), sub-harmonics (Park et al., 2016, Solodov et al., 2004), shift of resonance frequency (Kober and Prevorovsky, 2014) and mixed frequency response (Sohn et al., 2014), have been used for damage detection. Specifically, the generation of higher harmonics, which frequencies are in multiple times of the input signal frequency, has been widely used as an indicator for early detection of damages. Compared to the linear features of guided waves, the nonlinear features are more sensitive to the micro change of structural integrity and less influenced by varying temperature and operational condition of the structures.

6.1.2 Nonlinear guided wave

Early research into nonlinear guided waves focused on the bulk waves and Rayleigh surface waves (Herrmann et al., 2006). Different to bulk waves and Rayleigh surface waves, the guided waves are highly dispersive. Due to this nature, the guided waves generally contain multiple wave modes and their group and phase velocities usually vary with frequency. To effectively utilize the nonlinear guided waves, different studies have investigated the conditions on the generation of cumulative second harmonics of guided wave, such as internal resonance, group velocity matching and guided wave modes interaction (Liu et al., 2013). The results showed that under such conditions the detectability of the higher harmonics in nonlinear guided wave could be improved significantly.

Higher harmonic generated due to the nonlinearities existed in the structures, which are attributed to material behaviour, geometry, structural joints and damage. For an undamaged isotropic homogeneous solid medium, geometric nonlinearity and material nonlinearity can distort the passing guided waves to induce the higher harmonics. The geometric nonlinearity is due to the finite deformation of the structures. The material nonlinearity is mainly generated by the discontinuity of the medium at lattice level, i.e. imperfections in atomic lattices. The effect of higher harmonic generation is enhanced when there are additional imperfections in medium, such as distributed micro-cracks. In the literature the higher harmonic generation has been employed to evaluate material thermal degradation (Xiang et al., 2011), fatigue microstructure (Lissenden et al., 2014, Deng and Pei, 2007), micro-corrosive defect (Li and Cho, 2016) and the dislocation substructures in metals (Xiang et al., 2014, Pruell et al., 2009).

The higher harmonic can also be generated due to the contact nonlinearity at the contact-type damage. For a damaged medium, e.g. with a localized fatigue crack, when guided waves propagate through the contact interfaces of the fatigue crack, the compressive and tensile pressure of the wave closes and opens the contact interfaces, respectively. This behaviour alters the stiffness of the structure and generates the higher harmonics. In the literature the contact nonlinearity has been investigated for a number of contact-type damages, such as fatigue crack (Dziedziech et al., 2016), kissing bond (Najib and Nobari, 2015, Yan et al., 2012), delamination (Soleimanpour et al., 2016, Soleimanpour and Ng, 2016a) and breathing crack (Broda et al., 2014).

6.1.3 Numerical simulation of nonlinear guided wave

In the literature different numerical simulation methods have been proposed to simulate the nonlinear guided waves. For example, Shen and Giurgiutiu (2014) proposed an analytical and finite element (FE) method to simulate the nonlinear guided wave propagation induced by a breathing crack. The piezoelectric wafer active sensor was implemented to generate and receive the guided wave signal. Wan et al. (2016) utilised the analytical and FE method to study the higher harmonics induced by the material nonlinearity in plates. Approximate phase velocity matching condition for the generation of nonlinear signal was investigated using the low frequency primary mode Lamb waves. Hong et al. (2014) employed the FE method to simulate the nonlinear guided wave in aluminium plates with a fatigue crack. Zhu et al. (2016) utilized the FE method to study the plastic damages in martensite stainless steel. The nonlinear guided wave due to material and geometric nonlinearity was analysed by incorporating a nonlinear constitutive relationship to the FE model. Yamanaka et al. (2011) proposed a two dimensions (2D) finite difference (FD) method to analysis nonlinear guided wave. The subharmonic generation at closed stress corrosion cracks was successfully reproduced. Shen and Cesnik (2017) utilized the local interaction simulation approach (LISA) to simulate the nonlinear guided wave caused by the clapping mechanism of fatigue cracks. Joglekar and Mitra (Joglekar and Mitra, 2015) proposed a fast Fourier transform (FFT) based spectral finite element (SFE) model to study the nonlinear guided wave in beams due to the breathing crack.

The existing numerical simulation methods have different strengths and weaknesses. The FFT based SFE method is computational efficient in modelling the guided wave propagation but it is a semi-analytical method assuming infinite length of the structure. Although the FE method is suitable to simulate complex structures, the computational efficiency is unsatisfied as the discretization of the FE elements should be very small to ensure the accuracy of the simulation. The FD method is incapable to simulate the guided wave propagation in waveguides having material property changes with geometry (Xu et al., 2003). The LISA is efficient and effective in simulating complex geometries but it requires careful discretization to obtain accurate solutions.

Overall, it is found in the literature that most of the simulation concerns only the contact nonlinearity or, to a less extent, the material and geometric nonlinearity. Very limited papers (Hong et al., 2014) considered all the contribution of material, geometric and contact nonlinearities in the second harmonics generation, especially for beam structures. In this study, the effect of the material, geometric and contact nonlinearities on the second harmonic generation in beams with a breathing crack is studied in detail using the proposed time-domain SFE model. The findings of the study can provide physical insights into the second harmonics generation due to the material, geometric and contact nonlinearities. This can further advance the development of using second harmonic generation for damage detection.

6.1.4 Time-domain spectral finite element method

The time-domain SFE has been found to be computationally efficient in the simulation of guided wave propagation and capable in modelling of geometric complicated structures. The time-domain SFE method is as flexible as the conventional FE method in modelling different geometries of structures. The computational efficiency is significantly improved by using the high-order approximation polynomials. Due to the application of Gauss-Lobatto-Legendre (GLL) nodes, the mass matrix of the model becomes a diagonal form resulting in an efficient solution of the dynamic equilibrium using the explicit central difference method. The time-domain SFE method has been widely investigated by a number of research with respect to the linear features of guided waves (Żak and Krawczuk, 2010) and damage detection (Rucka et al., 2012, Kudela et al., 2007). However, the time-domain SFE method has not yet been developed to simulate nonlinear guided waves induced by material, geometric nonlinearities, and contact nonlinearities. In this chapter, the computationally efficient time-domain SFE method is extended to take into account the effect of the material, geometric and contract nonlinearities on the second harmonic generation.

The arrangement of the chapter is as follows. The time-domain SFE method for simulating the nonlinear guided waves is proposed in Section 6.2. The nonlinear guided waves resulted from material, geometric and contact nonlinearities are formulated in this section. The proposed SFE method for simulating material and geometric nonlinearities, and contact nonlinearity are then validated using analytical solutions and three-dimensional (3D) FE simulations in Section 6.3. Section 6.4 carries out a series of numerical case studies to investigate the performance of the proposed SFE method in simulating the generation of second harmonic at fatigue cracks with consideration of material, geometric and contact nonlinearities. Conclusions are drawn in Section 6.5.

6.2 Time-domain Spectral finite element method

The simulation of nonlinear guided waves using time-domain SFE method is presented in this section. The basic SFE formulation is described first in subsection 6.2.1. Then the modelling of material and geometric nonlinearities, and contact nonlinearities using the SFE method are described in subsections 6.2.2 and 6.2.3, respectively.

6.2.1 Basic SFE formulation

The dynamic equilibrium of the time-domain SFE method is the same as the conventional FE method, which is defined as (He and Ng, 2015, Kudela and Ostachowicz, 2009)

$$\mathbf{M}\ddot{\mathbf{U}}+\mathbf{C}\dot{\mathbf{U}}+\mathbf{K}\mathbf{U}=\mathbf{F}\left(t\right) \tag{6.1}$$

where **M**, **K** and **F**(*t*) are global mass matrix, global stiffness matrix and global force vector at time *t*, respectively. The global damping matrix **C** is a function of the global mass matrix denoted by $\mathbf{C}=\eta\mathbf{M}$, where η is the damping coefficient. $\ddot{\mathbf{U}}$, $\dot{\mathbf{U}}$ and $\mathbf{U}$ denote the vector of acceleration, velocity and displacement response, respectively. The elemental mass matrix $\mathbf{M}^e$, elemental stiffness matrix $\mathbf{K}^e$ and elemental force vector $\mathbf{F}^e$ that form the corresponding global terms in Equation (6.1) are given as:

$$\mathbf{M}^e \approx \sum_{i=1}^{n} w_i \mathbf{N}_e\left(\xi_i\right)^T \mathbf{r}\mathbf{N}_e\left(\xi_i\right)\det\left(J\left(\xi_i\right)\right) \tag{6.2}$$

$$\mathbf{K}^e \approx \sum_{i=1}^{n} w_i \mathbf{B}_e\left(\xi_i\right)^T \mathbf{E}_e\mathbf{B}_e\left(\xi_i\right)\det\left(J\left(\xi_i\right)\right) \tag{6.3}$$

$$\mathbf{F}^e\left(t\right) \approx \sum_{i=1}^{n} w_i \mathbf{N}_e\left(\xi_i\right)^T \mathbf{f}_e\left(t\right)\mathbf{N}_e\left(\xi_i\right)\det\left(J\left(\xi_i\right)\right) \tag{6.4}$$

where ξ_i is the local coordinate of the i-th node at the element, $i \in 1,...,n$, and n is the number of nodes. $J=\partial x/\partial\xi$ is the Jacobian functions transfers the local coordinate ξ to the global coordinate *x*. $\mathbf{r}_e$ is the mass matrix, $\mathbf{E}_e$ is the material property matrix and $\mathbf{f}_e(t)$ is the external force vector at time *t* applied to the element, respectively. Different to the conventional FE methods, the SFE method employs the GLL nodes in the element, which results in a more efficient solution than the FE method (He and Ng, 2017). The local coordinate ξ_i of the GLL nodes can be determined from the roots of the given equation:

$$\left(1-\xi_i^2\right)L'_{n-1}\left(\xi_i\right)=0 \text{ for } \xi_i \in [-1,1] \text{ and } i \in 1,...,n \tag{6.5}$$

where L'_{n-1} denotes the first derivative of (*n*-1)-th order Legendre polynomial. w_i is the weighting function of node *i* defined as:

$$w_i = \frac{2}{n(n-1)[L_{n-1}(\xi_i)]^2} \tag{6.6}$$

$\mathbf{N}_e$ is the shape function of the SFE element, which has the matrix form:

$$\mathbf{N}_e = \mathbf{N} \otimes \mathbf{I} \tag{6.7}$$

where $\mathbf{N} = [N_1(\xi), ..., N_n(\xi)]$ is a row vector. $\mathbf{I}$ is an identity matrix with the square size same as the number of the nodal degree of freedom. '$\otimes$' denotes the Kronecker product. The shape function $N_i(\xi)$ at node *i* can be calculated by:

$$N_i(\xi) = \prod_{m=1, m\neq i}^{n} \frac{\xi - \xi_m}{\xi_i - \xi_m} \tag{6.8}$$

where *m* is the sequence of the *n* GLL integration points in the element.

In this chapter, the first-order shear deformation theory considering the independent contraction due to Poisson effect is employed to formulate the beam element. The displacement field is defined as:

$$\bar{u}(x,y) \approx u(x) - \varphi(x) y \tag{6.9}$$

$$\bar{v}(x,y) \approx v(x) + \psi(x) y \tag{6.10}$$

where $u(x)$ is the longitudinal displacement in *x* axis direction, *v* is the transverse displacement, φ is the rotation of the cross section and ψ is the independent contraction accounts for the Poisson effect. The Lagrange strain (Nucera and Scalea, 2015) is employed and the strain field in the element is defined as:

$$\boldsymbol{\varepsilon}^e = \mathbf{B}^e \mathbf{q}^e = \left(\mathbf{B}_L^e + \mathbf{B}_{NL}^e\right) \mathbf{q}^e \tag{6.11}$$

where $\mathbf{q}^e = \left[u^e, \psi^e, v^e, \varphi^e\right]^T$ and $\mathbf{B}^e$ is strain-displacement operator. $\mathbf{B}_L^e$ and $\mathbf{B}_{NL}^e$ account for the first and second order terms of Lagrange strain and they are defined as:

$$\mathbf{B}_L^e = \begin{bmatrix} \frac{\partial}{\partial x} & 0 & 0 & 0 \\ 0 & 1 & 0 & 0 \\ 0 & \frac{\partial}{\partial x} & 0 & 0 \\ 0 & 0 & \frac{\partial}{\partial x} & -1 \\ 0 & 0 & 0 & \frac{\partial}{\partial x} \end{bmatrix} \mathbf{N}^e \tag{6.12}$$

and

$$\mathbf{B}_{NL}^e = \frac{1}{2} \begin{bmatrix} \frac{\partial u^e}{\partial x}\frac{\partial}{\partial x} & 0 & \frac{\partial v^e}{\partial x}\frac{\partial}{\partial x} & 0 \\ 0 & \psi^e & 0 & \varphi^e \\ 0 & 0 & 0 & 0 \\ 0 & 0 & 0 & 0 \\ 0 & 0 & 0 & 0 \end{bmatrix} \mathbf{N}^e \tag{6.13}$$

Using the first-order shear deformation theory, the mass matrix $\mathbf{r}_e$ in Equation (6.2) has the form:

$$\mathbf{r} = \begin{bmatrix} \rho bh & 0 & 0 & 0 \\ 0 & K_2^M \rho \frac{bh^3}{12} & 0 & 0 \\ 0 & 0 & \rho bh & 0 \\ 0 & 0 & 0 & K_2^T \rho \frac{bh^3}{12} \end{bmatrix} \tag{6.14}$$

where ρ is the density of the material, *b* is the width and *h* is the height of the beam, respectively.

6.2.2 Modelling of classical nonlinearity

Considering an isotropic homogeneous solid with purely elastic behaviour, the material and geometric nonlinearities can be represented by the constitutive relation between stress and strain using the second order approximation (Norris, 1998) as

$$\sigma_{ij} = \left(Q^{L}_{ijkl} + 1/2\, Q^{NL}_{ijklmn} \varepsilon_{mn} \right) \varepsilon_{kl} \tag{6.15}$$

where σ_{ij} is the stress tensor. ε_{mn} and ε_{kl} are the strain tensors. Q^{L}_{ijkl} is the second order elastic tensors, which can be expressed in a matrix form for two-dimensional plane stress situation as:

$$\left\{ Q^{L}_{ijkl} \right\} = \begin{bmatrix} Q^{L}_{1111} & Q^{L}_{1133} & 0 \\ Q^{L}_{1133} & Q^{L}_{3333} & 0 \\ 0 & 0 & Q^{L}_{3131} \end{bmatrix} = \frac{E}{\left(1-\upsilon^{2}\right)} \begin{bmatrix} 1 & \upsilon & 0 \\ \upsilon & 1 & 0 \\ 0 & 0 & \dfrac{1-\upsilon}{2} \end{bmatrix} \tag{6.16}$$

where $\upsilon = 0.5\lambda/(\lambda+\mu)$ is the Poisson's ratio and $E = \mu(3\lambda+2\mu)/(\lambda+\mu)$ is the Young's modulus of the material. λ and μ are the Lamé Constants. Q^{NL}_{ijklmn} is the tensor addresses both the material and geometric nonlinearities. If Q^{NL}_{ijklmn} is not considered, Equation (6.15) can be simplified into the linear situation following the Hooke's Law. The form of Q^{NL}_{ijklmn} is given as (Wan et al., 2016, Hong et al., 2014, Norris, 1998):

$$Q^{NL}_{ijklmn} = Q^{L}_{ijklmn} + Q^{L}_{ijln}\delta_{km} + Q^{L}_{jnkl}\delta_{im} + Q^{L}_{jlmn}\delta_{ik} \tag{6.17}$$

where

$$\begin{aligned} Q^{L}_{ijklmn} &= \frac{1}{2} A\left(\delta_{ik} I_{jlmn} + \delta_{il} I_{jkmn} + \delta_{jk} I_{ilmn} + \delta_{jl} I_{ikmn} \right) \\ &+ 2B\left(\delta_{ij} I_{klmn} + \delta_{kl} I_{mnij} + \delta_{mn} I_{ijkl} \right) + 2C\delta_{ij}\delta_{kl}\delta_{mn} \end{aligned} \tag{6.18}$$

In Equation (6.17) and (6.18), δ_{ij} and its similar forms with different subscript indexes are the Kronecker delta. I_{ijkl} and its similar forms with different index orders are the fourth order identity tensors.

The material nonlinearity is described by the third order elastic tensor Q_{ijklmn}^{NL}, where the geometric nonlinearity is addressed by the last three terms in Equation (6.17). The subscript *ij*, *kl*, *mn* = 11, 33, 31 in this chapter. The third order elastic tensor Q_{ijklmn}^{NL} is determined by three third order elastic constants *A*, *B* and *C*. Their values can be measured from experiment for the investigated materials. Let $Q_{ijkl} = Q_{ijkl}^{L} + 1/2\,Q_{ijklmn}^{NL}\varepsilon_{mn}$, the material property matrix $\mathbf{E}_e$ in Equation (6.3) is expressed as

$$\mathbf{E}_e = \begin{bmatrix} Q_{1111}bh & Q_{1133}bh & 0 & 0 & 0 \\ Q_{1133}bh & Q_{3333}bh & 0 & 0 & 0 \\ 0 & 0 & Q_{3131}K_1^M bh^3/12 & 0 & 0 \\ 0 & 0 & 0 & Q_{3131}K_1^T bh & 0 \\ 0 & 0 & 0 & 0 & Q_{3333}bh^3/12 \end{bmatrix} \tag{6.19}$$

where $K_1^M = 1.1$, $K_2^M = 3.1$, $K_1^T = 0.922$ and $K_2^T = 12K_1^T/\pi^2$ are adjustable parameters that calibrate the accuracy of guided wave propagation simulation (He and Ng, 2017). For one dimensional (1D) longitudinal waves propagation, Equation (6.15) can be simplified as (Wan et al., 2016, Hong et al., 2014):

$$\sigma = \left(E + E_2\varepsilon\right)\varepsilon \tag{6.20}$$

where σ, ε and E_2 are the stress, strain and the second order Young's modulus accounted for the nonlinearity of the medium (Liu et al., 2012). E_2 can be calculated from

$$E_2 = -\frac{1}{2}\left(3E + 2A + 6B + 2C\right) \tag{6.21}$$

In order to investigate the nonlinearity of the material, the acoustic nonlinearity parameter β is introduced as the ratio of the second order Young's modulus to Young's modulus as:

$$\beta = \frac{E_2}{E} = -\frac{1}{2}\left(3 + \frac{2A + 6B + 2C}{E}\right) \tag{6.22}$$

Equation (6.22) shows that the acoustic nonlinearity parameter β is a function of the Young's modulus, which accounts for the linear behaviour of the medium, and the third order elastic constants *A*, *B* and *C*, which accounts for the nonlinear behaviour of the medium. This shows that the acoustic nonlinearity parameter β quantifies the degree of material nonlinearity of the medium without any defect or plastic deformation. In practice, the relative acoustic nonlinearity parameter β' can be employed as an indicator to study the second order of the medium nonlinearity (Bermes et al., 2008), which is defined as the ratio between the spectral amplitude at the fundamental frequency (A_1) and the square of the spectral amplitude of the second harmonic frequency (A_2) as:

$$\beta' = \frac{A_2}{A_1^2} \tag{6.23}$$

According to the reference (Bermes et al., 2008), the relative acoustic nonlinearity parameter β' is linearly proportion to the nonlinear parameter β and the wave propagation distance if the measured guided wave modes are cumulative. Hence β' also has the following expression:

$$\beta' \propto \beta x \tag{6.24}$$

where x is the distance of propagation. Hence, the relative acoustic nonlinearity parameter β' indicates the nature of the nonlinear property of the wave propagation.

6.2.3 Modelling of contact nonlinearity

In this chapter, the contact nonlinearity induced by a breathing crack in a cracked beam is also simulated by the proposed SFE model. To achieve this, a SFE cracked element is proposed in this section. Considering a cracked beam with length L, width b and height h, the breathing crack with depth d_c is modelled at location L_c of the beam. Figure 6.1(a) shows the SFE discretization of the beam. The intact part of the beam is modelled using the SFE beam element and the cracked part is modelled by the proposed SFE cracked element. Eight GLL nodes are used by the SFE beam element while two GLL nodes are used in the proposed SFE cracked element. The nodes in the crack element considers three degrees-of-freedom (DoFs) i.e., longitudinal, transverse and rotational DoFs. The length of the crack element is assumed to be very small, i.e. $l \approx 0.001$ m, in the model. When the proposed cracked element is connected with the SFE beam element, the lateral contraction DoF induced by the longitudinal wave propagation is not considered due to the very small length of the proposed SFE crack element.

The contact nonlinearity due to the breathing phenomenon of the crack is modelled by a contact mechanism indicated in Figure 6.1(b). The nodal longitudinal displacements u_1 and u_2 at the SFE cracked element are examined to determine the status of the crack at each time step of the simulation:

$$u_1 - u_2 < 0 \text{, when the crack is opened} \tag{6.25}$$

$$u_1 - u_2 >= 0 \text{, when the crack is closed} \tag{6.26}$$

Based on the state of the crack, the stiffness matrix $\mathbf{K}_e^c$ of the SFE crack element can be determined. When the crack is open, the stiffness matrix $\mathbf{K}_e^c$ of the SFE crack element is calculated as (He and Ng, 2017)

$$\mathbf{K}_e^c = \mathbf{P}\mathbf{G}_c^{-1}\mathbf{P}^T \tag{6.27}$$

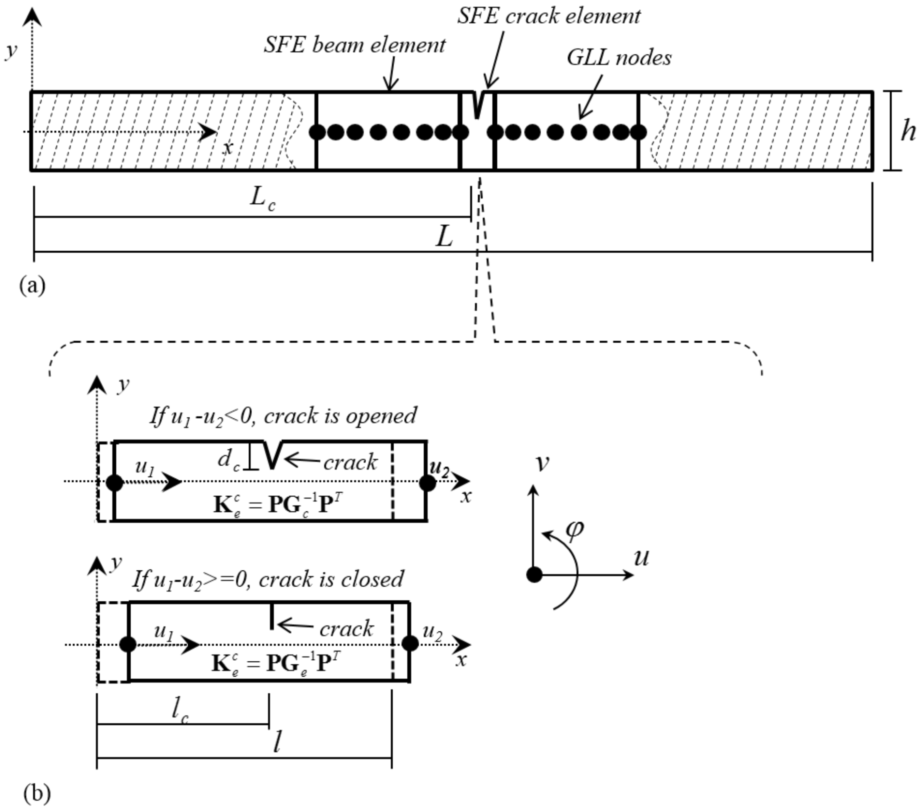

Fig. 6.1 Schematic diagram of a SFE model for simulating a cracked beam, (a) discretization of a cracked beam; (b) two-node SFE crack element when the crack is opened and closed.

$\mathbf{P}$ is the spatial transformation matrix as a function of the crack element length l:

$$\mathbf{P}^T = \begin{bmatrix} 1 & 0 & 0 & -1 & 0 & 0 \\ 0 & 1 & 0 & 0 & -1 & l \\ 0 & 0 & 1 & 0 & 0 & -1 \end{bmatrix} \tag{6.28}$$

$\mathbf{G}_c$ is the flexibility matrix for the open crack given as follows:

$$\mathbf{G}_c = \begin{pmatrix} g_{11}^c & g_{12}^c & g_{13}^c \\ g_{21}^c & g_{22}^c & g_{23}^c \\ g_{31}^c & g_{32}^c & g_{33}^c \end{pmatrix} \tag{6.29}$$

with

$$\begin{gathered} g_{11} = \frac{l}{EA} + I_{g1},\ g_{22} = \left(\frac{\kappa l}{GA} + \frac{l^3}{3EA} \right) + \left(I_{g3} + l_c^2 I_{g4} \right),\ g_{33} = \frac{l}{EI} + I_{g4} \\ g_{12} = g_{21} = l_c I_{g2},\ q_{13} = q_{31} = -I_{g2},\ q_{23} = q_{32} = -\frac{l^2}{2EI} - l_c I_{g4} \end{gathered} \tag{6.30}$$

where $\kappa = 10(1+\nu)/(12+11\nu)$ is the shear coefficient for rectangular shape of the beam cross section. I_{g1}, I_{g2}, I_{g3} and I_{g4} are the functions of the crack depth defined as:

$$\begin{gathered} I_{g1} = \frac{2\pi}{Eb} \int_0^{\alpha} \alpha F_1^2 d\alpha \\ I_{g2} = \frac{12\pi}{Ebh} \int_0^{\alpha} \alpha F_1 F_2 d\alpha \\ I_{g3} = \frac{2\kappa\pi}{Eb} \int_0^{\alpha} \alpha F_{II}^2 d\alpha \\ I_{g4} = \frac{72\pi}{Ebh^2} \int_0^{\alpha} \alpha F_2^2 d\alpha \end{gathered} \tag{6.31}$$

where l_c is the crack location in the SFE crack element. $\alpha = d_c / h$. F_1, F_2 and F_{II} are the empirical boundary calibration factors accounted for tension, bending and shear for the surface crack, respectively. According to (Tada et al., 2000), the factors F_1, F_2 and F_{II} produce less than 0.5% errors for the simulation of the crack with any depth d_c. Their formulations are given as (Tada et al., 2000)

$$F_1(\alpha) = \sqrt{\frac{2}{\pi\alpha} \tan\left(\frac{\pi\alpha}{2} \right)} \frac{0.752 + 2.02\alpha + 0.37 \left[1 - \sin\left(\frac{\pi\alpha}{2} \right) \right]^3}{\cos\left(\frac{\pi\alpha}{2} \right)} \tag{6.32}$$

$$F_2(\alpha) = \sqrt{\frac{2}{\pi\alpha}\tan\left(\frac{\pi\alpha}{2}\right)}\,\frac{0.923 + 0.199\left[1 - \sin\left(\frac{\pi\alpha}{2}\right)\right]^4}{\cos\left(\frac{\pi\alpha}{2}\right)} \tag{6.33}$$

$$F_{II}(\alpha) = \frac{1.122 - 0.561\alpha + 0.085\alpha^2 + 0.18\alpha^3}{\sqrt{1-\alpha}} \tag{6.34}$$

When the crack is closed, the crack element is considered as an intact beam element. The SFE crack element stiffness matrix $\mathbf{K}_e^c$ from Equation (6.27) becomes:

$$\mathbf{K}_e^c = \mathbf{P}\mathbf{G}_e^{-1}\mathbf{P}^T \tag{6.35}$$

where $\mathbf{G}_e$ is the flexibility matrix for the closed crack and is defined as:

$$\mathbf{G}_e = \begin{pmatrix} g_{11}^e & g_{12}^e & g_{13}^e \\ g_{21}^e & g_{22}^e & g_{23}^e \\ g_{31}^e & g_{32}^e & g_{33}^e \end{pmatrix} \tag{6.36}$$

with

$$\begin{gathered} g_{11}^e = \frac{l}{EA},\ g_{22}^e = \left(\frac{\kappa l}{GA} + \frac{l^3}{3EA}\right),\ g_{33}^e = \frac{l}{EI} \\ g_{12}^e = g_{21}^e = g_{13}^e = g_{31}^e = 0,\ g_{23}^e = g_{32}^e = -\frac{l^2}{2EI} \end{gathered} \tag{6.37}$$

6.3 Model validation

The effectiveness of the proposed model is validated at this section. The validation is conducted in two situations. First, the modelling of material and geometric nonlinearities is verified similar to the approach in reference (Wan et al., 2016). It compares the ratio of the relative nonlinear parameter β' between two different materials calculated using SFE and the analytical approach. After that, the conventional FE simulation is used to verify the contact nonlinearity generated due to the interaction between the guided wave and the breathing crack. The results of validations are presented in the following subsections.

6.3.1 Validation of material and geometric nonlinearity

The aluminium beams with the two different material properties, e.g., Al 6061-T6 and Al 7075-T651 are considered, where the material properties (Wan et al., 2016) are shown in Table 6.1. The beams have the same geometric dimensions, where the length L, width b and height h of the beams are 1000 mm, 12 mm and 5 mm, respectively. The schematic diagram of the SFE model is indicated in Figure 6.2(a). The excitation signal is an f_0 = 100 kHz, narrow-band, 16-cycle sinusoidal tone burst modulated by a Hanning window. The fundamental symmetric mode (S_0) guided wave is excited by applying the in-plane displacement at the left end of the beam, in which the maximal amplitude of the input displacement is 1×10^{-6} m.

Table 6.1 Material properties of Al-6061-T6 and Al-7075-T651 (Wan et al., 2016).

Material	ρ (kg m^{-3})	λ (GPa)	μ (GPa)	A (GPa)	B (GPa)	C (GPa)
Al-6061-T6	2704	67.6	25.9	-416	-131	-150.5
Al-7075-T651	2810	70.3	26.96	-351.2	-149.4	-102.8

The displacement response calculated by the SFE simulation at L_m = 500 mm is shown in Figure 6.3. The FFT is then employed to determine the spectral amplitude of the first harmonic (A_1) and the second harmonic (A_2) as shown in Figure 6.4. The figure shows that the second harmonic A_2 is generated as a result of both material and geometric nonlinearities.

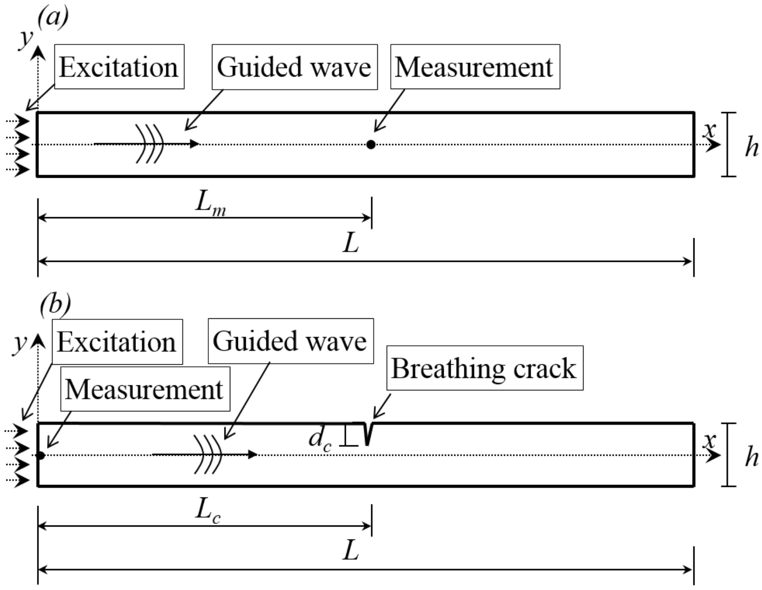

Fig. 6.2 Schematic diagram of the SFE beam with (a) material and geometric nonlinearities; and (b) material, geometric and contact nonlinearities.

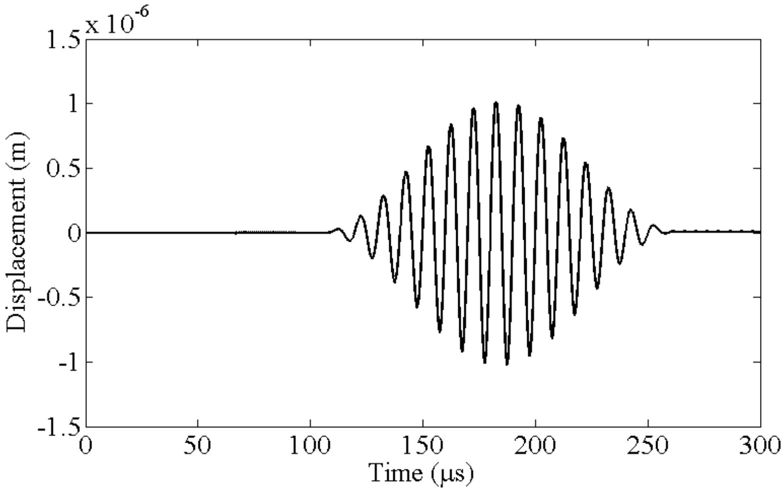

Fig. 6.3 The displacement response calculated by SFE simulation at L_m = 500 mm.

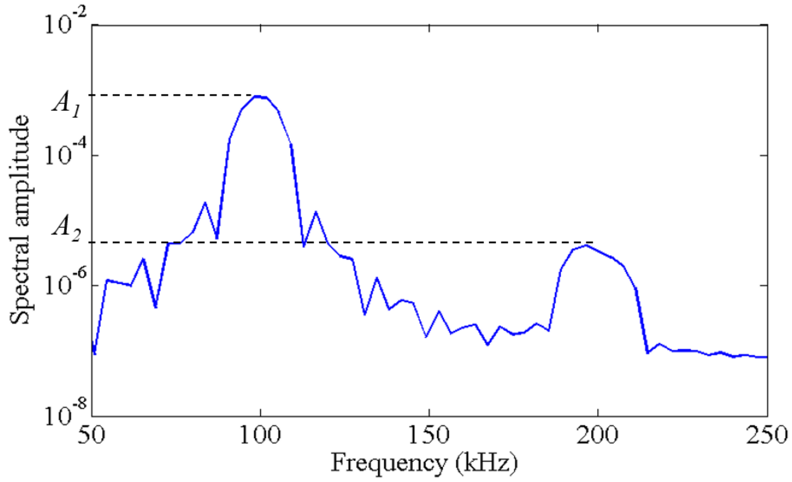

Fig. 6.4 The spectral amplitude of the displacement response calculated at L_m = 500 mm.

The spectral amplitudes of the second harmonic A_2 with propagation distance for A_l 6061-T6 and Al 7075-T651 are calculated in Figure 6.5. It shows that the magnitude of the second harmonic increases until it reaches the maximum cumulated propagation distance (504 mm for Al 6061-T6), after which it decreases due to dissatisfaction of the cumulative condition, i.e., the non-synchronization of the phase velocity between the harmonics at f_0 =100 kHz and $2f_0$ =200 kHz. It also shows that the spectral amplitude of the second harmonic A_2 does not increase linearly. In order to use Equation (6.23) to determine the relative nonlinearity parameter β' effectively, the linear regression analysis is utilized to determine the maximum linear cumulative propagation distance, where the coefficient of determination R^2 is set larger than 0.99 in the analysis (Wan et al., 2016). Based on the analysis, the maximum linear cumulative propagation distance is calculated (376 mm for Al 6061-T6) and within this distance the higher harmonics are considered 'cumulated'.

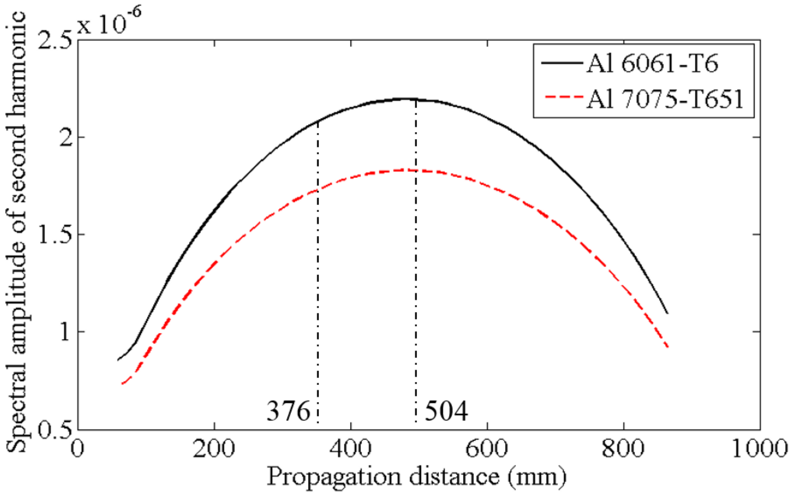

Fig. 6.5 Spectral amplitude of second harmonic against propagation distance for Al 6061-T6 and Al 7075-T651.

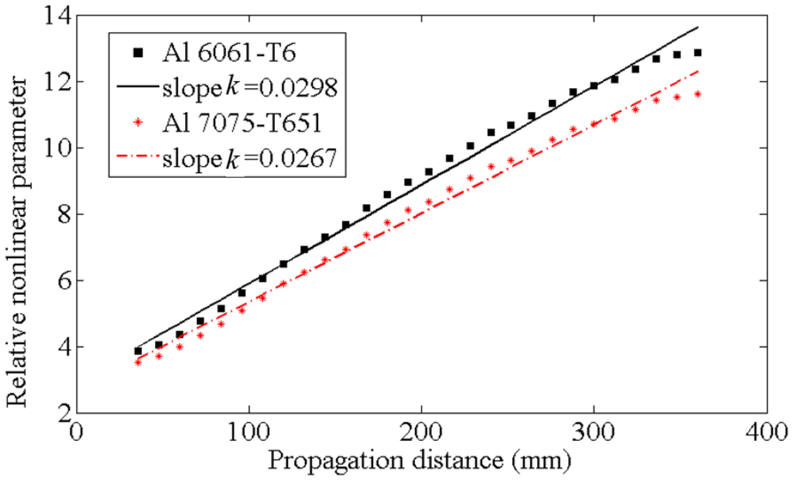

Fig. 6.6 The relative nonlinear parameter β' calculated from the measured displacement against the wave propagation distance for the S_0 incident guided wave at 100 kHz.

The calculated relative nonlinear parameter β' with propagation distance x and the corresponding linear regression are shown in Figure 6.6. k is the slope of the line, which is proportional to the nonlinear parameter β'. As shown in Figure 6.6, the slope k for the material Al 6061-T6 is larger than that of Al 7075-T651. Also, it is shown that the nonlinear parameter β' increases linearly, which indicates that the second harmonic of S_0 guided wave is cumulated in this propagation distance. Hence, the ratio of the nonlinear parameter of Al 6061-T6 to Al 7075-T651 is $\beta_{Al6061}/\beta_{Al7075} = k_{Al6061}/k_{Al7075}$ $= 0.0298/0.0267 = 1.116$, which is closed to the analytical result, i.e., 1.12, calculated using Equation (6.22). This shows that the SFE simulation is able to take into account the material and geometric nonlinearities in the guided wave simulations.

6.3.2 Validation of contact nonlinearity

This subsection validates the contact nonlinearity of the SFE simulation by comparing the SFE results with results calculated by conventional three-dimensional (3D) FE simulations. The material of the beam is Al 6061-T6 and the properties are shown in Table 6.1. The length L, width b and height h of the beam are 1000 mm, 6 mm and 12 mm, respectively. The crack is located at L_c = 500 mm and the crack depth is d_c =3 mm. The excitation signal is an f_0 = 50 kHz, narrow-band, 5-cycle sinusoidal tone burst modulated by a Hanning window (Aryan et al., 2016c). The S_0 guided wave is generated by applying the in-plane displacement at the left end of the beam. The displacement response is calculated at the same location as the excitation location. The simulation duration is long enough to cover the incident S_0 guided wave propagates from the excitation location to the right end of the beam, and then reflects back to the left end of the beam (the excitation and measurement location). 100 SFE beam elements are used to model the beam to ensure the convergence of simulation and each of SFE beam element has eight GLL nodes. The damping coefficient η is assumed to be 200 s^{-1}. The time step of the simulation is chosen at 2.5×10^{-8} s.

The conventional 3D FE simulations are carried out using the commercial FE software, ABAQUS v6.12-1, to simulate the wave propagation in the cracked beam. The eight-noded 3D solid brick elements (C3D8I) with the incompatible mode are used to model the cracked beam. The option of second-order accuracy is enabled in the incompatible mode in the simulations. The mesh size of the elements is 0.4mm×0.4mm×0.4mm to ascertain the stability of the FE simulations. The crack is modelled by duplicating the nodes at the crack interfaces (Soleimanpour and Ng, 2016b). The contact nonlinearity due to the breathing phenomenon is simulated by assigning the 'frictionless hard contact' property to the crack interfaces. The S_0 guided wave is excited by applying the in-plane nodal displacement at the FE nodes at the vertical surface of the left beam end. The excitation signal is the same as the SFE simulations. The explicit solver, ABAQUS/Explicit, is used to solve the dynamic problem. The time step is automatically controlled by ABAQUS/Explicit in the simulations.

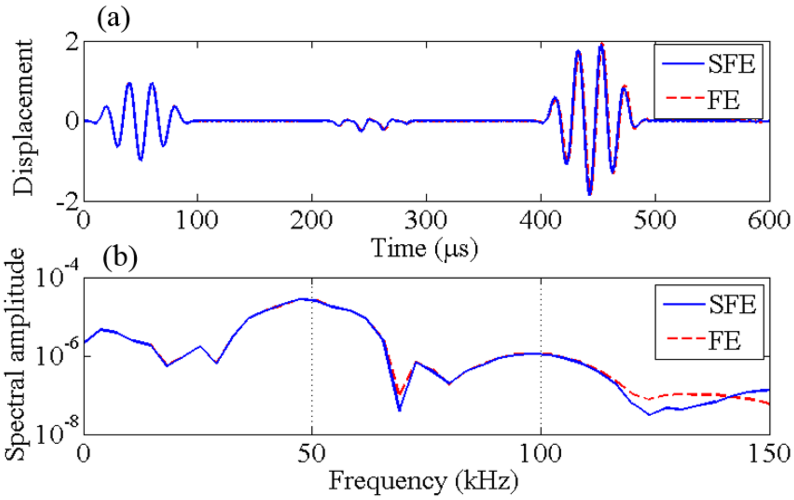

Fig. 6.7 Comparison of SFE and FE simulated results in (a) time-domain; (b) frequency domain.

The simulation results are shown in Figure 6.7. Figure 6.7(a) shows the response displacement in time-domain, which is normalized to the peak amplitude of the incident wave. There is good agreement between the results of the SFE and FE simulations. Figure 6.7(b) shows the FFT of the displacement response. The figure shows that the results of the SFE and FE have the same spectral amplitude of the second harmonic at $2f_0 = 100$ kHz. This demonstrates the accuracy of the proposed SFE method in simulating the nonlinear guided wave induced by the contact nonlinearity at the breathing crack.

6.4 Numerical case studies and discussions

A series of numerical case studies are carried out in this section to investigate the performance of the proposed SFE model. The performance of the SFE model in simulating the material and geometric nonlinearities is studied first, which investigates the influences of different numbers of cycles and amplitudes of the excitation signal on the generation of the second harmonic in Section 6.4.1. After that, the contribution of the material and geometric nonlinearities, and the contact nonlinearity to the second harmonic generation is studied in Section 6.4.2. The beam with length L=1000 mm, depth d=5 mm and width b=12 mm is simulated in this study and the material is assumed to be Al 6061-T6 and the material properties are shown in Table 6.1.

6.4.1 Second harmonic generation due to material and geometric nonlinearities

In this part, the influence of the geometric and material nonlinearities on the second harmonic generation is studied in Section 6.4.1.1. The influences of different numbers of cycles and the amplitudes of excitation signal on the second harmonic generation due to geometric and material nonlinearities are studied in Sections 6.4.1.2 and 6.4.1.3, respectively.

6.4.1.1 Influence of material and geometric nonlinearities

This section studies the influence of the material and geometric nonlinearities on the second harmonic generation. The excitation signal is a 100 kHz, narrow-band, 16-cycle sinusoidal tone burst modulated by a Hanning window. The S_0 guided wave is generated by applying the in-plane displacement with the maximum amplitude of 1×10^{-6} m to the left end of the beam, and the displacement response is measured at L_m= 500 mm. Based on Equation (6.17), the first term on the right hand side of the equation accounts for the material nonlinearity and the other three terms address the geometric nonlinearity. This section considers three different situations: 1) linear, 2) only geometrically nonlinear, and 3) nonlinear with both material and geometric nonlinearities. In the linear situation, the term Q^{NL}_{ijklmn} in Equation (6.15) is not considered in the simulation. For the geometrically nonlinear situation, the first term of right hand side of Equation (6.17), i.e. Q^{L}_{ijklmn} , is neglected. For the nonlinear situation that considers both material and geometric nonlinearities, all the terms at the right hand side of Equation (6.17) are considered in the simulations. The calculated time-domain displacement responses of these three situations are shown in Figure 6.8.

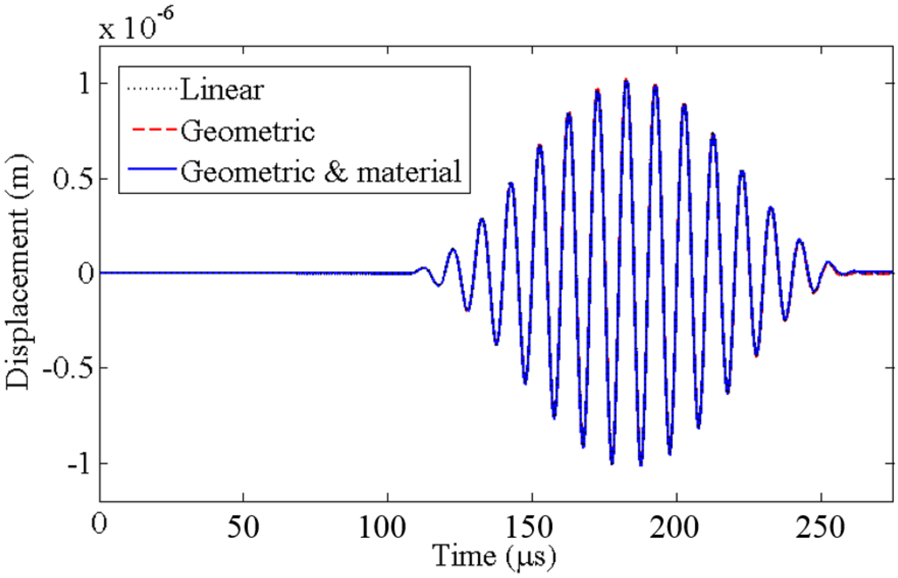

Fig. 6.8 The calculated time-domain displacement response at L_m=500 mm for linear situation, and situations consider only geometric nonlinearity, and both material and geometric nonlinearities in the SFE simulation.

From the time-domain signal shown in Figure 6.8, the difference between the nonlinear situations and the linear situation is hardly distinguished. Figure 6.9 shows the FFT of the calculated displacement responses at L_m=500 mm for the three aforementioned situations. Compared with the time-domain signal, the second harmonic in the nonlinear situation (with geometric and material nonlinearities) is clear observed. Furthermore, the results show that the spectral amplitude of the second harmonic for the situation considering both material and geometric nonlinearities is about 10 times greater than that of the situation considering only the geometric nonlinearity. This demonstrates that the second harmonic is mainly generated due to the material nonlinearity.

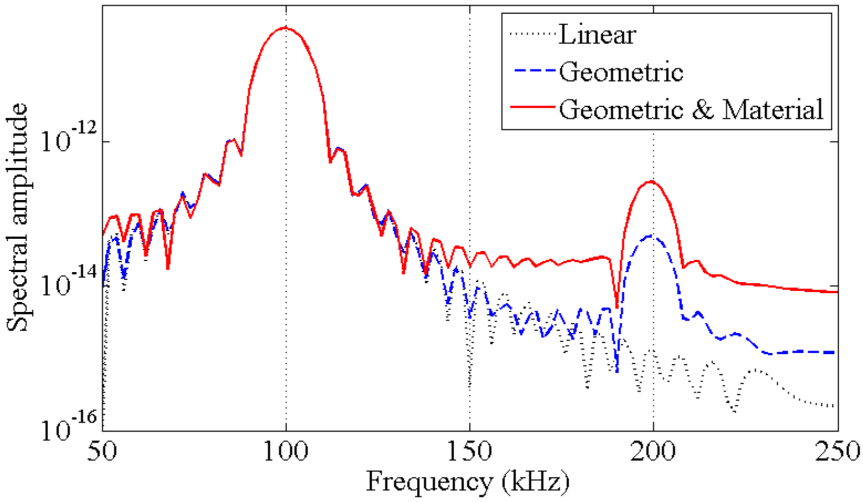

Fig. 6.9 FFT of the calculated displacement responses at L_m=500 mm for linear situation, and situations consider only geometric nonlinearity, and both material and geometric nonlinearities in the SFE simulation.

6.4.1.2 Influence of the numbers of cycles of the excitation signal

The influence of the numbers of cycles of the excitation signal on the generation of second harmonic due to material and geometric nonlinearities is studied in this section. The excitation signals with 8, 12, 16 and 20 cycles are considered in this study. The signal is a 100 kHz narrow-band sinusoidal tone burst modulated by a Hanning window. The S_0 guided wave is excited by applying the in-plane displacement with the maximal amplitude 1×10^{-6} m at the left end of the beam. The displacement responses are measured at L_m =500 mm. The FFT of the displacement responses for the cases considering different numbers of cycles of the excitation signals are shown in Figure 6.10. The results show that the bandwidth of the fundamental and the second harmonic become wider for excitation signal with less numbers of cycles and the amplitude of the second harmonic increases with the number of cycles.

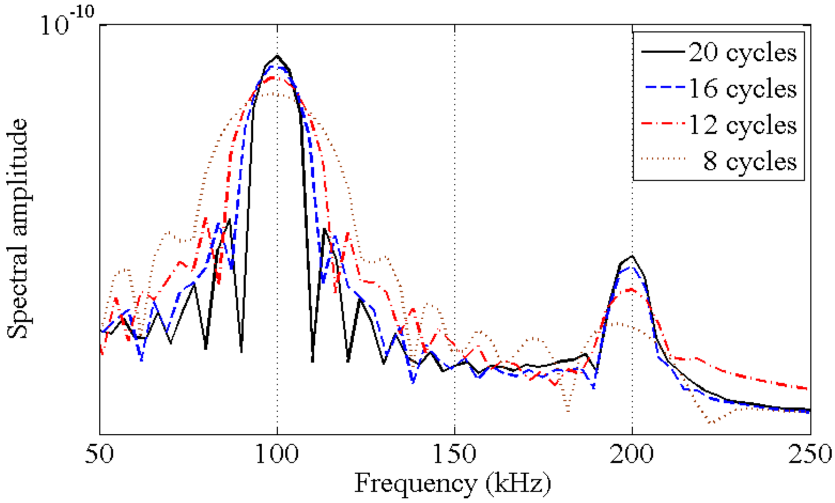

Fig. 6.10 FFT of the calculated displacement responses at L_m=500 mm for different excitation cycles.

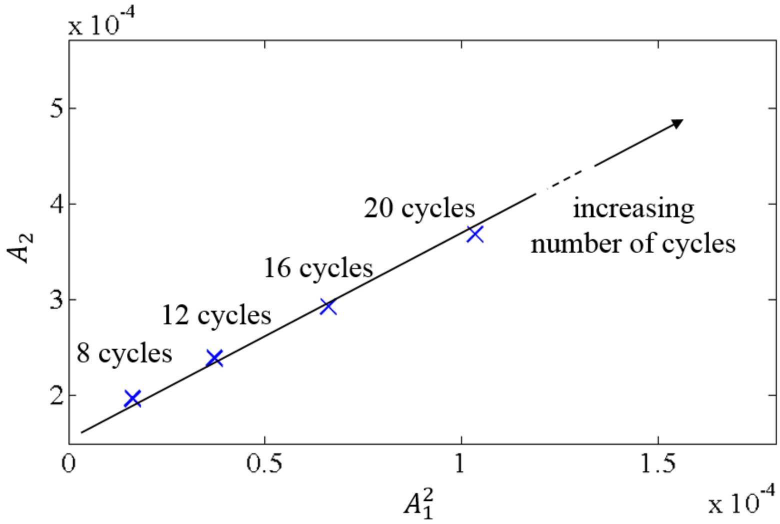

Fig. 6.11 The second harmonic amplitude versus the fundamental amplitude for varying number of cycles of the excitation signal.

Figure 6.11 shows the second harmonic amplitude versus the fundamental amplitude for different numbers of cycles of the excitation signal. Analytically, because the relative nonlinear parameter β' is a constant within the cumulated wave propagation distance x as shown in Equation (6.24), the ratio of the second harmonic amplitude to the square of the fundamental harmonic is also a constant from Equation (6.23). Therefore, the result is a straight line in Figure 6.11. There are good agreements between the analytical results and the SFE simulated results for different numbers of cycles. Overall, it is found that the magnitude of the second harmonic induced due to the material and geometric nonlinearities increases with the numbers of cycles of the excitation signal.

6.4.1.3 Excitation with different amplitudes

The influence of the amplitude of the excitation signal on the second harmonic generation due to geometric and material nonlinearities is studied in this section. The excitation signal applied at the left end of the beam is a 100 kHz narrow-band 16-cycle sinusoidal tone burst modulated by a Hanning window. Eight different amplitudes of the excitation signal are considered and magnitude increases from 1×10^{-6} m to 8×10^{-6} m with the step of 1×10^{-6} m. The displacement response is calculated at L_m =500 mm and the measured time duration is the same as that in Subsection 6.4.1.2. The amplitudes of the fundamental harmonic and second harmonic are extracted from the FFT of displacement responses. Figure 6.12 shows the second harmonic amplitude versus the fundamental amplitude for different excitation amplitudes, in which the asterisks denote the numerical results. The results in Figure 6.12 show that there is good agreement between results of SFE and the analytical results obtained from Equation (6.23). It is found that the second harmonic amplitude increases with the excitation amplitude.

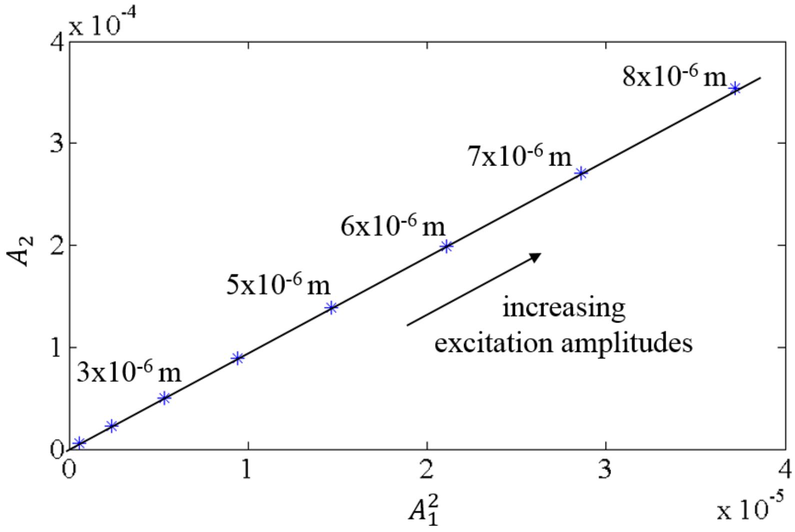

Fig. 6.12 The second harmonic amplitude versus the fundamental amplitude for varying excitation amplitudes.

6.4.2 Contribution of classical nonlinearity to contact nonlinearity

The contribution of the material and geometric nonlinearities, and contact nonlinearity in the second harmonic generation is studied in this subsection. The excitation signal is a 100 kHz, narrow-band, 5-cycle sinusoidal tone burst modulated by a Hanning window. The S_0 guided wave is excited by applying the in-plane displacement with the maximum amplitude of 1×10^{-6} m to the left end of the beam, and the displacement response is measured at L_m =0 mm. The breathing crack is located at L_c = 500 mm. Because the crack location L_c < 504 mm, it allows a simulation of the cumulated second harmonic generated from material and geometric nonlinearities as discussed in Section 6.3.1.

Two situations are considered: 1) only contact nonlinearity and 2) both material and geometric nonlinearities, and contact nonlinearity in the SFE simulation. The spectral amplitudes at the second harmonic as a function of normalized crack depth (d_c/h) are investigated for both situations. The short-time Fourier transformed (STFT) is used to obtain the spectral amplitude of the second harmonic induced by the crack. Figure 6.13(a) shows an example of the spectrogram obtained from STFT, and the corresponding time-domain displacement is shown in Figure 6.13(b). It should be noted that the amplitude of second harmonic guided wave reflected from the breathing crack is labelled as A_2 in Figure 6.13(a), which is normalized by amplitude of the fundamental harmonic A_1 of the incident guided wave.

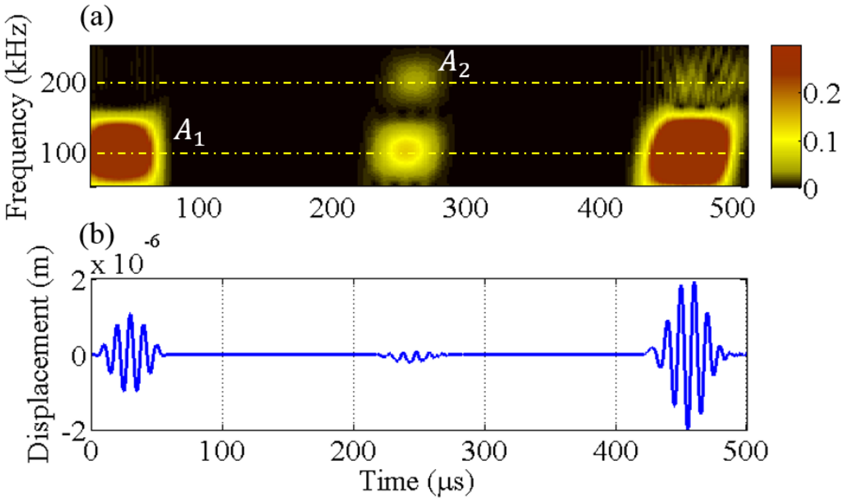

Fig. 6.13 (a) Spectrogram obtained by STFT and (b) the corresponding time domain displacement response.

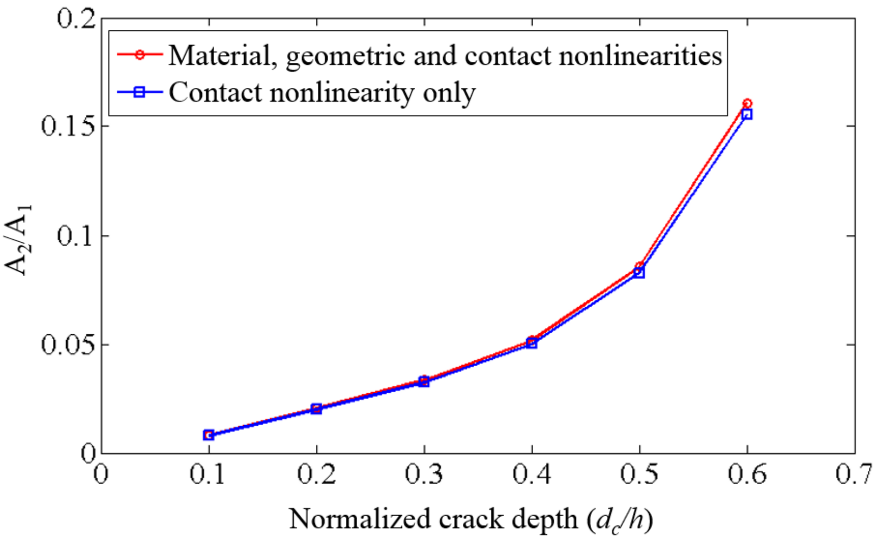

Fig. 6.14 Normalized second harmonic amplitude of the displacement responses as a function of normalized crack depth (d_c/h).

Figure 6.14 shows the ratio of the second harmonic amplitude of the wave reflected from the crack (A_2) to the fundamental harmonic amplitude of the incident wave (A_1) as a function of normalized crack depth (d_c/h). The results show that the amplitudes of the second harmonic calculated by the SFE model with the effect of both material and geometric nonlinearities, and contact nonlinearity are in general greater than that results calculated by the SFE model considering only the contact nonlinearity. In the case when the crack size is small, the second harmonic amplitude is mainly contributed by the contact nonlinearity. This can be explained by the fact that the amplitude of the wave reflected from the small size of the crack is small and Figure 6.12 shows that the contribution to the second harmonic amplitude by the material nonlinearity is linear proportional to the wave amplitude. As the amplitude of the reflected wave is small, the material nonlinearity has only a very small contribution to the second harmonic generation. In the case when the crack size is large, although the contribution of the material nonlinearity to the second harmonic generation is larger (because the amplitude of the reflected wave is larger), the second harmonic amplitude is still mainly contributed by the contact nonlinearity. The largest difference of the ratio of the second harmonic amplitude of the wave reflected from the crack to the fundamental harmonic amplitude of the incident wave is less than 3%.

6.5 Conclusions

This study has proposed a time-domain SFE modelling of second harmonic generation of nonlinear guided wave in beam structures, which allows take into account both material and geometric nonlinearities, and contact nonlinearity. Specifically, the material and the geometric nonlinearities have been modelled by adapting the constitutive relation between strain and stress using a second order approximation, and the contact nonlinearity resulted from a breathing crack has been simulated by a bilinear SFE crack model. The time-domain SFE simulations of the second harmonic generation due to material and geometric nonlinearities, and contact nonlinearity have been validated using analytical results and 3D FE simulations, respectively. The results show that the time-domain SFE method is able to provide an accurate prediction in the second harmonic generation.

A series of numerical case studies have been carried out to investigate the influence of the material and geometric nonlinearities and contact nonlinearity on the generation of second harmonic using the proposed SFE model. The numerical case studies have considered the generation the second harmonic due to the material and geometric nonlinearities. The results have shown that the material nonlinearity in the contribution to the generation of the second harmonic is much greater than geometric nonlinearity. In addition the amplitude of the second harmonic increases with the number of cycles and amplitude of the excitation signal. The numerical case studies have also investigated the amplitude of the second harmonic generation at a breathing crack, in which the time-domain SFE model takes into account both material and geometric nonlinearities and contact nonlinearity. The spectral amplitude of the second harmonic has been studied as a function of the normalized crack depth. The results have shown that the contribution of the material and geometric nonlinearities to the second harmonic is generally smaller that the contact nonlinearity. It has also shown that as the crack size becomes smaller, the second harmonic due to the material and geometric nonlinearities become smaller. In general the material and geometric nonlinearities can be ignored in the practice of damage identification. Overall the numerical case studies have gained insights into the second harmonic generation due to the material and geometric nonlinearities and contact nonlinearity. The findings of this study could further advance the development of damage detection using second harmonic generation of nonlinear guided wave.

Acknowledgement

This work was supported by the Australian Research Council (ARC) under Grant Numbers DP160102233 and DE130100261. The support is greatly appreciated.

References for Chapter 6

AN, Y. K. & SOHN, H. 2010. Instantaneous crack detection under varying temperature and static loading conditions. *Structural Control and Health Monitoring,* 17**,** 730-741.

ARYAN, P., KOTOUSOV, A., NG, C. T. & CAZZOLATO, B. 2016a. A baseline‐free and non‐contact method for detection and imaging of structural damage using 3D laser vibrometry. *Structural Control and Health Monitoring*.

ARYAN, P., KOTOUSOV, A., NG, C. T. & WILDY, S. 2016b. Reconstruction of baseline time-trace under changing environmental and operational conditions. *Smart Materials and Structures,* 25**,** 035018.

ARYAN, P., KOTOUSOV, A., NG, C. T. & CAZZOLATO, B. 2016c. A model‐based method for damage detection with guided waves. *Structural Control and Health Monitoring*.

BERMES, C., KIM, J.-Y., QU, J. & JACOBS, L. J. 2008. Nonlinear Lamb waves for the detection of material nonlinearity. *Mechanical Systems and Signal Processing,* 22**,** 638-646.

BRODA, D., STASZEWSKI, W. J., MARTOWICZ, A., UHL, T. & SILBERSCHMIDT, V. V. 2014. Modelling of nonlinear crack–wave interactions for damage detection based on ultrasound—A review. *Journal of Sound and Vibration,* 333**,** 1097-1118.

DENG, M. & PEI, J. 2007. Assessment of accumulated fatigue damage in solid plates using nonlinear Lamb wave approach. *Applied physics letters,* 90**,** 121902.

DZIEDZIECH, K., PIECZONKA, L., KIJANKA, P. & STASZEWSKI, W. J. 2016. Enhanced nonlinear crack‐wave interactions for structural damage detection based on guided ultrasonic waves. *Structural Control and Health Monitoring*.

HE, S. & NG, C. T. 2016. A probabilistic approach for quantitative identification of multiple delaminations in laminated composite beams using guided waves. *Engineering Structures,* 127**,** 602-614.

HE, S. & NG, C. T. 2017. Guided wave-based identification of multiple cracks in beams using a Bayesian approach. *Mechanical Systems and Signal Processing,* 84**,** 324-345.

HE, S. & NG, C. T. 2015. Analysis of mode conversion and scattering of guided waves at cracks in isotropic beams using a time-domain spectral finite element method. *Elec J Struct Eng,* 14**,** 20-32.

HERRMANN, J., KIM, J. Y., JACOBS, L. J., QU, J., LITTLES, J. W. & SAVAGE, M. F. 2006. Assessment of material damage in a nickel-base superalloy using nonlinear Rayleigh surface waves. *Journal of Applied Physics,* 99**,** 124913.

HONG, M., SU, Z., WANG, Q., CHENG, L. & QING, X. 2014. Modeling nonlinearities of ultrasonic waves for fatigue damage characterization: Theory, simulation, and experimental validation. *Ultrasonics,* 54**,** 770-778.

HUANG, T., ICHCHOU, M. & BAREILLE, O. 2012. Multi‐mode wave propagation in damaged stiffened panels. *Structural Control and Health Monitoring,* 19**,** 609-629.

JOGLEKAR, D. & MITRA, M. 2015. Analysis of nonlinear frequency mixing in 1D waveguides with a breathing crack using the spectral finite element method. *Smart Materials and Structures,* 24**,** 115004.

KOBER, J. & PREVOROVSKY, Z. 2014. Theoretical investigation of nonlinear ultrasonic wave modulation spectroscopy at crack interface. *NDT & E International,* 61**,** 10-15.

KUDELA, P., KRAWCZUK, M. & OSTACHOWICZ, W. 2007. Wave propagation modelling in 1D structures using spectral finite elements. *Journal of Sound and Vibration,* 300**,** 88-100.

KUDELA, P. & OSTACHOWICZ, W. 2009. A multilayer delaminated composite beam and plate elements: reflections of Lamb waves at delamination. *Mechanics of Advanced Materials and Structures,* 16**,** 174-187.

LAM, H. F. & YIN, T. 2010. Statistical detection of multiple cracks on thin plates utilizing dynamic response. *Engineering structures,* 32**,** 3145-3152.

LI, W. & CHO, Y. 2016. Combination of nonlinear ultrasonics and guided wave tomography for imaging the micro-defects. *Ultrasonics,* 65**,** 87-95.

LISSENDEN, C., LIU, Y., CHOI, G. & YAO, X. 2014. Effect of localized microstructure evolution on higher harmonic generation of guided waves. *Journal of Nondestructive Evaluation,* 33**,** 178-186.

LIU, S., BEST, S., NEILD, S. A., CROXFORD, A. J. & ZHOU, Z. 2012. Measuring bulk material nonlinearity using harmonic generation. *NDT & E International,* 48**,** 46-53.

LIU, Y., CHILLARA, V. K. & LISSENDEN, C. J. 2013. On selection of primary modes for generation of strong internally resonant second harmonics in plate. *Journal of Sound and Vibration,* 332**,** 4517-4528.

MAHAPATRA, D. R., SINGHAL, A. & GOPALAKRISHNAN, S. 2006. A higher-order finite waveguide model for spectral analysis of composite structures. *Computer methods in applied mechanics and engineering,* 195**,** 1116-1135.

MATLACK, K. H., KIM, J.-Y., JACOBS, L. J. & QU, J. 2011. Experimental characterization of efficient second harmonic generation of Lamb wave modes in a nonlinear elastic isotropic plate. *Journal of Applied Physics,* 109**,** 014905.

NAJIB, M. F. & NOBARI, A. S. 2015. Kissing bond detection in structural adhesive joints using nonlinear dynamic characteristics. *International Journal of Adhesion and Adhesives,* 63**,** 46-56.

NG, C. T. 2015a. On accuracy of analytical modeling of Lamb wave scattering at delaminations in multilayered isotropic plates. *International Journal of Structural Stability and Dynamics,* 15**,** 1540010.

NG, C. T. 2014. Bayesian model updating approach for experimental identification of damage in beams using guided waves. *Structural Health Monitoring,* 13**,** 359-373.

NG, C. T. 2015b. A two-stage approach for quantitative damage imaging in metallic plates using Lamb waves. *Earthquake and Structures,* 8**,** 821-841.

NORRIS, A. 1998. Finite-amplitude waves in solids. *Nonlinear acoustics,* 624.

NUCERA, C. & SCALEA, F. L. D. 2015. Modeling of Nonlinear Guided Waves and Applications to Structural Health Monitoring. *Journal of Computing in Civil Engineering,* 29.

OSTACHOWICZ, W. M. 2008. Damage detection of structures using spectral finite element method. *Computers & structures,* 86**,** 454-462.

PARK, C. S., KIM, J. W., CHO, S. & SEO, D.-C. 2016. A high resolution approach for nonlinear sub-harmonic imaging. *NDT & E International,* 79**,** 114-122.

PRUELL, C., KIM, J. Y., QU, J. & JACOBS, L. J. 2009. A nonlinear-guided wave technique for evaluating plasticity-driven material damage in a metal plate. *NDT & E International,* 42**,** 199-203.

PUTKIS, O. & CROXFORD, A. J. 2013. Continuous baseline growth and monitoring for guided wave SHM. *Smart Materials and Structures,* 22**,** 055029.

QIAN, Y. & MITA, A. 2007. Structural damage identification using Parzen - window approach and neural networks. *Structural Control and Health Monitoring,* 14**,** 576-590.

RAUTER, N., LAMMERING, R. & KÜHNRICH, T. 2016. On the detection of fatigue damage in composites by use of second harmonic guided waves. *Composite Structures,* 152**,** 247-258.

RUCKA, M. 2010. Experimental and numerical studies of guided wave damage detection in bars with structural discontinuities. *Archive of Applied Mechanics,* 80**,** 1371-1390.

RUCKA, M., WITKOWSKI, W., CHRÓŚCIELEWSKI, J. & WILDE, K. 2012. Damage detection of a T-shaped panel by wave propagation analysis in the plane stress. *Archives of Civil Engineering,* 58**,** 3-24.

SHEN, Y. & CESNIK, C. E. S. 2017. Modeling of nonlinear interactions between guided waves and fatigue cracks using local interaction simulation approach. *Ultrasonics,* 74**,** 106-123.

SHEN, Y. & GIURGIUTIU, V. 2014. Predictive modeling of nonlinear wave propagation for structural health monitoring with piezoelectric wafer active sensors. *Journal of Intelligent Material Systems and Structures,* 25**,** 506-520.

SOHN, H., LIM, H. J., DESIMIO, M. P., BROWN, K. & DERRISO, M. 2014. Nonlinear ultrasonic wave modulation for online fatigue crack detection. *Journal of Sound and Vibration,* 333**,** 1473-1484.

SOLEIMANPOUR, R. & NG, C.-T. 2016a. Locating delaminations in laminated composite beams using nonlinear guided waves. *Engineering Structures*.

SOLEIMANPOUR, R. & NG, C.-T. 2016b. Scattering of the fundamental anti-symmetric Lamb wave at through-thickness notches in isotropic plates. *Journal of Civil Structural Health Monitoring,* 6**,** 447-459.

SOLEIMANPOUR, R., NG, C. T. & WANG, C. H. 2016. Higher harmonic generation of guided waves at delaminations in laminated composite beams. *Structural Health Monitoring***,** 1475921716673021.

SOLODOV, I., WACKERL, J., PFLEIDERER, K. & BUSSE, G. 2004. Nonlinear self-modulation and subharmonic acoustic spectroscopyfor damage detection and location. *Applied physics letters,* 84**,** 5386-5388.

TADA, H., PARIS, P. C., IRWIN, G. R. & TADA, H. 2000. *The stress analysis of cracks handbook,* ASME press New York.

WAN, X., TSE, P., XU, G., TAO, T. & ZHANG, Q. 2016. Analytical and numerical studies of approximate phase velocity matching based nonlinear S0 mode Lamb waves for the detection of evenly distributed microstructural changes. *Smart Materials and Structures,* 25**,** 045023.

XIANG, Y., DENG, M. & XUAN, F.-Z. 2014. Creep damage characterization using nonlinear ultrasonic guided wave method: A mesoscale model. *Journal of Applied Physics,* 115**,** 044914.

XIANG, Y., DENG, M., XUAN, F.-Z. & LIU, C.-J. 2011. Experimental study of thermal degradation in ferritic Cr–Ni alloy steel plates using nonlinear Lamb waves. *NDT & E International,* 44**,** 768-774.

XU, F., ZHANG, Y., HONG, W., WU, K. & CUI, T. J. 2003. Finite-difference frequency-domain algorithm for modeling guided-wave properties of substrate integrated waveguide. *Microwave Theory and Techniques, IEEE Transactions on,* 51**,** 2221-2227.

YAMANAKA, K., OHARA, Y., OGUMA, M. & SHINTAKU, Y. 2011. Two-Dimensional Analyses of Subharmonic Generation at Closed Cracks in Nonlinear Ultrasonics. *Applied physics express,* 4**,** 076601.

YAN, D., NEILD, S. A. & DRINKWATER, B. W. 2012. Modelling and measurement of the nonlinear behaviour of kissing bonds in adhesive joints. *NDT & E International,* 47**,** 18-25.

YIN, T., LAM, H. F., CHOW, H. M. & ZHU, H. 2009. Dynamic reduction-based structural damage detection of transmission tower utilizing ambient vibration data. *Engineering Structures,* 31.

ŻAK, A. & KRAWCZUK, M. 2010. Assessment of rod behaviour theories used in spectral finite element modelling. *Journal of Sound and Vibration,* 329**,** 2099-2113.

ZHU, W., DENG, M., XIANG, Y., XUAN, F.-Z., LIU, C. & WANG, Y.-N. 2016. Modeling of ultrasonic nonlinearities for dislocation evolution in plastically deformed materials: Simulation and experimental validation. *Ultrasonics,* 68**,** 134-141.

ZHU, X. & RIZZO, P. 2013. Guided waves for the health monitoring of sign support structures under varying environmental conditions. *Structural Control and Health Monitoring,* 20**,** 156-172.

Chapter 7

Conclusions and recommendations

7.1 Conclusions

Damage detection is one of the key components for structural health monitoring (SHM). It provides valuable information of any damage and deterioration at the early stage. The model-based approach has the potential to provide satisfying damage identification results. However, existing modelling methods are hard to provide both accurate and efficient simulation for the model-based approach. The optimisation methods solve the inverse algorithm for the model-based approach also confront similar difficulty in the efficiency and accuracy in identifying multiple damages.

The research focus on developing and improving both the modelling and optimisation methods for the model-based approach. The major research contributions and outcomes of the thesis are listed as follows:

1. An efficient time-domain spectral finite element (SFE) model has been proposed to simulate the guided wave propagation and interaction with an open crack in a beam. An SFE crack element has been developed to accurately simulate the crack-wave interaction. The mode-converted guided wave induced by the crack is simulated by coupling the longitudinal, transverse and rotational displacement in the SFE crack element. Good agreement from finite element (FE) validation demonstrates the accuracy of the propose SFE model in simulating guided waves in the cracked beam for damage identification. Parametric studies provide physical insight into the crack-wave

interaction with different crack depth for both transmitted and reflected guided waves.

2. Multiple cracks identification in an aluminium beam has been achieved using the model-based approach. The developed SFE model with the developed SFE crack element has been successfully applied in the identification. The Bayesian methods implemented with the Transitional Markov Chain Monte Carlo (TMCMC) sampler has been proposed to solve the optimisation problem for the model base approach. The number of cracks, the location and the size of the crack have been identified with providing corresponding uncertainties. Successful experimental verification using the guided wave data obtained from laser vibrometer proved the practicability of the proposed approach for isotropic material.

3. Multiple delaminations identification in a composite beam has been successfully conducted using the model-based approach. The developed SFE model has been extended to simulate guided waves in delaminated composite beams. The Bayesian methods combined with the Subset simulation (SuS) has been proposed to identify the multiple delaminations in the beam. The number of delaminations, and the location and the length of each delamination have been accurately characterised with quantifying associated uncertainties. Successful experimental identification using laser vibrometer proved the practicability of the proposed approach for composite structures.

4. The developed SFE method has been extended to the simulation of nonlinear guided waves resulted from classical nonlinearity and contact nonlinearity, respectively. The effectiveness of the simulation of the classical nonlinearity has been validated analytically, where that of the contact nonlinearity has been validated numerically using FE method. Parametric studies provide physical insights into the performance of nonlinear guided waves resulted from contact

nonlinearity. The results suggest that when using S0 guided wave as incident wave, the mode-converted second harmonic is more sensitive to small cracks. Parametric studies also show that the classical nonlinearity has minor contribution to the generation of the second harmonic compared with that of contact nonlinearity. This indicates that the classical nonlinearity can be ignore in the identification of contact-type damages.

7.2 Recommendations

It should be noted that there are some limitations in this research. Further work is recommended for the future research as follows:

1. The model-based approach only employs the one-dimensional (1D) SFE method. This limits the accurate identification of damages with more complicated geometry. Future work is suggested to extend the SFE method to three-dimensional (3D) situation and implement more precise damage model.

2. The 3D SFE model is, however, inefficient for the model-based approach. This is because in the process of identification, there will be numerous (e.g. 50,000) times of simulation using model-based approach. The sum up of the computational time for each simulation run will result in a large amount of time. Therefore, future effort is suggested to focus on improving the efficiency of the modelling method.

3. The nonlinear guided wave simulated by the 1D SFE method has not been experimentally validated due to the laboratory limitation. Thus, the proposed SFE model is open to further improvement when the experimental data is available.

4. The nonlinear guided wave has not been employed for the model-based damage identification. The nonlinear guided wave is more sensitive to small and contact-type of damage. It has the potential to achieve better accuracy for the damage identification. Therefore, further research is suggested to apply the nonlinear guided wave to the model base approach for damage identification.

Appendix: Copies of Papers (as published)

HE, S. & NG, C. T 2015. Analysis of mode conversion and scattering of guided waves at cracks in isotropic beams using a time-domain spectral finite element method. *Elec J Struct Eng*, 14, 20-32.

NOTE:
This publication is included on pages 5 – 44 in the print copy of the thesis held in the University of Adelaide Library.

HE, S. & NG, C. T. 2017. Guided wave-based identification of multiple cracks in beams using a Bayesian approach. *Mechanical Systems and Signal Processing*, 84, 324-345.

NOTE:
This publication is included on pages 45 – 98 in the print copy of the thesis held in the University of Adelaide Library.

HE, S. & NG, C. T. 2016. A probabilistic approach for quantitative identification of multiple delaminations in laminated composite beams using guided waves. *Engineering Structures*, 127, 602-614.

NOTE:
This publication is included on pages 99 – 142 in the print copy of the thesis held in the University of Adelaide Library.